Leandro Augusto Grandin Pereira

Synthesis and genetic algorithm-based optimization to reduce dry weight and footprint of topsides oil & gas processing

São Paulo
2021

Leandro Augusto Grandin Pereira

Synthesis and genetic algorithm-based optimization to reduce dry weight and footprint of topsides oil & gas processing

Thesis submitted to the Escola Politécnica de São Paulo for partial fulfillment of the requirements for the degree of Doctor of Science

São Paulo
2021

Leandro Augusto Grandin Pereira

Synthesis and genetic algorithm-based optimization to reduce dry weight and footprint of topsides oil & gas processing

Versão Corrigida

Thesis submitted to the Escola Politécnica da Universidade de São Paulo for the partial fulfillment of the requirements for the degree of Doctor of Science

Research area: Mechanical Engineering on Energy and Fluids

Supervisor: Prof. Dr. Jurandir Itizo Yanagihara

São Paulo
2021

Este exemplar foi revisado e corrigido em relação à versão original, sob responsabilidade única do autor e com a anuência de seu orientador.

São Paulo, _____ de _____ de _____

Assinatura do autor: _____

Assinatura do orientador: _____

Catalogação-na-publicação

Pereira, Leandro Augusto Grandin
Synthesis and genetic algorithm-based optimization to reduce dry weight and footprint of topsides oil & gas processing system / L. A. G. Pereira -- versão corr.—São Paulo, 2021.
255 p.

Tese (Doutorado) - Escola Politécnica da Universidade de São Paulo. Departamento de Engenharia Mecânica.

1.Algoritmos Genéticos 2.Plataforma Continental – projeto. 3.Petróleo – processamento I. Universidade de São Paulo. Escola Politécnica. Departamento de Engenharia Mecânica II.t.

I dedicate this thesis to my wife Mariane, my daughter Stela, my mother Sandra and my father Valmiro (in memoriam).

ACKNOWLEDGEMENTS

I would like to acknowledge Professor Jurandir Itizo Yanagihara, who supervised my activities and enhanced the quality of this work.

I also would like to acknowledge professors José Luis Paiva, Antônio Marinho, Pedro Pessoa, and Leandro Salviano, who contributed to the development of this thesis.

I also would like to thank Dr. Edgard Malta, Dr. Felipe Ruggeri, and Dr. Cassiano Aimoli, who also provided valuable contribution.

I would like to acknowledge Prof. Kazuo Nishimoto, who stimulated me to obtain a PhD degree and provided the required infrastructure in the Tanque de Provas Numérico (TPN) laboratory.

I would like to acknowledge the Research Center for Gas Innovation (RCGI), which provided me several opportunities in the past years.

I also would like to thank my wife Mariane and my daughter Stela for their support and patience.

I thank my mother Sandra and my father Valmiro (in memoriam) for the education they provided me, which was key to enable development of my career.

I thank my father-in-law Silvestre and my mother-in-law Célia (in memoriam).

Finally, I also acknowledge Universidade de São Paulo.

Abstract

Key-words: *topsides design, process synthesis, process optimization, genetic algorithm.*

Oil and gas will remain relevant in the incoming decades, with several new offshore platforms being necessary to satisfy demand, maintaining a high level of greenfield projects activity. The platform design can be accelerated and improved if the typical knowledge-based design is substituted by a framework comprising process synthesis and optimization.

A general-purpose mathematical programming process synthesis and optimization tool, with an immediate application in topsides oil & gas processing systems, has been developed in Matlab, comprising elements such as thermophysical properties estimation, process and preliminary mechanical design of several equipment, development of a superstructure and extraction of flowsheets for two types of fluids (oil with low and high CO_2 content), parametric analysis, and genetic algorithm-based optimization seeking maximization of oil production and minimization of equipment dry weight and footprint.

For each of the assessed fluids in the given inlet conditions, maximum oil production is approximately equal regardless the flowsheet, with an asymptotic behavior between oil production and equipment dry weight or footprint, demonstrating the possibility of achieving oil production very close to the maximum found in the respective Pareto Fronts while significantly reducing equipment dry weight and footprint.

Considering the best attributes of assessed flowsheets for oil with low CO_2 content, the flowsheet combining pre-compression with TEG dehydration presented equipment dry weight 25.6% and 57.7% lower and equipment footprint 13.6% and 10.6% lower than the other two assessed flowsheets, which relied on TEG (without pre-compression) and molecular sieve (with pre-compression). Considering the best attributes of flowsheets for oil with high CO_2 content, the flowsheet combining acetate cellulose membranes (bulk CO_2 separation) with MEA (CO_2 polishing) showed the best compromise between equipment footprint, equipment dry weight and energy consumption, with equipment dry weight 22% and equipment footprint 26% lower

than a flowsheet solely relying on acetate cellulose membranes. A flowsheet solely relying on MEA chemical absorption for CO_2 removal presented the best equipment footprint and dry weight, but heating demand is extremely high compared to flowsheets that adopt membranes.

The developed process synthesis and optimization tool is efficient, powerful and can be expanded to cover different inlet conditions, production systems and attributes, achieving objectives such as footprint reduction, dry weight reduction, decarbonization, and cost reduction.

Resumo

Palavras-chave: *projeto de topsides, síntese de processos, otimização de processos, algoritmo genético.*

Petróleo e gás se manterão relevantes nas próximas décadas, com várias novas plataformas marítimas sendo necessárias para satisfazer a demanda, mantendo um nível elevado de desenvolvimento de novos projetos. O projeto de plataforma pode ser acelerado e melhorado se o típico método de projeto baseado em conhecimento substituído por uma estrutura contemplando síntese e otimização de processos.

Uma ferramenta de programação matemática de propósito geral para síntese e otimização de processos foi desenvolvida em Matlab, com aplicação imediata em sistemas marítimos de processamento de petróleo e gás, contemplando elementos como estimativa de propriedades termofísicas, projeto de processo e projeto mecânico preliminar de diversos equipamentos, desenvolvimento de uma superestrutura e extração de fluxogramas de processo para dois tipos de fluidos (petróleo com baixo e alto teor de CO_2), análise paramétrica, e otimização baseada em algoritmo genético buscando a maximização de produção de petróleo e a minimização do peso seco e área de equipamentos.

Para cada um dos fluidos avaliados nas condições de entrada fornecidas, a produção máxima de petróleo é aproximadamente igual independente do fluxograma avaliado, com um comportamento assintótico entre produção de petróleo e peso seco ou área dos equipamentos, demonstrando a possibilidade de se atingir produção de petróleo muito próxima ao máximo encontrado na fronteira de Pareto enquanto reduzindo significativamente o peso seco e área dos equipamentos.

Considerando os melhores atributos dos fluxogramas avaliados para o fluido de baixo teor de CO_2, o fluxograma que combina pré-compressão com desidratação por TEG apresentou, em relação aos fluxogramas baseados em TEG sem pré-compressão e peneira molecular com pré-compressão, peso seco de equipamentos 25.6% e 57.7% respectivamente menor e área de equipamentos 13.6% e 10.6% respectivamente menor. Considerando os melhores atributos dos fluxogramas avaliados para o fluido com alto teor de CO_2, o fluxograma que combina membranas de acetato de celulose (separação do excesso de CO_2) e absorção química por MEA

(polimento de CO_2) mostrou o melhor compromisso entre produção de petróleo, peso seco de equipamentos, área de equipamentos e consumo de energia, com peso seco e área de equipamentos respectivamente 22% e 26% menores do que o fluxograma que somente emprega membranas de acetato de celulose para remoção de CO_2. O fluxograma que emprega exclusivamente absorção química por MEA para separação de CO_2 apresentou o menor peso seco e a menor área de equipamentos, entretanto o consumo de calor é extremamente elevado comparado aos fluxogramas que empregam membranas de acetato de celulose.

A ferramenta de síntese e otimização de processos desenvolvida é eficiente, poderosa e pode ser expandida para outras condições de entrada, diferentes sistemas de produção, diferentes atributos, atingindo objetivos como redução de área, redução de peso seco, descarbonização e redução de custo.

List of Figures

List of Tables

List of Abbreviations

BS&W – Basic Sediments & Water

FPSO – Floating Production Storage and Offloading

Mbpd – million barrels per day

RVP – Reid Vapor Pressure

SS – Semi-Submersible

TLP – Tension Leg Platform

SPAR – Single Point Anchor Reservoir

List of Symbols

All units in SI, except where indicated in the text.

A	cross section area
a	activity
A_{gc}	cross section area for gas continuous phase
A_{HE}	heat exchange area
A_{lc}	cross section area for liquid continuous phase
A_{oc}	cross section area for oil continuous phase
a_{pack}	packing specific area
$A_{t,ext}$	tube external area
$A_{t,int}$	tube internal area
A_{wc}	cross section area for free water continuous phase
C	molar concentration per volume
C_{H2O}	associated gas water concentration
cl	clearance between shell and tube bundle
Cp	heat capacity coefficient at constant pressure
Cp_{id}	ideal heat capacity coefficient at constant pressure
Cp_{res}	residual heat capacity coefficient at constant pressure
Cp_t	fluid Cp in the tube
Cv	heat capacity coefficient at constant volume
Cv_{id}	ideal heat capacity coefficient at constant volume
Cv_{res}	residual heat capacity coefficient at constant volume
D	internal diameter
D	mass diffusivity
D_{baffle}	baffle diameter
d_{ec}	distance between electrodes
$D_{int,ST}$	internal diameter of stripper column
d_p	diameter of dispersed droplet
dp_{pack}	packing nominal size
$D_{t,ext}$	tube external diameter
$D_{t,int}$	tube internal diameter
E	electric field
e_{go}	separation efficiency of dispersed gas in oil continuous phase
Enh	Enhancement factor
e_{og}	separation efficiency of dispersed oil in gas continuous phase
e_{ow}	separation efficiency of dispersed oil in free water continuous phase
e_{pack}	packing void fraction

e_{wo}	separation efficiency of dispersed free water in oil continuous phase
f	fugacity
f	friction factor
Fe	iron content
$f_{dc,i}$	fraction of droplet class i
f_l	liquid fugacity
F_p	packing factor for flooding condition estimation
f_v	vapor fugacity
g	gravity acceleration
H	enthalpy
h	level
H_2O_o	outlet water percentage (mass basis)
h_c	level of continuous phase
HE	heat exchange
He	Henry constant
HE_{cool}	heat exchanged to cool adsorbent and vessel
HE_{heat}	heat exchanged to heat adsorbent and vessel
H_{form}	formation enthalpy
$H_{g,ads}$	adsorption gas enthalpy
$H_{g,reg}$	regeneration gas enthalpy
H_{id}	ideal enthalpy
H_{res}	residual enthalpy
h_s	shell convection coefficient
h_t	tube convection coefficient
IG	information gain
I_s	incrustation resistance in shell
I_t	incrustation resistance in tube
K	equilibrium constant
k	ideal gas Cp/Cv
k_{ij}	binary interaction coefficient
L	length of separator
l_{ae}	length of the section above the electrodes
L_{bc}	space between baffles
l_{be}	length between the lower part of the electrodes and the water level
L_{bi}	distance between the first baffle and the beginning of the shell
L_{bo}	distance between the last baffle and the end of the shell
l_c	baffle length
l_e	length of the electrodes
LPB	packing channel base
LPH	packing channel height
LPS	packing channel width
L_t	tube length

M	molar flowrate
MW	molecular weight
n	molar composition of a given phase
Nb	number of baffles
nc	total number of components
N_e	number of electrodes
N_p	number of pass divider lanes
n_p	number of tube passes
n_{dc}	number of droplet classes
N_{ss}	number of sealing strips
Nu_t	Nusselt number in the tube
P	pressure
P_c	critical pressure
Pr_t	Prandtl number in the tube
Q	volumetric flowrate
Q_d	volumetric flowrate of dispersed fluid in a given continuous phase
Q_{dw}	required volumetric flowrate of dilution water
Q_g	volumetric flowrate of gas stream
$Q_{g,std}$	volumetric gas flowrate in standard conditions
Q_{gc}	volumetric flowrate of gas continuous phase
$Q_{go,out}$	outlet volumetric flowrate of dispersed gas in oil continuous phase
Q_l	volumetric liquid flowrate
Q_{lc}	volumetric flowrate of liquid continuous phase
Q_{mp}	volumetric flowrate of multiphase stream
Q_o	volumetric flowrate of oil stream
$Q_{og,out}$	outlet volumetric flowrate of dispersed oil in gas continuous phase
$Q_{ow,out}$	outlet volumetric flowrate of dispersed oil in free water continuous phase
Q_{TEG}	TEG solution volumetric flowrate
Q_w	water volumetric flowrate
Q_{we}	emulsioned water volumetric flowrate
Q_{wf}	free water volumetric flowrate
$Q_{wo,out}$	outlet volumetric flowrate of dispersed free water in oil continuous phase
R	Avogadro constant of ideal gas
r	radius
REC	recovery in permeate
Re_s	Reynolds number in the shell side
Re_t	Reynolds number in the tube
S_{dw}	natural salinity of dilution water
S_o	oil salinity
S_{res}	salinity of dilution water after dissolving the required salt
S_{sat}	salinity in saturation state

S_w	water salinity
T	temperature
T_b	normal boiling point
T_c	critical temperature
T_r	reduced temperature
$t_{r,v}$	vertical residence time
T_{ref}	reference temperature
t_{RP}	residence time between electrodes
T_{sm}	average temperature in the shell
U	voltage (in electrostatic coalescer design)
U	global heat transfer coefficient (in heat exchanger design)
V	vapor molar fraction
V_{ADS}	required volume of adsorbent
$V_{dc,i}$	volume of dispersed droplet of class i
v	flow speed
V_l	necessary volume in separator for the liquid phase
VOL_{es}	volume of electrostatic section
v_p	droplet speed at vertical direction
v_t	flow speed in the tube
w	acentric factor
W	mass flowrate
$W_{g,reg}$	regeneration gas mass flowrate
W_{H2O}	water adsorption capacity
W^{so}	water content of a sour gas
W^{sw}	water content of a sweet gas
x	liquid molar composition (in initial part of section 5.1)
X	TEG mass concentration
y	vapor molar composition
z	molar composition of raw stream
Z	compressibility factor (in initial part of section 5.1)
Z_{av}	average compressibility factor

Greek symbols

α_{gl}	dispersion coefficient of gas in liquid continuous phase
α_{go}	dispersion coefficient of gas in oil continuous phase
α_{lg}	dispersion coefficient of liquid in gas continuous phase
α_{og}	dispersion coefficient of oil in gas continuous phase
α_{ow}	dispersion coefficient of oil in free water continuous phase
α_{sat}	percentage of saturation dilution water is allowed to achieve
α_{wo}	dispersion coefficient of free water in oil continuous phase
β	ratio between length and diameter
Δ_{Hvap}	heat of vaporization
δ_{pack}	packing formation factor
ΔP_{fl}	pressure drop in flooding condition
ΔP_s	pressure drop on the shell side
ΔP_t	pressure drop on the tube side
ΔW_s	mass of salt to be diluted by dilution water
η	isentropic efficiency
λ	thermal conductivity
λ_t	tube material thermal conductivity
μ	dynamic viscosity
μ_c	continuous phase dynamic viscosity
μ_o	oil dynamic viscosity
μ_t	dynamic viscosity in the tube
ν	molar volume
ξ	chemical reaction advancement degree
ρ	density
ρ_{100}	density at 100 °F
ρ_{35}	density at 35 °F
ρ_{60}	density at 60 °F
ρ_c	continuous phase density
ρ_{dw}	dilution water density
ρ_g	gas density
ρ_o	oil density
ρ_p	dispersed droplet density
ρ_{pack}	packing density
ρ_r	reduced density
ρ_t	fluid density in the tube
ρ_w	water density
σ	surface tension
φ	rate of H_2S deposition

ψ	TEG circulation rate

Subscripts

g	gas
i	a given component
in	inlet
j	a given component
l	liquid
out	outlet
v	vapor

CONTENTS

Chapter 1

1. Introduction and motivation

The design of new oil & gas offshore production platforms will remain a relevant activity at least in the incoming decades, as oil and natural gas will remain important energy sources, as shown in Figure 1-1. World oil production is expected to increase to **103.4 Mbpd** in 2040 (IEA, International Energy Agency, 2018-A).

Figure 1-1: Total primary energy demand in the new policies scenario

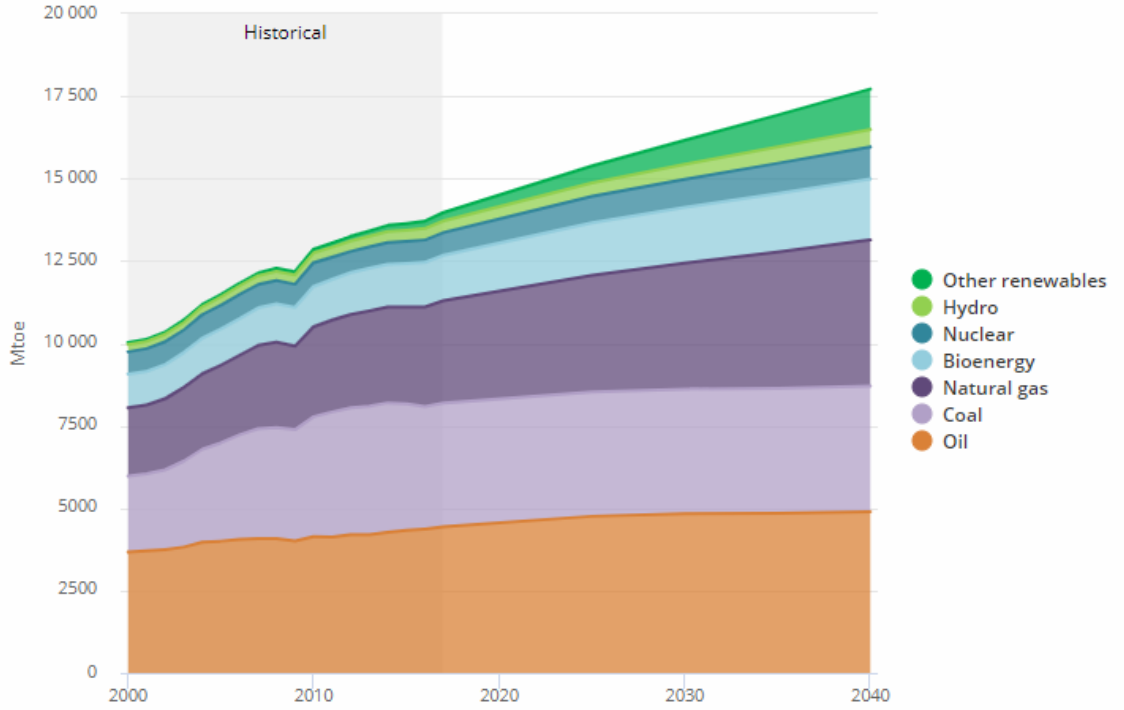

Source: IEA-International Energy Agency (2018-A)

Offshore fields account for a significant portion of oil and natural gas production, as seen in Figure 1-2. Deepwater (>500 m water depth) and ultra-deepwater (>1500 m water depth) production require floating platforms, such as FPSO, SS, TLP, and SPAR. In shallow water production (<=500 m), fixed platforms, which extend to the seabed, can compete with floating units, especially if the water depth does not exceed 150 m.

Figure 1-2: Global offshore oil and natural gas production by water depth in the new policies scenario

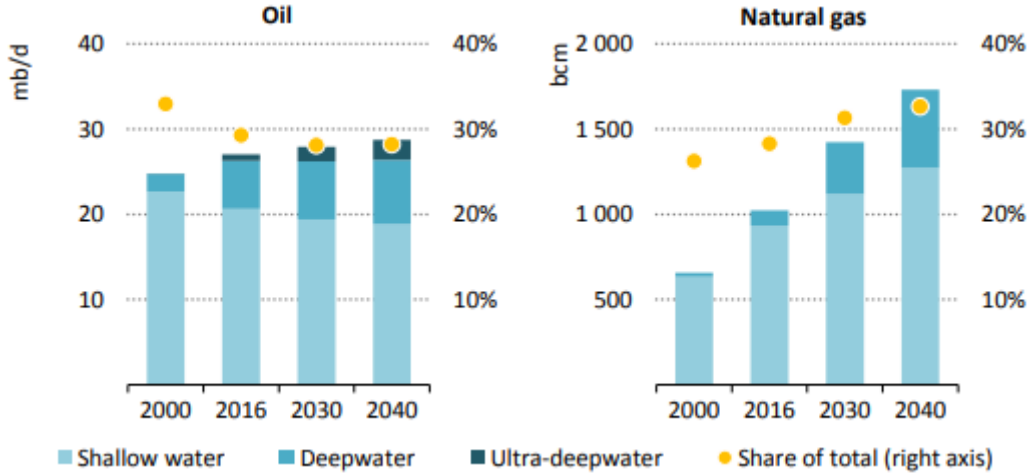

Source: IEA-International Energy Agency (2018-B)

The functions of the offshore production platform are hosting the system that processes the produced and injected streams, typically referred as a topsides processing system, and store specified oil. Part of such systems can also be installed directly on the seabed, being referred as subsea processing systems. The produced stream typically contains oil, water, gas and sand, and the injected stream composition will depend on the field recovery strategy. Typical injection streams are composed of seawater, hydrocarbon gas, and CO_2. In addition, some types of platforms can also store the produced oil, such as the ship-shaped FPSO shown in Figure 1-3:

Figure 1-3: Ship-Shaped FPSO example

The design life of such platforms is not very high. In the case of FPSOs, the average design life is 15 to 25 years (Marine Link, 2015; Tanker Shipping & Trade, 2013). Considering the future oil and natural gas demand, the relevant participation of offshore production and the typical design life of offshore platforms, it can be concluded that there is a significant level of new offshore platform design activities in the incoming decades.

Regarding ship-shaped FPSOs, the hull designer will have two options with respect to the hull: converting an existing oil tanker or design and built a new hull. Such options are respectively referred as “converted hull” and “new-built”. A converted hull will necessarily impose constraints related to the footprint and weight of the processing system. Such constraints may not be so severe in new-builts. Despite the use of a converted hull or a new built, the processing system designer will face constraints related to maximum footprint and weight imposed on the hull by the processing system. Ultimately, the designers will have the objective of maximizing oil production while observing the aforementioned constraints. Other constraints may be imposed by the business, such as carbon footprint, measured as equivalent kg of CO_2 per barrel of oil equivalent.

Various authors show the advantages of a compact topsides processing system. The lower the topsides weight the higher are the deepwater floating platform options to develop a field (D'Souza & Basu, 2011). In case a liquefied natural gas system can be made more compact, the platform motions will cause fewer disturbances to its performance (Hwang, Roh & Lee, 2013). In certain cases, such as high CO_2 high GOR (gas-oil ratio) oil fields found in Brazilian pre-salt cluster, the topsides processing system required larger footprint to cope with gas treatment.

Process system engineering is an interdisciplinary field, focusing on the design and operation of complex production systems. It involves at least five different topics: process simulation, conceptual design/process synthesis, process control, process operations, and optimization (Grossmann & Harjunkoski, 2019). Process synthesis is a systematic approach aiming at conceiving the best process configuration according to established performance criteria, based

on the characteristics of the raw materials, the desired products and its respective specifications, and the technologies available.

Conceptual engineering of processing systems typically starts from pre-existing traditional configurations that inspire certain variations, which are then simulated in commercial software such as Aspen HySys (Allahyarzadeh-Bigdoli et al., 2018; Hwang, Roh & Lee, 2013). Alternatively, process synthesis methods and further intensification/integration/optimization tasks can be used to generate processing configurations.

Conceptual engineering involves at least modeling and simulation and may involve optimization depending on the designer choice. The three tasks are hardly performed by single software. In certain cases, modeling is split into at least two software (Reis, et al., 2017), as the commercial process simulator may not contain all desired process technologies, requiring development of add-ins or use of a second software. Modeling, simulation and optimization are typically executed by coupling a commercial process simulator to software that contains the desired optimization algorithm (Allahyarzadeh-Bigdoli et al., 2018; Hwang, Roh & Lee, 2013). Another approach is when modeling, simulation and optimization are executed in single software, which tends to reduce optimization time compared to coupling of two or more software. In such case, the chosen software must contain the thermodynamic, process technologies and optimization models. Matlab® is an example of software that contains optimization models and allows modeling and simulation of any other necessary elements.

The rise of digitalization and artificial intelligence (AI) opens a new frontier for the design of any system, including oil & gas processing facilities. The design of an oil & gas processing system comprises much more than process design. It also includes activities related to disciplines such as process instrumentation and control, process safety, mechanical design, flow assurance, electrical design, and structural design. Such activities can be simple, such as selecting a temperature transmitter to equip a separation vessel, or very complex, such as a CFD study to investigate the path of hydrocarbon gas in case of leakage in the platform. In an analysis of artificial intelligence application in chemical

engineering problems, the author states that AI-based models are becoming an essential part of the modeling arsenal (Venkatasubramanian, 2019). It may be explained by the availability of more powerful and easy-to-use software and hardware. Conceptual design tends to not demand very complex engineering tasks such as CFD simulations, so developing a single platform for conceptual design of topsides processing systems aided by artificial intelligence should lead to relevant benefits. Parameterized models driven by optimization methods such as genetic algorithms are part of a concept named generative design (Nordin, 2018). It allows the exploration of a larger design space in addition to support design generation, achieving benefits such as efficiency (multiple design instances in limited time), cost reduction (reduced time and labor), optimization, accuracy, and consistency (Singh & Gu, 2012).

In this work it is developed a new mathematical programming tool for process synthesis, sensitivity analysis, simulation and optimization of topsides processing systems.

The text is structured as follows:

Chapter 2 presents the objectives of this work.

Chapter 3 presents a literature review about process synthesis, integration, intensification and optimization. It includes examples of conceptual design in oil & gas production but also other industries.

Chapter 4 presents the methodology adopted in this work, including explanations about two parametric analyses techniques and the genetic algorithm.

Chapter 5 presents how the thermophysical properties of the various streams involved in an oil & gas processing system were estimated, including hydrocarbon and CO_2 dominated, seawater, brine, MEA (monoethanolamine) solution and TEG (triethylene glycol) solution.

Chapter 6 presents how each equipment has been modeled, including process and mechanical design. It includes a screening analysis of the process design

parameters of certain technologies, seeking reduction of the number of variables to be optimized.

Chapter 7 presents the developed process synthesis and optimization framework, explaining how the different processing technologies have been integrated in order to form the processing systems that were modeled, simulated and optimized. Such processing systems comprise oil and gas treatment, which form the core of the topsides processing system. It also presents the optimization results, including a comparison between the various selected processing systems in terms of maximum oil production, dry weight and footprint.

Chapter 8 presents the conclusions and suggested future developments.

Chapter 2

2. Objectives

The main objective of this work is to execute a sensitivity analysis and optimization of typical topsides oil and gas processing plants to reduce the dry weight and footprint while maintaining near maximum oil production.

The main contributions are:

- Dry weight and footprint minimization of typical topsides processing plants;
- Sensitivity analysis utilizing two methods for comparison and validation purposes: regression tree and smoothing-spline analysis of variance;
- Development of a new mathematical programming tool in Matlab, centralizing process synthesis, simulation and genetic algorithm-based optimization;
- Development of a topsides oil & gas processing system superstructure, which aims at representing all possible processing systems, constrained to the considered equipment;
- Process modeling of several oil & gas processing technologies, some of them not available in the most traditional process simulators (Aspen HySys, UniSim), allowing estimation of process performance, equipment dry weight and equipment footprint;
- Inclusion of vendor's information to estimate compression weight and footprint based on power and flowrate. It is known that compression imposes significant weight to the platform;
- Development of a robust and fast thermophysical properties estimator taking advantage of matrix calculations in Matlab®, including use of validated properties from vendors for fluids such as TEG solution and MEA solution;
- Quick estimation of the processing system outputs (oil production, equipment dry weight, equipment footprint) when changes in key parameters occurs, such as specifications of products and rejects or characteristics of inlet fluids.

Chapter 3

3. Literature review

In this chapter, various examples of advanced methods to improve conceptual design of processing systems are presented. Considering the context of this work, it was searched for relevant publications in conceptual design of offshore and onshore oil & gas production, liquefied natural gas (LNG), oil refining, gas processing, petrochemicals production, and renewable industry. The literature review related to the estimation of thermophysical properties and modeling of process technologies are shown along chapters 5 and 6, respectively.

3.1. **Engineering design process**

Typically, large industrial projects follow a stage-gated approach, divided into front-end engineering design (FEED) and execution. FEED is typically divided in 3 phases, named feasibility, conceptual design, and basic design. In the front-end loading (FEL) method, they are respectively referred as FEL 1, FEL 2, and FEL 3 (Independent Project Analysis, 2013). In FEL 2, the key goal is to assess various alternatives and select a concept that is further assessed during basic design, being the last real opportunity to modify or kill a project without substantial economic damage because during FEL 3 the rate of expenditure rises rapidly (Independent Project Analysis, 2013).

Typical deliveries of FEL 2 (conceptual design) include block flow diagrams (preliminary or completed), process flow diagrams (preliminary), plot plans (started or preliminary), heat & material balances (started or preliminary) (AACE International, 2011). Process system engineering discipline covers at least five different topics (Grossmann & Harjunkoski, 2019): process simulation, conceptual design/process synthesis, process control, process operations, and optimization. It is the key to perform a sound conceptual design.

3.2. **Process synthesis**

Process Synthesis is a systematic approach to screen process configurations according to defined performance criteria, characteristics of the raw materials, the desired products and its respective specifications, and the technologies available (Baldea, 2015; Chen & Grossmann, 2017; Cremaschi, 2015; Farkas, Rev & Lelkes, 2005; Skiborowski, 2018; Yuan & Chen, 2012).

Examples of process synthesis methodologies are total enumeration of an explicit case, tree search in the space of design decisions, evolutionary methods, superstructure optimization, targeting, problem abstraction, and combinations of these (Yuan & Chen, 2012). Process synthesis has been evolving, taking advantage of advancements in computer science, allowing more layers of rigor to be considered, such as optimization, economics, and control (Martín & Adams II, 2019). The use of process synthesis is recommended to accelerate the transition between petroleum-derived fuels to biorenewable-derived fuels (Yuan, Chen & Gani, 2013). There is a lack of general-purpose mathematical programming synthesis tools akin to Aspen for flowsheet simulation, with few alternatives in the market such as ICAS, PROSYN and PNS Editor (Chen & Grossmann, 2017).

The first process synthesis methods were evolutionary in nature, whereby heuristics and engineering judgment were used on a base case process flowsheet to propose enhancements by adding or modifying process units one at a time, limiting the exploration to the neighborhood of the base case (Chen & Grossmann, 2017). There is strong reliance on a set of rules based on a combination of experience, insights and engineering knowledge to come up with a feasible process alternative that will likely be sub-optimal (Tula, Eden & Gani, 2015). Some of the most common examples of application lie in the area of heat exchanger network (Martín & Adams II, 2019). Such methods are also referred as knowledge-based methods.

Two classes of approaches emerged to address the limitation of the knowledge-based methods: optimization-based methods (Chen & Grossmann, 2017; Cremaschi, 2015) and hybrid methods (Tula, Eden & Gani, 2015).

Optimization-based methods rigorously search through a proposed design space for optimal configuration, still subject to limitations related to the definition of appropriate search space, suitable degree of approximation and resolution of the resulting optimization problems (Chen & Grossmann, 2017), usually limited to moderately sized problems (Tula, Eden & Gani, 2015). Various authors propose how to implement an optimization-based method. Three major steps are necessary: postulation of a set of process alternatives represented by a superstructure, its formulation as a mathematical programming model, and determination of the optimal configuration by solving the model with an optimization algorithm (Chen & Grossmann, 2017). A systematic framework has been proposed based on 3 stages, where process integration and intensification are only used in the last stage (Bertran et al., 2017). A decision-making systematic framework was developed for the synthesis and design of processing networks under uncertainty (Quaglia et al., 2013).

Hybrid methods use the physical insights from knowledge-based methods, narrowing the search space and decomposing the synthesis problem into a collection of related but smaller mathematical problems (Tula, Eden & Gani, 2015).

A common task in all these frameworks is the need to develop a superstructure, which should incorporate all potentially useful unit operations and all relevant interconnections (Wu, Henao & Maravelias, 2016), containing all plausible processing alternatives (Demirel, Li & Hasan, 2017). Systematic methods for superstructure generation are needed to ensure that a comprehensive yet concise design space is defined (Chen & Grossmann, 2017). Many authors proposed superstructures to generate flowsheet options (Albahri et al., 2018; Chen & Grossmann, 2017; Li, Demirel & Hasan, 2018; Yeomans & Grossmann, 1999; Yuan & Chen, 2012).

A superstructure can be represented in various manners, two commonly methods are the State Task Network (STN) and State Equipment Network (SEN), but variations can be developed (Wu, Henao & Maravelias, 2016). Typically, superstructures are manually developed based on the expertise of the designers, but approaches have been emerging to automate the process

(Demirel, Li & Hasan, 2017), which starts from fundamental constituents of unit operations until representing the superstructure as a result of the developed process configurations.

An example of STN is shown in Figure 3-1. In such network, state nodes (initial, pure, intermediate) are connected by different processing tasks (in this case only separation). Equipment assignment is handled implicitly in the model, allowing single equipment performing multiple tasks. The blue square box either indicates a splitter, which leads to at least two processing options for the inlet stream, or a mixer, to which at least two streams having the same components converge.

Figure 3-1: State-task network example

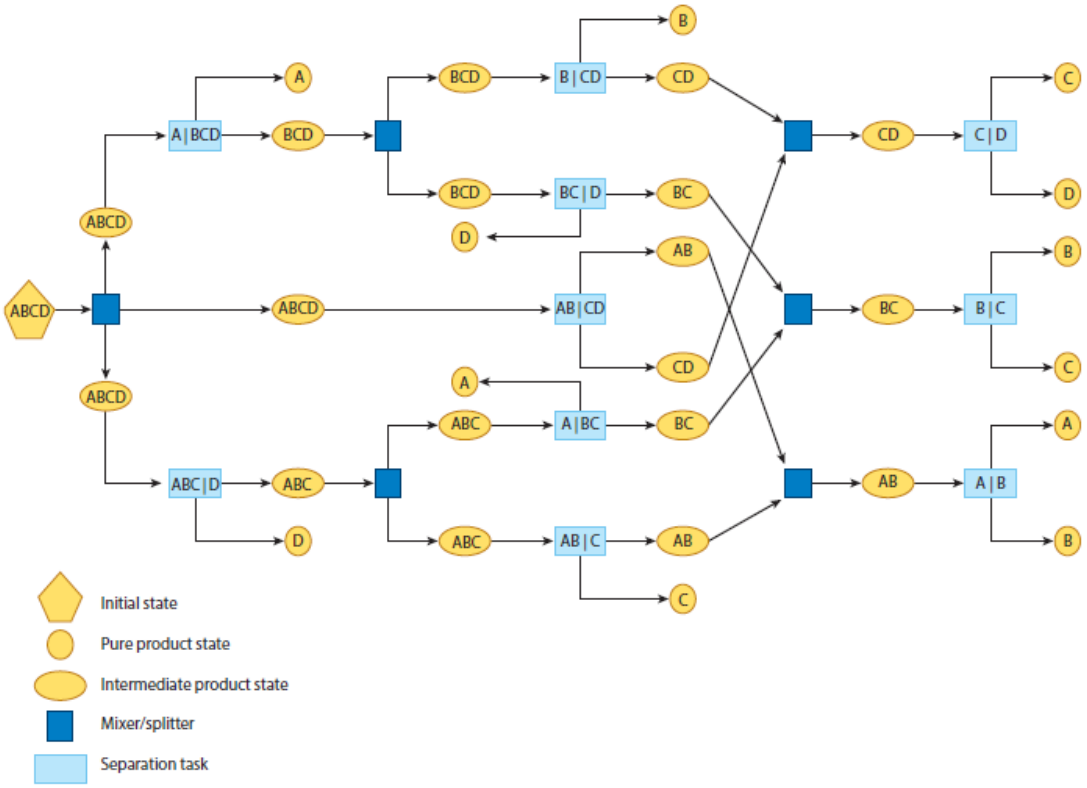

Source: Chen & Grossmann (2017)

A SEN includes the equipment considered in the process synthesis, as shown in Figure 3-2, and may be better than STN in certain cases.

Figure 3-2: State-equipment network example

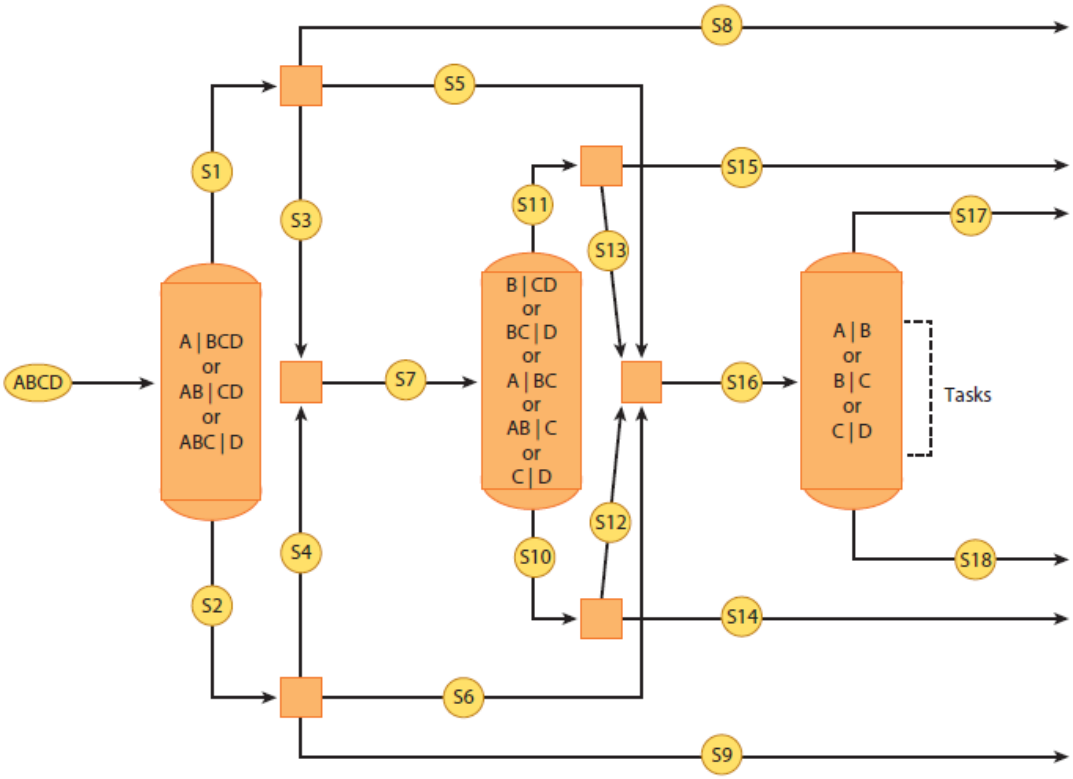

Source: Chen & Grossmann (2017)

It is understood that, after defining one or more feasible processes in any of the process synthesis methods above, process optimization, integration, and intensification can be applied in order to further assess the performance of each of the feasible processes. The next paragraphs show some examples of conceptual engineering work that adopted any of the three aforementioned process synthesis methods: optimization-based, knowledge-based, and hybrid.

Regarding optimization-based models, a mixed-integer linear programming (MILP) approach was used to determine the configuration of a new petroleum refinery, considering 96 different technologies based on 3 conventional schemes, generating a total of more than 2 million process alternatives that arose from a decomposition-based state-task network superstructure (Albahri et al., 2018). The authors used simplified correlations represented by linear equations to represent product yields of process units and decomposed the superstructure into 3 processing pools in order to speed-up convergence. A MINLP formulation proposed by Gooty, Agrawal & Tawarmalani (2019) for the optimization of multicomponent distillation configurations relied on global solver

BARON. The authors divided the design into three phases, named screening, simulation and intensification. In the screening phase the superstructure arose from a matrix method (Shah & Agrawal, 2010). A process synthesis and global optimization framework was developed to determine the most profitable routes of producing liquid fuels from natural gas through competing technologies, including heat, power and water integration (Tso et al., 2018). The authors had to develop simplified input-output models for certain technologies that only had complex models available, unsuitable to be used in an optimization framework. Similar work was based on surrogate models for microchannel reactors in order to enable optimization (Onel et al., 2017). An optimization-based framework was developed for simultaneous process synthesis and heat integration, creating a superstructure consisting of master reaction stages and lower-level separation stages, determining optimal reaction pathways based on MILP to find the most profitable bio-based platform and its production pathways (Kong & Shah, 2017). A process synthesis-intensification framework for the development of sustainable membrane-based operations was proposed, involving up to two steps of process synthesis in order to conceive a base case (if necessary) and identify alternatives to improve sustainability aspects of the base case (Babi et al., 2014).

Regarding knowledge-based methods, a generic liquefaction mixed refrigerant natural gas liquefaction cycle was conceived based on typical configuration strategies (Hwang & Lee, 2014). Such generic scheme was the base case for the proposition of 27 variations, which were optimized in commercial process simulator Aspen HySys in order to minimize power. Certain researchers developed several process alternatives derived from pre-existing base cases in order to separate ethylbenzene from styrene, coupling commercial process simulator Aspen Plus and Matlab, using the genetic algorithm to minimize total annual cost (Li et al., 2019).

Regarding hybrid methods, the group contribution approach used for chemical property estimation inspired development of a method to synthesize chemical processes (Tula, Eden & Gani, 2015). A combinatorial algorithm was employed to generate the superstructure of all process alternatives, which were compared in order to select the most promising. Finally, the most promising alternatives

were assessed in rigorous simulators (like PROII) for further refinement and optimization. A combined methodology has been developed for the synthesis and analysis of topological pathways for the processing of microalgae, based on main approaches of hierarchical and mathematical programming process synthesis (González-Delgado, Kafarov, El-Halwagi, 2015).

3.3. **Process integration**

Process integration is focused on enhancing the use of raw materials and utilities (energy, water), contributing to the reduction of negative consequences to the environment. Examples of techniques are Pinch Analysis (a heat integration technique), and mass integration (Baldea, 2015; Dunn & El-Halwagi, 2003; Li, Demirel & Hasan, 2018).

A general mathematical model addressed various process integration problems such as mass integration, heat integration, and simultaneous mass and heat integration (Li, Demirel & Hasan, 2018). The process units were represented by blocks arranged in a two-dimensional grid, allowing the necessary interactions regarding mass and energy flows. The mathematical model is formulated as a MINLP problem with the minimization of total annual cost as objective.

3.4. **Process intensification**

Process intensification is defined by several authors (Baldea, 2015; Lutze et al., 2010). The key differences compared to Process Integration are additional focus on compactness and the use of certain techniques and methods for the drastic improvement of efficiency of a single unit or device (Keil, 2018; Portha, Falk & Commenge, 2014).

Process integration focuses on connecting different units with fixed operations in the presence of material holdups and recycling, while process intensification enables multi-tasking by combining reaction, separation or other phenomena within a single unit (Demirel, Li & Hasan, 2017). Process intensification can be divided in local and global, where local means improvement of efficiency of a single unit or device and global means the holistic overall process-based intensification (Portha, Falk & Commenge, 2014). Global intensification is understood to present many similarities to Process Integration, but a key

difference would be that in a global intensification the process is mostly comprised of equipment that were intensified by local intensification techniques.

3.5. **Process optimization**

In the majority of the aforementioned process synthesis frameworks, process optimization is involved. It is applied to select certain process configurations from all possible alternatives that arise from a superstructure and/or to assess the most promising configurations more rigorously. In the screening of process configurations, simplified linear models may be used (Albahri, et al., 2018; Kong & Shah, 2017), but more rigorous assessment will require treating non-linear non-convex behavior of the desired optimization objectives, leading to the need of global optimization methods.

Process optimization comprises the use of methods to minimize or maximize an objective function that relates the process parameters to be optimized (such as cost, weight, footprint, energy) and the process design variables (such as operational pressure in given equipment). Optimization techniques can be categorized as local or global, constrained or unconstrained, single objective or multi-objective, deterministic or stochastic.

Global optimization methods can be divided into two broad categories: deterministic and stochastic (Arora et al., 1995). According to the authors, deterministic methods are not very useful since they are not applicable to general problems. Stochastic methods, on the other hand, are widely applied in global optimization. They are divided in 3 categories: global random search, stochastic assumptions about the objective function, and heuristics/meta-heuristics (Zilinskas & Zhigljavsky, 2016).

Some of the heuristic global optimization algorithms are based on analogies with natural processes, such as simulated annealing, genetic, and particle swarm methods. Genetic-based methods were used in process synthesis based conceptual engineering (Li et al., 2019), in a specific process optimization (Allahyarzadeh-Bigdoli et al., 2018), and in a specific multi-objective optimization aiming at maximizing oil production, and minimizing water production and energy consumption (Liu, Gao & Wang, 2015).

The simulated annealing algorithm mimics the process of heating and cooling a metal to increase size of its crystals and reduce their defects (Jia & Lichti, 2017). During the search of the global minimum, the initial candidate solution is perturbed so new solutions in its vicinity are obtained. The new solutions are accepted if they are better than the initial candidate or worse but with a certain probability that defines the dynamic threshold for accepting the worse solution (Tenne, 2017).

The particle swarm algorithm mimics swarm behavior in birds flocking and fish schooling to guide the particles to search for the global optimal solutions, adopting three basic behaviors: separation, alignment and cohesion. It is effective in global search, it is insensitive to scale of design variables, and tends to converge fast and prematurely in mid optimum points (Wahab, Meziani & Atyabi, 2015).

The genetic algorithm mimics the natural selection process, using the concept of the survival of the fittest. It is a population based process where the members of the population (chromosomes) are ranked according to their fitness. A new population is formed by use of specific evolutionary operators such as crossover, mutation, and reproduction (Wahab, Meziani & Atyabi, 2015). Various multi-objective genetic-based algorithms exist, such as the fast and elitist multi-objective algorithm NSGA-II (Deb et al., 2002), the controlled elitist available in Matlab (a variant from NSGA-II), and the improved NSGA-II (Liu, Gao & Wang, 2015). Some advantages of the genetic algorithm are limited parameter setting and initialization from a set of possible solutions instead of a single solution, but convergence is slow since crossover and mutation are random processes (Wahab, Meziani & Atyabi, 2015).

3.6. **Other topsides process design**

This topic covers research related to topsides process design, in order to collect information of the main methods, tools and tasks performed.

A typical high GOR high CO_2 topsides oil & gas processing system has been optimized, aiming at reduced fuel consumption (Allahyarzadeh-Bigdoli et al., 2018). The researchers coupled commercial process simulators Aspen HySys

and GateCycle with Esteco ModeFrontier, utilizing the genetic algorithm in optimization. No process synthesis related activities were found in such work.

A methanol production plant in a FPSO was simulated and optimized, proposing a flowsheet apparently from experience obtained in other similar methanol production processes (Kim et al., 2014). Tonkovich et al. (2008) also proposed a flowsheet for methanol production in FPSOs, in this case based on microchannel reactors. No process synthesis related activities were found in such publications.

Reis et al. (2018) assessed CO_2 removal by combination of acetate cellulose membranes and chemical absorption (MDEA+Piperazine) in transient GOR and CO_2 fraction, concluding that such processing scheme provides flexibility when gas production decreases and CO_2 fraction increases along the field lifetime.

Allahyarzadeh-Bigdoli et al. (2019) optimized energy consumption in three different conditions over the field life, achieving relevant fuel gas consumption reduction in all cases.

Veloso et al. (2018) optimized an ORC (organic rankyne cycle) system for energy recovery from low temperature streams, achieving 2,063 kW power production from the MCU (main compressor unit) aftercooler stream based on R245CB2 fluid.

The topsides system may be enhanced by layout optimization. Souza et al. (2019) optimized the processing plant layout of a certain Brazilian FPSO applying mixed integer linear programming (MILP), achieving 27.4% piping cost reduction. Sung-Kyoom et al. (2017) also optimized a processing plant layout, applying the genetic algorithm to achieve better arrangements than manual designs

Other relevant publications regarding FPSO design are related to optimization of staged separation pressures by genetic algorithm (Ghaedi et al., 2014), and minimization of water production and energy consumption while maximizing oil production, also using the genetic algorithm (Liu et al., 2015).

3.7. **Summary of findings**

According to this literature review, no process synthesis related activities have been used in the determination of an optimal configuration for a topsides oil & gas processing system. Optimization methods are used, but they rely on process configurations based on previous experience.

Another interesting finding is the lack of general-purpose mathematical programming synthesis tools (Chen & Grossmann, 2017), a gap that this work will contribute to close.

.

Chapter 4

4. Methodology

A synthesis and optimization method is proposed aiming at identifying the bets topsides oil & gas processing system in terms of equipment dry weight, equipment footprint and oil production given the characteristics of the inlet streams, the required specifications of the outlet streams, the technologies available and any other considered constraints. The framework is shown in Figure 4-1.

4.1. **Inlet and outlet characteristics**

The first level is comprised of four elements:

- collect information of inlet streams, such as pressure, temperature, composition and flowrates;
- collect specifications of outlet streams, such as RVP and BS&W for oil, export pressure and maximum CO_2 content for export gas;
- identify the equipment that will form the superstructure, typically equipment with high technology readiness levels;
- thermophysical properties estimation.

4.2. **Equipment models**

The second level is formed by the development of equipment models, based on information available in recognized publications. For certain equipment, a parametric analysis is used to verify if any of the initial design inputs can be held constant in order to reduce optimization complexity.

4.3. **Superstructure**

The third level is formed by the development of the superstructure, which is a representation aiming at capturing all possible flowsheets considering the available equipment and the inlet and outlet streams information. The

superstructure considers process integration measures such as material recycling and heat recovery.

4.4. Selection of flowsheets

The fourth level is comprised by the selection of certain flowsheets from the superstructure. In such level, the superstructure can be coded in order to automatically extract all possible flowsheets.

4.5. Selection of most complex flowsheet

In the fifth level, for a given fluid, it is selected the flowsheet that enables the parametric analysis of all parameters initially deemed optimizable.

4.6. Design of experiments

In the sixth level, a design of experiments (DOE) dataset is obtained in order to run the objective function in order to perform a screening analysis on system level for the most complex flowsheet selected in the previous level. The SOBOL sequence was chosen to generate the DOE dataset.

4.7. Screening analysis and determination of initial population

In the seventh level, a screening analysis on system level is performed aiming reduction of optimization complexity, verifying if any of the design inputs can be held constant and therefore discarded from the optimization. Two parametric analysis techniques are used: decisions trees and smoothing spline analysis of variance (SS-ANOVA). In addition, a set of feasible designs is obtained in order to provide initial populations for the genetic algorithm based optimization.

Figure 4-1: Synthesis and optimization method

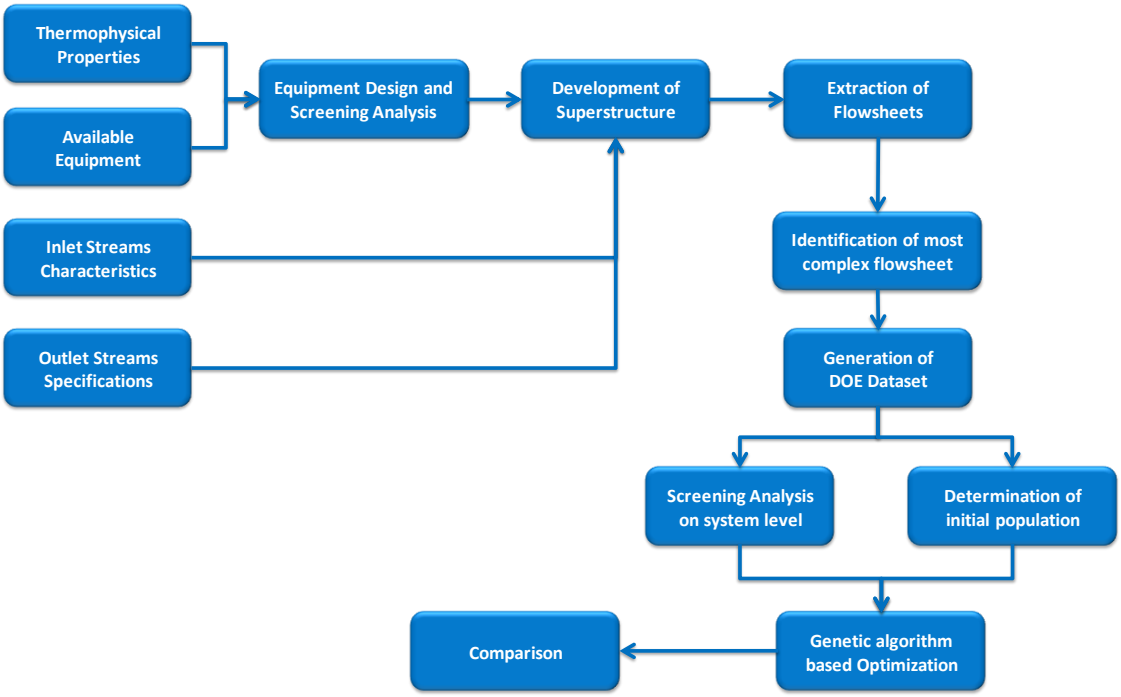

Source: author

4.7.1. Decision trees

A decision tree is a supervised machine learning model, where the input data that may explain how the output behaves is broken down by making decisions (Li, 2019).

The splitting of cases into groups at each level is guided by a measure of impurity. A group is called pure if all cases have the same value of the dependent variable, and it is called impure if an equal number of cases belong to a different value of the dependent variable (peak of impurity). If the group is pure, that part of the tree is terminated, leading to a terminal node. If the group is impure, it must be decided if it can become a terminal node or if it can be split using one of the independent variables. One popular measure of impurity is the entropy impurity, given below (Ma, 2018):

$$i(\tau) = -\sum P(c_j) \cdot \log_2 P(c_j) \qquad 4.7\text{-}1$$

In such equation, the term $P(c_j)$ is the probability that a case has a certain value of the dependent variable. The impurity is calculated for the two partitions

(left and right) of the parent node. Another popular impurity is the Gini measure of dispersion (Ma, 2018):

$$i(\tau) = 1 - \sum P(c_j)^2 \qquad 4.7\text{-}2$$

The tree will grow based the reduction of impurity, starting from the root node, analyzing each independent variable as a potential candidate to split the root node into two child nodes. Such analysis can use different values of a given independent variable, verifying which leads to the highest reduction of impurity. After all independent variables are considered, the one with the highest reduction of impurity is selected to split the root node into two child nodes. The same process is repeated with the child nodes (Ma, 2018).

The tree theoretically can grow until each terminal node has a single value of the dependent variable, so the number of terminal nodes is equal to the size of the dependent variable dataset. In order to prevent the tree from growing too large, a cost-complexity measure is adopted, increasing the penalty as the tree grows larger. The tree will stop growing depending on the adopted stopping criteria. Typically, it is verified if any of the independent variables can split a node that is statistically significantly different from a random split. Another approach is called validation, when the tree is grown with a certain part of the dataset, and the other part is used to validate the tree. The larger the tree the lower the error, but at a certain size the error may bound back due to overfitting, so when the error reaches the first minimum it may be the time to stop the tree from growing (Ma, 2018).

Stopping splitting a node comes at the cost of not knowing if further splitting such node by using other independent variables would lead to a relevant reduction of impurity. The strategy to avoid premature termination is to let the tree grow until the minimum impurity standard is met everywhere in the tree. Then, each pair of child nodes is analyzed in order to verify if relevant reduction of impurity is achieved, otherwise such nodes are pruned from the tree, and the respective parent node becomes a tentative terminal node (Ma, 2018).

The tree may also be adjusted in order to consider prior knowledge about the behavior of a certain population (for instance, it may be expected that certain

individuals have more chance of being classified as A instead of B) and the consequences of misclassification (for instance, misclassifying an individual as smoker instead of non-smoker may be worse than misclassifying an individual as non-smoker instead of smoker). The impurity measure can be modified in order to consider such aspects, affecting how the tree is grown (Ma, 2018).

A regression tree is a type of decision tree where the dependent variable is continuous, while a classification tree is a type of decision tree where the dependent variable is a categorical variable. In regression trees, the within-node variance is the impurity measure used to split nodes, as seen below, where y_i is the value of the dependent variable for case i and $y.$ is the node mean of the dependent variable (Ma, 2018).

$$i(\tau) = \sum (y_i - y.)^2 \qquad \text{4.7-3}$$

Such impurity measure is calculated for the parent and the two child nodes. The larger the sum of the impurities of the child nodes the better is the split, so the independent variable that lead to the largest summed impurities of the child nodes is selected to split the parent node (Ma, 2018).

A regression tree example is shown in Figure 4-2, predicting the mean number of cigarettes (M) smoked by students (N) as a function of age (months) and parent-related stress.

The regression tree can be used to identify the independent variables that mostly influence the dependent variable. From the regression tree above, age tends to be more important than parent-related stress as two of the three splits were related to age.

Figure 4-2: Example of regression tree

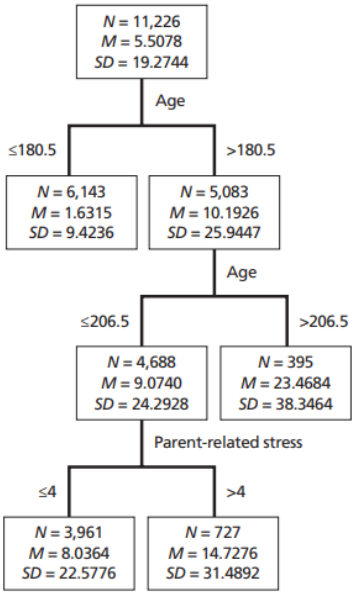

Source: (Ma, 2018)

A certain independent variable, when successfully splitting the parent node into two child nodes, will reduce impurity. Whenever it happens, the importance of such independent variable is increased by dividing the node risk reduction (parent node risk minus the sum of the child nodes risks) by the number of total branches in the tree. The node risk is the multiplication of the node probability by the node impurity if the tree is grown by minimizing an impurity criterion (MathWorks, 2021).

4.7.2. Smoothing spline analysis of variance

SS-ANOVA models are a family of smoothing methods suitable for univariate and multivariate modeling/regression problems. It is a statistical modeling algorithm based on function decomposition similar to the classical analysis of variance (ANOVA).

In a general multivariate case, the following function is minimized (Ricco, Rigoni & Turco, 2013):

$$\frac{1}{n}\sum_{i=1}^{n}\left(f_i - f(\boldsymbol{x}_i)\right)^2 + \lambda\sum_{k=1}^{p}\Theta_k^{-1}\cdot(f,g)_k \qquad 4.7\text{-}4$$

In the above function, the term multiplying λ, $\sum_{k=1}^{p} \Theta_k^{-1} \cdot (f, g)_k$, is the roughness penalty function J(f), which measures in a proper way the roughness/smoothness of the model f(x). The parameters λ and Θ_k are smoothing parameters, and n is the sample set size. The term f_i is the sum of the model function f(x) and a Gaussian type error:

$$f_i = f(\boldsymbol{x}_i) + \epsilon_i \qquad \text{4.7-5}$$

After minimizing the function given by 4.7-4 and determining parameters λ and Θ_k , the function ANOVA decomposition can be written as:

$$f^* = \sum_{k=1}^{p} f_k^* \qquad \text{4.7-6}$$

The star symbol (*) indicates that the constant term was not considered. The parameter p is determined by the number and type (main/interaction) of effect terms introduced in the ANOVA decomposition model. The relative significance of each of such terms can be assessed by contribution indices, defined as (Rigoni & Ricco, 2011):

$$\pi_k = \frac{(f_k^*, f^*)}{\|f^*\|^2} \qquad \text{4.7-7}$$

The numerator indicates the scalar product between two vectors and the denominator is the square of the vector norm. It is possible to conclude that the sum of π_k terms is equal to 1. The higher the value of π_k indicate the higher its importance to predict the outcome of interest. The SS-ANOVA gives quantitative measurement of an input significance in a given output, so it can be used as a screening tool.

The quality if the SS-ANOVA model can be measured by collinearity indices. Each of such indices (k_k) is the square root of a diagonal element of the inverse ($\sqrt{C_{kk}^{-1}}$) of the following matrix:

$$C_{ij} = \frac{(f_i^*, f_j^*)}{\|f_i^*\| \cdot \lceil f_j^* \rceil} \qquad \text{4.7-8}$$

If each of the collinearity indices is very close to 1, the trained model has sufficient quality, but if two or more collinearity indices present values much higher than 1 there is linear dependence between them, indicating that the trained model is not good enough, which may be explained by bad dataset (inappropriate DOE), too low sample size, dependent input variables.

4.8. **Optimization**

In the eighth level, the selected flowsheets in the fifth level are optimized, seeking minimization of equipment dry weight and footprint while maximizing oil production.

Optimization aims at finding the minimum of an objective function with respect to a certain number of design parameters. In constrained optimization, equality and/or inequality constraints must be observed, while in unconstrained optimization not. The objective function can be convex (single minimum) or non-convex (various local minima). The optimization can be local (finding a local minimum is sufficient) or global (global minimum is the goal). When optimization involves several objectives, it is called multi-objective optimization (MOO). The genetic algorithm is a common choice for solving global non-linear constrained multi-objective problems when numerical or analytical derivatives are not easily obtained.

The working principle of a genetic algorithm is shown in Figure 4-3. It begins with a set (population) of initial solution strings, which are evaluated in terms of the objective value and constraints (if existent), leading to the assignment of fitness to each solution string. If a termination condition is satisfied, the algorithm halts, otherwise three genetic operators called reproduction, crossover and mutation are used to modify the population and create a new generation, hopefully better than the previous generation.

Figure 4-3: Working Principle of a Genetic Algorithm

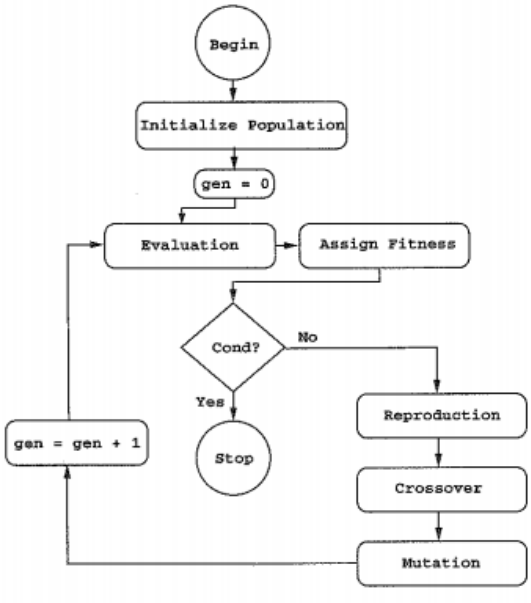

Source: Deb (2001)

A genetic algorithm represents the decision variables in binary strings, where the size of the string l_i is based on the level of precision. When the value of a position is 0, it does not add to the total value of the string. If it is 1, it contributes with a value that is equal to 2 to the power of the position. At the right end, the position is equal to 0, and at the left end, is equal to the size of the string minus 1. For example, the diameter of a vessel can be represented by a binary string of seven elements, where the value of each position was set randomly in this example:

1 1 0 1 0 0 1

The decoded value $DV(s_i)$ of the string is:

$$1 \cdot 2^6 + 1 \cdot 2^5 + 0 \cdot 2^4 + 1 \cdot 2^3 + 0 \cdot 2^2 + 0 \cdot 2^1 + 1 \cdot 2^0 = 105$$

The maximum value of the string is 127 (when all positions are equal to 1). If the maximum (x_i^{max}) diameter of a vessel is 4 m and the minimum (x_i^{min}) is 1 m, then a string having a decoded value of 105 will lead to the following diameter:

$$x_i = x_i^{min} + \frac{x_i^{max} - x_i^{min}}{2^{l_i} - 1} \cdot DV(s_i) = 1 + \frac{4 - 1}{2^7 - 1} \cdot 105 = 3.48m$$

A problem where the solution comprises, for example, three decision variables, will have solution strings combining the strings of the three decision variables. For example, if in a problem, diameter, length, and flowrate of a substance are decision variables, and each of the decision variables are represented by strings with 6 positions, the solution string will contain 18 positions, properly arranged so the value of a given decision variable can be obtained from the solution string.

The reproduction operator identifies above average solution strings in the population and creates copies to fill a mating pool. The most common method to reproduce the best solutions strings is called tournament selection, where tournaments are played between two solutions strings and the best solution string is chosen to reproduce. This process can be carried out systematically, where a solution string will participate in two tournaments. The best solution strings will win both tournaments, therefore scoring twice.

The crossover operator is applied in the solution strings of the mating pool created by the reproduction operator. The crossover operator picks two solutions strings of the mating pool and a portion of the strings are exchanged between the strings to create two new strings. If it is intended to preserve a certain number of solution strings, a crossover probability is set in order to determine the portion of the solution strings in the mating pool that will be crossed over. An example is shown below, where a single point crossover is performed in the 5^{th} position (all positions to the right of the 5^{th} position are changed):

String A from mating pool: 0 0 1 1 0 0 1 0 1 1

String B from mating pool: 1 1 0 1 0 0 1 1 0 0

String C after crossover between A and B, where A receives positions 6 to 10 of string B: 0 0 1 1 0 0 1 1 0 0

String D after crossover between A and B, where B receives positions 6 to 10 of string A: 1 1 0 1 0 0 1 0 1 1

The mutation operator simply changes one position of the solution string from 0 to 1 or vice-versa, maintaining diversity of the population. A mutation probability is assigned to determine how much of the solutions strings (after crossover) suffer mutation.

The NSGA-II adopts a fast non dominated sorting approach that increases efficiency of the reproduction step and maintains diversity of the population while not requiring any user inputs for such purpose (Deb, et al., 2002). When using such algorithm in Matlab, a list of options is available, and the user can define certain values instead of accepting default values. The only change made was the selection of a heuristic crossover function, which is designed to honor linear, non-linear and bound constraints, returning a child that lies on the line containing the two parents, closer to the parent with the better fitness.

Given the non-linearity of most of the equations used to estimate thermophysical properties and design the equipment, a non-convex behavior of the three objectives can be expected. In addition, several inequality constraints are imposed, such as the specifications of the products. Therefore, the optimization to be performed in this work can be classified as a global constrained non-convex multi-objective optimization.

4.9. **Comparison**

In the ninth (last) level, the optimized flowsheets are compared in order to identify the best flowsheet. In addition to the optimization objectives, other attributes can be considered, such as energy (power, heating, cooling) demands, export gas flowrate and hydrocarbon condensate production. Such comparison will identify the best flowsheet for a given set of inlet conditions.

When designing a new processing plant, it must be simulated for all relevant sets of inlet conditions. For instance, minimum water occurs in early field life, and maximum water cut in end field life. System and equipment design must be robust enough to cope with variations in inlet conditions. Selection of the best flowsheet may depend on the inlet conditions, for instance, in minimum water cut flowsheet A may be better than B, but flowsheet B may be better than

flowsheet A in maximum water cut. It is not under scope of this work designing and optimizing for variable inlet conditions, which is subject of future research.

Chapter 5

5. Thermophysical properties

This chapter shows the formulation related to the thermophysical properties estimator implemented in Matlab, comprising five types of fluids: hydrocarbons, MEA solution, TEG solution, seawater, and brine.

5.1. **Hydrocarbons**

The classical Peng-Robinson equation of state (PR-EOS) (Peng & Robinson, 1976) is the typical choice for estimating thermophysical properties of hydrocarbon dominated streams. It is one of the most successful equations of state (Echeverry, Acherman & Lopes, 2017):

$$P = \frac{R \cdot T}{v - b} - \frac{a}{v \cdot (v + b) + b \cdot (v - b)} \quad \text{5.1-1}$$

The compressibility factor Z is given by the real gas equation:

$$Z = \frac{P \cdot v}{R \cdot T} \quad \text{5.1-2}$$

Combining equations 5.1-1 and 5.1-2, the compressibility factor can be determined from the cubic equation 5.1-3. The parameter m is calculated by equation 5.1-6 if w is lower or equal than 0.49, otherwise by equation 5.1-7.

$$Z^3 - (1 - B) \cdot Z^2 + (A - 3B^2 - 2B) \cdot Z - (A \cdot B - B^2 - B^3) = 0 \quad \text{5.1-3}$$

$$a_{c_i} = 0.45724 \frac{R^2 \cdot T_{c_i}^2}{P_{c_i}} \quad \text{5.1-4}$$

$$b_i = 0.0778 \frac{R \cdot T_{c_i}}{P_{c_i}} \quad \text{5.1-5}$$

$$m_i = 0.37464 + 1.54226 w_i - 0.269922 \cdot w_i^2 \quad \text{5.1-6}$$

$$m_i = 0.379642 + 1.48503 \cdot w_i - 0.164423 \cdot w_i^2 + 0.016667 \cdot w_i^3 \quad \text{5.1-7}$$

$$a_i = a_{c_i} \cdot \sqrt{1 + m_i \cdot \left(1 - T_{r_i}^{1/2}\right)} \quad \text{5.1-8}$$

$$a = \sum_{i=1}^{nc} \sum_{j=1}^{nc} \left(n_i \cdot n_j \cdot a_i^{1/2} \cdot a_j^{1/2} \cdot \left(1 - k_{i,j}\right) \right) \quad \text{5.1-9}$$

$$b = \sum_{i=1}^{nc} (n_i \cdot b_i) \quad \text{5.1-10}$$

$$A = \frac{a \cdot P}{R^2 \cdot T^2} \quad \text{5.1-11}$$

$$B = \frac{b \cdot P}{R \cdot T} \quad \text{5.1-12}$$

$$K_i = \frac{P_{c_i}}{P} \cdot e^{\left(5.373 \cdot (1+w_i) \cdot \left(1 - \frac{T_{c_i}}{T}\right)\right)} \quad \text{5.1-13}$$

Equations 5.1-1 to 5.1-12 form the basis of the method developed by Peng-Robinson. The parameter n can be x (molar composition of liquid phase) or y (molar composition of vapor phase), depending on the phase under assessment. The following properties have been estimated by use of the PR-EOS:

- Molar fraction of vapor and liquid and respective compositions, by the isothermal flash procedure;
- Density;
- Enthalpy;
- Heat capacity at constant pressure;
- Heat capacity at constant volume.

The isothermal flash procedure is outlined in Figure 5-1. When an estimation of K is not available, Wilson's approximation provided by equation 5.1-13 can be used.

Figure 5-1: Isothermal Flash Procedure

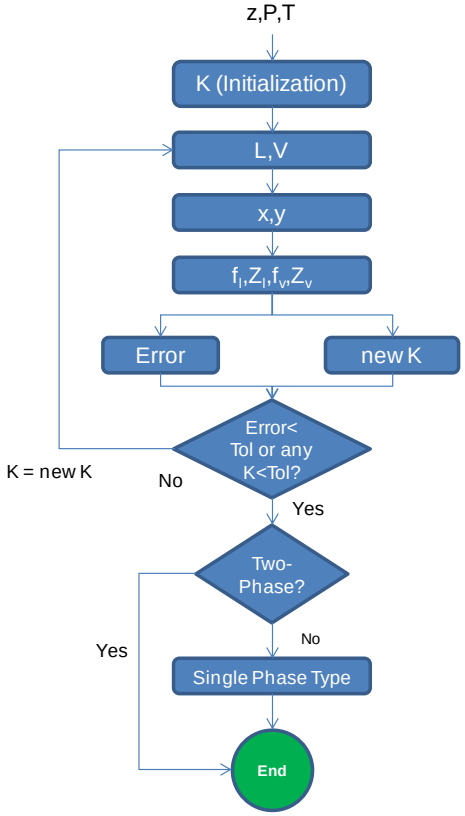

Source: author

The classical Rachford-Rice equation is given by:

$$F(V) = \sum_{i}^{nc} \frac{z_i \cdot (K_i - 1)}{1 + V \cdot (K_i - 1)} \qquad 5.1\text{-}14$$

It estimates the vapor fraction given K and z. It is a sum of hyperbolas, and the existence of an inflection point prevents the use of second-order Newton method without caution. Simple convex transformations allow the use of certain Newton methods without any control (Nichita & Leibovici, 2013). The second algorithm provided by the authors is used, which is shown below together with equations 5.1-15 to 5.1-25. The composition vector z is organized in descending order, from the component with the highest K value (subscript 1) to the component with the lowest K value (subscript n). Vector K also follows such order.

Algorithm:

1 Calculate the solution window a_L and a_R

2 Calculate $F(a_L)$ and $F(a_R)$

3 Calculate the initial guess a0; a = a0

4 Calculate F(a) and F'(a)

5 If F'(a) > 0 go to step 9

6 Newton step: $a_{k+1} = a_k - F(a_k)/F'(a_k)$

7 Test convergence: if the relative error is less than required tolerance, calculate V* = V(a*) and stop

8 If $a_{k+1} \in (a_L, a_R)$ go to step 4

9 If F(a) > 0 then

$a_{k+1} = a_k - G(a_k)/G'(a_k)$

else

$a_{k+1} = a_k - H(a_k)/H'(a_k)$

10 Go to step 4

$$a_L = \frac{z_1}{1 - z_1} \tag{5.1-15}$$

$$a_R = \frac{1 - z_n}{z_n} \tag{5.1-16}$$

$$c_i = \frac{1}{1 - K_i} \tag{5.1-17}$$

$$d_i = \frac{c_1 - c_i}{c_n - c_1} \tag{5.1-18}$$

$$a = \frac{V - c_1}{c_n - V} \tag{5.1-19}$$

$$F(a) = z_1 + \sum_{i=2}^{nc-1} \frac{z_i \cdot a}{d_i + a \cdot (1 + d_i)} - z_n \cdot a \tag{5.1-20}$$

$$F'(a) = \sum_{i=2}^{nc-1} \frac{z_i \cdot d_i}{\left(d_i + a \cdot (1 + d_i)\right)^2} - z_n \tag{5.1-21}$$

$$G(a) = \sum_{i=1}^{nc} \frac{z_i \cdot (1 + a)}{d_i + a \cdot (1 + d_i)} \tag{5.1-22}$$

$$G'(a) = -\frac{z_1}{a^2} - \sum_{i=2}^{nc-1} \frac{z_i}{\left(d_i + a \cdot (1 + d_i)\right)^2} - z_n \quad \text{5.1-23}$$

$$H(a) = -\sum_{i=1}^{nc} \frac{z_i \cdot a \cdot (1 + a)}{d_i + a \cdot (1 + d_i)} \quad \text{5.1-24}$$

$$H'(a) = -z_1 - \sum_{i=2}^{nc-1} \frac{z_i \cdot (d_i \cdot (1 + a)^2 + a^2)}{\left(d_i + a \cdot (1 + d_i)\right)^2} + z_n.(1 + 2a) \quad \text{5.1-25}$$

After finding V, L is obtained by the relationship of equation 5.1-26, since the sum of liquid and vapor molar fractions must be equal to 1.

$$L = 1 - V \quad \text{5.1-26}$$

The liquid composition (x) and vapor composition (y) are calculated according to equations 5.1-27 and 5.1-28:

$$x = \frac{z}{1 + V.(K - 1)} \quad \text{5.1-27}$$

$$y = K \cdot x \quad \text{5.1-28}$$

Parameters f_x and f_y are calculated according to equation 5.1-30, where the parameter n can be x (molar composition of liquid phase) or y (molar composition of vapor phase), depending on the phase under assessment. The same applies to the other parameters.

$$\psi_i = \sum_{j=1}^{nc} \left(n_j \cdot a_i^{1/2} \cdot a_j^{1/2} \cdot \left(1 - k_{i,j}\right)\right) \quad \text{5.1-29}$$

$$\ln\left(\frac{f}{n.P}\right) = (Z - 1) \cdot \frac{b}{B} - \ln(Z - B) - \left(\frac{A}{\left(2\sqrt{2} \cdot B\right)}\right) \cdot \left(\left(\frac{2 \cdot \psi}{A}\right) - \left(\frac{b}{B}\right)\right) \cdot \ln\left(\frac{Z + \left(1 + \sqrt{2}\right) \cdot B}{Z + \left(1 - \sqrt{2}\right) \cdot B}\right) \quad \text{5.1-30}$$

The parameters Z_l and Z_v, respectively the compressibility factors of the liquid and vapor phase, are calculated by equation 5.1-3. Z_l is the real root with the lowest value, and Z_v is the real root with the highest value. Having the compressibility factors of both phases, the molar volume (v) of each phase is calculated by equation 5.1-2.

The error is calculated according to equation 5.1-31 and the new K (K') according to equation 5.1-32:

$$error = \sum \left(\frac{f_l}{f_v} - 1\right)^2 \quad \text{5.1-31}$$

$$K' = K \cdot \frac{f_l}{f_v} \quad \text{5.1-32}$$

In case the error or any K is lower than respective tolerances, the loop is broken. In case the mixture is in two-phase (vapor/liquid), the process is finished, otherwise the single-phase type (either liquid or vapor) shall be determined in order to select appropriate methods to estimate the transport properties such as viscosity and thermal conductivity.

The single-phase type is determined by the method provided by (Venkatarathnam & Oellrich, 2011). From partial derivatives of pressure, volume and temperature without reference to saturated properties, the fluid phase is determined. The parameter Π is determined by equation 5.1-33, and other support parameters are determined by equations 5.1-34 to 5.1-44. If Π is greater than 1 the fluid is in liquid phase, otherwise is in vapor phase. Constants δ_1 and δ_2 are respectively equal to $1 + \sqrt{2}$ and $1 - \sqrt{2}$.

$$\Pi = v \cdot \left(\frac{\left(\partial^2 P/(\partial v\, \partial \mathrm{T})\right)}{(\partial P/\, \partial \mathrm{T})_v} - \frac{(\partial^2 P/\, \partial v^2)_T}{(\partial P/\, \partial v)_T}\right) \quad \text{5.1-33}$$

$$\frac{da}{dT} = -\sum_{i=1}^{nc}\left(\sum_{j=1}^{nc}\left(\left((1/2)\cdot a_{c_{ij}}\right)\cdot\left(\sqrt{\alpha_i}\cdot\left(m_j/\sqrt{T}\right)\cdot\left(1/\sqrt{T_{c_j}}\right) + \sqrt{\alpha_j}\cdot\left(m_i/\sqrt{T}\right)\cdot\left(1/\sqrt{T_{c_i}}\right)\right)\right)\right) \quad \text{5.1-34}$$

$$g_1 = \frac{1}{v - b} \quad \text{5.1-35}$$

$$g_2 = \frac{1}{v + \delta_1 \cdot b} \quad \text{5.1-36}$$

$$g_3 = \frac{1}{v + \delta_2 \cdot b} \quad \text{5.1-37}$$

$$g_4 = g_2 + g_3 \quad \text{5.1-38}$$

$$g_5 = \frac{da}{dT} \quad \text{5.1-39}$$

$$g_6 = g_2 . g_3 \quad \text{5.1-40}$$

$$\left(\frac{\partial^2 P}{\partial v\, \partial \mathrm{T}}\right) = -R \cdot g_1^2 + g_4 . g_5 . g_6 \quad \text{5.1-41}$$

$$\left(\frac{\partial \mathrm{P}}{\partial \mathrm{T}}\right)_v = R \cdot g_1 - g_5 . g_6 \quad \text{5.1-42}$$

$$\left(\frac{\partial^2 P}{\partial v^2}\right)_T = 2R \cdot T \cdot g_1^3 - 2a(T) \cdot g_6 \cdot (g_2^2 + g_6 + g_3^2) \quad \text{5.1-43}$$

$$\left(\frac{\partial \mathrm{P}}{\partial v}\right)_T = -R \cdot T \cdot g_1^2 + a(T) \cdot g_4 \cdot g_6 \quad \text{5.1-44}$$

A correction of the molar volume estimated by the PR-EOS can be calculated by equations 5.1-45 to 5.1-47.

$$Z_{RA_i} = 0.29056 - 0.08775 \cdot w_i \quad \text{5.1-45}$$

$$c_i = \frac{-0.5033R \cdot T_{c_i} \cdot \left(0.25969 - Z_{RA_i}\right)}{P_{c_i}} \quad \text{5.1-46}$$

$$v_{corr} = v + \sum_{i=1}^{nc} n_i \cdot c_i \quad \text{5.1-47}$$

Density is obtained by equation 5.1-48. In case molar volume correction is necessary, v is substituted by v_{corr}.

$$\rho = \frac{MW}{v} \quad \text{5.1-48}$$

$$H_{form} = \sum_{i=1}^{nc} n_i \cdot H_{form_i} \quad \text{5.1-49}$$

$$H_{id} = \sum_{i=1}^{nc} \left(n_i \cdot \left(C_{pa_i} + C_{pb_i} \cdot \left(T - T_{ref}\right) + C_{pc_i} \cdot \left(T - T_{ref}\right)^2 + C_{pd_i} \cdot \left(T - T_{ref}\right)^3 + C_{pe_i} \cdot \left(T - T_{ref}\right)^4 + C_{pf_i} \cdot \left(T - T_{ref}\right)^5 \right) \right) \quad \text{5.1-50}$$

$$H_{res} = R \cdot T \cdot (Z - 1) + \left(\frac{\left(T \cdot \frac{da}{dT} - a\right)}{2\sqrt{2}b} \right) \cdot \ln\left(\frac{Z + \left(1 + \sqrt{2}\right)B}{Z + \left(1 - \sqrt{2}\right)B} \right) \quad \text{5.1-51}$$

$$H = \left(H_{form} + H_{id} + H_{res}\right) \quad \text{5.1-52}$$

The heat capacity at constant pressure is a sum of ideal and residual elements. The ideal element is the first derivative of ideal enthalpy, as seen in 5.1-53, and

the residual element is a complex sum of elements involving partial derivatives, as seen from equations 5.1-54 to 5.1-58.

$$C_{p_{id}} = \sum_{i=1}^{nc} n_i \cdot \left(C_{pb_i} + 2C_{pc_i} \cdot \left(T - T_{ref}\right) + 3C_{pd_i} \cdot \left(T - T_{ref}\right)^2 + 4C_{pe_i} \cdot \left(T - T_{ref}\right)^3 + 5C_{pf_i} \cdot \left(T - T_{ref}\right)^4 \right) \quad \text{5.1-53}$$

$$\left(\frac{\partial \mathrm{A}}{\partial T}\right)_P = \left(\frac{P}{R^2 \cdot T^2}\right) \cdot \left(\frac{da}{dT} - \frac{2a}{T}\right) \quad \text{5.1-54}$$

$$\left(\frac{\partial \mathrm{B}}{\partial T}\right)_P = \frac{-b \cdot P}{R \cdot T^2} \quad \text{5.1-55}$$

$$\left(\frac{\partial Z}{\partial T}\right)_P = \frac{\left(\frac{\partial \mathrm{A}}{\partial T}\right)_P \cdot (B - Z) + \left(\frac{\partial \mathrm{B}}{\partial T}\right)_P \cdot (6B \cdot Z + 2Z - 3B^2 - 2B + A - Z^2)}{3Z^2 + 2(B-1) \cdot Z + (A - 3 \cdot B^2 - 2 \cdot B)} \quad \text{5.1-56}$$

$$\frac{d^2 a}{dT^2} = \sum_{i=1}^{nc} \left(\sum_{j=1}^{nc} \left(\left(-(1/2) \cdot a_{c_{ij}}\right) \cdot \left(\left(\left(\frac{m_j}{\sqrt{T_{c_j}}} \right) \cdot \left(\left(\sqrt{\alpha_i}\right) \cdot \left(\frac{-1}{(2T^{3/2})} \right) + \left(\frac{-m_i}{2T_{c_i} \cdot \sqrt{\frac{T}{T_{c_i}}}} \right) \cdot \frac{1}{\sqrt{T}} \right) \right) + \left(\frac{m_i}{\sqrt{T_{c_i}}} \right) \cdot \left(\sqrt{\alpha_j} \cdot \frac{-1}{2T^{3/2}} + \left(\frac{-m_j}{2T_{c_j} \cdot \sqrt{\frac{T}{T_{c_j}}}} \right) \cdot \frac{1}{\sqrt{T}} \right) \right) \right) \right) \quad \text{5.1-57}$$

$$C_{p_{res}} = \left(\frac{1}{2\sqrt{2}b}\right) \cdot T \cdot \left(\frac{d^2 a}{dT^2}\right) \cdot \ln\left(\frac{Z + \left(1 + \sqrt{2}\right)B}{Z + \left(1 - \sqrt{2}\right)B}\right) + R\left(Z - 1 + T \cdot \left(\frac{\partial Z}{\partial T}\right)_P\right) + \frac{\left(T \cdot \frac{da}{dT} - a\right)}{2\sqrt{2}b} \cdot \frac{2\sqrt{2}}{\left(Z + \left(1 + \sqrt{2}\right)B\right) \cdot \left(Z + \left(1 - \sqrt{2}\right)B\right)} \cdot \left(-B \cdot \left(\frac{\partial Z}{\partial T}\right)_P + Z \cdot \left(\frac{\partial \mathrm{B}}{\partial T}\right)_P\right) \quad \text{5.1-58}$$

$$C_p = C_{p_{id}} + C_{p_{res}} \quad \text{5.1-59}$$

The heat capacity at constant volume is also a sum of ideal $C_{v_{id}}$ and residual $C_{v_{res}}$ elements, as seen in equations 5.1-60 and 5.1-61:

$$C_{v_{id}} = C_{p_{id}} - R \tag{5.1-60}$$

$$C_{v_{res}} = \frac{T \cdot \frac{d^2a}{dT^2}}{b\sqrt{8}} \cdot \ln\left(\frac{Z + \left(1+\sqrt{2}\right)B}{Z + \left(1-\sqrt{2}\right)B}\right) \tag{5.1-61}$$

$$C_v = C_{v_{id}} + C_{v_{res}} \tag{5.1-62}$$

In order to validate the estimation of the aforementioned properties in Matlab, some compositions were simulated in commercial simulator Aspen HySys and compared to the estimation provided by the code implemented in Matlab, as seen in the following tables:

Table 5-1: Validation PR-EOS – Set 1

Molar Composition: 20% C1, 20% C2, 20% C3, 20% iC4, 20% nC4		
Pressure: 3 bar		
Temperature: -10°C		
Property	**Aspen HySys**	**Matlab**
V	0.6898	0.6895
ρ	Vapor: 5.122 / Liquid: 622.2	Vapor: 5.122 / Liquid: 622.2
H/1000	Vapor: -2,786 / Liquid: -2,718	Vapor: -2,786 / Liquid: -2,718
C_p	Vapor: 1,675 / Liquid: 2,222	Vapor: 1,675 / Liquid: 2,222
C_v	Vapor: 1,402 / Liquid: 1,672	Vapor: 1,402 / Liquid: 1,672

Table 5-2: Validation PR-EOS – Set 2

Molar Composition: 10% C1, 90% CO2 **Pressure: 100 bar** **Temperature: 50°C**		
Property	**Aspen HySys**	**Matlab**
V	1	1
ρ	277.4	277.4
H/1000	-8,874	-8,874
C_p	2,822	2,822
C_v	842	842

Table 5-3: Validation PR-EOS – Set 3

Molar Composition: 5% C1, 5% C2, 5% C3, 5% iC4, 5% nC4, 5% iC5, 5% nC5, 5% C6, 5% C7, 5% C8, 5% C9, 5% C10, 5% C11, 3% C12, 3% C13, 3% C14, 3% C15, 3% C16, 3% C17, 3% C18, 3% C19, 9% C20+, 2% CO2 **Pressure: 10 bar** **Temperature: 30°C**		
Property	**Aspen HySys**	**Matlab**
V	0.0445	0.0445
ρ	Vapor: 11.22 / Liquid: 669.5	Vapor: 11.22 / Liquid: 669.5
H/1000	Vapor: -4,468 / Liquid: -2,167	Vapor: -4,468 / Liquid: -2,167
C_p	Vapor: 1,821 / Liquid: 2,046	Vapor: 1,821 / Liquid: 2,046
C_v	Vapor: 1,445 / Liquid: 1,890	Vapor: 1,445 / Liquid: 1,890

The three tables above show excellent agreement between Aspen HySys and the code implemented in Matlab.

In this work only vapor-liquid or single-phase (vapor or liquid) were modeled. As a consequence, water cannot be included in the composition vector because a three phase system (vapor-liquid-liquid) may form whenever water is mixed with hydrocarbons. Whenever water is present in any given stream, it is considered formation of a liquid phase dominated by water, except in the cases where the stream is known to be in the vapor or supercritical state, in which correlations can be applied to estimate the amount of vaporized water in the given vapor stream. Another exception is when it is known that a certain amount of water is either dispersed or emulsioned in a liquid phase dominated by hydrocarbons.

The correlation proposed by Bahadori, Vuthaluru & Mokhatab (2009) estimates water saturation in the vapor phase, as shown in equations 5.1-63 to 5.1-68. Constants A1-A4, B1-B4, C1-C4 and D1-D4 can be found in the publication. After estimating the water content of a sweet (with no CO_2 and H_2S) gas, in case the gas contains substances like CO_2 or H_2S, an adjustment is made by the calculation of parameter R_j, which depends on pressure and a parameter (Y) that incorporates the amount of CO_2 (molar fraction y_{CO_2}) and H_2S (molar fraction y_{H_2S}). The correlation is valid for H_2S molar concentration below 40%, CO_2 below 50%, pressure below 1000 bar for sweet gas and below 700 bar for sour gas, and temperature from 10°C to 200°C for sweet gas and 10°C -150°C for sour gas. Such validity range should cover most of the operating conditions of topsides oil & gas processing plants.

$$W^{sw} = 10^{\left(a+b\cdot\log_{10}(P/1000)+c\cdot(\log_{10}(P/1000))^2+d\cdot(\log_{10}(P/1000))^3\right)} \quad \text{5.1-63}$$

$$a = A_1 + B_1 \cdot T + C_1 \cdot T^2 + D_1 \cdot T^3 \quad \text{5.1-64}$$

$$b = A_2 + B_2 \cdot T + C_2 \cdot T^2 + D_2 \cdot T^3 \quad \text{5.1-65}$$

$$c = A_3 + B_3 \cdot T + C_3 \cdot T^2 + D_3 \cdot T^3 \quad \text{5.1-66}$$

$$d = A_4 + B_4 \cdot T + C_4 \cdot T^2 + D_4 \cdot T^3 \quad \text{5.1-67}$$

$$W^{sour} = W^{sweet} \cdot R_j \quad \text{5.1-68}$$

$$R_j = \left[\frac{T_j - T_{j-1}}{T_{j+1} - T_{j-1}}\right] \cdot \left(R_{j+1} - R_{j-1}\right) + R_{j-1} \quad \text{5.1-69}$$

$$R_j = a + b \cdot \log_{10} P + c \cdot (\log_{10} P)^2 + d \cdot (\log_{10} P)^3 \quad \text{5.1-70}$$

$$a = A_1 + B_1 \cdot Y + C_1 \cdot Y^2 + D_1 \cdot Y^3 \quad \text{5.1-71}$$

$$b = A_2 + B_2 \cdot Y + C_2 \cdot Y^2 + D_2 \cdot Y^3 \quad \text{5.1-72}$$

$$c = A_3 + B_3 \cdot Y + C_3 \cdot Y + D_3 \cdot Y^3 \quad \text{5.1-73}$$

$$d = A_4 + B_4 \cdot Y + C_4 \cdot Y^2 + D_4 \cdot Y^3 \quad \text{5.1-74}$$

$$Y = y_{CO_2} + 0.7 y_{H_2S} \quad \text{5.1-75}$$

In order to validate the method, a comparison between the code implemented in Matlab and Aspen HySys was performed comprising certain sets of composition, pressure and temperature, as seen in Table 5-4. It shows that the agreement between Aspen HySys and the code implemented in Matlab is very good.

Table 5-4: Validation of water content in vapor phase correlation

Molar Composition: 80% C1, 20% C2		
Pressure: 20 bar - Temperature: 30°C		
Property	**Aspen HySys**	**Matlab**
Water content	1,702.1	1,737.7
Molar Composition: 80% C1, 10% C2, 10% CO_2		
Pressure: 2 bar - Temperature: 40°C		
Property	**Aspen HySys**	**Matlab**
Water content	27,834.2	27,021.2
Molar Composition: 70% C1, 10% C2, 18% CO2, 2% H2S		
Pressure: 5 bar - Temperature: 50°C		
Property	**Aspen HySys**	**Matlab**
Water content	19,045.7	18,675.8

If the operational conditions do not allow the use of the correlation, water saturation can be estimated by varying the water composition in the vapor or supercritical state and verifying formation of a second phase. This can be done with the implemented PR-EOS.

Another important property of hydrocarbon streams is the Reid Vapor Pressure (RVP) of treated crude oil, which is a sales specification. RVP is a measure of volatility of liquid hydrocarbon streams, and is it determined experimentally by placing a sample in a container such that the ratio of vapor volume to liquid volume is 4:1. The resulting pressure at 37.8°C is the RVP.

In order to provide a computational estimate, a code was developed based on an existent algorithm (Esparragoza et al., 1994). The estimation procedure is shown in Figure 5-2:

Figure 5-2: Procedure for RVP Estimation

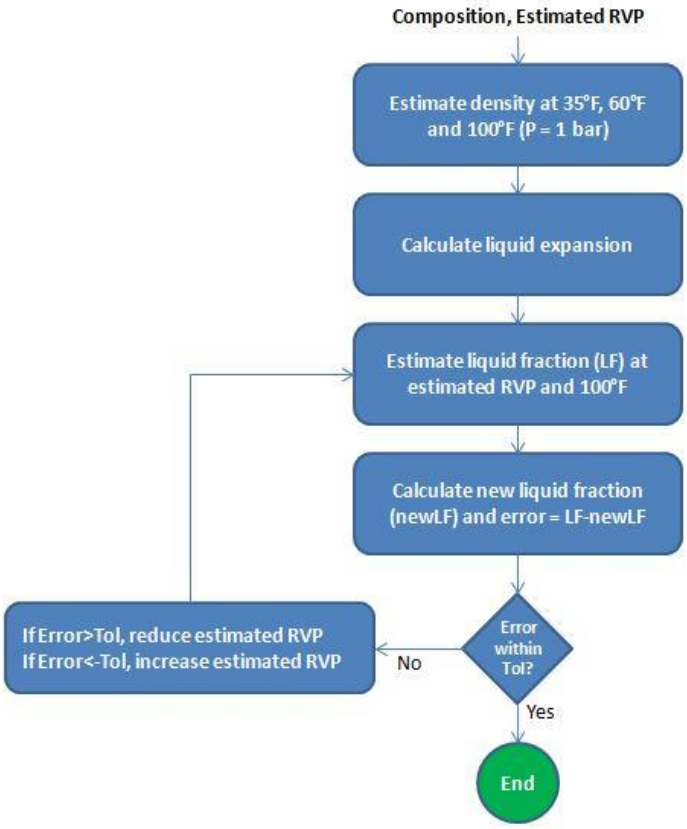

Source: author

The liquid expansion is calculated according to equation 5.1-76, where n is equal to 4. The liquid fraction is estimated at the estimated RVP and at 100°F (37.8°C), where the densities and molecular weight of liquid and vapor must be computed. The new liquid fraction is calculated according to equation 5.1-77:

$$v_0 = \rho_{60} \cdot \left(\frac{n+1}{\rho_{35}} - \frac{1}{\rho_{100}}\right) \qquad 5.1\text{-}76$$

$$newLF = \frac{1}{\left(1 + \left(\frac{\rho_v \cdot MW_l}{\rho_l \cdot MW_v}\right) \cdot \left(\frac{v_0}{1 - \frac{\rho_v}{\rho_{100}}}\right)\right)} \qquad 5.1\text{-}77$$

In order to validate the method, results have been compared to Aspen HySys, which uses a proprietary method. Table 5-5 shows an overestimation of approximately 20%, which is considered satisfactory.

Table 5-5: Validation of RVP

Molar Composition: 0.5% C1, 0.5% C2, 0.5% C3, 0.5% iC4, 0.5% nC4, 0.5% iC5, 1% nC5, 1% C6, 3% C7, 3% C8, 5% C9, 5% C10, 5% C11, 5% C12, 10% C13, 10% C14, 10% C15, 10% C16, 5% C17, 5% C18, 5% C19, 14% C20+		
Property	**Aspen HySys**	**Matlab**
RVP	26,440	32,000
Molar Composition: 1.5% C1, 0.5% C2, 0.5% C3, 0.5% iC4, 0.5% nC4, 0.5% iC5, 1% nC5, 1% C6, 3% C7, 3% C8, 5% C9, 5% C10, 5% C11, 5% C12, 10% C13, 9% C14, 10% C15, 10% C16, 5% C17, 5% C18, 5% C19, 14% C20+		
Property	**Aspen HySys**	**Matlab**
RVP	44,060	55,000
Molar Composition: 1.5% C1, 1% C2, 1% C3, 1% iC4, 0.5% nC4, 0.5% iC5, 1% nC5, 1% C6, 3% C7, 3% C8, 5% C9, 5% C10, 5% C11, 5% C12, 10% C13, 9% C14, 10% C15, 10% C16, 5% C17, 5% C18, 5% C19, 12.5% C20+		
Property	**Aspen HySys**	**Matlab**
RVP	58,310	71,000

Thermal conductivity is estimated by one of the methods available in commercial simulator PVTsim, a modified Lohrenz-Bray-Clark type expression. Constant values are: C1 = 2.30528, C2 = -0.59394, C3 = 0.06928, a1 = 270.28341, a2 = -148.95858, a3 = 408.63577; a4 = -127.74598; a5 = 13.52979. Pressure (P) is used in atm and molecular weight (MW) in g/mol.

$$\lambda = \lambda_{trans} + \lambda_{int} \quad \text{5.1-78}$$

$$\lambda_{trans} = C_1 \cdot T^{C_2} \cdot P^{C_3} \cdot (a_1 + a_2 \cdot \rho + a_3 \cdot \rho_r^2 + a_4 \cdot \rho_r^3 + a_5 \cdot \rho_r^4) \quad \text{5.1-79}$$

$$\lambda_{int} = 1.1865 \cdot \zeta \cdot C_v \cdot \frac{\rho_r'}{MW} \quad \text{5.1-80}$$

$$\rho_r' = 1 + 0.05343 \cdot \rho_r - 0.30182 \cdot \rho_r^2 - 0.029725 \cdot \rho_r^3 \quad \text{5.1-81}$$

$$\zeta = \frac{\sum_i^{nc} \left(n_i \cdot \varepsilon_i \cdot MW_i^{1/2} \right)_i}{\sum_i^{nc} \left(n_i \cdot MW_i^{1/2} \right)} \quad \text{5.1-82}$$

$$\varepsilon_i = 0.00034 \cdot \frac{1}{\xi_i} \cdot T_{r_i}^{0.94} \quad \text{5.1-83}$$

$$\varepsilon_i = 0.0001778 \cdot \frac{1}{\xi_i} \cdot \left(4.58 \cdot T_{r_i} - 1.67 \right)^{5/8} \quad \text{5.1-84}$$

$$\xi_i = \frac{T_{c_i}^{1/6}}{MW_i^{1/2} \cdot P_{c_i}^{2/3}} \quad \text{5.1-85}$$

In order to validate the method, a comparison between the code implemented in Matlab and Aspen HySys was performed comprising certain sets of composition, pressure and temperature, as seen in Table 5-6.

Aspen HySys uses another method to estimate thermal conductivity (API 12A1.2-1 or API 12A3.2-1). There is certain disagreement, but the results are considered good enough to proceed as deviation is within the range of +/- 30%.

Vapor viscosity is estimated by a certain existent method (Lohrenz, Bray & Clark, 1964). Constant values are: a1 = 0.1023, a2 = 0.023364, a3 = 0.058533; a4 = -0.040758; a5 = 0.0093324.

$$\mu_v = \zeta + \xi^{-1} \cdot ((a_1 + a_2 \cdot \rho_r + a_3 \cdot \rho_r^2 + a_4 \cdot \rho_r^3 + a_5 \cdot \rho_r^4)^4 - 10^{-4}) \qquad 5.1\text{-}86$$

In order to validate the method, a comparison between the code implemented in Matlab and Aspen HySys was performed comprising certain sets of composition, pressure and temperature, as seen in Table 5-7. Aspen HySys uses a proprietary method to estimate vapor viscosity. The results are considered good enough to proceed.

Table 5-6: Validation of thermal conductivity

Molar Composition: 1.5% C1, 1% C2, 1% C3, 1% iC4, 0.5% nC4, 0.5% iC5, 1% nC5, 1% C6, 3% C7, 3% C8, 5% C9, 5% C10, 5% C11, 5% C12, 10% C13, 9% C14, 10% C15, 10% C16, 5% C17, 5% C18, 5% C19, 12,5% C20+		
Pressure: 10 bar - Temperature: 30°C		
Property	**Aspen HySys**	**Matlab**
λ	0.1318	0.0924
Molar Composition: 1.5% C1, 1% C2, 1% C3, 1% iC4, 0.5% nC4, 0.5% iC5, 1% nC5, 1% C6, 3% C7, 3% C8, 5% C9, 5% C10, 5% C11, 5% C12, 10% C13, 9% C14, 10% C15, 10% C16, 5% C17, 5% C18, 5% C19, 12,5% C20+		
Pressure: 15 bar - Temperature: 50°C		
Property	**Aspen HySys**	**Matlab**
λ	0.1277	0.0909
Molar Composition: 5% C10, 5% C11, 10% C12, 10% C13, 10% C14, 10% C15, 10% C16, 10% C17, 10% C18, 10% C19, 10% C20+		
Pressure: 5 bar - Temperature: 50°C		
Property	**Aspen HySys**	**Matlab**
λ	0.1346	0.0923
Molar Composition: 80% C1, 10% C2, 10% CO_2		
Pressure: 15 bar - Temperature: 50°C		
Property	**Aspen HySys**	**Matlab**
λ	0.0346	0.0457
Molar Composition: 80% C1, 20% C2		
Pressure: 15 bar - Temperature: 50°C		
Property	**Aspen HySys**	**Matlab**
λ	0.0359	0.0469

Table 5-7: Validation of vapor viscosity

Molar Composition: 80% C1, 10% C2, 10% CO2		
Pressure: 15 bar - Temperature: 50°C		
Property	**Aspen HySys**	**Matlab**
μ	1.261E-5	1.259E-5
Molar Composition: 80% C1, 20% C2		
Pressure: 1 bar - Temperature: 20°C		
Property	**Aspen HySys**	**Matlab**
μ	1.083E-5	1.066E-5
Molar Composition: 70% C1, 20% C2, 10% C3		
Pressure: 5 bar - Temperature: 50°C		
Property	**Aspen HySys**	**Matlab**
μ	1.188E-5	1.114E-5

Liquid viscosity is estimated by the method provided by (Twu, 1984), as shown in the following equations. Normal boiling point is a necessary parameter, as it is estimated as shown in (Twu, 1985). Temperatures are in °R. T_1 is 559.7°R and T_2 is 669.7°R.

$$T_b = e^{\left(5.7149+2.71579\cdot\theta-0.28659\cdot\theta^2-39.8544/\theta-0.122488/\theta^2\right)} - 24.7522\cdot\theta + 35.3155\cdot\theta^2 \quad \text{5.1-87}$$

$$x = \left|\left(1.99873 - 56.7394/T_b^{0.5}\right)\right| \quad \text{5.1-88}$$

$$T_c^o = T_b \cdot \left(0.533272 + 0.000191017\cdot T_b + 0.779681\cdot 10^{-7}\cdot T_b^2 - 0.28437 \cdot 10^{-10}\cdot T_b^3 + \frac{0.959468\cdot 10^{28}}{T_b^{13}}\right)^{-1} \quad \text{5.1-89}$$

$$\alpha = 1 - \frac{T_b}{T_c^o} \quad \text{5.1-90}$$

$$SG^o = 0.843596 - 0.128624\cdot\alpha - 3.36159\cdot\alpha^3 - 13749.5\cdot\alpha^{12} \quad \text{5.1-91}$$

$$\Delta SG = SG - SG^o \quad \text{5.1-92}$$

$$\ln(\nu_2^o + 1.5) = 4.73227 - 27.0975\cdot\alpha + 49.4491\cdot\alpha^2 - 50.4706\cdot\alpha^4 \quad \text{5.1-93}$$

$$\ln\nu_1^o = 0.801621 + 1.37179\cdot\ln\nu_2^o \quad \text{5.1-94}$$

$$f_1 = 1.33932 \cdot x \cdot \Delta SG - 21.1141 \cdot \frac{\Delta SG^2}{T_b^{1/2}} \quad \text{5.1-95}$$

$$f_2 = x \cdot \Delta SG - 21.1141 \cdot \frac{\Delta SG^2}{T_b^{1/2}} \quad \text{5.1-96}$$

$$\ln\left(\upsilon_2 + \frac{450}{T_b}\right) = \ln\left(\nu_2^o + \frac{450}{T_b}\right) \cdot \left(\frac{1+2f_2}{1-2f_2}\right)^2 \quad \text{5.1-97}$$

$$\ln\left(\upsilon_1 + \frac{450}{T_b}\right) = \ln\left(\nu_1^o + \frac{450}{T_b}\right) \cdot \left(\frac{1+2f_1}{1-2f_1}\right)^2 \quad \text{5.1-98}$$

$$Z_2 = \upsilon_2 + 0.7 + e^{\left(-1.47-1.84\cdot\upsilon_2-0.51\cdot\nu_2^2\right)} \quad \text{5.1-99}$$

$$Z_1 = \upsilon_1 + 0.7 + e^{\left(-1.47-1.84\cdot\upsilon_1-0.51\cdot\nu_1^2\right)} \quad \text{5.1-100}$$

$$B = \frac{\ln\ln Z_1 - \ln\ln Z_2}{\ln T_1 - \ln T_2} \quad \text{5.1-101}$$

$$Z = e^{e^{(\ln\ln Z_1 + B\cdot(\ln T - \ln T_2))}} \quad \text{5.1-102}$$

$$\nu_l = Z - 0.7 - e^{\left(-0.7487-3.295\cdot(Z-0.7)+0.6119\cdot\left((Z-0.7)^2\right)-0.3193\cdot\left((Z-0.7)^3\right)\right)} \quad \text{5.1-103}$$

$$\mu_l = \nu_l \cdot \rho_l \cdot 10^{-6} \quad \text{5.1-104}$$

In order to validate the method, a comparison between the code implemented in Matlab and Aspen HySys was performed comprising certain sets of composition, pressure and temperature, as seen in Table 5-8. Aspen HySys uses a proprietary method to estimate liquid viscosity. Although in some cases the viscosity estimated by Matlab is overestimated in more than 30%, the results are considered good enough to proceed as the same order of magnitude is kept.

Table 5-8: Validation of liquid viscosity

Molar Composition: 1.5% C1, 1% C2, 1% C3, 1% iC4, 0.5% nC4, 0.5% iC5, 1% nC5, 1% C6, 3% C7, 3% C8, 5% C9, 5% C10, 5% C11, 5% C12, 10% C13, 9% C14, 10% C15, 10% C16, 5% C17, 5% C18, 5% C19, 12,5% C20+		
Pressure: 10 bar - Temperature: 30°C		
Property	**Aspen HySys**	**Matlab**
μ	4.078E-3	4.623E-3
Molar Composition: 1.5% C1, 1% C2, 1% C3, 1% iC4, 0.5% nC4, 0.5% iC5, 1% nC5, 1% C6, 3% C7, 3% C8, 5% C9, 5% C10, 5% C11, 5% C12, 10% C13, 9% C14, 10% C15, 10% C16, 5% C17, 5% C18, 5% C19, 12,5% C20		
Pressure: 10 bar - Temperature: 30°C		
Property	**Aspen HySys**	**Matlab**
μ	1.641E-3	2.448E-3
Molar Composition: 20% C16, 20% C17, 20% C18, 20% C19, 20% C20		
Pressure: 1 bar - Temperature: 20°C		
Property	**Aspen HySys**	**Matlab**
μ	3.493E-3	6.387E-3
Molar Composition: 20% C11, 20% C12, 20% C13, 20% C14, 20% C15		
Pressure: 3 bar - Temperature: 20°C		
Property	**Aspen HySys**	**Matlab**
μ	1.631E-3	2.023E-3
Molar Composition: 20% C11, 20% C12, 20% C13, 20% C14, 20% C15		
Pressure: 30 bar - Temperature: 90°C		
Property	**Aspen HySys**	**Matlab**
μ	0.636E-3	0.702E-3

5.2. **Seawater and brine**

Seawater and brine are present in the processing of oil and gas. In the case of seawater, it is used to reduce oil salinity during the desalination process. In the case of brine, the formation water produced together with the hydrocarbons may have its thermophysical properties estimated by brine formulations.

Seawater properties density, heat capacity at constant pressure, enthalpy and thermal conductivity were estimated by the method proposed by Nayar et al. (2016). Viscosity was estimated by the method proposed by Sharqawy, Lienhard & Zubair (2010).

Brine density was estimated by the method proposed by Spivey, McCain & North (2004). The NaCl molality (m_{NaCl}) is estimated by the method proposed by Sawamura et al. (2007).

Brine thermal conductivity was estimated by the method proposed by Ozbek & Phillips, (s.d.). Brine viscosity was estimated by the method proposed by Mao & Duan (2009) for water-NaCl mixtures. Brine heat capacity coefficient at constant pressure was estimated by the same method used for seawater.

5.3. **TEG solution**

One of the technologies utilized to dehydrate natural gas is physical absorption by a solution comprising TEG (triethylene glycol) and water. The following properties were estimated: density, heat capacity at constant pressure, viscosity, thermal conductivity, boiling point and heat of vaporization.

Density was estimated by the method proposed by Bahadori & Mokhatab (2009). Heat capacity at constant pressure, viscosity, thermal conductivity and boiling point were estimated by methods proposed by DOW (2007).

5.4. **MEA solution**

One of the technologies utilized to remove CO_2 and H_2S from natural gas is chemical absorption by a solution comprising MEA (monoethanolamine) and water. The following properties were estimated: density, heat capacity at constant pressure, viscosity, thermal conductivity and surface tension.

Density and viscosity were estimated by methods proposed by Sobrino et al. (2016). Heat capacity at constant pressure was estimated by the method proposed by Greer (2008). Surface tension was estimated by the method proposed by Jayarathna et al. (2013). Thermal conductivity is estimated by the method proposed by DiGullio, McGregor & Teja (1992).

Chapter 6

6. Equipment modeling

This chapter presents how each of the selected equipment involved in oil & gas processing have been modeled. The following equipment are included:

- Horizontal three-phase (oil/water/gas) separator;
- Horizontal two-phase (gas/liquid) separator;
- Vertical two-phase (gas/liquid) separator;
- Shell & tube heat exchanger;
- Isenthalpic valve;
- Pump;
- Compressor;
- Electrostatic coalescer for emulsioned water removal from oil;
- Oil desalting;
- TEG physical absorption gas dehydration;
- Solid desiccant gas dehydration;
- H_2S removal from gas by iron oxide;
- Heavy hydrocarbons removal from gas by Joule-Thomson effect;
- CO_2 removal from gas by MEA chemical absorption;
- CO_2 removal from gas by cellulose acetate membrane.

In this work, the surge volume due to slug flow, which may occur in certain production systems, has not been considered in the design of first stage separation due to lack of information of slugging flow. In the future it is planned to incorporate such design consideration.

6.1. **Horizontal three-phase (oil/water/gas) separator**

The modeling of this equipment is based on Backi, Grimes & Skogestad (2018) and Bothamley (2017). A three-phase separator schematic is shown in Figure 6-1, where a multiphase stream enters the separator at the upper left nozzle, reaching a flow dampener that reduces turbulence, promoting initial separation. Such section is typically isolated from the main body of the separator. Along the main body of the separator, the stream is separated into a gas phase that leaves at the upper right nozzle, an oil-continuous phase that leaves at the lower right nozzle at the right of the weir plate, and a water-continuous phase that leaves at the other lower-right nozzle at the left of the weir plate. The weir plate height must be sufficient to avoid ingress of the water-continuous phase into the oil-continuous phase.

Figure 6-1: Horizontal Three-Phase Separator Schematic

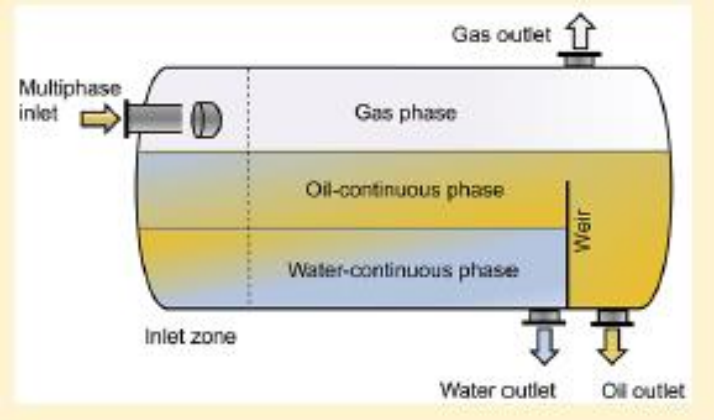

Source: Backi, Grimes & Skogestad (2018)

The separator is modeled considering two main parts: the first section is the inlet section comprising the multiphase stream inlet and the flow dampener, modeled as a flash separator, in which the multiphase flow is divided in three phases, a gas-continuous phase containing dispersed oil droplets, an oil-continuous phase containing dispersed gas droplets and dispersed water droplets, and a water-continuous phase containing dispersed oil droplets. As estimating the amount of each of the dispersed substances in a given continuous phase would be a cumbersome task depending on factors such as the turbulence of the inlet multiphase stream and geometry of the internal flow dampener, a required user input is the amount of each of the dispersed

substances in a given continuous phase, represented as a weight fraction of the inlet substance flowrate. It is assumed that emulsioned water Q_{w_e} in oil remains mixed with the oil. The following equations represent the inlet section:

$$Q_{mp} = Q_o + Q_g + Q_{w_f} + Q_{w_e} \quad \text{6.1-1}$$

$$Q_{gc} = Q_g \cdot (1 - \alpha_{go}) + \alpha_{og} \cdot Q_o \quad \text{6.1-2}$$

$$Q_{oc} = Q_o \cdot (1 - \alpha_{og} - \alpha_{ow}) + \alpha_{go} \cdot Q_g + \alpha_{wo} \cdot Q_{w_f} + Q_{w_e} \quad \text{6.1-3}$$

$$Q_{wc} = Q_{w_f} \cdot (1 - \alpha_{wo}) + \alpha_{ow} \cdot Q_o \quad \text{6.1-4}$$

The second section is the main body of the separator, where the amount of dispersed substances will be reduced in the given continuous phase until reaching the required efficiencies. The dispersed oil droplets in the gas continuous phase will settle, the dispersed gas droplets in the oil continuous phase will rise, the dispersed water droplets in the oil continuous phase will settle, and the dispersed oil droplets in the water continuous phase will rise. For each dispersed substance, a droplet size distribution must be given and the percentage of each of the droplet sizes, allowing the calculation of the total number of dispersed droplets as per equation 6.1-5:

$$n_d = \frac{Q_d}{\sum_i^{n_{dc}} (V_{dc,i} \cdot f_{dc,i})} \quad \text{6.1-5}$$

The settling or rising velocity of a spherical droplet results from a balance of forces considering laminar flow of the droplet, leading to equation 6.1-6:

$$v_p = \frac{g \cdot d_p^2 \cdot (\rho_p - \rho_c)}{18 \cdot \mu_c} \quad \text{6.1-6}$$

The horizontal residence time in a given section of the separator is given by equation 6.1-7. The separator is divided in a certain number of segments, where the flow from the previous segment enters into the next:

$$t_{r,h} = \frac{A \cdot (L/N_s)}{Q_c} \quad \text{6.1-7}$$

The vertical residence time of a given droplet is given by equation 6.1-8:

$$t_{r,v} = \frac{h_c}{v_p} \quad \text{6.1-8}$$

In case the horizontal residence time is greater than the vertical residence time, the droplet will migrate to the other continuous phase, otherwise it will remain in its original continuous phase but in a different position.

The cross section areas are given by the following equations:

$$A = \frac{\pi D^2}{4} \quad \text{6.1-9}$$

$$A_{wc} = \left(\frac{r^2}{2}\right) \cdot \left(2\cos^{-1}\left(\frac{r - h_w}{r}\right) - \sin\left(2\cos^{-1}\left(\frac{r - h_w}{r}\right)\right)\right) \quad \text{6.1-10}$$

$$A_l = \left(\frac{r^2}{2}\right) \cdot \left(2\cos^{-1}\left(\frac{r - h_l}{r}\right) - \sin\left(2\cos^{-1}\left(\frac{r - h_l}{r}\right)\right)\right) \quad \text{6.1-11}$$

$$A_{oc} = A_l - A_{wc} \quad \text{6.1-12}$$

$$A_{gc} = A - A_l \quad \text{6.1-13}$$

Separation efficiency, in a given continuous phase, is the ratio of the remaining dispersed substance by the inlet dispersed substance. The inlet dispersed substance in a given continuous phase is dictated by the flow conditions from the well to the platform and the performance of separator inlet section. Efficiencies are calculated by the following equations:

$$e_{og} = 1 - \frac{Q_{og,out}}{\alpha_{og} \cdot Q_o} \quad \text{6.1-14}$$

$$e_{go} = 1 - \frac{Q_{go,out}}{\alpha_{go} \cdot Q_g} \quad \text{6.1-15}$$

$$e_{wo} = 1 - \frac{Q_{wo,out}}{\alpha_{wo} \cdot Q_{w_f}} \quad \text{6.1-16}$$

$$e_{ow} = 1 - \frac{Q_{ow,out}}{\alpha_{ow} \cdot Q_o} \quad \text{6.1-17}$$

Many parameters are unknown, as they would only be determined based on the performance of the inlet section. Such parameters are the droplet size distributions and the dispersion coefficients α_{og}, α_{og}, α_{ow} and $\alpha_{w_f o}$.

Regarding the droplet size distribution, the same values adopted by Backi, Grimes & Skogestad (2018) have been used for all types of droplets, being 500 droplet size classes equally distributed between 2 µm and 1000 µm (2, 4, 6, 8…..1000 µm).

Regarding the dispersion coefficients, a sensitivity analysis has been executed to verify how each coefficient affects the dimensions of the separator when aiming 99% separation efficiencies, fixing the values of process inputs such as mass flowrate, composition, pressure, temperature, etc. A total of 12 values for each coefficient were set, from 0.03 to 0.69 (0.03, 0.09, 0.15…0.69). Regression trees have been trained and predictor importance on D and L/D are shown in Figure 6-2:

Figure 6-2: Effect of dispersion coefficients on D and L/D

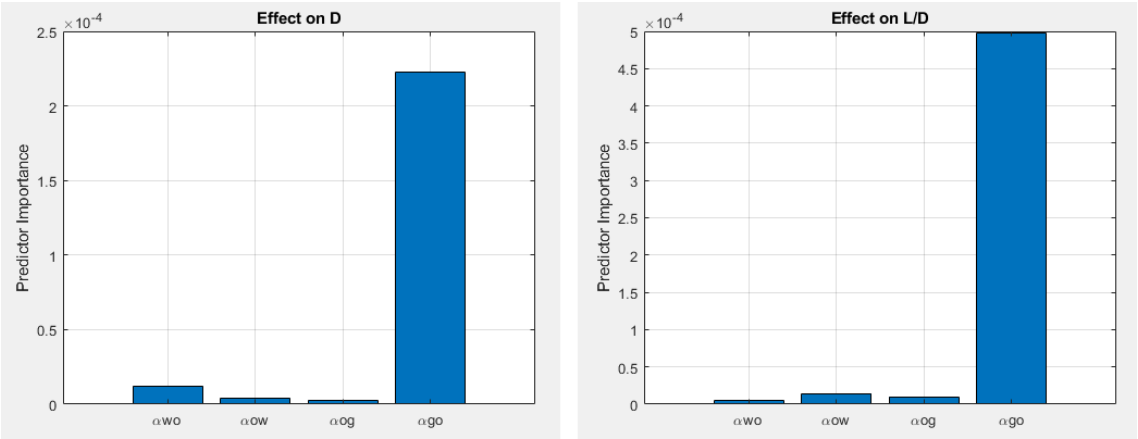

It is clear from Figure 6-2 that the amount of gas dispersed in oil (α_{go}) is the main parameter affecting diameter and L/D ratio. The following dispersion coefficients for water in oil and oil in water are typically used (Bothamley, 2017):

Table 6-1: Typical water-in-oil and oil-in-water fractions

Feed Condition	Water-in-Oil Minimum Fraction	Oil-in-Water Minimum Fraction
Easy	0.05	0.02
Average	0.10	0.05
Difficult	0.15	0.08

Regarding gas in oil (α_{go}) and oil in gas (α_{og}) dispersions, no recommended values have been found in the literature.

It was assumed a value of 0.15 for each of the dispersion coefficients, which is deemed conservative.

The initial variable design inputs are diameter, ratio between length and diameter (L/D), liquid level (h_l), and water level (h_w). A set of 4 variables would already significantly increase complexity of a multi-objective optimization. A regression tree has been created, and the importance of each parameter was estimated. Figure 6-3 shows the relative importance of each of the input parameters on the key outcomes of the three-phase separator: footprint, dry weight, e_{og}, e_{go}, e_{wo}, and e_{ow}.

Figure 6-3: Three-phase Separator – Relative importance of input parameters

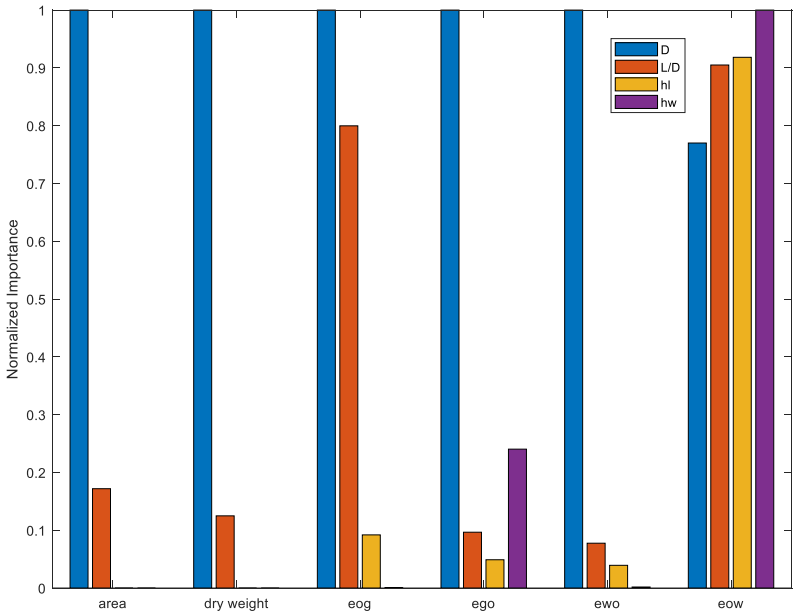

Source: Author

Diameter is the most important input on all outcomes, except on e_{ow}, which also has strong dependence on diameter. The ratio L/D strongly influences e_{og} and e_{ow}. The parameters h_l and h_w strongly influence e_{ow}. Given that footprint and dry weight, part of the optimization objectives, are only influenced by D and L/D, it is possible to eliminate h_l and h_w as variables to be optimized, as long as a set of constraints related to acceptable separation performances is imposed on the separator performance. Therefore, when optimizing a processing plant, if a combination of D and L/D leads to unacceptable separation performances (e_{og}, e_{go}, e_{wo}, and e_{ow}), such combination is discarded.

The other required inputs are the characteristics of the multiphase stream (composition, mass flowrate, pressure and temperature).

Minimum separation efficiency is set as 99% for e_{og}, e_{go}, e_{wo}, and e_{ow}.

Breakage or coalescence of droplets and mass diffusion between phases are not considered, which is an opportunity for future work in order to increase rigor of the model.

6.2. **Horizontal two-phase (gas/liquid) separator**

The modeling of this equipment is a simplification of the previous 3-phase separator. It is allowed dispersion of the gas in the liquid phase, and dispersion of the liquid in the gas phase. The main objective is to provide clean outlet streams, a gas stream containing as low as possible dispersed liquid and a liquid stream containing as low as possible dispersed gas. A schematic is shown in Figure 6-4:

Figure 6-4: Horizontal Two-Phase Separator Schematic

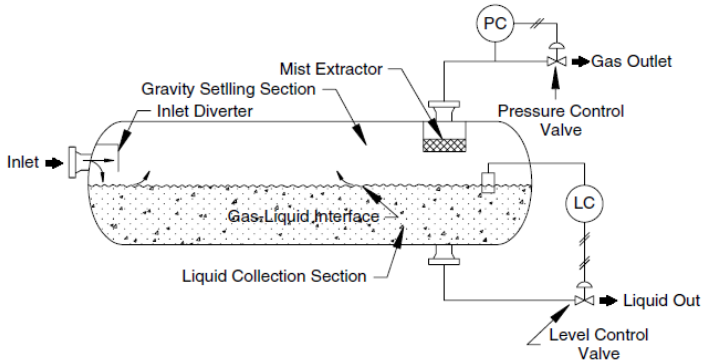

Source: Arnold & Stewart (2008)

Equations 6.1-5 to 6.1-8 and 6.2-1 to 6.2-6 are used to model the equipment.

The initial variable design inputs are diameter, ratio between length and diameter (L/D), and liquid level (h_l).

$$Q_{gc} = Q_g \cdot (1 - \alpha_{gl}) + \alpha_{lg} \cdot Q_l \quad \text{6.2-1}$$

$$Q_{lc} = Q_l \cdot (1 - \alpha_{lg}) + \alpha_{gl} \cdot Q_g \quad \text{6.2-2}$$

$$A_{lc} = \left(\frac{r^2}{2}\right) \cdot \left(2\cos^{-1}\left(\frac{r - h_l}{r}\right) - \sin\left(2\cos^{-1}\left(\frac{r - h_l}{r}\right)\right)\right) \quad \text{6.2-3}$$

$$A_{gc} = A - A_{lc} \quad \text{6.2-4}$$

$$e_{lg} = 1 - \frac{Q_{lg,out}}{\alpha_{lg} \cdot Q_l} \quad \text{6.2-5}$$

$$e_{gl} = 1 - \frac{Q_{gl,out}}{\alpha_{gl} \cdot Q_g} \quad \text{6.2-6}$$

A set of 3 variables would already significantly increase complexity of a multi-objective optimization. A regression tree has been created, and the importance of each parameter is estimated as described on section 4. Figure 6-5 shows the relative importance of each of the input parameters on the key outcomes of the three-phase separator: area, dry weight, e_{gl}, and e_{lg}.

Figure 6-5: Horizontal gas-liquid separator – Relative importance of input parameters

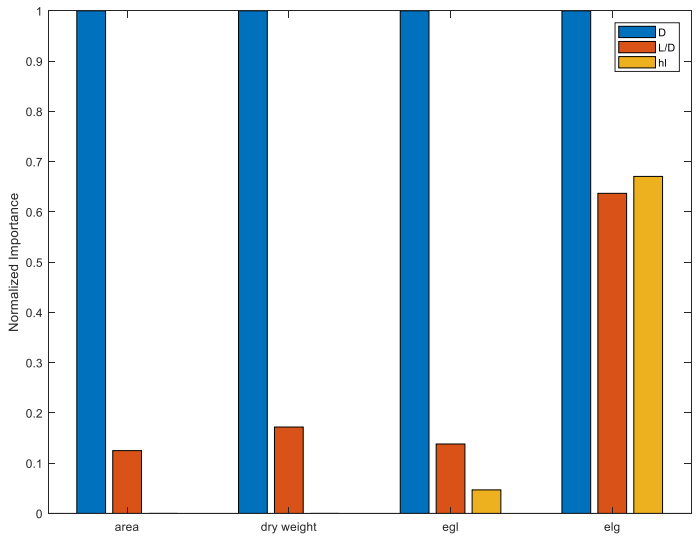

Diameter is the most important input for all outcomes. The ratio L/D and hl strongly influences e_{lg}. Given that footprint and dry weight, part of the optimization objectives, are only influenced by D and L/D, it is possible to eliminate h_l as variable to be optimized, as long as a set of constraints related to acceptable separation performances is imposed on the separator performance. Therefore, when optimizing a processing plant, if a combination of D and L/D leads to unacceptable separation performance (e_{gl} or e_{lg}), such combination is discarded.

The required inputs are the characteristics of the inlet stream (composition, mass flowrate, pressure and temperature), dispersion coefficients (It was assumed a value of 0.15 for each of the dispersion coefficients), droplet profile (size distribution and amount of each size) and required separation efficiencies.

The same values adopted by Backi, Grimes & Skogestad (2018) have been used for all types of droplets, being 500 droplet size classes equally distributed between 2 μm and 1000 μm (2, 4, 6, 8,…1000 μm).

Minimum separation efficiency is set as 99% for e_{gl} and e_{lg}.

6.3. **Vertical two-phase (gas/liquid) separator based on residence time**

The design of vertical gas-liquid separator is based on Baidoo et al. (2011), where the settling velocity of liquid droplets (equation 6.3-1) dispersed in the gas phase only depends on the densities of both fluids. A key required input is the residence time of the liquid phase (t_{rl}), typically based on operational experience. It is assumed use of a demister pad. A schematic is shown in Figure 6-6:

The total height of the vessel ($\mathrm{H_{vgls}}$) is the sum of the height necessary to hold the liquid ($\mathrm{H_l}$), the height required below ($\mathrm{H_{bi}}$) and above ($\mathrm{H_{ai}}$) the inlet, and the height of the demister pad ($\mathrm{H_m}$), which is assumed equal to 0.4 m.

There are no parameters to be optimized since the diameter is a function of gas flowrate and the densities of gas and liquid, and the height is a function of the diameter and the residence time, which is set based on operational experience.

Figure 6-6: Schematic of vertical gas-liquid separator

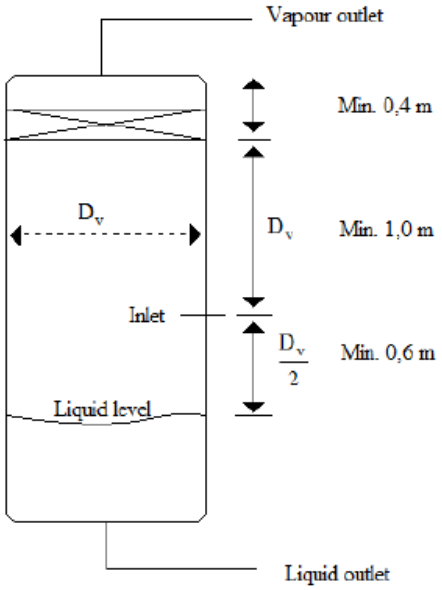

Source: Baidoo et al. (2011)

$$v_p = 0.07 \cdot \sqrt{\frac{\rho_l - \rho_g}{\rho_g}} \quad \text{6.3-1}$$

$$D = min\left(\sqrt{\frac{4 \cdot Q_g}{\pi \cdot v_p}}; 0.8\right) \quad \text{6.3-2}$$

$$V_l = Q_l \cdot t_{rl} \quad \text{6.3-3}$$

$$H_l = \frac{V_l}{A} \quad \text{6.3-4}$$

$$H_{ai} = \min(D; 1) \quad \text{6.3-5}$$

$$H_{bi} = \min\left(\frac{D}{2}; 0.6\right) \quad \text{6.3-6}$$

$$H_{vgls} = H_l + H_{ai} + H_{bi} + H_m \quad \text{6.3-7}$$

6.4. **Shell and tube heat exchanger**

Shell and tube heat exchangers are typically used in topsides applications, especially when involving fluids that can lead to corrosion or clogging. The amount of design methods available in the literature regarding shell and tube type is greater than gasket-plate type, therefore it was selected in this work. In the future, it is intended to include gasket-plate type in the development of oil &

gas processing schemes, as they are already found in certain topsides applications. A schematic of a shell and tube heat exchanger is shown in Figure 6-7:

Figure 6-7: Schematic of shell and tube heat exchanger

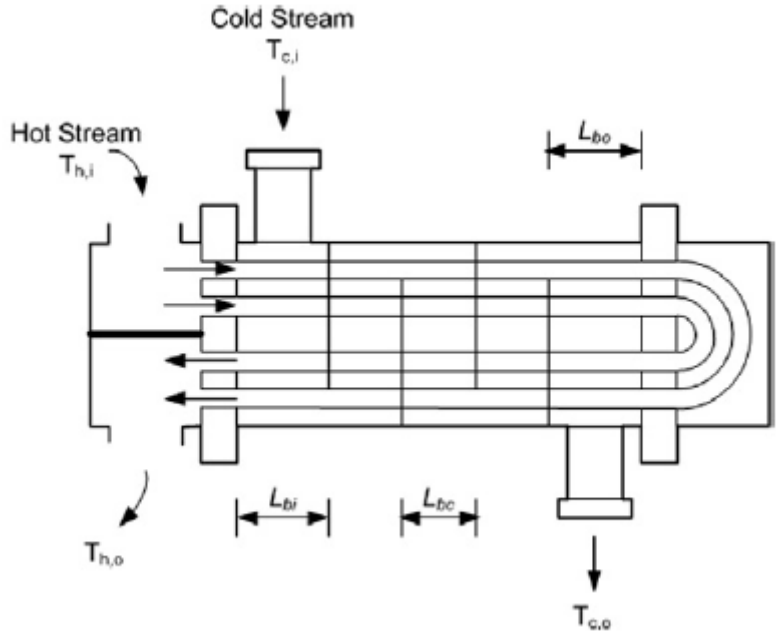

Source: Fettaka, Thibaut & Gupta (2013)

The design of the shell and tube heat exchanger is based on the procedure shown in Figure 6-8. It starts with the following inputs: information from the inlet fluids, such as density and viscosity, the approach temperature, the desired outlet temperature of the process fluid (in case an utility is used), which fluid is in the shell, initial estimates of internal tube diameter and tube length, maximum allowable pressure drop in shell and tube sides, maximum shell length, minimum tube length, maximum and minimum shell diameter, maximum and minimum tube internal diameter, number of tube passes, thermal conductivity of the fabrication material, and percentages to calculate certain parts of the heat exchanger.

In case both the shell diameter and tube length fall inside the limits, the global heat transfer coefficient U is estimated, otherwise an iteration procedure starts in order to set a new tube internal diameter. In case the new tube internal diameter falls outside the limits, the tube length is modified.

The parameter U is estimated in an iteration procedure. When the value of U converges, another iteration procedure starts to estimate pressure drop in the shell and tube. In case both are below limits, the design is successful; otherwise the tube internal diameter is increased. The procedure starts with one heat exchanger, and in case no convergence is achieved, the code will increase the number of heat exchangers by one and so on, until convergence.

Figure 6-8: Procedure for shell and tube heat exchanger design

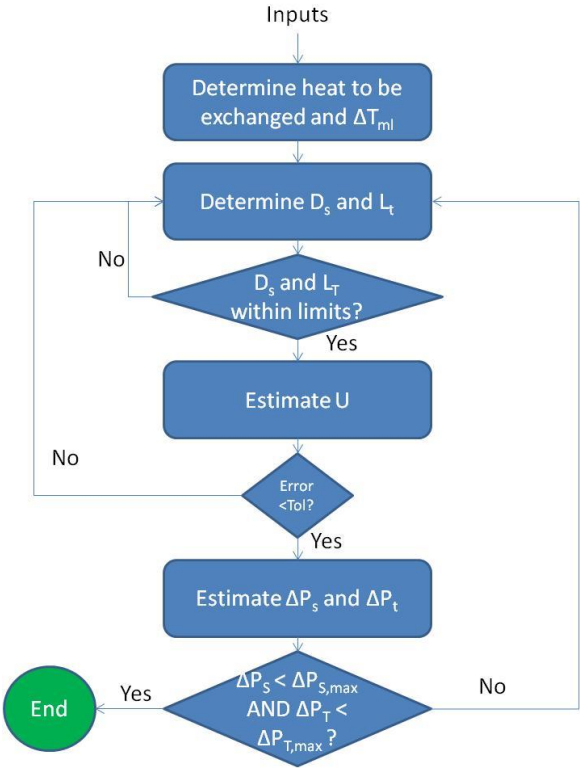

Source: author

For heat recovery applications, when the flowrates of both fluids are given, an approach temperature must be set. It is a positive number that reflects the difference between the inlet temperature of fluid 1 and outlet temperature of fluid 2. For applications that involve an utility (such as water, steam) to cool or heat a fluid, it is given the outlet temperature of the process fluid, and the flowrate of the utility is calculated considering a certain outlet temperature of the utility, that will depend on the given approach. In the case of a heat recovery application, assuming 1 is the hot fluid and 2 the cold fluid, equations 6.4-1 and 6.4-2 are used to calculate the heat exchanged by stream 1 (HE_1) if it leaves the heat exchanger with a temperature equal to its inlet temperature minus the approach, and the heat exchanged by stream 2 (HE_2) if it leaves the heat

exchanger with a temperature equal to its inlet temperature plus the approach. The lower absolute value is the heat exchanged, and one of the outlet temperatures must be recalculated considering the real heat exchanged.

$$HE_1 = W_1 \cdot \left(H_{1,o} - H_{1,i}\right) \quad \text{6.4-1}$$

$$HE_2 = W_2 \cdot \left(H_{2,o} - H_{2,i}\right) \quad \text{6.4-2}$$

In case an utility is used, than the heat balance is calculated as follows, where W_1 is the mass flowrate of the process fluid, W_2 is the mass flowrate of the utility, and respective inlet and outlet temperatures are known:

$$HE = W_1 \cdot \left(H_{1,out} - H_{1,in}\right) \quad \text{6.4-3}$$

$$W_2 = abs\left(\frac{HE}{\left(H_{2,oout} - H_{2,in}\right)}\right) \quad \text{6.4-4}$$

The logarithmic mean temperature is given by equation 6.4-5 and the required heat exchange area by equation 6.4-6, where F is a correction factor for counter-current flow given by equation 6.4-7 for an even number of passes in the shell:

$$\Delta T_{ml} = abs\left(\frac{\left(T_{1,in} - T_{2,out}\right) - \left(T_{1,out} - T_{2,in}\right)}{\ln\left(\frac{\left(T_{1,in} - T_{2,out}\right)}{\left(T_{1,out} - T_{2,in}\right)}\right)}\right) \quad \text{6.4-5}$$

$$A_{HE} = \frac{HE}{U \cdot \Delta T_{ml} \cdot F} \quad \text{6.4-6}$$

$$F = \frac{\sqrt{(R^2+1) \cdot \ln\left(\frac{1-S}{1-R \cdot S}\right)}}{(R-1) \cdot \ln\left[\frac{2-S \cdot \left(R+1-\sqrt{R^2+1}\right)}{2-S \cdot \left(R+1+\sqrt{R^2+1}\right)}\right]} \quad \text{6.4-7}$$

$$R = \frac{T_{1,in} - T_{1,out}}{T_{2,in} - T_{2,out}} \quad \text{6.4-8}$$

$$S = \frac{T_{2,in} - T_{2,out}}{T_{1,in} - T_{2,out}} \quad \text{6.4-9}$$

The global heat transfer coefficient U is estimated by equation 6.4-10:

$$\frac{1}{U.A_{t,ext}} = \frac{1}{h_t \cdot A_{t,int}} + \frac{1}{h_s \cdot A_{t,ext}} + \ln\left(\frac{D_{t,ext}/D_{t,int}}{2\pi \cdot \lambda_t \cdot L_t}\right) + I_t + I_s \qquad 6.4\text{-}10$$

The convection coefficient on the shell side (h_s) is estimated by the Bell-Delaware method as seen in equations 6.4-11 to 6.4-46. The parameters a, a_1 and a_2 in equation 6.4-13 are functions of the Reynolds number in the shell. The baffle length (l_c) is set as a percentage of the shell diameter (in this case 25%). The parameters n and K1 in equation 6.4-22 depend on the number of tube passes in the shell. The baffle diameter (D_{baffle}) is set as a percentage of the shell diameter (in this case 98%). The clearance between the shell and the tube bundle is set as 5% of D_{otl}. The value of parameter C in equation 6.4-33 depends on the Reynolds number in the shell. The parameter N_{ss} is the number of sealing strips, in this case set equal to 1. The parameter X_t is equal to the pitch (p_t). The number of pass divider lanes is equal to 2. The parameter wp is set equal to $D_{t,ext}$. The space between baffles (L_{bc}) is set as a percentage of the shell length (in this case set as 20%). The parameter n in equation 6.4-40 is equal to 1/3 if the flow is laminar, otherwise 0.6. In case the parameter N_{ss}^+ in equation 6.4-33 is greater than 0.5, J_b Is equal to 1. Some of the parameters shown in equations below are shown in Figure 6-9:

Figure 6-9: Nomenclature for basic baffle geometry relations for a single segmental exchanger

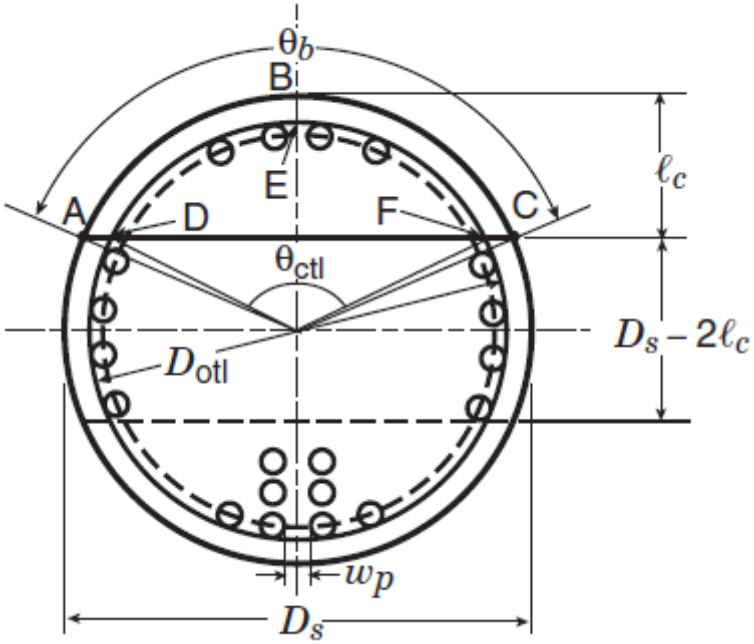

Source: Shah & Sekulic (2003)

$$h_s = h_{id} \cdot J_c \cdot J_l \cdot J_b \cdot J_s \cdot J_r \quad \text{6.4-11}$$

$$h_{id} = j \cdot C_{p,s} \cdot G \cdot \phi \cdot Pr_s^{-2/3} \quad \text{6.4-12}$$

$$j = a_1 \cdot \left(\frac{1.33}{p_t/D_{t,ext}}\right)^a \cdot (Re_s)^{a_2} \quad \text{6.4-13}$$

$$G = \frac{W_s}{S_m} \quad \text{6.4-14}$$

$$Re_s = \frac{G \cdot D_{t,ext}}{\mu_s} \quad \text{6.4-15}$$

$$S_m = L_{b,c} \cdot \left((D_s - D_{otl}) + \frac{(D_{otl} - D_{t,ext}) \cdot (p_t - D_{t,ext})}{p_{t,eff}}\right) \quad \text{6.4-16}$$

$$\phi = \left(\frac{\mu_s}{\mu_{ref}}\right)^{0.14} \quad \text{6.4-17}$$

$$J_c = 0.55 + 0.72 \cdot (1 - 2 \cdot F_w) \quad \text{6.4-18}$$

$$F_w = \frac{1}{2\pi} \cdot (\theta_{ctl} - \sin\theta_{ctl}) \quad \text{6.4-19}$$

$$\theta_{ctl} = 2\cos^{-1}\left(\frac{D_s - 2 \cdot l_c}{D_{ctl}}\right) \quad \text{6.4-20}$$

$$D_{ctl} = D_{otl} - D_{t,ext} \quad \text{6.4-21}$$

$$D_{otl} = \left(\frac{N_t}{K_1}\right)^{1/n} \quad \text{6.4-22}$$

$$D_s = D_{otl} + cl \quad \text{6.4-23}$$

$$N_t = \frac{A_{HE}}{\pi \cdot L_t \cdot D_{t,ext}} \quad \text{6.4-24}$$

$$J_l = 0.44 \cdot (1 - r_s) + \left(1 - 0.44 \cdot (1 - r_s)\right) \cdot e^{-2.2 r_{lm}} \quad \text{6.4-25}$$

$$r_s = \frac{A_{o,sb}}{A_{o,sb} + A_{o,tb}} \quad \text{6.4-26}$$

$$r_{lm} = \frac{A_{o,sb} + A_{o,tb}}{A_{o,cr}} \quad \text{6.4-27}$$

$$A_{o,sb} = \pi \cdot D_s \cdot \frac{\delta_{sb}}{2} \cdot \left(1 - \frac{\theta_b}{2 \cdot \pi}\right) \quad \text{6.4-28}$$

$$\delta_{sb} = D_s - D_{baffle} \quad \text{6.4-29}$$

$$\theta_b = 2\cos^{-1}\left(1 - \frac{2l_c}{D_s}\right) \quad \text{6.4-30}$$

$$A_{o,tb} = \frac{\pi \cdot D_{t,ext} \cdot \delta_{tb} \cdot N_t \cdot (1 - F_w)}{2} \quad \text{6.4-31}$$

$$\delta_{tb} = \frac{\delta_{sb}}{4} \quad \text{6.4-32}$$

$$J_b = exp\left(-C \cdot r_b \cdot \left[1 - (2N_{ss}^{+})^{1/3}\right]\right) \quad \text{6.4-33}$$

$$N_{ss}^{+} = \frac{N_{ss}}{N_{r,cc}} \quad \text{6.4-34}$$

$$N_{r,cc} = \frac{D_s - 2l_c}{X_l} \quad \text{6.4-35}$$

$$X_l = \frac{\sqrt{3}}{2} \cdot p_t \quad \text{6.4-36}$$

$$p_t = 1.25 \cdot D_{t,ext} \quad \text{6.4-37}$$

$$r_b = \frac{A_{o,bp}}{A_{o,cr}} \quad \text{6.4-38}$$

$$A_{o,cr} = L_{b,c} \cdot \left[D_s - D_{otl} + 2 \cdot \frac{D_{ctl}}{X_t} \cdot \left(p_t - D_{t,ext}\right)\right] \quad \text{6.4-39}$$

$$A_{o,bp} = L_{b,c} \cdot \left(D_s - D_{otl} + 0.5 \cdot N_p \cdot w_p\right) \quad \text{6.4-40}$$

$$J_s = \frac{(N_b - 1 + (L_i^{+})^{1-n} + (L_o^{+})^{1-n})}{N_b - 1 + L_i^{+} + L_o^{+}} \quad \text{6.4-41}$$

$$L_i^{+} = \frac{L_{b,i}}{L_{b,c}} \quad \text{6.4-42}$$

$$L_o^{+} = \frac{L_{b,o}}{L_{b,c}} \quad \text{6.4-43}$$

$$J_r = \left(\frac{10}{N_{r,c}}\right)^{0.18} + \frac{Re_s - 20}{80} \quad \text{6.4-44}$$

$$N_{r,c} = N_{r,cc} + N_{r,cw} \quad \text{6.4-45}$$

$$N_{r,cw} = \frac{0.8}{X_l} \cdot \left(l_c - 0.5 \cdot (D_s - D_{ctl})\right) \quad \text{6.4-46}$$

The convection coefficient on the tube side (h_t) is estimated according to equations 6.4-47 to 6.4-50:

$$h_t = \frac{Nu_t \cdot \lambda_t}{D_{t,int}} \quad \text{6.4-47}$$

$$Nu_t = 0.023 \cdot (Re_t)^{0.8} \cdot (Pr_t)^{1/3} \quad \text{6.4-48}$$

$$Re_t = \frac{\rho_t \cdot v_t \cdot D_{t,int}}{\mu_t} \quad \text{6.4-49}$$

$$Pr_t = \frac{C_{p,t} \cdot \mu_t}{\lambda_t} \quad \text{6.4-50}$$

The resistance to heat transfer caused by incrustation in the shell (I_s) and tube (I_t) must be given.

The pressure drop on the shell side is estimated by equations 6.4-51 to 6.4-62. Parameter g_c is equal to 1 and the parameter f_{id} is equal to 0.23. In case a liquid flows through the shell, equation 6.4-52 estimates $\Delta p_{b,id}$, otherwise equation 6.4-53. The parameter D in equation 6.4-59 depends on the Reynolds number in the shell side. Equation 6.4-55 is used when Re_s is greater than 100, otherwise a more complicated equation must be used. The parameter n' in equation 6.4-62 depends on Re_s.

$$\Delta P_s = \left[(N_b - 1) \cdot \Delta p_{b\,id} \cdot \zeta_b + N_b \cdot \Delta p_{w,id}\right] \cdot \zeta_l + 2\Delta p_{b,id} \cdot \left(1 + \frac{N_{r,cw}}{N_{r,cc}}\right) \cdot \zeta_b \cdot \zeta_s \quad \text{6.4-51}$$

$$\Delta p_{b\,id} = \frac{4 f_{id} \cdot G_c^2}{2 \cdot g_c \cdot \rho_s} \cdot N_{r,cc} \cdot \left(\frac{\mu_s}{\mu_{ref}}\right)^{0.25} \quad \text{6.4-52}$$

$$\Delta p_{b\,id} = \frac{4 f_{id} \cdot G_c^2}{2 \cdot g_c \cdot \rho_s} \cdot N_{r,cc} \cdot \left(\frac{T_s}{T_{sm}}\right)^{m} \quad \text{6.4-53}$$

$$G_c = \frac{W_s}{A_{o,cr}} \quad \text{6.4-54}$$

$$\Delta p_{w\,id} = \frac{\left(2 + 0.6N_{r,cw}\right) \cdot \rho_s \cdot u_z^2}{2 \cdot g_c} \quad \text{6.4-55}$$

$$u_z = \sqrt{\frac{W_s}{A_{o,cr} \cdot \rho_s} \cdot \frac{W_s}{A_{o,w} \cdot \rho_s}} \quad \text{6.4-56}$$

$$A_{o,w} = \frac{D_s^2}{4} \cdot \left(\frac{\theta_b}{2} - \left(1 - 2\frac{l_c}{D_s}\right) \cdot \sin\left(\frac{\theta_b}{2}\right)\right) \quad \text{6.4-57}$$

$$\theta_b = 2\cos^{-1}\left(1 - 2\frac{l_c}{D_s}\right) \quad \text{6.4-58}$$

$$\zeta_b = \exp\left(-D \cdot r_b \cdot \left(1 - \left((2 * N_{ss}^{+})^{1/3}\right)\right)\right. \quad \text{6.4-59}$$

$$\zeta_l = \exp\left(-1.33 \cdot (1 + r_s) \cdot \left(r_{lm}^{p}\right)\right) \quad \text{6.4-60}$$

$$p = -0.15 \cdot (1 + r_s) + 0.8 \quad \text{6.4-61}$$

$$\zeta_s = \left(\frac{L_{b,c}}{L_{b,o}}\right)^{2-n'} + \left(\frac{L_{b,c}}{L_{b,i}}\right)^{2-n'} \quad \text{6.4-62}$$

The pressure drop in the tube side is given by equations 6.4-63 to 6.4-65. If Reynolds number in the tube side Re_t is lower than 2000, equation 6.4-64 estimated the friction factor f_t, otherwise equation 6.4-65.

$$\Delta P_t = \frac{f_t \cdot \rho_t \cdot v_t^2 \cdot n_p \cdot L_t}{D_{t,int}} \quad \text{6.4-63}$$

$$f_t = \frac{64}{Re_t} \quad \text{6.4-64}$$

$$f_t = \left(\frac{1}{-4\log_{10}\left(\frac{0.27e}{D_{t,int}} + \left(\frac{7}{Re_t}\right)^{0.9}\right)}\right)^2 \quad \text{6.4-65}$$

The tube internal diameter and length could be parameters to be optimized, but in the proposed design procedure, after initial estimates of such parameters, the code self-adjusts (even increasing the number of heat exchangers) in order to find a feasible design in case the initial estimates do not succeed. The set of the initial estimates will influence the ultimate feasible design; therefore they can be included in the optimization routine.

6.5. **Isenthalpic valve**

The isenthalpic valve is designed according to the procedure shown in Figure 6-10. The enthalpy upstream and downstream the valve must remain constant after a depressurization, therefore the inputs are the composition of the fluid, the inlet and required outlet pressure, and an estimate of the outlet temperature. Having an estimate of the outlet temperature it is possible to estimate the outlet enthalpy. In case it is sufficiently close to the inlet enthalpy, the algorithm halts and the outlet temperature is computed, otherwise the outlet temperature is adjusted and a new outlet enthalpy is calculated. This step is repeated until convergence is reached.

Figure 6-10: Procedure for isenthalpic valve design

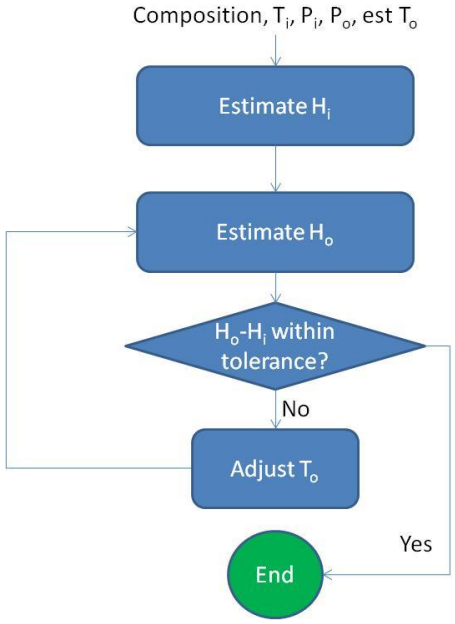

Source: author

6.6. **Pump**

The pump is modeled according to equations 6.6-1 and 6.6-2, where the inputs are the inlet fluid information (pressure, temperature, volumetric flowrate, and composition), required outlet pressure and pump efficiency. The outputs are power and outlet temperature, calculated according to GPSA - Gas Processors Suppliers Association (2004) and Toolbox (2020):

$$Power = \frac{Q_{in} \cdot (P_{out} - P_{in})}{\eta} \qquad 6.6\text{-}1$$

$$T_{out} = T_{in} + \frac{Power \cdot (1 - \eta)}{C_{p_{in}} \cdot Q_{in} \cdot \rho_{in}} \quad \text{6.6-2}$$

6.7. **Compressor**

The compressor is designed according to the procedure shown in Figure 6-11, where the inputs are the inlet fluid information (pressure, temperature, mass flowrate, composition), maximum outlet temperature allowed by compressor, compressor isentropic efficiency (η) and required discharge pressure. It assumes the stream to be compressed is already conditioned (no liquid and at the required inlet temperature) when feeding the compressor.

Firstly, the discharge pressure is estimated assuming the discharge temperature is the maximum allowed. In case the discharge pressure exceeds the required discharge pressure, the outlet temperature is estimated based on the required discharge pressure. In case the discharge pressure does not exceed the required discharge pressure, then a new compression stage is designed starting from the cooler and, if required, a knock-out (KO) drum to separate liquid, leading to the new inlet pressure of the next compression stage. The cooler is designed according to section 6.4 and the KO drum according to section 6.3.

In Equation 6.7-2, molecular weight (MW) is given in g/mol and temperature (T) in °R. In equation 6.7-3 mass flowrate (W) is given in lb/min. All equations have been obtained in (GPSA - Gas Processors Suppliers Association, 2004).

$$P_{out} = P_{in} \cdot \left(1 + \eta \cdot \left(\frac{T_{out} - T_{in}}{T_{in}}\right)\right)^{\frac{k}{k-1}} \quad \text{6.7-1}$$

$$Head = \frac{1{,}545}{MW} \cdot \frac{Z_{av} \cdot T_{in}}{((\eta - 1)/\eta)} \cdot \left[\left(\frac{P_{out}}{P_{in}}\right)^{((\eta-1)/\eta)} - 1\right] \quad \text{6.7-2}$$

$$Power = \frac{W \cdot Head \cdot 746}{\eta \cdot 33{,}000} \quad \text{6.7-3}$$

Figure 6-11: Procedure for compressor design

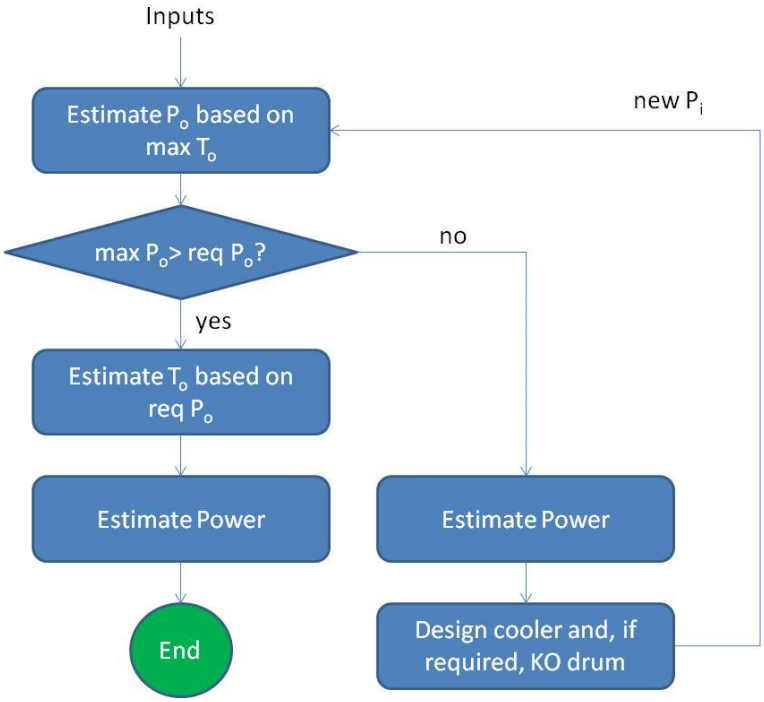

Source: author

6.8. **Electrostatic coalescer for emulsioned water removal from oil**

In general, part of the produced water is emulsioned by the oil, and can be removed by methods such as heating, chemical treatment by injection of demulsifier, or electrostatic coalescence. In this work the effect of heating or chemicals in emulsion breaking was not modeled due to lack of information available in the open literature.

Electrostatic coalescence is typically seen in topsides applications. It applies an electric field that reduces stability of the emulsion, generating forces that assist in creating conditions for improved coalescence, leading to the creation of larger water droplets that settle by gravity. There are three primary electrostatic forces: dipolar attraction, electrophoresis and dielectrophoresis (Sams, Sellman & Mandewalkar, 2013). Dipolar attraction is the electrostatic attraction force between oppositely charged ends of water droplet. Electrophoresis is the electrical attraction between a charged electrode and an oppositely charger water droplet in a uniform electric field. Dielectrophoresis is the movement of polarized water droplets in a non-uniform electrostatic field with the movement toward the direction of convergence of the field. Representations of the three forces are shown in Figure 6-12, from top to bottom.

There are at least three types of electric field: AC (alternate current), DC (direct current), and AC/DC. The AC/DC type tends to exceed performance of AC and DC types, as it benefits from the features of both fields.

Figure 6-12: The three primary electrostatic forces: dipolar attraction (top), electrophoresis (middle), dielectrophoresis (bottom)

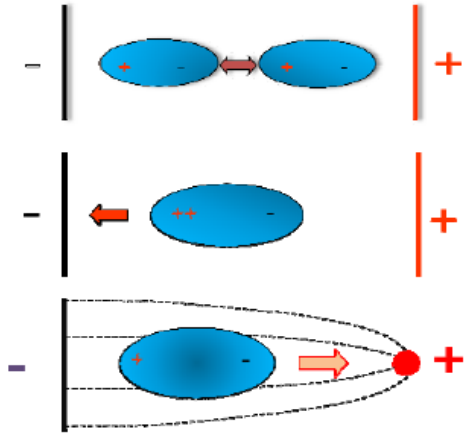

Source: Sams, Sellman & Mandewalkar (2013)

The most rigorous approach to model an electrostatic coalescer involves a droplet population balance. An analysis of a certain rigorous model (Rossi, et al., 2017) indicates that it would be impractical to be used in an optimization routine where the characteristics of the inlet stream could change in each run, as such model can consist of many thousands of equations that are resolved by a numerical procedure where computational effort is not negligible, according to the authors. The same authors adopted certain simplifications in the rigorous model and achieved quicker convergence, but the model complexity suggests that it would still be impractical to be used in the optimization routine. An analysis of another model (Khajehesamedini et al., 2018) leads to the same conclusion, as it depends on the resolution of a set of many ordinary differential equations. Therefore it was searched for simplified models able to estimate the outlet water concentration as a function of key design parameters of the electrostatic coalescer.

A number of models have been reviewed by certain researchers in order to compare the performance of the research group rigorous model (Khajehesamedini et al., 2018). Suemar et al. (2012) developed a simplified model with experimental data obtained with oils from 13°API to 29.5°API,

operating temperature from 78.4°C to 161.1°C, among other parameters, comprising both pilot scale and industrial scale (refinery) units. The developed model is shown in equation 6.8-1, where μ_o is given in g/(cm.s), densities in g/cm^3, residence time between electrodes in s and voltage gradient (E) in kV/cm. It is unclear which type of electric field has been used in the experiments. The voltage gradient is the ratio between the voltage and the distance between electrodes d_{ec}:

$$H_2O_o = 3.0781 \cdot \frac{\mu_o^{0.1466}}{(\rho_w - \rho_o)^{0.6517} \cdot t_{RP}^{0.4140} \cdot E^{0.8548}} \quad \text{6.8-1}$$

The residence time between electrodes can be estimated by dividing the volume of the electrostatic coalescence section by the inlet volumetric flowrate:

$$t_{RP} = \frac{VOL_{es}}{Q_{in}} \quad \text{6.8-2}$$

In order to calculate the volume of the electrostatic section, as per equation 6.8-5, some assumptions had to be taken to estimate the diameter of the electrostatic coalescer. An analysis of a certain vendor's electrostatic coalescer (Armstrong & Sams, 2007) indicates that there are four sections: the water level section dedicated to separate oil droplets from the separated water, a section between the lower part of the electrode and the water level, the electrodes section, and a section above the electrodes, as seen in Figure 6-13. The diameter (D_{ec}) is the sum of the heights of all sections, as per equation 6.8-3:

The authors inform that the section above the electrodes is 6 inches high and that the electrodes have a length of 6 inches, separated by 6 inches. There was no information about the height of the section between the lower part of the electrodes and the water level. The following assumptions were adopted: Parameter l_{ae} is equal to the length of the electrodes, and parameter l_{be} is equal to 80% of l_e.

The water level section height (h_w) is estimated by setting the minimum oil droplet diameter that must be separated from water in order to avoid that unacceptable water quality is produced by the electrostatic coalescer. By using Stokes law, the speed of such droplet is calculated. The water level section

height divided by such speed equals the residence time of the oil droplet. In case it is lower than the water residence time, which is calculated by dividing the volume of the water level section by the water flowrate, separation is achieved.

Figure 6-13: Dual Polarity Vessel Configuration

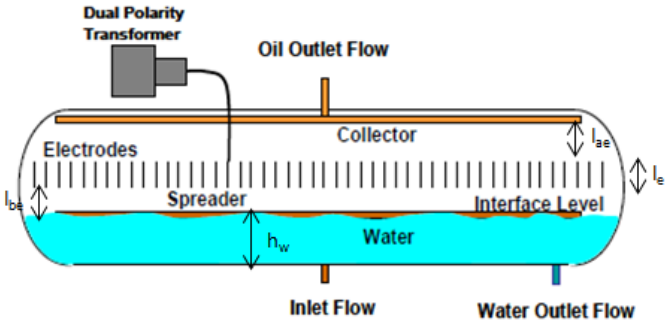

Source: adapted from Armstrong & Sams (2007))

The separation length is a function of the number of electrodes (N_e) and the distance between electrodes as per equation 6.8-4.

$$D = h_w + l_{be} + l_e + l_{ae} \quad \text{6.8-3}$$

$$L = (N_e + 1) \cdot d_{ec} \quad \text{6.8-4}$$

$$VOL_{es} = A_{es} \cdot L \quad \text{6.8-5}$$

$$A_{es} = A_e - A_{be} \quad \text{6.8-6}$$

$$A_{be} = \left(\frac{r^2}{2}\right) \cdot \left(2\cos^{-1}\left(\frac{r-(h_w+h_{be})}{r}\right) - \sin\left(2\cos^{-1}\left(\frac{r-(h_w+h_{be})}{r}\right)\right)\right) \quad \text{6.8-7}$$

$$A_e = \left(\frac{r^2}{2}\right) \cdot \left(2\cos^{-1}\left(\frac{r-(h_w+h_{be}+h_e)}{r}\right) - \sin\left(2\cos^{-1}\left(\frac{r-(h_w+h_{be}+h_e)}{r}\right)\right)\right) \quad \text{6.8-8}$$

$$E = \frac{U/1000}{d_{ec} \cdot 100} \quad \text{6.8-9}$$

The design of the electrostatic coalescer presents the following parameters that can be optimized: N_e, d_e, h_e, U, and h_w. A set of 5 design inputs would already significantly increase complexity of a multi-objective optimization. A regression tree has been created, and the importance of each parameter is estimated as

described on section 4. Figure 6-14 shows the relative importance of each of the input parameters on the key outcomes of the electrostatic coalescer: area, dry weight, outlet BS&W, and difference between residence time of water phase and required time of oil droplet to rise (Δ_{oiw}).

Figure 6-14: Electrostatic Coalescer – Relative importance of input parameters

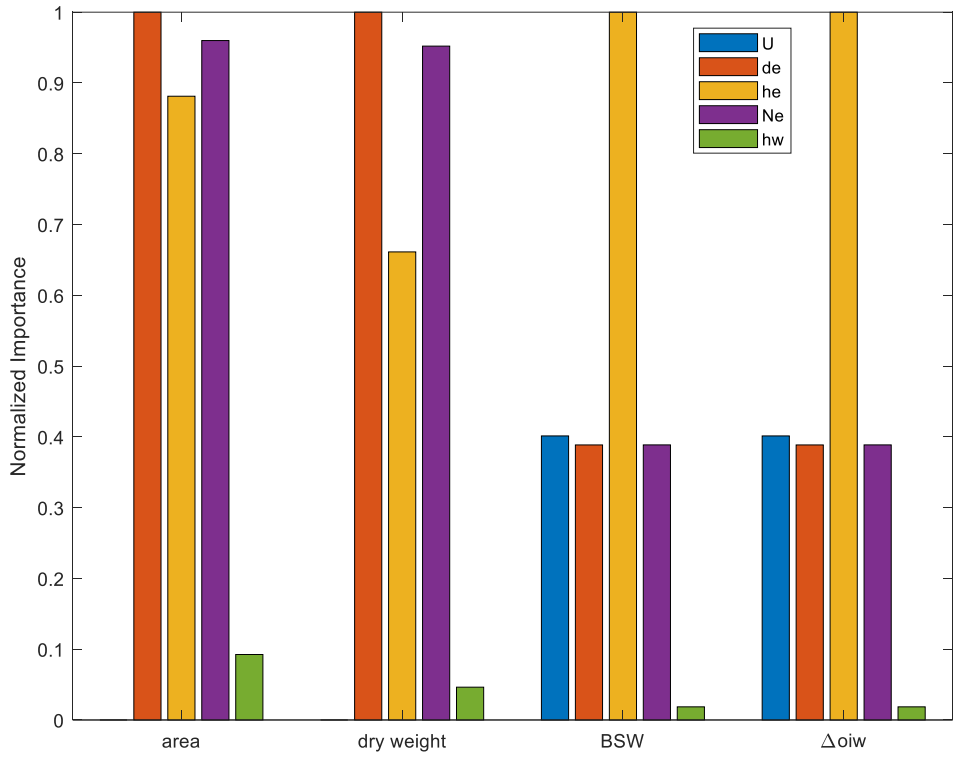

The parameters d_e and h_e are the most important, followed by N_e. The importance of parameter U is relatively low. The importance of parameter h_w is negligible. Therefore, parameters U and h_w have been eliminated as variable parameters.

6.9. **Oil desalting**

The maximum allowable salinity is one of the oil sales specifications. It is a sum of the salt dissolved in the oil (which is nearly zero) and the salt dissolved in the remaining water. Achieving the BS&W specification may not be sufficient to achieve the salinity specification, as formation water may be too salty. The typical solution is to add low-salt water (e.g., seawater, desalinized water) to the oil dominated stream upstream the electrostatic coalescer. Such process is

denominated dilution, where a mixing device provides adequate contact between the oil dominated stream and the dilution water.

Considering a single stage process, the amount of necessary dilution water is given by Eq. 6.9-1 (Manning & Thompson, 1995), where D is the volume of dilution water (in bbl) per 1000 bbl of clean (no water) crude, X_A is the volume fraction of brine in the crude oil stream feeding the desalter, X_B is the volume fraction of crude oil leaving the desalter, K_A is the salinity of the brine contained in the crude oil stream feeding the desalter, K_B is the salinity of the brine contained in the crude oil stream leaving the desalter, and K_D is the salinity of the dilution water. In a single-stage process, the desalter is the electrostatic coalescer, so in the same equipment both oil dehydration and desalting occur. The parameter Z is the salt specification, given in pounds of salt per 1000 bbl of clean crude.

$$D = \frac{A \cdot (B \cdot K_A - Z)}{E \cdot (Z - B \cdot K_D)} \quad \text{6.9-1}$$

$$Z = B \cdot K_B \quad \text{6.9-2}$$

$$A = \frac{1000 \cdot X_A}{1 - X_A} \quad \text{6.9-3}$$

$$B = \frac{1000 \cdot X_B}{1 - X_B} \quad \text{6.9-4}$$

6.10. **TEG physical absorption gas dehydration**

After separation from oil, the associated gas will be saturated with water. Water must be removed for various reasons, such as to reduce risk of hydrate formation, reduce corrosion, and protect certain equipment that tolerates only small amounts of water.

Physical absorption by TEG is traditionally used in topsides applications, able to decrease water concentration to very low levels. In this equipment, a solution formed by triethylene glycol (TEG) and water, herein referred as lean TEG, absorbs the water contained in the associated gas stream in an absorption column. The water rich TEG solution, herein referred as rich TEG, leaves the absorption tower, and is regenerated in another column, denominated stripper,

where heat is used to vaporize the excess of water contained in rich TEG, generating the lean TEG. In case heating is insufficient to achieve the desired concentration of TEG in the lean TEG, an extra column is added, where stripping gas is used to separate more water from rich TEG. Some examples of processes are shown in Figure 6-15 and Figure 6-16:

Figure 6-15: TEG Process – Alternative 1

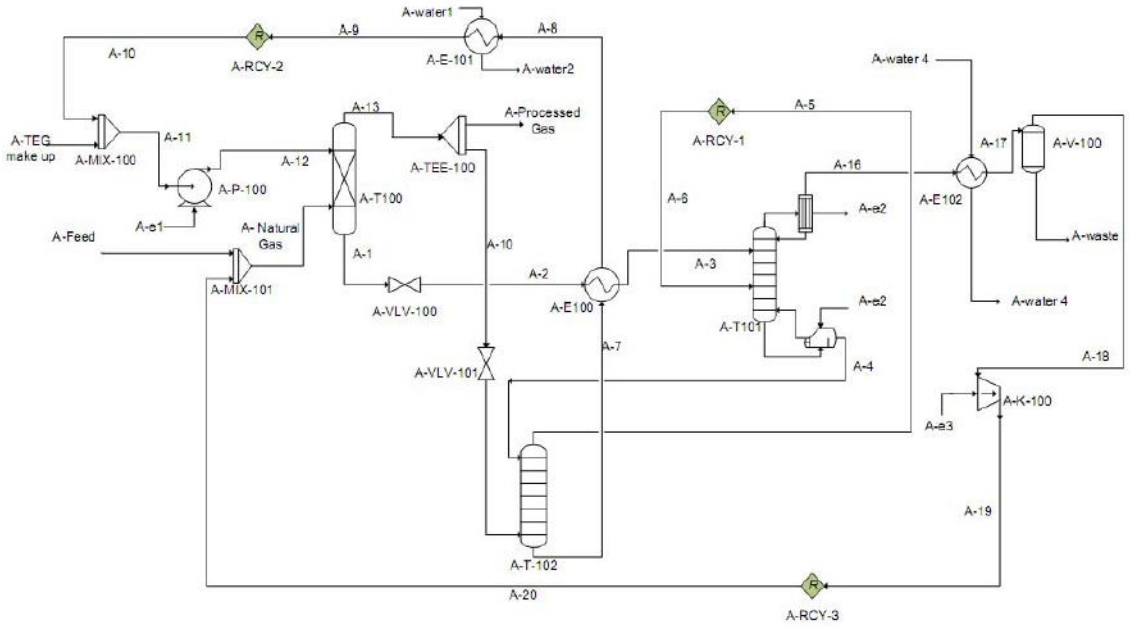

Source: Baidoo et al. (2011)

Figure 6-16: TEG Process – Alternative 2

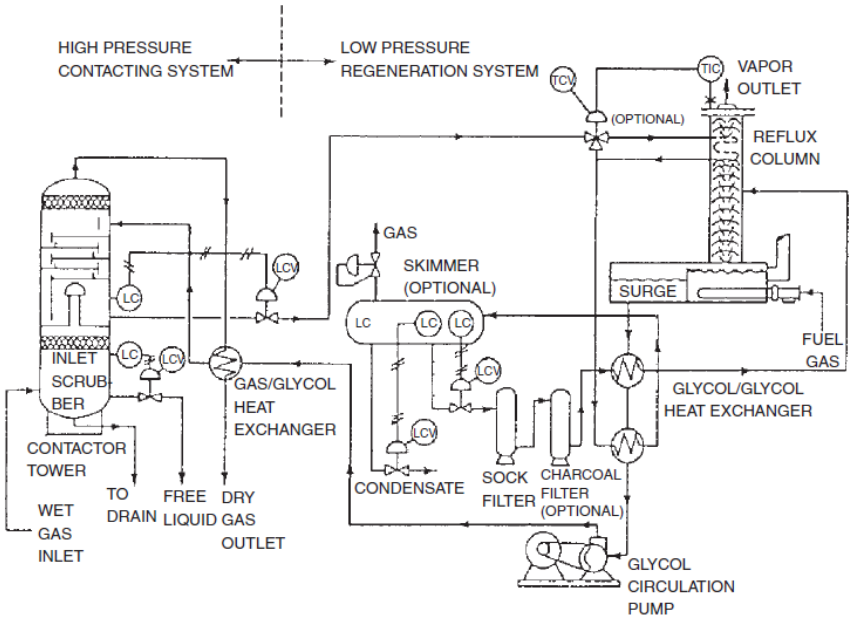

Source Mokhatab et al. (2006)

The processes show similarities, such as the use of stripping gas in column A-T-102 in Process 1 and fuel gas being fed into the reflux (stripping) column in Process 2, the heat recovery of lean TEG by rich TEG in heat exchanger A-E100 in Process 1 and the two glycol/glycol heat exchangers in Process 2. The main differences are the cooling of lean glycol by dry gas in Process 2, the use of a second column in Process 1 to enhance water separation by stripping gas, and the use of a cooler to condense the separated water and recover the stripping gas in Process 1. As the publication related to Process 1 is more recent, it was selected as the TEG process to be modeled.

The absorber is the key equipment in terms of weight, since it typically operates at high pressure and handles a large amount of gas. The diameter of a packed column is estimated by the use of the pressure drop in the flooding point (ΔP_{fl}), given by equation 6.10-1, in inH2O/ft (Kister et al., 2007),:

$$\Delta P_{fl} = 0.12 \cdot F_P^{0.7} \tag{6.10-1}$$

The pressure drop in packed columns (ΔP_{pc}) is given by the following equation (Mackowiak, 1991):

$$\Delta P_{pc} = \psi_{V,L} \cdot \left(\frac{1 - e_{pack}}{{e_{pack}}^3}\right) \cdot \left(\frac{F_v^2}{D_a \cdot K}\right) \cdot \left(1 + \frac{h_l}{\left(1 - e_{pack}\right)}\right) \cdot \left(1 - \frac{h_l}{e_{pack}}\right)^{-3} \tag{6.10-2}$$

$$h_l = 2.2 \cdot B_L^{0.5} \tag{6.10-3}$$

$$B_L = \left(\frac{\mu_l}{\rho_l \cdot g^2}\right)^{1/3} \cdot \left(\frac{v_l}{e_{pack}}\right) \cdot \left(\frac{1 - e_{pack}}{e_{pack} \cdot D_a}\right) \tag{6.10-4}$$

$$F_v = v_g \cdot \rho_g^{1/2} \tag{6.10-5}$$

$$D_a = \frac{6 \cdot \left(1 - e_{pack}\right)}{a_{pack}}$$

$$K = \left(1 + \frac{2}{3} \cdot \frac{1}{\left(1 - e_{pack}\right)} \cdot \frac{D_a}{D_{flood}}\right)^{-1} \tag{6.10-6}$$

$$\psi_{V,L} = 3.8 \cdot \delta_{pack} \tag{6.10-7}$$

$$\psi_{V,L} = 5.4 \cdot \nu \cdot Re_L^{-0.14} \tag{6.10-8}$$

$$Re_L = \frac{\rho_l \cdot v_l}{a_{pack} \cdot \mu_l} \qquad 6.10\text{-}9$$

In a flooding condition, the result of equation 6.10-1 (after conversion to SI) will be equal to the result of equation 6.10-2, leading to the value of the unknown flooding diameter. The Reynolds number in flooding condition is calculated, and if it is greater than a certain limit, the flooding diameter is determined again, but the parameter $\psi_{V,L}$ is now calculated with equation 6.10-8. By having the flooding diameter, the gas speed under flooding conditions is determined. The operational gas speed will be the multiplication of the gas speed under flooding by a factor that reflects how close to the flooding condition the column will operate. Finally, the column diameter is obtained from the operational gas speed.

The height of the column depends on the packing height and an additional height to allow distribution of the inlet and outlet fluids. The packing height is estimated by the method proposed by Bahadori & Vuthaluru (2009). In equation 6.10-10, the required water removal efficiency is calculated. The removal efficiency provided by the design is given by equation 6.10-11 to 6.10-15, where ψ is the TEG solution circulation rate, in m^3/kgH2O and X is the TEG concentration (mass fraction). Coefficients A_1-A_4, B_1-B_4, C_1-C_4, and D_1-D_4 are available in the publication, depending on the number of theoretical stages. Each theoretical stage accounts for 150 cm packing height, adequate for planning purposes according to the authors. According to this method, the maximum packing height is 6 m as the maximum number of theoretical stages is 4. The method is implemented in order to give the lowest packing height that meets the required water removal efficiency, given a TEG concentration (X) and circulation rate (ψ), which are the parameters that can be optimized.

$$R_{req} = \frac{C_{H_2O,in} - C_{H_2O,out}}{C_{H_2O,in}} \qquad 6.10\text{-}10$$

$$\ln R = a + \frac{b}{\psi} + \frac{c}{\psi^2} + \frac{d}{\psi^3} \qquad 6.10\text{-}11$$

$$a = A_1 + \frac{B_1}{X} + \frac{C_1}{X^2} + \frac{D_1}{X^3} \qquad 6.10\text{-}12$$

$$b = A_2 + \frac{B_2}{X} + \frac{C_2}{X^2} + \frac{D_2}{X^3} \quad \text{6.10-13}$$

$$c = A_3 + \frac{B_3}{X} + \frac{C_3}{X^2} + \frac{D_3}{X^3} \quad \text{6.10-14}$$

$$d = A_4 + \frac{B_4}{X} + \frac{C_4}{X^2} + \frac{D_4}{X^3} \quad \text{6.10-15}$$

The additional height to allow distribution of the inlet and outlet fluids is estimated between 6 ft-10 ft (Mokhatab, Poe & Speight, 2006). In this work is it considered as 8 ft.

The stripping column packing height is considered as 1.8 m (KLM Technology Group, 2015a) and an additional 0.4 m is considered to allow distribution of inlet and outlet fluids. The required heat is provided by the reboiler, which is designed as a shell & tube heat exchanger according to section 6.4. According to (Petroskills, 2019), achieving a TEG purity of more than 98.7% requires heating the rich TEG solution to a temperature greater than 206°C, which is the temperature that destabilizes the TEG molecule, therefore cannot be exceeded. In such case, a second stripping column is necessary, where stripping gas will be added to achieve the required purity. The ratio of stripping gas by rich TEG solution (Sm^3 gas/Sm^3 TEG) is estimated by equation 6.10-16 (PetroSkills, 2013), assuming reboiler temperature equal to 204°C (close to the maximum allowed temperature) and number of theoretical stages equal to 1. Coefficients a to g are shown in the publication and T is given in °C.

$$Q_g = \frac{a \cdot X - 10}{1 + b \cdot X + c \cdot X^2} + d \cdot y + e \cdot y^2 + f \cdot y^3 \quad \text{6.10-16}$$

$$y = (g - T) \cdot X \quad \text{6.10-17}$$

The height of the second stripping column is assumed equal to the first stripping column. The internal diameter of both stripping columns $D_{int,ST}$ is estimated by equation 6.10-18 where Q_{TEG} is given in gal/min and diameter in inches (Mokhatab, Poe & Speight, 2006).

$$D_{int,st} = 9 \cdot Q_{TEG}^{0.5} \quad \text{6.10-18}$$

The following simplifications were adopted as they should not lead to relevant impact in weight, footprint or energy consumption of the unit:

- TEG make-up is not considered as TEG losses to both natural gas in the absorber and to water in the stripper are still not modeled;
- Recycling of stripping gas to absorber is not considered as flow is very small compared to inlet stream.

6.11. **Solid desiccant gas dehydration**

Another method to remove water from natural gas is by use of solid desiccants, adopting the principle of physical adsorption and desorption in order to respectively separate water and regenerate the adsorption medium. Such method is typically more effective than glycol dehydrators, achieving less than 0.1 PPMV of water in natural gas (Mokhatab, Poe & Speight 2006).

A typical process is shown in Figure 6-17, showing 2 x 100% adsorbers. While the adsorber in the left is in the adsorption mode, removing water from the natural gas that flows from top to bottom, the adsorber in the right is under regeneration, or desorption mode. Regeneration depends on a certain amount of the dry gas produced by the adsorber in the left. Such amount is heated to a high temperature (from 450-600°F) and flows through the adsorber under regeneration from bottom to top, removing the adsorbed water. The high temperature gas with water is cooled in order to separate the water, and is then recycled to the adsorber in the adsorption mode.

Figure 6-17: Solid Desiccant Gas Dehydration

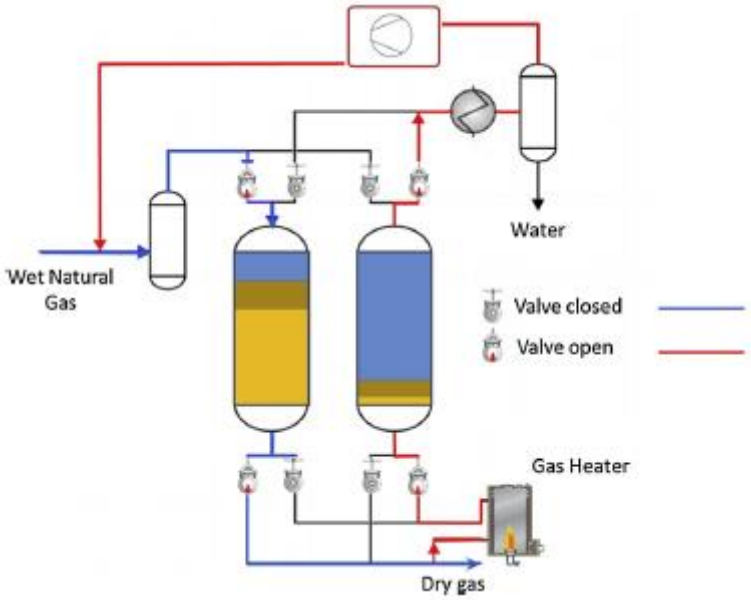

Source Santos et al. (2017)

The choice of the solid desiccant depends on several factors. In this work the 4Å zeolite molecular sieve is chosen, as it is typically employed in the FPSOs operating in the pre-salt cluster in Brazil. There are three capacity terms adopted:

- static equilibrium capacity: the maximum adsorption capacity of the solid desiccant, obtained in no flow condition, typically referred as isotherms;
- dynamic equilibrium capacity: the adsorption capacity under flow conditions;
- useful capacity: account for loss of desiccant capacity and the fact that not all of the desiccant will be used.

The modified Langmuir isotherm known as Langmuir III estimates water adsorption capacity in equation 6.11-1, where IP_1 to IP_4 are coefficients that can be found in the publication, T is temperature in K and P_{H_2O} is partial pressure of water in bar (Santos et al., 2017):

$$W_{H_2O} = \frac{(IP_1 + IP_2 \cdot T) \cdot IP_3 \cdot e^{(IP_4/T)} \cdot P_{H_2O}}{1 + IP_3 \cdot e^{(IP_4/T)} \cdot P_{H_2O}} \qquad 6.11\text{-}1$$

Santos et al. (2017) suggests that the value estimated by equation 6.11-1 is the useful capacity of the 4Å zeolite molecular sieve, although one may infer that it is the static equilibrium capacity as it is referred as adsorption isotherm.

Having the water adsorption capacity, the adsorbent mass is calculated, but it needs to be corrected since other molecules than H_2O compete for the adsorption sites. Santos et al (2017) showed that the main constituents of natural gas that compete for the adsorption sites are CO_2 and CH_4. Using data of a specific chart available in Santos et al. (2017), a second degree polynomial curve dependent on CO_2 concentration and pressure was fitted, estimating the correction factor, which will increase the necessary mass of adsorbent.

Adopting a typical ratio between height and diameter, in order to allow proper distribution of fluids and acceptable pressure drop, the diameter of the vessel is calculated by equation 6.11-2 and height of adsorbent by equation 6.11-3:

$$D = \left(\frac{4 \cdot V_{ads}}{\pi \cdot \beta}\right)^{1/3} \quad \text{6.11-2}$$

$$h_{ads} = \beta \cdot D \quad \text{6.11-3}$$

The height of the vessel is the sum of adsorbent height plus an additional height for supports and sufficient space to ensure good flow distribution at the top of the bed.

The maximum regeneration time (t_{reg}) is calculated according to equation 6.11-4, where t_{ads} is the adsorption time and n_{ads} is the number of adsorption vessels. In case of two adsorption vessels, the maximum regeneration time will be equal to the adsorption time.

$$t_{reg} = \frac{t_{ads}}{n_{ads} - 1} \quad \text{6.11-4}$$

Regeneration time considers heating and cooling times. Heating time ensures the bed is heated until the desired temperature, accounting for the mass of adsorbent, adsorbed water and vessel material. The heat provided to water accounts for sensible and latent heat. The heat required by the adsorbent and vessel material is simply obtained by multiplying their masses by their respective heat capacities.

The amount of regeneration gas is estimated by equation 6.11-5 (KLM Technology Group, 2015b), where HE_{heat} is the heat provided to adsorbent,

adsorbed water and vessel material. The regeneration temperature considered is the maximum between the vaporization temperature of water at the given pressure, and the regeneration temperature of the adsorbent. The resulting regeneration time is the sum of heating time and cooling time (t_{cool}), given by equations 6.11-5 and 6.11-6 (KLM Technology Group, 2015b):

$$W_{g,reg} = \frac{2.5 \cdot HE_{heat}}{\left(H_{g,reg} - H_{g,ads}\right) \cdot t_{heat}} \quad \text{6.11-5}$$

$$t_{cool} = \frac{HE_{cool}}{W_{g,reg} \cdot \left(H_{g,ads} - H_{g,reg}\right)} \quad \text{6.11-6}$$

$$t_{reg} = t_{heat} + t_{cool} \quad \text{6.11-7}$$

The term HE_{cool} is the heat that must be removed from the solid adsorbent and the vessel material in order to reach the adsorption temperature. This is accomplished by circulating dry gas at the adsorption temperature.

The recycling of regeneration gas to the vessel in the adsorption mode is considered in the code. Initially, an estimate of the regeneration gas flowrate is provided. The new regeneration gas flowrate is estimated according to equation 6.11-5, and in case it is not close enough to the estimate, the value provided by equation 6.11-5 becomes the new estimate, and the algorithm runs until convergence. For each run in the gas regeneration flowrate loop, another loop leads to the heating time, as the sum of heating and cooling time must be sufficient close to the regeneration time provided by equation 6.11-4. Various combinations of cooling and heating time are tested, and the one with the lowest regeneration gas flowrate is selected.

The heater is modeled as a shell & tube heat exchanger as provided in section 6.4, where the utility has the composition obtained when burning methane, flowing in the shell side as it presents much lower pressure than the regeneration gas.

The inputs required for modeling this equipment are the characteristics of the inlet gas stream (mass flowrate, pressure, temperature, and composition), the duration of the adsorption cycle, the number of vessels and required water concentration in natural gas (specification).

6.12. **H_2S removal from gas by iron oxide**

The presence of H_2S in associated gas may lead consequences such as corrosion and poisoning of living beings, therefore its level must be reduced to a certain threshold. H_2S can be removed through several processes, such as iron oxide, sulfa-treat, molecular sieve and chemical absorption by amines.

In the pre-salt cluster in Brazil, the Angra dos Reis FPSO is equipped with metal oxide fixed bed, lowering the H_2S content from 170 ppmv to 5 ppmv (de Andrade et al., 2015). This is the key reason why such equipment is modeled in this work.

The iron oxide process is designed according to formulation provided in Stewart (2014), shown in equations 6.12-1 to 6.12-3. The following chemical reactions occur:

$$Fe_2O_3 + 3H_2S \rightarrow Fe_2S_3 + 3H_2O$$

$$FeO + H_2S \rightarrow FeS + H_2O$$

In equation 6.12-1, $Q_{g,std}$ is given in std m^3/h and φ is the rate of H_2S deposition in grains/($h.m^2$). Equation 6.12-1 gives the minimum diameter necessary to satisfy the deposition allowed, which should not exceed 628 grains/($h.m^2$). Equation 6.12-2 gives the diameter related to the minimum or maximum superficial velocity allowed in the vessel. If the superficial velocity is lower than 0.61 m/s, channeling of gas through the bed may occur. If the superficial velocity is greater than 3 m/s, excessive pressure drop may occur. The minimum internal diameter is the maximum value between equations 6.12-1 or 6.12-2, where the maximum allowed superficial velocity is used in equation 6.12-2. The maximum internal diameter will be given by equation 6.12-2, using the minimum allowed superficial velocity. Any combination between diameter and height (h) that satisfies equation 6.12-3, as long as the bed height is at least 3 m high for H_2S removal and the diameter falls into minimum and maximum thresholds, will lead to a feasible design. In equation 6.12-1 and 6.12-3, the internal diameter is given in cm, Fe is the iron content (kg/m^3), e is the efficiency and t_c is the cycle time in days.

$$D = 4{,}255 \cdot \left(\frac{Q_{g,std} \cdot y_{H_2S}}{\varphi}\right)^{1/2} \quad \text{6.12-1}$$

$$D = \left(\frac{4 \cdot Q_g}{\pi \cdot v}\right)^{1/2} \quad \text{6.12-2}$$

$$D^2 \cdot h = \frac{t_c \cdot Q_{g,std} \cdot y_{H_2S}}{1.48 \cdot 10^{-6} \cdot e \cdot Fe} \quad \text{6.12-3}$$

The temperature and pressure variation across the bed can be neglected. In addition, no regeneration is considered, so after the cycle time is achieved the bed must be replaced.

6.13. **Heavy hydrocarbons removal from gas by Joule-Thomson effect**

The associated gas contains heavy hydrocarbons, typically up to decane, which can condensate when subjected to low enough temperature. Condensation may lead to several consequences, such as slugging flow in pipelines when exporting the natural gas to shore, and compromise operation of certain processing technologies like cellulose acetate membranes used to remove CO_2 from associated gas. Therefore the heavy hydrocarbons must be removed, and the respective specification is typically the dew point in a given pressure, which shall not be exceeded.

There are several technologies that can be applied in heavy hydrocarbons removal from gas, such as the Joule-Thomson (JT) based process, turbo-expansion, and mechanical refrigeration. In this work the Joule-Thomson based process is modeled as it is used in several FPSOs.

A typical heavy hydrocarbons removal process based on the JT effect is shown in Figure 6-18. The gas to be specified is first pre-cooled in a heat exchanger by the gas stream that leaves the gas-liquid separator located downstream the JT valve. The gas to be specified then is cooled in the JT valve, and the condensate is separated in the gas-liquid separator. Then, it is finally heated by the gas to be specified. A polishing filter coalescer may be used to remove, from the gas stream that leaves the gas-liquid separator, any liquid that was carried over in the gas-liquid separator.

Figure 6-18: Typical heavy hydrocarbons removal from gas by JT effect

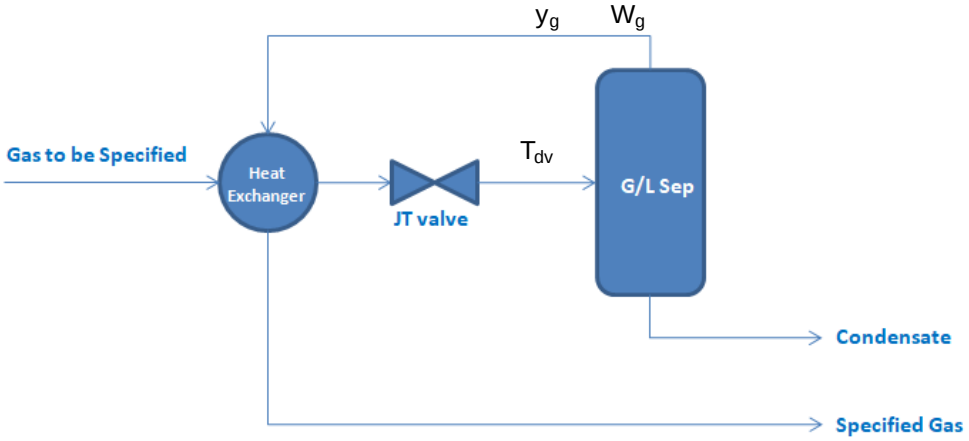

Source: author

A different process is shown in Figure 6-19, including injection of ethylene glycol to avoid hydrate formation, a by-pass of the feed gas, a pre-separator to remove condensates after feed gas pre-cooling, a gas-liquid exchanger in order to pre-cool part of the feed gas with the cold condensate stream, and finally a low pressure separator that recovers the ethylene glycol and separates the condensate.

Figure 6-19: Process flow diagram of heavy hydrocarbons removal from gas by JT effect

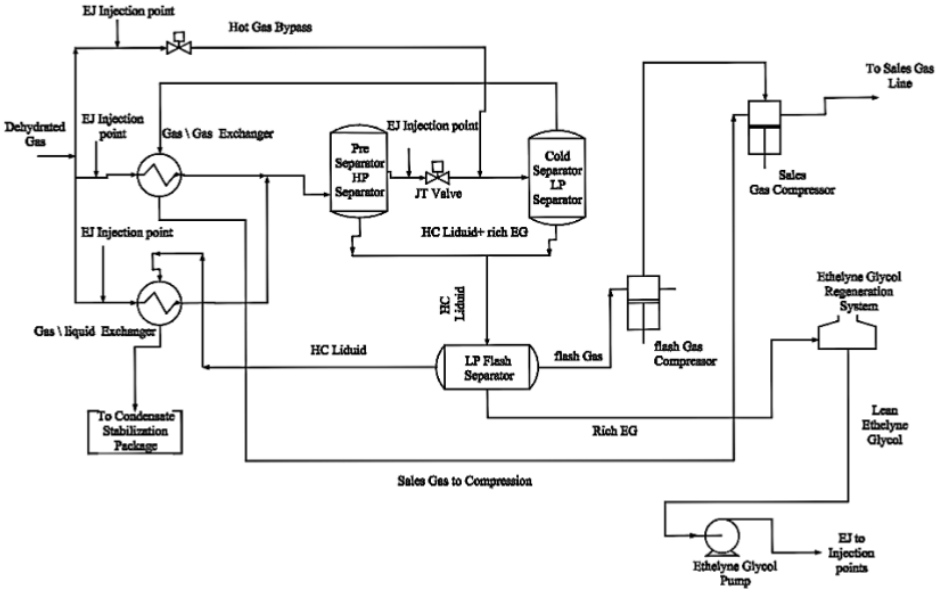

Source: Shoaib et al. (2018)

In this work it is adopted the process shown in Figure 6-18. In order to model it, several temperatures (T_{dv}) downstream the Joule-Thomson valve are tested until, in the heat exchanger, one of such temperatures leads to the lowest

difference between the heat received by the cold stream and the heat released by the hot stream. Depending on the inlet pressure, the pressure drop that occurs in the JT valve does not lead to a gas-liquid state. The temperature approach in the gas-gas exchanger is an input, typically set around 5 to 10°C. In this work it is adopted 7 °C.

The temperature downstream the Joule-Thomson valve (T_{dv}) has been estimated in Matlab and Aspen HySys for five inlet compositions, 80 bar inlet pressure, 38 bar pressure drop, 40°C inlet temperature and 7°C approach in heat exchanger. The results are shown in Table 6-2, indicating good agreement between Matlab and Aspen HySys.

Two parameters can be varied in the optimization process: the inlet pressure and the pressure drop across the JT valve.

Table 6-2: Validation of dew point control unit

Molar Composition (%)	T_{dv} (K)	
(C1, C2, C3, iC4, nC4, iC5, nC5, CO_2)	Matlab	HySys
77 / 10 / 5 / 3 / 3 / 1 / 1 / 0	285.15	284.99
67 / 8 / 7 / 5 / 4 / 2 / 1 / 6	291.15	290.73
72 / 5/ 4 / 2 / 2 / 1 / 1 / 13	276.15	276.45
63 / 5 / 4 / 2 / 2 / 1 / 1 / 22	276.15	275.52
10 / 0 / 0 / 0 / 0 / 0 / 0 / 90	273.65	273.33

6.14. **CO_2 removal by MEA chemical absorption**

Carbon dioxide is a contaminant that is present in many oil fields around the world, especially in the pre-salt cluster in Brazil. Typical specifications of maximum CO_2 molar content in export natural gas range between 2% to 5%, which are determined considering maximum allowed corrosion in the gas export pipeline and also the fact that CO_2 has no economic value. The molar CO_2 content in associated gas may be very high (more than 50%), leading to the need of CO_2 removal technologies in case associated gas cannot be fully reinjected in the producing reservoir or another destination.

Traditional CO_2 removal equipment relies on separation by chemical absorption. A solution composed of an amine species and water reacts in an absorption tower with the CO_2 contained in the associated gas. The amine solution is then

regenerated in a stripper column, where heat is provided by a reboiler. This process is very similar to the TEG process shown in section 6.10.

A typical CO_2 removal based on amine chemical absorption process is shown in Figure 6-20. The contaminated associated gas stream (S1) reacts with lean amine (S13) in the absorption column A. The treated gas (S2) leaves the absorption tower and is ready to be fed into the next process step. The rich amine (S3) exchanges heat with the hot lean amine recovered in the stripper column D and is fed into the stripper (S4). Recovery of amine is performed by the stripper column, which reverts the chemical reactions occurred in the absorber by increase of temperature, releasing the CO_2 from the amine solution. Depending on the absorption pressure, a pump is required to send the rich amine to the stripper, otherwise a valve is required to decrease the pressure. The reboiler (E) heats stream S7 and generates the vapor stream S8, which absorbs the CO_2 released from the descending liquid, generating a stream with high CO_2 content (S10). It is then condensed in F, generating a vapor stream (S11) that is very rich in CO_2, and a liquid stream (S5) that is rich in water, which is recycled. This process in energy intensive, and is typically applied in associated gas streams that present low CO_2 content.

Figure 6-20: Typical CO_2 removal based on amine chemical absorption process

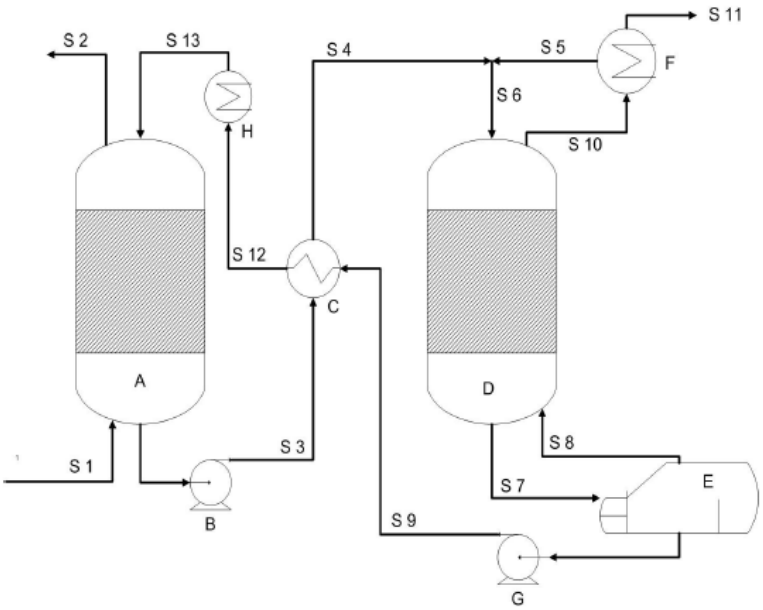

Source: Greer (2008)

The two-film mass transfer theory is used to model the absorber and stripper. Two films are formed between the bulk gas and bulk liquid stream: a gas film and a liquid film, as seen in Figure 6-21. The CO_2 diffuses through the gas film, is absorbed in the liquid and then diffuses through the liquid film. Given low presence of MEA in the gas phase and the high speed of the involved chemical reactions, they take place especially in the liquid phase.

The modeling is based on the work of Greer (2008) and Flores (2015). The absorber is discretized adopting the same approach of Greer (2008), as shown in Figure 6-22. The diameter is estimated by the same procedure explained in section 6.11, with the estimation of the flooding diameter and then the real diameter.

Figure 6-21: Reactive absorption based on two-film mass transfer theory

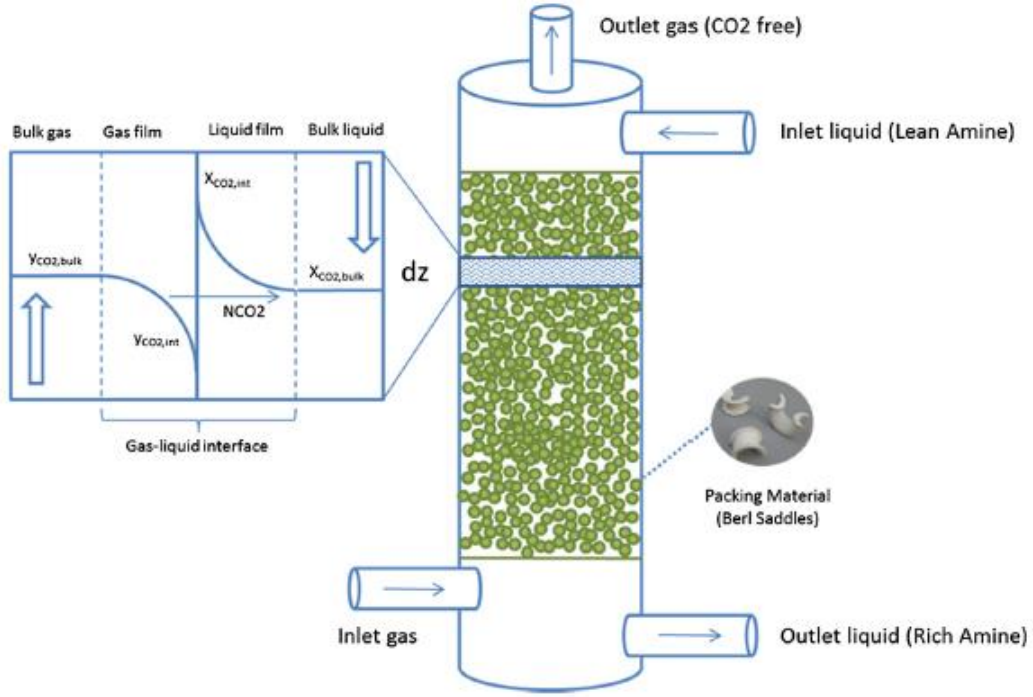

Source: Koronaki, Prentza & Papaefthimiou (2017)

Figure 6-22: Control volume of absorber

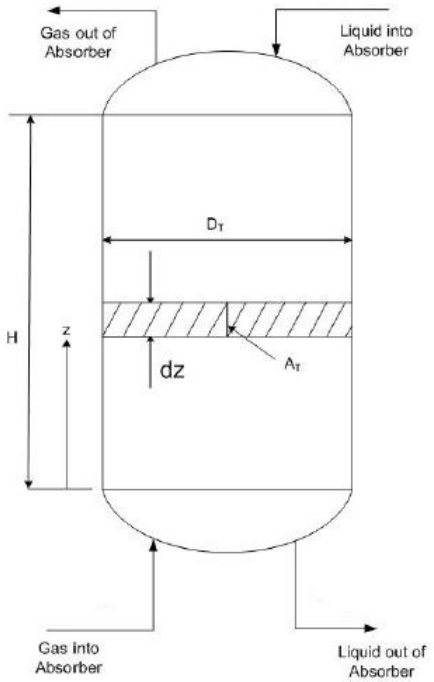

Source: adapted from Greer (2008)

Henry's law is used to convert the concentration of a component in the liquid into an equivalent interface pressure, allowing calculation of the CO_2 flow between liquid and gas phases, as seen in equations 6.14-9 to 6.14-23. The parameters kc_l and kc_g are the mass diffusion coefficients of CO_2 respectively in the liquid and gas phases, obtained from Onda, Takeuchi & Okumoto (1968). The enhancement factor, Enh, reflects the fact that CO_2 does not have to diffuse through all the liquid film since MEA continuously removes CO_2 from the liquid film due to the fast chemical reactions.

Once CO_2 achieves the liquid phase, chemical reactions occur between CO_2 and MEA, assuming chemical equilibrium. The following set of reactions is considered, according to Plaza, Wagener & Rochelle (2010). The forward and reverse rates are shown below each reaction.

Reaction 1 $\quad CO_2 + 2MEA \leftrightarrow MEAH^+ + MEACOO^-$

$$k_{f,R1} = 5.31E9 \cdot exp\left(\frac{-14{,}610}{R} \cdot \left(\frac{1}{T_l} - \frac{1}{298}\right)\right) \cdot a_{MEA}^2 \cdot a_{CO_2} \qquad 6.14\text{-}1$$

$$k_{r,R1} = 4.75E5 \cdot exp\left(\frac{-102{,}740}{R} \cdot \left(\frac{1}{T_l} - \frac{1}{298}\right)\right) \cdot a_{MEACOO^-} \cdot a_{MEAH^+} \qquad 6.14\text{-}2$$

Reaction 2 $MEA + CO_2 + H_2O \leftrightarrow HCO_3^- + MEAH^+$

$$k_{f,R2} = 9{,}026 \cdot exp\left(\frac{-49{,}000}{R} \cdot \left(\frac{1}{T_l} - \frac{1}{298}\right)\right) \cdot a_{MEA} \cdot a_{CO_2} \quad \text{6.14-3}$$

$$k_{r,R2} = 2{,}917 \cdot exp\left(\frac{-114{,}250}{R} \cdot \left(\frac{1}{T_l} - \frac{1}{298}\right)\right) \cdot \frac{a_{HCO_3^-} \cdot a_{MEAH^+}}{a_{H_2O}} \quad \text{6.14-4}$$

In chemical equilibrium, the following equalities simultaneously occur, leading to a system of two non-linear equations that must be solved in each increment of volume in the absorber or stripper columns, to find the advancement degrees of each of the reactions, respectively ξ_1 and ξ_2, and update the molar concentrations.

$$K_{R1} = \frac{k_{f,R1}}{k_{r,R1}} = \frac{\left(C_{l,MEAH^+} + \xi_1 + \xi_2\right) \cdot \left(C_{l,MEACOO^-} + \xi_1\right)}{\left(C_{l,CO_2} - \xi_1 - \xi_2\right) \cdot \left(C_{l,MEA} - 2\xi_1 - \xi_2\right)^2} \quad \text{6.14-5}$$

$$K_{R2} = \frac{k_{f,R2}}{k_{r,R2}} = \frac{\left(C_{l,HCO_3^-} + \xi_2\right) \cdot \left(C_{l,MEAH^+} + \xi_1 + \xi_2\right)}{\left(C_{l,MEA} - 2\xi_1 - \xi_2\right) \cdot \left(C_{l,CO_2} - \xi_1 - \xi_2\right) \cdot \left(C_{l,H_2O} - \xi_2\right)} \quad \text{6.14-6}$$

Finding the roots of the non-linear system formed by equations 6.14-5 and 6.14-6 requires an iterative procedure that does meet the fast convergence requirement of the model. Therefore only reaction 1, the main reaction, has been considered to estimate equilibrium concentrations. When simplifying equation 6.14-5 for a single reaction, the advancement degree can be obtained from the analytical resolution of a cubic equation, which is a very fast calculation. Another necessary modification is to simplify the enhancement factor calculation to only account for the forward rate of the main reaction (k1f).

Therefore, the enhancement factor, which is a number greater than 1, ends up reducing the resistance in the liquid phase, increasing the value of the parameter KH, given by equation 6.14-10.

$$dS = dz \cdot A \cdot a_e \quad \text{6.14-7}$$

$$dV = dz \cdot A \cdot e_{pack} \quad \text{6.14-8}$$

$$dM_{CO_2 tr} = KH \cdot a_e \cdot dV \cdot \left(y_{CO_2} \cdot P - He_{CO_2} \cdot C_{l,CO_2}\right) \quad \text{6.14-9}$$

$$KH = \frac{1}{\frac{He_{mod}}{Enh \cdot kc_l} + \frac{R \cdot T_g \cdot Z_g}{kc_g}} \quad 6.14\text{-}10$$

$$He_{CO_2} = x_{H_2O} \cdot He_{CO_2,H_2O} + x_{MEA} \cdot He_{CO_2,MEA} \quad 6.14\text{-}11$$

$$He_{CO_2,H_2O} = \frac{exp\left(170.7126 - \frac{8477.711}{T_l} - 21.95743 \cdot \ln T_l + 0.005781 \cdot T_l\right)}{\sum_i^{nc} C_{l,i}} \quad 6.14\text{-}12$$

$$He_{CO_2,MEA} = \frac{exp\left(89.452 - \frac{2934.6}{T_l} - 11.592 \cdot \ln T_l + 0.01644 \cdot T_l\right)}{\sum_i^{nc} C_{l,i}} \quad 6.14\text{-}13$$

$$He_{mod} = \frac{He_{CO_2}}{\sum_{i=1}^{nc} Cl_i} \quad 6.14\text{-}14$$

$$a_e = a_{pack} \cdot 1.34 \cdot \left(\frac{\rho_l}{\sigma_l} \cdot g^{1/3} \cdot \left(\frac{Q_l}{L_p}\right)^{4/3}\right)^{0.116} \quad 6.14\text{-}15$$

$$L_p = \frac{4 \cdot LPS}{LPH \cdot LPB} \cdot A \quad 6.14\text{-}16$$

$$Fr_l = \frac{v_l^2 \cdot a_{pack}}{g} \quad 6.14\text{-}17$$

$$We_l = \frac{(W_l/A)^2}{\rho_l \cdot \sigma_l \cdot a_{pack}} \quad 6.14\text{-}18$$

$$kc_l = 0.0051 \cdot \left(\frac{\mu_l \cdot g}{\rho_l}\right)^{1/3} \cdot \left(\frac{v_l \cdot \rho_l}{a_e \cdot \mu_l}\right)^{2/3} \cdot \left(\frac{D_{l,CO_2} \cdot \rho_l}{\mu_l}\right)^{0.5} \cdot \left(a_{pack} \cdot dp_{pack}\right)^{0.4} \quad 6.14\text{-}19$$

$$kc_g = 5.23 \cdot \left(a_{pack} \cdot D_{gCO_2}\right) \cdot \left(\frac{W_g}{A \cdot (1 - h_l) \cdot a_{pack} \cdot \mu_g}\right)^{0.7} \cdot \left(\frac{\mu_g}{\rho_g \cdot D_{gCO_2}}\right)^{1/3} \cdot \left(a_{pack} \cdot dp_{pack}\right)^{-2} \quad 6.14\text{-}20$$

$$Enh = \frac{\sqrt{D_{lCO_2} \cdot \left(k_{1f} \cdot C_{l,MEA} + k_{3f} \cdot C_{l,CO_2}\right)}}{kc_l} \quad 6.14\text{-}21$$

$$k_{1f} = 4.4E8 \cdot exp\left(\frac{-5{,}400}{T_l}\right) \quad 6.14\text{-}22$$

$$k_{3f} = \frac{10^{(13.65 - 2{,}895/T_l)}}{1000} \quad 6.14\text{-}23$$

The absorber is solved from top to bottom, depending on an estimation of the outlet gas temperature in order to estimate the remaining unknowns, which are the rich amine temperature, mass flowrate and composition, the outlet gas mass flowrate, composition and temperature. In order to simplify the problem and achieve quick convergence, the following is adopted:

- The diffusion of other gases than CO_2 in the liquid phase is not considered. As their solubilities in amine solutions are much lower than CO_2, the concentration profile in the amine solution should not significantly change if such gases were considered;
- H_2S removal is not considered due to lack of information regarding the reaction equilibrium constant between H_2S and MEA;
- No MEA make-up is considered since MEA vaporization is neglected due to the high boiling temperature.

In order to obtain temperatures T_l and T_v along the absorption or stripper column, their respective variations are calculated according to equations 6.14-25 to 6.14-36, considering steady state. Liquid and gas temperatures vary due to several reasons:

- heat of reaction 1, leading to a variation in the liquid temperature. In the stripper, the sign of equation 6.14-28 is positive, so the liquid temperature decreases when the reverse reaction is favored;
- latent heat of water vaporization or condensation. In case water vaporizes, the liquid is cooled (sign of equation 6.14-27 is negative) and vapor is heated. As it is counter-current, gas temperature variation is negative from top to bottom (sign of equation 6.14-31 is negative). When water condenses, the liquid is heated and vapor is cooled, and signs of both equations are positive. The term kc_{gH_2O} is calculated the same way as equation 6.4-19, but substituting the diffusivity of CO_2 by the diffusivity of H_2O;
- heat of convection between liquid and gas phases (equations 6.14-29 and 6.14-32).

$$dT_l = dT_{l_{H2Otransf}} + dT_{l_{reac}} + dT_{l_{conv}} \qquad \text{6.14-24}$$

$$dM_{H2O_{tr}} = \left(\frac{P_{v_{H2Ol}}}{R \cdot T_l} - \frac{P_{v_{H2Og}}}{R \cdot T_g}\right) \cdot kc_{gH_2O} \cdot dS \quad \text{6.14-25}$$

$$E_{H2O} = |dM_{H2O_{tr}} \cdot 0.018 \cdot \Delta H_{v,H2O}| \quad \text{6.14-26}$$

$$dT_{l_{H2Otransf}} = \frac{\pm E_{H2O}}{W_l \cdot C_{p_l}} \quad \text{6.14-27}$$

$$dT_{l_{reac}} = \frac{-dM_{CO_2tr} \cdot \Delta H_{r,MEA-CO_2}}{W_l \cdot C_{p_l}} \quad \text{6.14-28}$$

$$dT_{l_{conv}} = -\frac{dS \cdot h_v \cdot (T_l - T_g)}{W_l \cdot C_{p_l}} \quad \text{6.14-29}$$

$$dT_g = dT_{g_{H2Otransf}} + dT_{g_{conv}} \quad \text{6.14-30}$$

$$dT_{g_{H2Otransf}} = \frac{\pm E_{H2O}}{W_g \cdot C_{p_g}} \quad \text{6.14-31}$$

$$dT_{g_{conv}} = \frac{-dS \cdot h_v \cdot (T_l - T_g)}{W_g \cdot C_{p_g}} \quad \text{6.14-32}$$

$$h_v = kc_g \cdot \left(\rho_g \cdot C_{p_g}\right)^{1/3} \cdot \left(\frac{g}{D_{gCO2}}\right)^{2/3} \quad \text{6.14-33}$$

$$\Delta H_{r,MEA-CO_2} = (-2.798 \cdot lo^5 + 1.6545 \cdot lo^4 - 0.1686 \cdot lo^3 - 0.04535 \cdot lo^2 + 0.00839 \cdot lo + 0.085017) \cdot 10^6 \quad \text{6.14-34}$$

$$\Delta H_{r,MEA-CO_2} = (-0.1256 \cdot lo^5 + 0.6377 \cdot lo^4 - 1.2818 \cdot lo^3 + 1.2757 \cdot lo^2 - 0.6319 \cdot lo + 0.129077) \cdot 10^6 \quad \text{6.14-35}$$

$$lo = \frac{x_{CO_2} + x_{MEACOO^-} + x_{HCO_3^-}}{x_{MEA} + x_{MEACOO^-} + x_{MEAH^+}} \quad \text{6.14-36}$$

In the absorber, the following boundary conditions are known:

- Associated gas inlet stream: mass flowrate, pressure, temperature, composition;
- Associated gas outlet stream: CO_2 specification;
- Lean amine inlet temperature, which must be at least 5.5°C greater than the inlet gas (KLM Technology Group, 2012), therefore it is a function of the inlet gas temperature.

The stripper column is modeled in the same way of the absorber. In the stripper, the rich amine, containing $MEACOO^-$ concentration much higher than the lean amine, releases CO_2 from $MEACOO^-$ as the high temperature provided by the reboiler favors the reverse path of reaction 1. The released CO_2 will diffuse to the vapor stream generated by the reboiler. The rich amine characteristics are known (pressure, temperature, mass flowrate, composition) as the characteristics of the rich amine leaving the absorber are estimate when running the absorption model, and the changes that occur in the heat exchanger C are modeled according to section 6.4. A certain percentage of the water contained in the rich lean amine vaporizes in the reboiler, and such quantity is summed to the rich amine stream coming from the absorber, as full water condensation occurs in the condenser, leading to the mass flowrate and composition of stream S6. The composition of stream S10 is known since it contains the vaporized water in the reboiler and the CO_2 separated in the absorber.

A mass balance between the water contained in streams S7, S8 and S9 is done in order to compute the water flowrate in S7, as the water flowrate in S9 is known (the lean amine composition and flowrate are inputs) and in S8 is also known (as the amount of vaporized water in stream S7 in the reboiler is also an input). It is necessary an initial estimation of the water flowrate in S7 in order to converge the mass balance.

By setting the condenser pressure (an input), the condensation temperature is estimated, and in case it is lower than the minimum possible condensation temperature (as the cooling medium temperature is an input), the vaporized water in the reboiler must be increased.

The vapor temperature leaving the stripper (stream S10) should be estimated, leading to an iterative procedure that only halts when the vapor temperature at the last iteration (bottom) is sufficiently close to the reboiler temperature. As the iterative procedure is from top to bottom, in case the CO_2 concentration in the vapor stream exceeds the threshold that changes the flow of CO_2 from vapor to liquid, the algorithm stops and increases the water flowrate vaporized in the

reboiler. When the water flowrate is sufficient, the iterative procedure will stop when all the required CO_2 is desorbed from the liquid.

Regarding the lean amine characteristics, in order to reduce the number of parameters that can be optimized and reduce the optimization time, its composition must be given and the ratio between mass flowrate of lean amine and mass flowrate of inlet gas. In case the combination of lean amine mass flowrate and its composition leads to a non-feasible design due to lack of MEA, the absorption algorithm automatically increases the ratio between mass flowrate of lean amine and mass flowrate of inlet gas. In order to speed up convergence, such ratio is estimated by the stoichiometry of reaction 1 and a percentage increment to enable convergence in the first ratio estimation as the reverse reaction path will not allow convergence when using the ratio estimated by the stoichiometry. The lean amine composition is defined by adopting 70% water mass composition and MEA, $MEACOO^-$ and $MEAH^+$ content that observes the reaction stoichiometry.

All other elements of the process, such as the lean amine cooler, valves, reboiler, condenser, pumps, are modeled according to the previous sections and are considered in the weight, footprint, and energy estimations.

Examples of estimated temperature profiles for absorber and stripper are respectively given in Figure 6-23 and Figure 6-24, for the following characteristics of the absorber inlet gas:

- Molar concentration (%): CO_2 9 / C1: 76 / C2: 10 / C3: 5;
- Mass flowrate: 19.3 kg/s;
- Temperature: 311 K;
- Pressure: 38 bar.

Figure 6-23: Temperature profiles in absorber for a specific input data

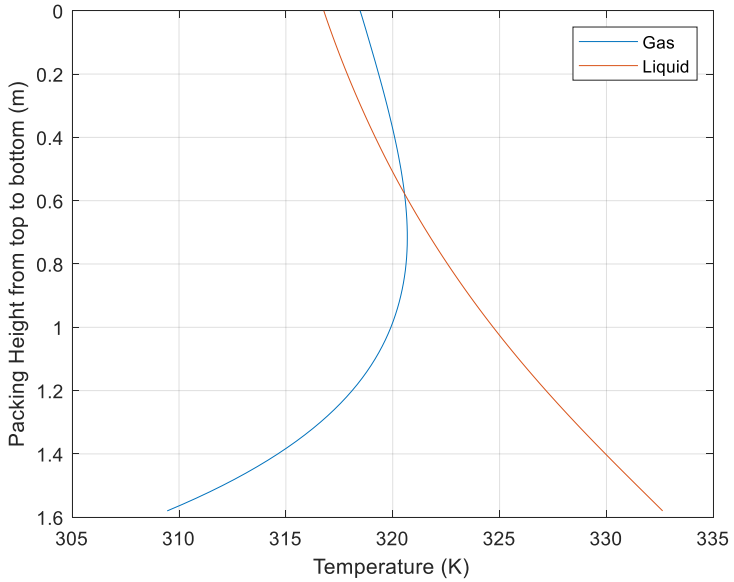

Figure 6-24: Temperature profiles in stripper for a specific input data

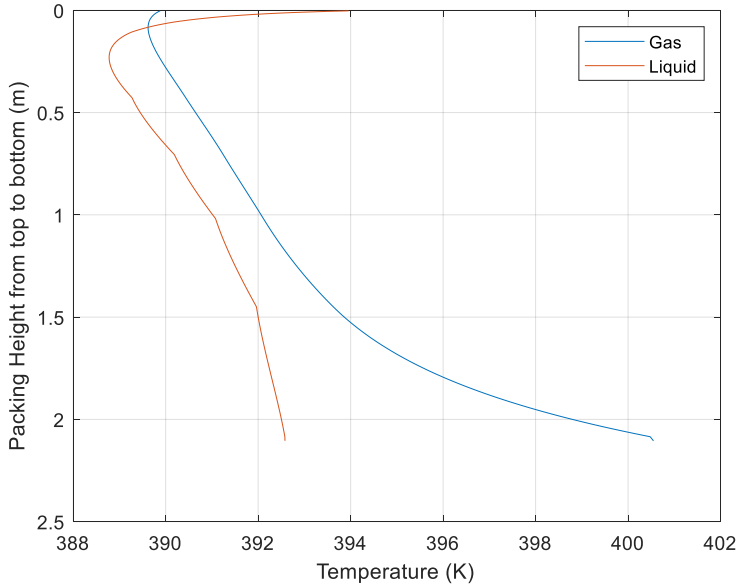

The packing characteristics are given in Table 6-3:

Table 6-3: Packing characteristics

Property	Value
ρ_{pack}	275 kg/m^3
dp_{pack}	50 mm
a_{pack}	250 m^2/m^3
e_{pack}	0.975
δ_{pack}	0.3
LPS	0.0171 m

LPB	0.0241 m
LPH	0.0119 m
F_p	85 m^{-1}

Even though several simplifications have been applied, convergence is still slow due to the need to vary both outlet gas temperatures at absorber and stripper towers in order to achieve convergence. In addition, the amount of water vaporized in the reboiler must be varied until all necessary CO_2 desorbs from the rich amine. A DOE dataset has been generated by the SOBOL algorithm by varying CO_2 content, mass flowrate, temperature and pressure of the inlet associated natural gas stream at the absorption tower. This dataset contains 200 combinations to run the full CO_2 removal amine system algorithm in order to estimate dry weight, footprint, heating, cooling, power, and other necessary outputs. Then, inputs have been screened for each of the outputs by using trained regression trees. Finally, new regression trees for each of the outputs have been trained, using only the relevant inputs, in order to be later used by the genetic algorithm when optimizing the full plant.
The SOBOL dataset containing 200 points has been created using the following inlet gas inputs:

- Mass flowrate (kg/s): 5 (min), 80 (max);
- Temperature (K): 273.15 (min), 333.15 (max);
- CO_2 molar concentration (%): 0.03 (min), 0.20 (max);
- Pressure (bar): 5 (min), 120 (max).

The molar gas composition includes methane, 10% of ethane, 5% of propane, and CO_2. The CO_2 molar specification, the concentration the associated gas downstream the absorber must attain, was set at maximum 3%.

Most of the charts below show that the regression tree prediction is close to the model predictions, meaning that regression trees can be used instead of the slow convergent model, providing fast estimations when optimizing the full plant by the genetic algorithm. The associated gas temperature downstream the absorber showed significance dependence only on the inlet associated gas temperature at the absorber, therefore a line was fitted as seen in Figure 6-27.

Figure 6-25: Comparison between dry weight estimated by the model and regression tree

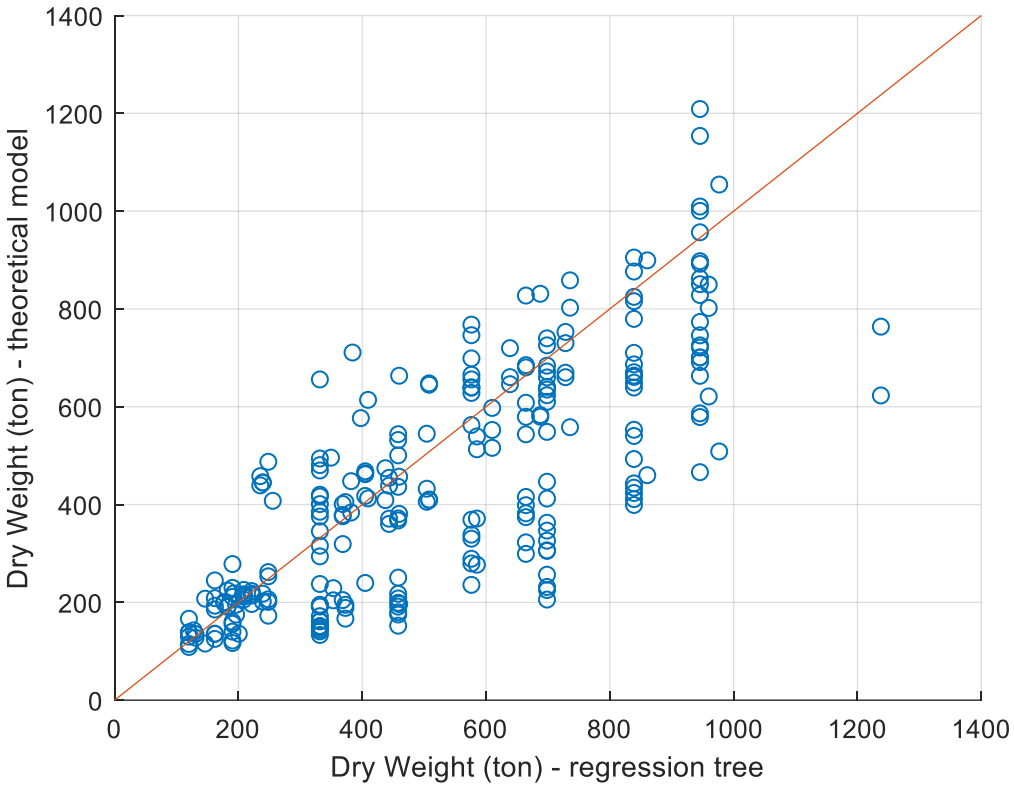

Figure 6-26: Comparison between footprint estimated by the model and regression tree

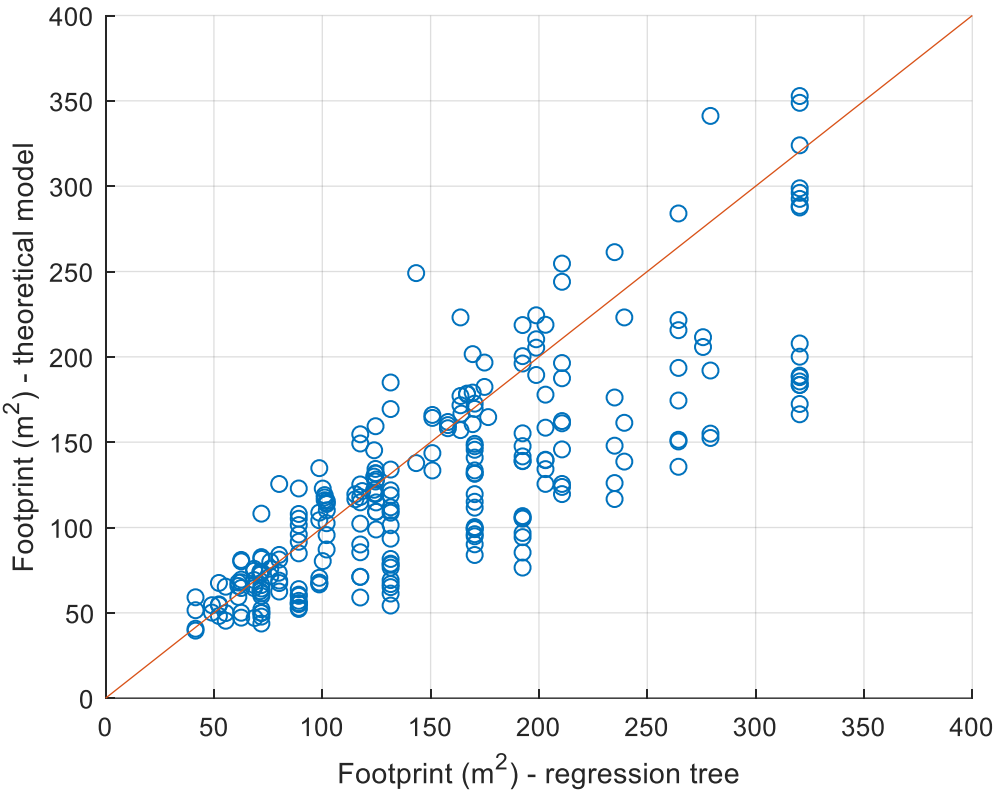

Figure 6-27: Absorber outlet gas temperature as function of absorber inlet gas temperature

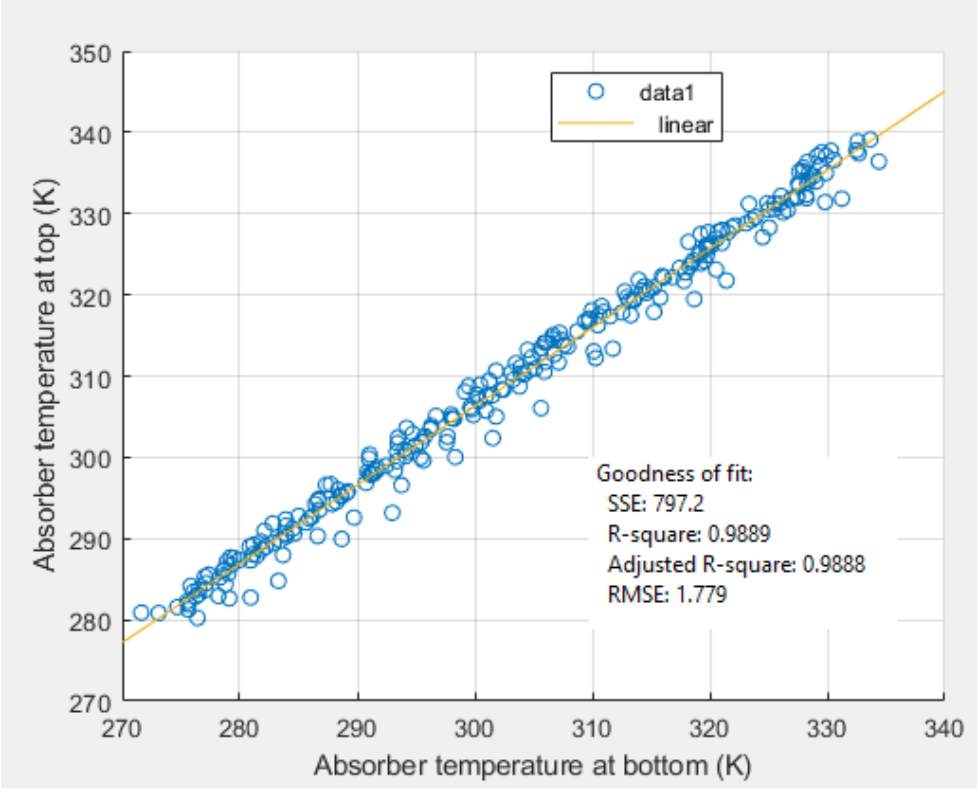

Figure 6-28: Comparison between heating demand estimated by the model and regression tree

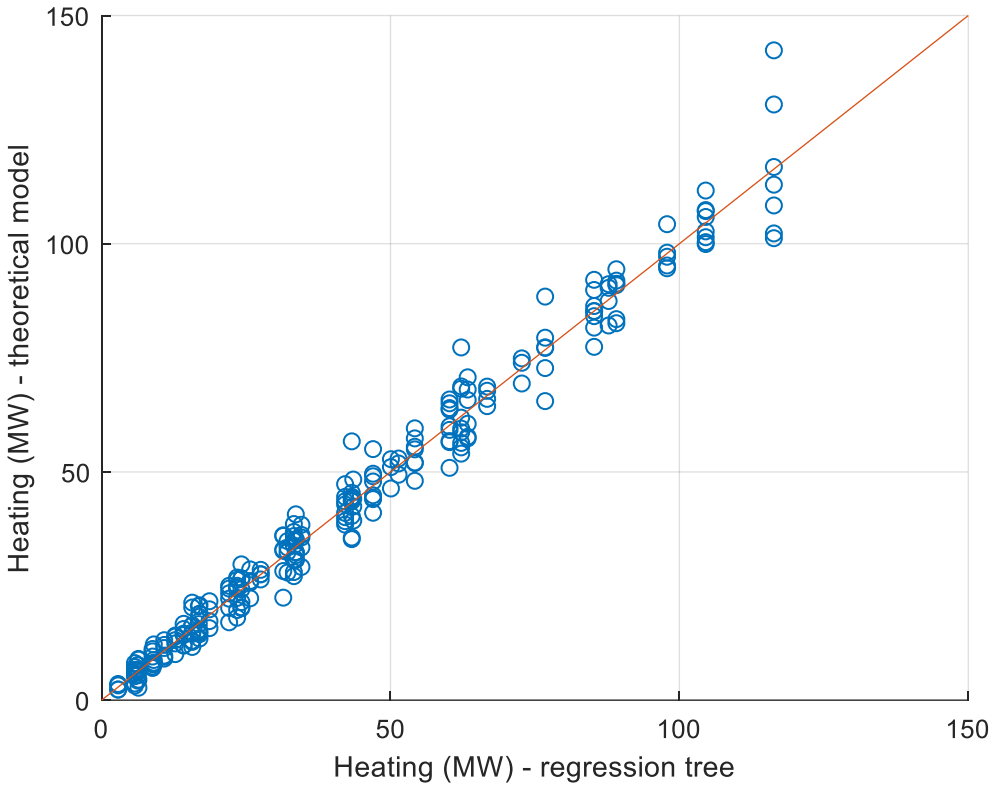

Figure 6-29: Comparison between cooling demand estimated by the model and regression tree

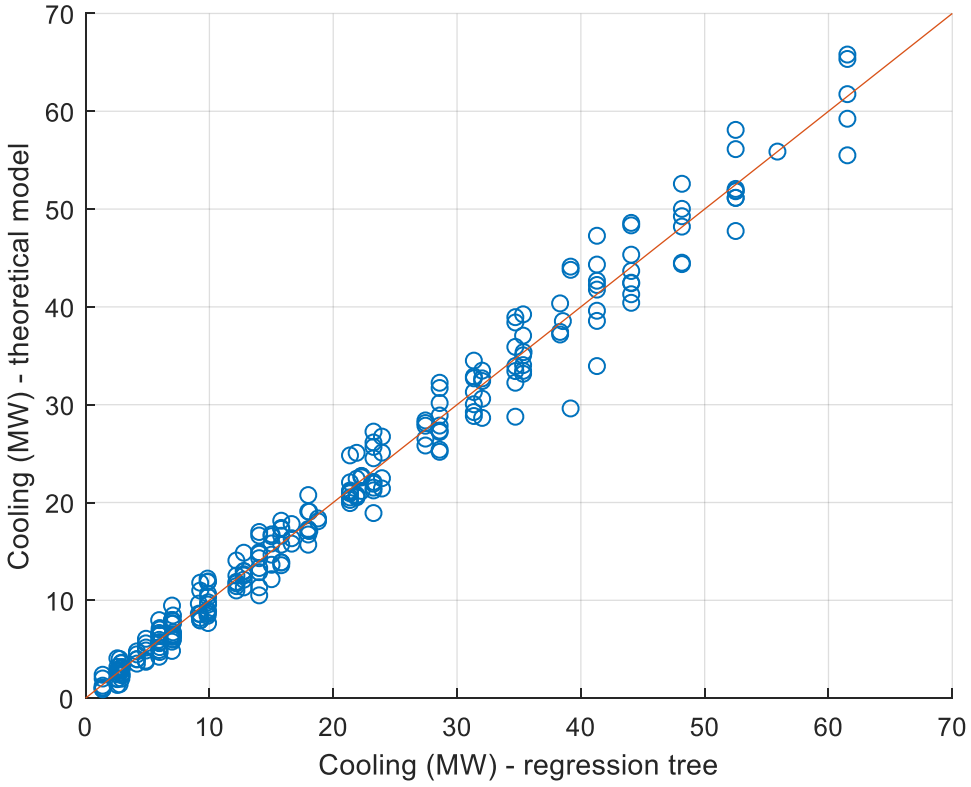

Figure 6-30: Comparison between power demand estimated by the model and regression tree

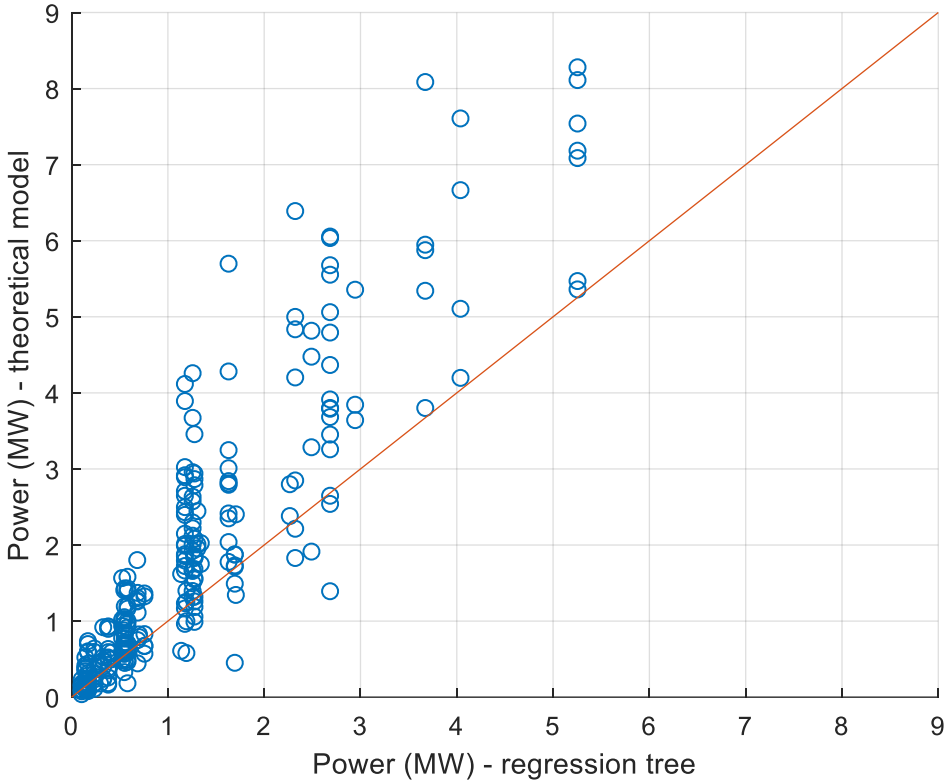

Figure 6-31: Comparison between absorber packing height estimated by the model and regression tree

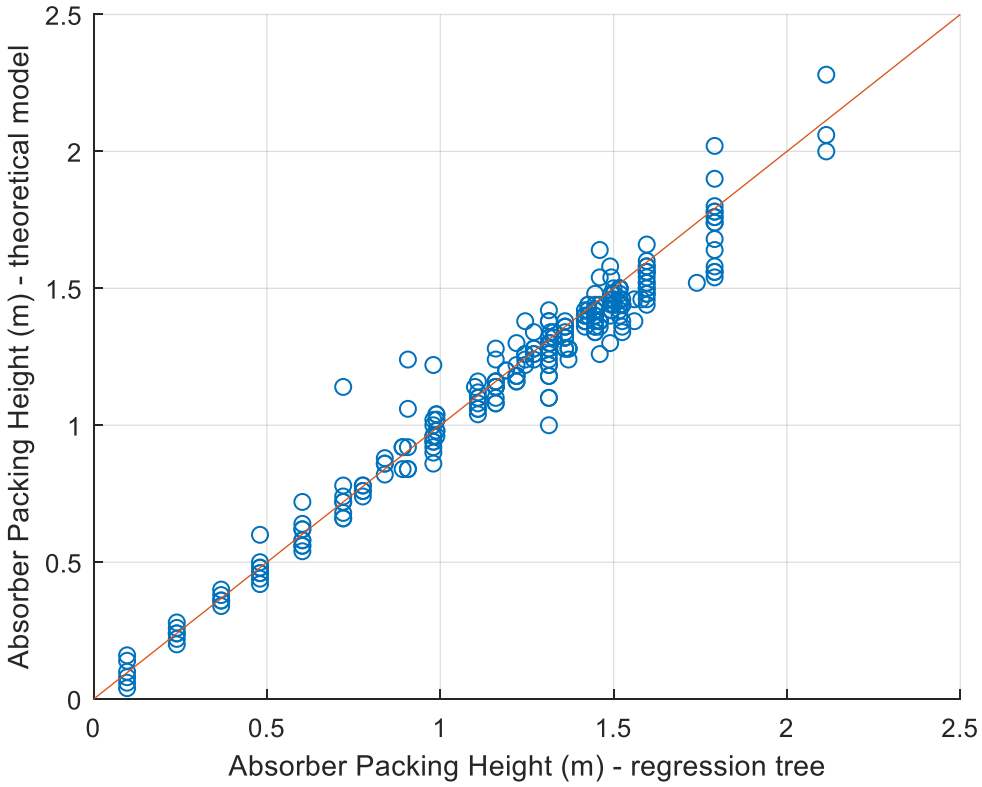

Figure 6-32: Comparison between stripper packing height estimated by the model and regression tree

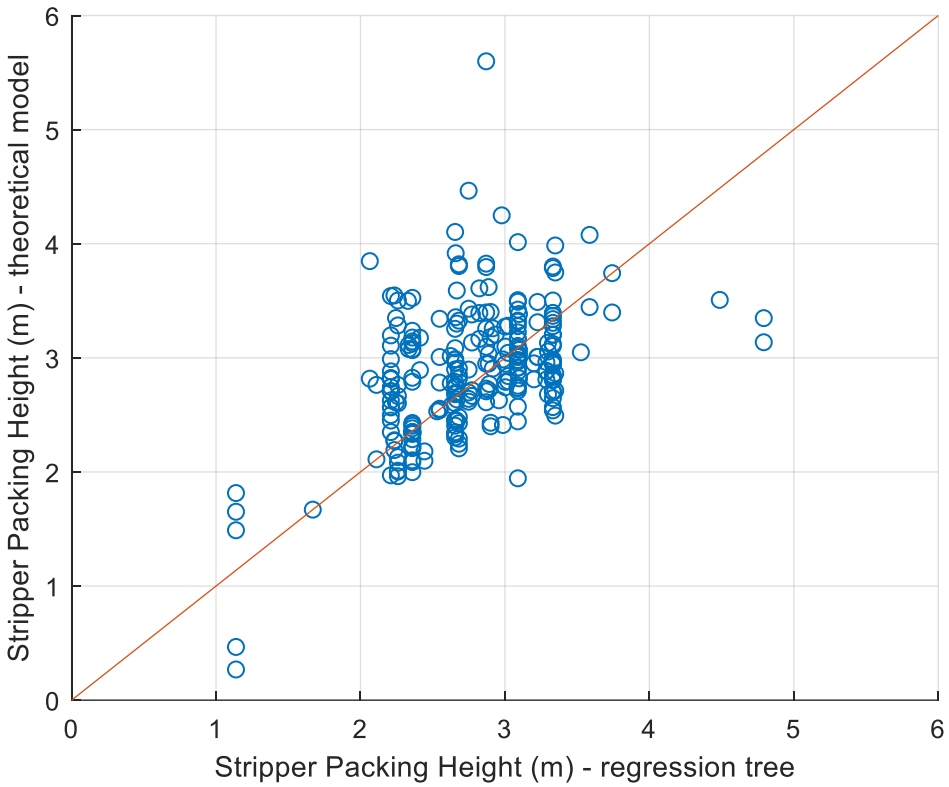

The quality of the regression tree estimations can also be assessed by boxplots of the deviations to the theoretical model results, as seen in Figure 6-33, which indicates most of the median close to 0% deviation, although the quantity of outliers in all attributes is not negligible. In addition, power demand estimation deviation is not negligible, with median close to -30%.

Results from regression tree analyses indicate that inlet pressure has very low influence on total dry weight and footprint of the MEA absorption system, as seen in Figure 6-34 and Figure 6-35.

Figure 6-33: Boxplot of MEA system estimations deviations by using regression tree

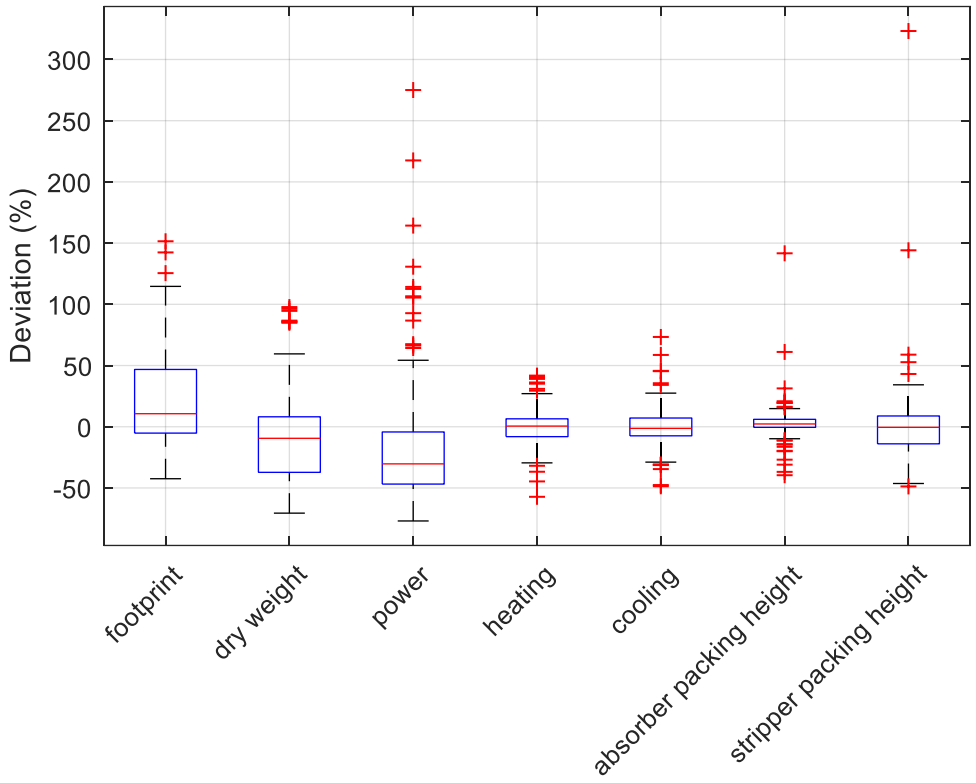

Figure 6-34: Influence of inlet parameters on MEA absorption system dry weight

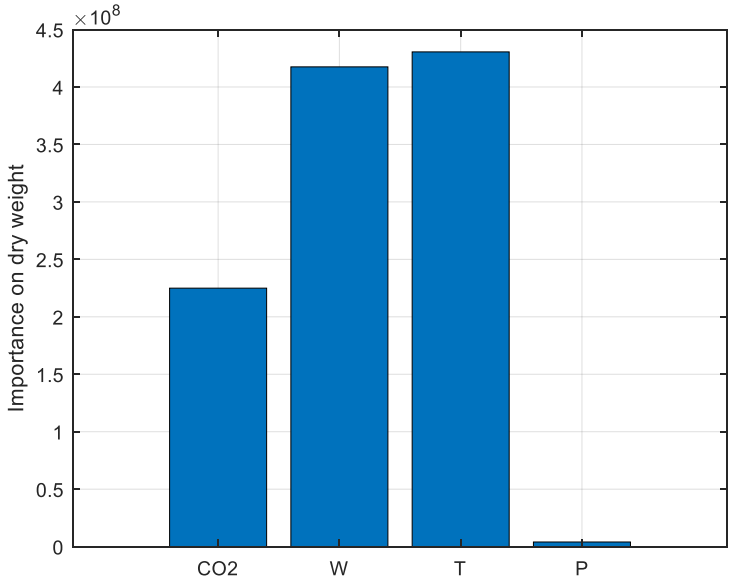

Figure 6-35: Influence of inlet parameters on MEA absorption system footprint

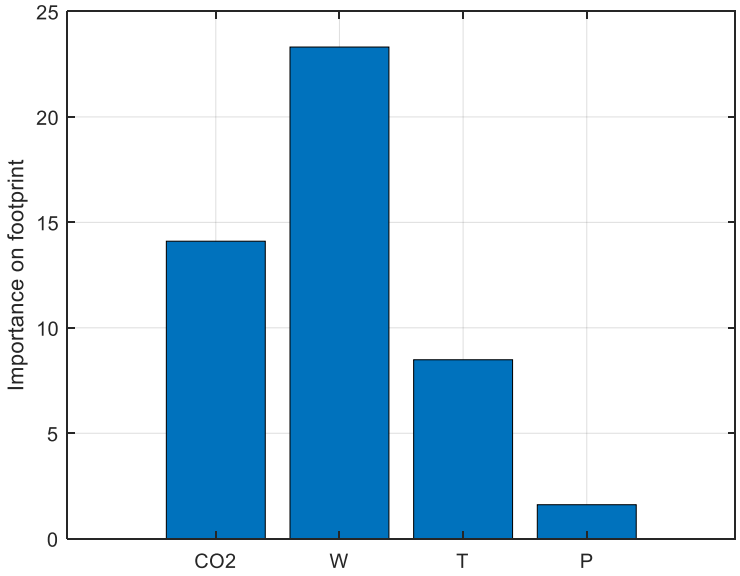

6.15. CO_2 removal by cellulose acetate membrane

The removal of CO_2 by use of membranes has also been adopted in both onshore and offshore oil & gas production. According to Zhang et al. (2013), conventional industrial methods such as chemical absorption by reactive solvents suffer from operational problems (such as flooding, excessive loading, and weeping) as well as high energy consumption and capital expenditure. According to the same authors, membrane separation shows advantages with respect to energy efficiency, process design, scale-up, modular construction and footprint. Three major membrane categories are identified: polymeric, inorganic and mixed matrix. Polymeric membranes are further classified according to the transport mechanism, e.g. gas permeation, facilitated transport and asymmetric microporous. Cellulose acetate membranes, a type of asymmetric membrane, was initially developed by UOP and has been used in offshore fields such as the high CO_2 oil fields found in the pre-salt cluster in Brazil.

Reis et al. (2017) developed correlations to estimate the performance of UOP spiral-wounded cellulose acetate membranes based on operational data from FPSOs. Such membrane generates two streams from the feed: a permeate stream, containing most of the CO_2 and some CH_4, and the reject stream, containing most of CH_4, all other heavier hydrocarbons (simplification), and

some CO_2. In the following correlations shown in 6.15-1 and 6.15-2, REC_{CH_4} is the percentage of CH_4 from the feed in the permeate stream and REC_{CO_2} is the percentage of CO_2 from the feed in the permeate stream. Coefficients B_1 to B_{15} can be found in the publication. In equation 6.15-1, variables F_1 to F_5 respectively are the partial pressure of CO_2 (bar), partial pressure of CH_4 (bar), membrane area per feed standard volumetric flowrate ($m^2/(Sm^3/h)$), permeate pressure (bar), and feed temperature (K). In equation 6.15-2, F_1 is the partial pressure of CH_4 (bar) and F_2 is the partial pressure of CO_2 (bar), and variables F_3 to F_5 are the same as equation 6.15-1. The authors also provided a correlation to estimate the skid footprint based on the membrane area, shown in equation 6.15-3.

$$REC_{CH_4} = B_0 + B_1 \cdot F_1 + B_2 \cdot F_2 + B_3 \cdot F_3 + B_4 \cdot F_4 + B_5 \cdot F_1^2 + B_6 \cdot F_4^2 + F_1 \cdot (B_7 \cdot F_2 + B_8 \cdot F_3 + B_9 \cdot F_4 + B_{10} \cdot F_5) + F_2 \cdot (B_{11} \cdot F_3 + B_{12} \cdot F_4) + F_3 \cdot (B_{13} \cdot F_4 + B_{14} \cdot F_5) + B_{15} \cdot F_4 \cdot F_5 \quad \text{6.15-1}$$

$$REC_{CO_2} = B_0 + B_1 \cdot F_2 + B_2 \cdot F_3 + B_3 \cdot F_4 + B_4 \cdot F_1^2 + B_5 \cdot F_2^2 + B_6 \cdot F_3^2 + F_1 \cdot (B_7 \cdot F_2 + B_8 \cdot F_3 + B_9 \cdot F_4 + B_{10} \cdot F_5) + F_2 \cdot (B_{11} \cdot F_3 + B_{12} \cdot F_4) + F_3 \cdot (B_{13} \cdot F_4 + B_{14} \cdot F_5) + B_{15} \cdot F_4 \cdot F_5 \quad \text{6.15-2}$$

$$FP_{skid,mp} = 0.00296 \cdot A_{memb} \quad \text{6.15-3}$$

The above equations close the mass balance in the membrane. The typical pressure drop in the reject side is low, typically 2 bar, but in the permeate side it is high, typically 45 bar to 55 bar.

At this moment there is no model to estimate heat exchange between permeate and reject within the membrane. As heat exchange between the membrane and the environment is negligible, permeate and reject temperatures may be reasonably estimated by assuming the permeate temperature is slightly cooler (3 K) than the inlet temperature in a typical counter-current configuration. The reject temperature is then estimated by an energy balance assuming an isenthalpic process, as seen in 6.15-4:

$$H_{rej} = \frac{W_{in} \cdot H_{in} - W_{perm} \cdot H_{perm}}{W_{rej}} \quad \text{6.15-4}$$

An iterative procedure is necessary to estimate the reject temperature that leads to the estimated reject enthalpy.

The following membrane configuration is considered, shown in Figure 6-36:

Figure 6-36: Membrane configuration 2

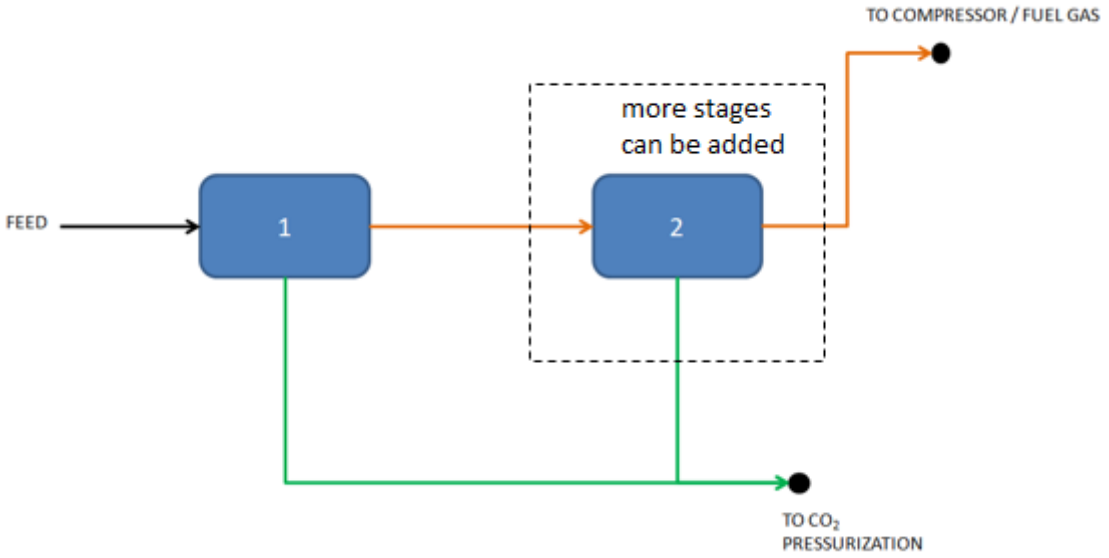

Source: author

One or more stages are used to purify the inlet stream. The reject stream from the previous stage feeds the next. The reject will have sufficient pressure to overcome as many stages are necessary if the inlet pressure is sufficient. The permeate streams are commingled and sent to CO_2 pressurization. A one stage configuration is used in pre-salt FPSOs *Cidade de São Paulo* and *Cidade de Paraty* (de Andrade et al., 2015). In this work two stages are considered, following the configuration shown in Figure 6-36. Many other membrane configurations can be considered, but they are not object of this work.

According to UOP (2009), the maximum feed pressure is 138 bar, maximum pressure drop (permeate side) is 100 bar, feed temperature ranges between 16°C to 65°C, and permeate pressure is typically below 3.5 bar. However, equations 6.15-1 and 6.15-2 can only be used when the feed pressure is lower than 70 bar according to the authors of the model, so in an optimization routine this is imposed as a constraint.

In this work, maximum membrane inlet water concentration is 1 ppmv. The following can be varied in an optimization routine: inlet temperature, inlet pressure (limited to 70 bar), pressure drop in the permeate side and membrane area.

6.16. **Weight and footprint estimation**

The following pieces of equipment are considered in the estimation of weight:

- Any pressure vessel contained in any equipment, such as the absorption column, the horizontal three-phase separator, the stripper column, the membrane housing, the shell in a shell & tube heat exchanger;
- The tube bundle contained in the shell & tube heat exchanger;
- Compressor;
- The packing contained in packed columns such as the absorber and stripper;
- Membrane element and housing.

The following pieces of equipment are excluded from the weight estimation either given to lack of estimation methods or because they have low enough weight that will not significantly affect the analysis:

- Pumps, due to lack of estimation methods and expected low dry weight and footprint;
- Valves, due to very low weight;
- Vessels internals (except packing), due to low weight;
- Vessels nozzles, due to low weight;

The weight of pressure vessels is calculated according to Moss & Basic (2013). The wall thickness t_{cs} of a cylindrical shell, in inches, is given by equation 6.16-1 or 6.16-2 (in case the maximum internal pressure exceeds $0.385 \cdot S \cdot E$), where P is the pressure in psi, R_{int} is the internal radius in inches, S is the maximum allowable stress in psi, E is the joint efficiency and c is the corrosion allowance. It is assumed use of hemispherical heads, with its thickness estimated by equation 6.16-4, in inches. The weight of the cylindrical shell w_{cs} is

estimated by equation 6.16-5 and the weight of each hemispherical head w_{hh} by equation 6.16-6.

$$t_{cs} = \frac{P \cdot R_{int}}{S \cdot E - 0.6 \cdot P} + c \quad \text{6.16-1}$$

$$t_{cs} = R_i \cdot \left(Z_t{}^{0.5} - 1\right) \quad \text{6.16-2}$$

$$Z_t = \frac{S + P}{S - P} \quad \text{6.16-3}$$

$$t_{hh} = \frac{P \cdot R_i}{S \cdot E - 0.2 \cdot P} + c \quad \text{6.16-4}$$

$$w_{cs} = \frac{\pi}{4} \cdot \left(D_{ext}^2 - D_{int}^2\right) \cdot L \cdot \rho_m \quad \text{6.16-5}$$

$$w_{hh} = \frac{\pi \cdot \left(D_{ext}^3 - D_{int}^3\right) \cdot \rho_m}{12} \quad \text{6.16-6}$$

The calculation of the weight of the tube bundle inside the shell & tube heat exchanger is straight forward since the number of tubes is known as well as the internal and external diameters. The tubes outside diameter is assumed as 130% of the internal diameter, based on the following table containing information extracted from P.I.T. Pipe (2021) and using schedule 40 as reference:

The weight and footprint of compressors have been obtained through access to a specific vendor's data (Dresser-Rand, s.d.), which shows different weights and frame sizes according to actual volumetric flowrate and discharge pressure.

The footprint estimation is also straight forward. In case it is a vertical vessel, it is the area of the circle, and in case it is a horizontal vessel, it is the multiplication of the length by the external diameter. The compressor area estimation method was explained in section 6.7.

Table 6-4: ANSI Pipe Schedules (40 and 80)

Nominal pipe size	OD	Schedule 40			Schedule 80		
		Wall thickness	ID	OD/ID	Wall thickness	ID	OD
0.125	0.405	0.068	0.269	1.506	0.095	0.215	1.884
0.25	0.540	0.088	0.364	1.484	0.119	0.302	1.788
0.375	0.675	0.091	0.493	1.369	0.126	0.423	1.596
0.5	0.840	0.109	0.622	1.350	0.147	0.546	1.538
0.75	1.050	0.113	0.824	1.274	0.154	0.742	1.415
1	1.315	0.133	1.049	1.254	0.179	0.957	1.374
1.25	1.660	0.140	1.380	1.203	0.191	1.278	1.299
1.5	1.900	0.145	1.610	1.180	0.200	1.500	1.267
2	2.375	0.154	2.067	1.149	0.218	1.939	1.225
			average	1.308		average	1.487

Regarding CO_2 removal membranes, the following information has been obtained from a specific source:

- element diameter: 8”;
- element length: 1 m;
- element membrane area: 20 m^2;
- element weight: 20 kg;
- housing length: 10 m;
- housing linear weight: 30 lb/ft.

Chapter 7

7. Process synthesis and optimization

7.1. Superstructure

A first version of a SEN superstructure, still not considering process integration, is shown in Figure 7-1, representing all flowsheets potentially capable of transforming an inlet stream with given characteristics into outlet streams with given specifications.

In the above superstructure, the yellow pentagon represents the state of the raw inlet stream and the letters representing the following: G the export gas, C the carbon dioxide rich stream, W the produced water, and H the hydrogen sulfide. The yellow circles represent states (set of composition, flowrate, pressure and temperature) and the blue boxes the equipment (description in the table at the right).

In oil processing, the inlet stream can be routed directly to a three phase separator (E1) or to a gas-liquid separator (E2). From the gas-liquid separator (E2), a free-water knock out drum (E3) may separate free water. The resulting stream (state 3) may be heated (E5), and its pressure is reduced by a valve.

State 7 is reached by a depressurization followed either by a gas-liquid separator (E6) or a three-phase separator (E7). Depending on the quality of the raw inlet stream, not more than two remaining equipment (depressurization followed by E10 and E11) may be necessary, but most often it is necessary to remove emulsioned water in order to specify the BS&W. In such case, an electrostatic coalescer (E8) separates emulsioned water and a gas-liquid separator installed at its top (not shown in the figure) separates gas in order to aid in oil stabilization and protect the electrostatic separator from ingress of gas.

In case the oil salinity specification is not reached by reducing the BS&W to the level of the specification, another electrostatic coalescer (E9) may be used, depending on the injection of dilution water.

After achieving state 11, an additional gas-liquid separation (E10) stage may be necessary to achieve the required RVP specification, and cooling (E11) may be required depending on the maximum temperature oil can be stored.

States 9, 11, 13 or 42 may already attain the oil specifications, so they are represented with green in their boundaries, meaning that the oil process can stop at such states.

In gas processing, the associated gas represented by state 14 is routed to a cooler (E12) or directly to a gas-liquid separator (E13), reaching state 17. Most often S14 temperature will be higher than the temperature that can be achieved by a cooler using seawater as cooling medium, so E12 is typically present. Depending on the quality of state 17, hydrogen sulfide removal (E14) may be required, reaching state 18. The gas stream may be compressed (E15) upstream dehydration, in order to reduce the amount of water to be removed.

In case of CO_2 removal purely by MEA system (E16A), it is followed by dehydration by TEG (E17A) or by molecular sieve (E17B), and then the gas stream is compressed to be exported (E20). The arrows in yellow show such paths. In case dehydration by TEG (E17A) is selected as first stage, it can be followed by molecular sieve (E17B).

Figure 7-1: State-equipment network superstructure for topsides oil & gas processing system

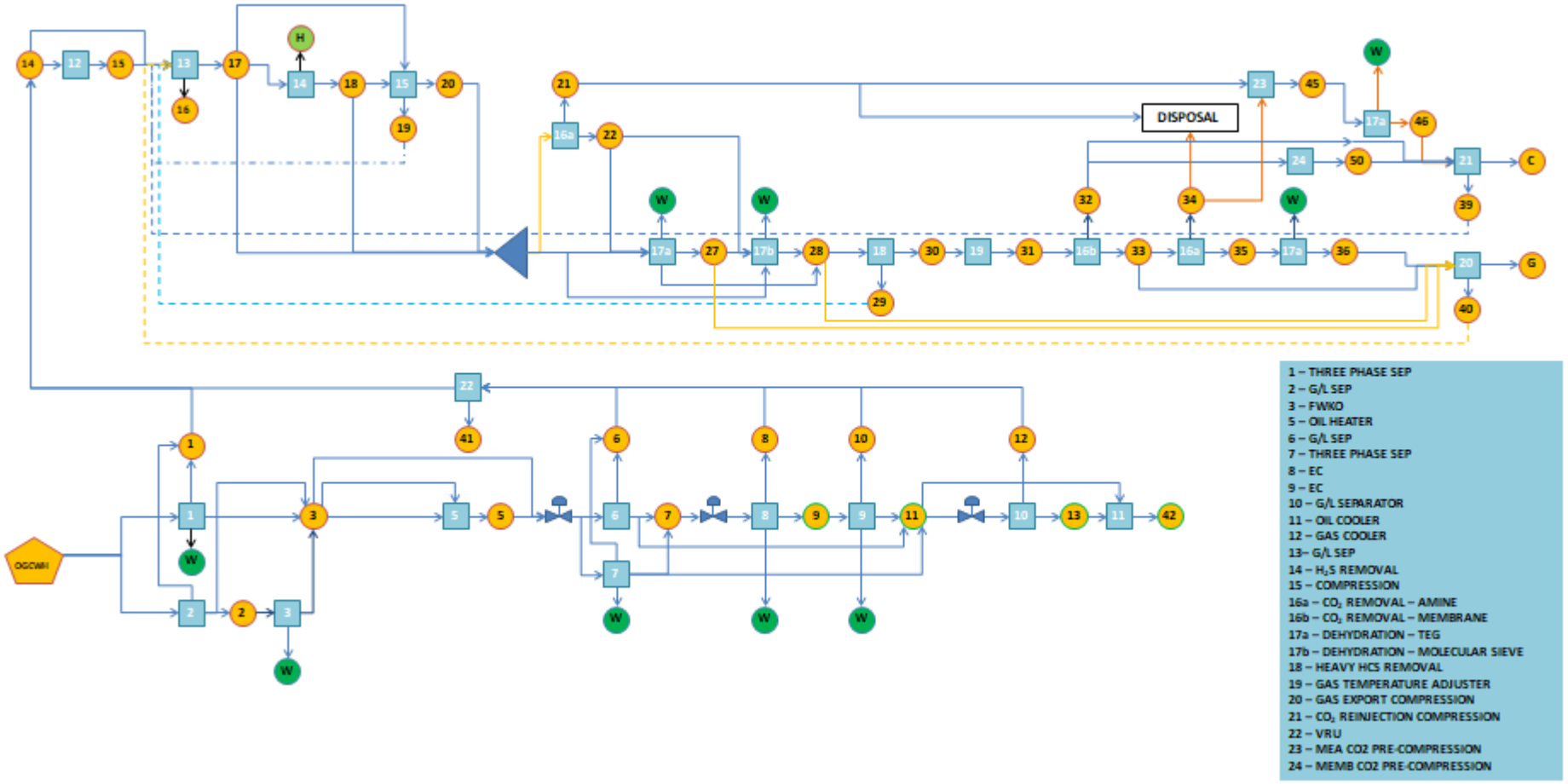

Source: author

In case CO_2 removal by membranes (E16B) is selected as first stage, gas must first be conditioned as membranes are sensitive to condensation of water and hydrocarbons. Dehydration by molecular sieve (E17B) is typical, as the technology is more robust than TEG dehydration, providing stable low water content. In addition, heavy hydrocarbons must be removed (E18), to avoid hydrocarbons condensation within the membranes. Finally, the gas may be heated (E19) to avoid condensation within the membranes, as the level of water and heavy hydrocarbons removal may not totally prevent condensation.

In case MEA (E16A) is selected as second stage CO_2 removal, the treated hydrocarbon gas (S35) shall be dehydrated as it is saturated with water after leaving the absorption tower. For export purposes, dehydration by TEG (E17A) should be sufficient, generating S36, which is then routed to the export compressor (E20). The CO_2 rich stream generated by the MEA system (S34) presents very low pressure and it is saturated with water, so a compressor (E23) pressurizes it until a certain level to reduce the amount of water to be separated in another TEG process, generating S46. Such level is assumed as 35 bar, as TEG absorption for CO_2 rich gas has an optimum between 30 and 40 bar (Øi & Fazlagic, 2014). The permeate stream from the membrane separation (E16B) is also compressed (E24) to 35 bar in order to commingle with the CO_2 stream separated in the MEA process. The resulting stream is then routed to the CO_2 injection compressor (E21). In case S34 flowrate is small, disposal to the atmosphere may be authorized by environmental entities.

7.2. **Process integration**

As previously mentioned, process integration mainly involves heat recovery and material recycling. An analysis of the superstructure shown in Figure 7-1 indicates several opportunities related to process integration, such as:

1. The specified oil, represented by state O in the superstructure, may not need a cooler (E11) if it exchanges heat with the oil dominated stream represented by state 3. It will also reduce heating demand in the oil heater;
2. Streams that contain liquid heavy hydrocarbons removed from gas, represented by states 41 and 16, can be recycled to different points of the

process in order to increase oil production by stabilizing part of the separated heavy hydrocarbons;

3. The water dominated streams separated in E7, E8 and E9 can aid in water separation in E1 or E3. The first reason is that streams 7, 8 and 9 are warmer than the raw inlet stream. The second reason is that it will also increase water concentration, promoting water separation due to two reasons: emulsions are less stable under warmer temperatures, and increased water concentration can increase coalescence of the emulsioned water droplets. As in this work no mathematical models have been implemented to quantify the effect of temperature and coalescence in the stability of water in oil emulsions, the opportunity 3 was not considered for now.

In order to take advantage of opportunity 1, new equipment is added upstream the oil heater. This new equipment is denominated pre-heater, a shell & tube heat exchanger where a stream represented either by state 9, 11, 13 or 42, depending on the flowsheet, transfers heat to stream 4. Consequently, the oil cooler (E11) may not be necessary depending on the maximum oil storage temperature, so state 43 may attain the necessary oil specifications. Arrows in black, connecting state 43 to the oil cooler (E11) and the oil cooler to state 44, are used to indicate that, in case state 43 is generated, it may only generate one additional state, represented by 44.

Regarding opportunity 2, which involves material recycling, the specific points where each stream is recycled must be determined. Stream 16 may have relevant amount of water, so it must be recycled at an upstream equipment that separates water; in this case it may be commingled with the raw inlet stream, by use of a pump, or commingled with the stream upstream the gas-liquid separator (E6) or three-phase separator (E7). Stream 41, generated by the vapor recovery unit (22), may be commingled with the stream upstream E6 or E7, by use of a pump, or commingled with the stream upstream the electrostatic coalescer (E8).

The updated superstructure, with process integration measures, is shown in Figure 7-2.

7.3. **Flowsheets**

From the superstructure, multiple flowsheets arise, potentially capable of achieving the specifications of the outlet streams. Certain authors (Albahri, et al., 2018) automatically generated all possible flowsheets from a superstructure using logic propositions that account for mandatory existence of certain equipment in any flowsheet, and also when the use of certain equipment excludes the use of other equipment. In this work the process is still manual, and in the future it is planned to develop an algorithm to generate all possible flowsheets. The flowsheet is a specific route followed by the fluids, shown in purple in the superstructure.

Two types of inlet fluid are considered, each leading to a set of flowsheets to be further passed through process integration and optimization:

- Fluid 1: Low amount of CO_2;
- Fluid 2: High amount of CO_2.

The characteristics of fluid 1 and fluid 2 are shown in Table 7-1. The only change between fluid 1 and fluid 2 is the molar composition of the hydrocarbons, which contains more CO_2 than fluid 1.

For fluid 1, three flowsheets are considered, shown in Figure 7-3, Figure 7-4, and Figure 7-5. Oil processing is fixed, depending on a single electrostatic coalescer. Gas processing varies from simple dehydration by TEG (Figure 7-3), pre-compression upstream dehydration by TEG (Figure 7-4), and pre-compression upstream dehydration by molecular sieves (Figure 7-5).

For fluid 2, three flowsheets are considered, shown in Figure 7-6, Figure 7-7 and Figure 7-8. The oil processing scheme is the same of fluid 1. Due to the high CO_2 concentration, it is necessary to remove CO_2 from the associated gas to meet the export specification.

Figure 7-2: Updated state-equipment network superstructure for topsides oil & gas processing system, considering process integration

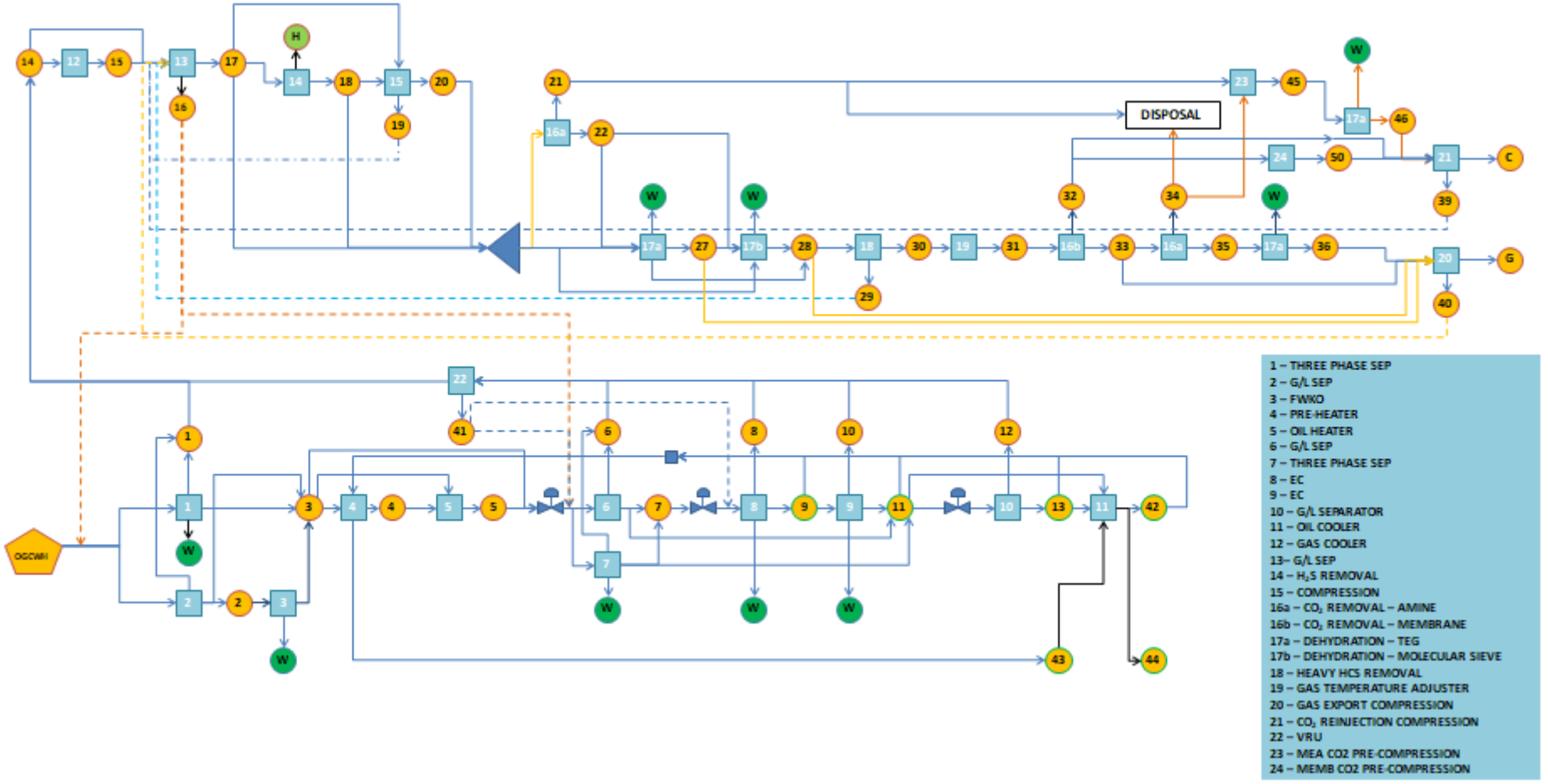

Source: Author

In fluid 1 oil processing section, the wellstream feeds a horizontal three-phase separator (E1), removing at least 99% of free water. The rich oil stream (S3) is pre-heated by the treated oil in a heat exchanger (E4) and is further heated by another heat exchanger (E5) that uses hot water as heating medium. The rich oil stream (S5) is depressurized and feeds a gas-liquid separator (E6). The partially stabilized rich oil stream (S7) is depressurized again, feeding a horizontal gas-liquid separator (V-EC) placed above the electrostatic coalescer (EC). The V-EC generates a liquid oil rich stream that feeds the EC, removing the emulsioned water. In case dilution water is necessary, it is heated to E8 treating temperature and mixed with S7. The associated gas separated in the V-EC (S8) is pressurized to E6 pressure, and mixed with S6. The resulting stream is pressurized to E1 pressure, and mixed with S1. As knock-out drums may be present within each vapor recovery unit, the resulting liquid is recycled to the inlet of heat exchanger E4.

In fluid 1 flowsheet 1 (F1F1) gas processing section, the resulting associated gas stream (S14) from the oil processing section is cooled in a heat exchanger (E12), liquids are separated in a gas-liquid separator (E13), and the resulting gas stream (S17) is dehydrated by a TEG system (E17A). Finally, the dry gas stream (S24) is pressurized in a set of compressors (E20). Any liquid separated in E20 is recycled to the gas-liquid separator E13. The liquid separated in E13 is recycled to the inlet of the 3-phase separator E1.

In fluid 1 flowsheet 2 (F1F2) gas processing section, the difference compared to F1F1 gas processing section is the compression system (E15) placed upstream the TEG system. The water load to the TEG system is reduced as a consequence. An additional input is added: the level of pressurization in E-15.

In fluid 1 flowsheet 3 (F1F3) gas processing system, the difference compared to F1F2 gas processing section is the use of molecular sieve (E17B) instead of TEG. A typical configuration has been adopted: number of beds equal to 2 x 100% (one under operation and the other under regeneration), adsorption cycle equal to 12 hours, and length per diameter ratio of 3. The introduction of molecular sieve decreases the number of inputs to the optimization, as two of the inputs are associated with the TEG system

Table 7-1: Wellstream Properties and Oil/Gas Export Specifications - Fluid 1

Property	**Value**
Common inlet characteristics	
Hydrocarbon mass flowrate (kg/s)	264.97
Produced water mass flowrate (kg/s)	160
Emulsioned water (% of produced water)	40
Temperature (K)	323.15
Pressure (bar)	24
Produced water salinity (mg/l)	160,000
Common final specifications	
Export oil max RVP (Pa)	70,965
Export oil max BS&W (%)	0.5
Export oil max salinity (mg/l)	270
Export gas max water content (ppmv)	10
Export gas pressure (Pa)	24,500,000
Export gas temperature (K)	313.15
Fluid 1 specific information	
Inlet hydrocarbon molar composition[1]	[0.5329 0.0707 0.0487 0.009 0.0179 0.0059 0.0086 0.0113 0.0164 0.021 0.0169 0.0155 0.0126 0.0115 0.0119 0.0198 0.0196 0.0175 0.0168 0.0169 0.0063 0.0862 0.0037 0.0024 0 0 0 0]
Fluid 2 specific information	
Inlet hydrocarbon molar composition	[0.53 0.04 0.02 0.01 0.01 0.005 0.015 0.015 0.02 0.02 0.02 0.01 0.01 0.01 0.01 0.009 0.008 0.007 0.006 0.005 0.005 0.08 0.005 0.13 0 0 0 0]
CO_2 injection max water content (ppmv)	10
CO_2 injection pressure (bar)	245
Max water content membrane inlet (ppmv)	1
Hydrocarbon dew point (P (bar) / T (K)) at membrane inlet	50 / 283.15

[1] [C1 C2 C3 iC4 nC4 iC5 nC5 C6 C7 C8 C9 C10 C11 C12 C13 C14 C15 C16 C17 C18 C19 C20 N2 CO2 H2S H2O MEA C20+]

In fluid 2 gas processing section, the resulting stream (S14) is cooled in a heat exchanger (12), any condensate is separated in a gas-liquid separator (E13), and the resulting gas stream is compressed in E15. Then the differences between the 3 flowsheets appear.

In fluid 2 flowsheet 1 (F2F1), the associated gas is then dehydrated by molecular sieves (E17B) to meet a 1 ppmv specification, necessary to prevent water condensation within the membranes. The associated gas is then fed to the Joule-Thomson hydrocarbon removal system (E18), to adjust the hydrocarbon dew point and prevent hydrocarbons condensation within the membrane system (E16B). The resulting gas stream is then heated (E19), which is an additional measure to prevent condensation within the membranes, and is finally fed to the membrane system. The reject stream from the membrane system is treated in the MEA absorption system (E16A) to reduce the CO_2 content to the specification. The methane rich gas leaving the absorber is dehydrated by TEG and is ready to be compressed by E20. The CO_2 rich stream leaving the stripper is pre-compressed to 35 bar by E23 and dehydrated by TEG. The permeate stream (CO_2 rich) from the membrane system is also pre-compressed to 35 bar, by E24. Both CO_2 rich streams are mixed and compressed by E21 to meet the injection pressure.

In fluid 2 flowsheet 2 (F2F2), there is no MEA absorption. The CO_2 specification is achieved solely by membranes, generating reject (export gas) and permeate (CO_2 rich) streams that meet the water content specification, not requiring further dehydration respectively upstream E20 and E21.

In fluid 2 flowsheet 3 (F2F3) there is no membrane system. The CO_2 specification is achieved by the MEA absorption, placed downstream E15. In this case, it is not necessary to dehydrate the gas upstream the MEA absorption, therefore molecular sieves (E17B) are not required. In addition, there is no need for hydrocarbon dew point control (E18) and gas heater (E19), as they are necessary due to the membrane system. The associated gas from the absorber is dehydrated by TEG and compressed by E20. The CO_2 rich stream from the stripper is pre-compressed by E24, dehydrated by TEG and compressed by E21.

7.4. **Identification of most complex flowsheet for fluid 1**

The inputs for each of the flowsheets change, as seen in Table 7-2 for fluid 1 (inputs for fluid 2 are shown in section 7.8). Inputs are marked with Y if they affect design of a given flowsheet and N if not. Such inputs are determined based on the equipment design rules and screening analyses explained in section 6.

Internal diameter and L/D ratio of separation vessels directly influence dry weight and footprint. Higher diameters lead to higher cross section areas, which combined with higher lengths increase the residence time in the separator, improving separation efficiency. The higher the diameter the higher the required wall thickness, reason why longer separators may be better suited when dry weight constraint is more important than footprint.

The pressure drops in valves between vessels that separate gas from liquid are key parameters influencing oil production. The higher the pressure drop in a certain valve, the higher the gas fraction in the resulting phase equilibrium, reducing oil production. On the other hand, light hydrocarbons must be separated from oil to achieve the required RVP specification, increasing gas production and decreasing oil production. Therefore, such parameters have to be part of the optimization process.

The efficiency of the electrostatic coalescence process is dictated by the treatment temperature (I5) and electrodes related parameters (I8, I9 and I10). The higher the treatment temperature the higher the efficiency, but more heating is required. The number of electrodes (I10) will directly influence the length of the coalescer, but if the space between electrodes (I8) can be reduced, a high number of electrodes will not necessarily lead to a very long electrostatic coalescer. Finally, the higher the electrode length (I9), the higher the coalescer diameter, increasing wall thickness and the dry weight. As the operation pressure of an electrostatic coalescer is typically low, the wall thickness should not significantly change if the length of the electrodes changes.

The TEG dehydration related parameters (I13 and I14) directly influence the absorber height and diameter, directly affecting its dry weight and footprint.

Finally, in process configurations adopting a compressor (E15) upstream the dehydration system, the higher the pressurization the less amount of water is separated in the dehydration step. On the other hand, the operation pressure of the dehydration system will increase, increasing the dry weight due to higher wall thickness of the vessels exposed to higher pressure.

The most complex flowsheet is the one with the highest number of inputs. In the case of fluid 1, it is the flowsheet represented in Figure 7-4, with 15 inputs

Table 7-2: Inputs for each of fluid 1 flowsheets

Input	Description	LB	UB	F1F1	F1F2	F1F3
I1	E1 internal diameter (m)	2	5	Y	Y	Y
I2	E1 L/D ratio	2	5	Y	Y	Y
I3	Pressure drop E5 to E6 (%)	10	85	Y	Y	Y
I4	Pressure drop E6 to V-E8 (%)	10	85	Y	Y	Y
I5	E8 temperature (K)	353.15	393.15	Y	Y	Y
I6	E6 diameter (m)	2	5	Y	Y	Y
I7	E6 L/D ratio	2	5	Y	Y	Y
I8	Space between electrodes in E8 (m)	0.25	1.25	Y	Y	Y
I9	Length of electrodes in E8 (m)	0.2	1.8	Y	Y	Y
I10	Number of electrodes in E8	20	200	Y	Y	Y
I11	V-E8 diameter (m)	1.5	5	Y	Y	Y
I12	V-E8 L/D ratio	2	5	Y	Y	Y
I13	TEG specific rate (m^3 TEG/kg H_2O)	0.015	0.05	Y	Y	N
I14	TEG mass fraction (%)	98.5	99.995	Y	Y	N
I15	Level of pressurization in E-15	5%	80%	N	Y	Y

.

Figure 7-3: Fluid 1 – Flowsheet 1 (F1F1)

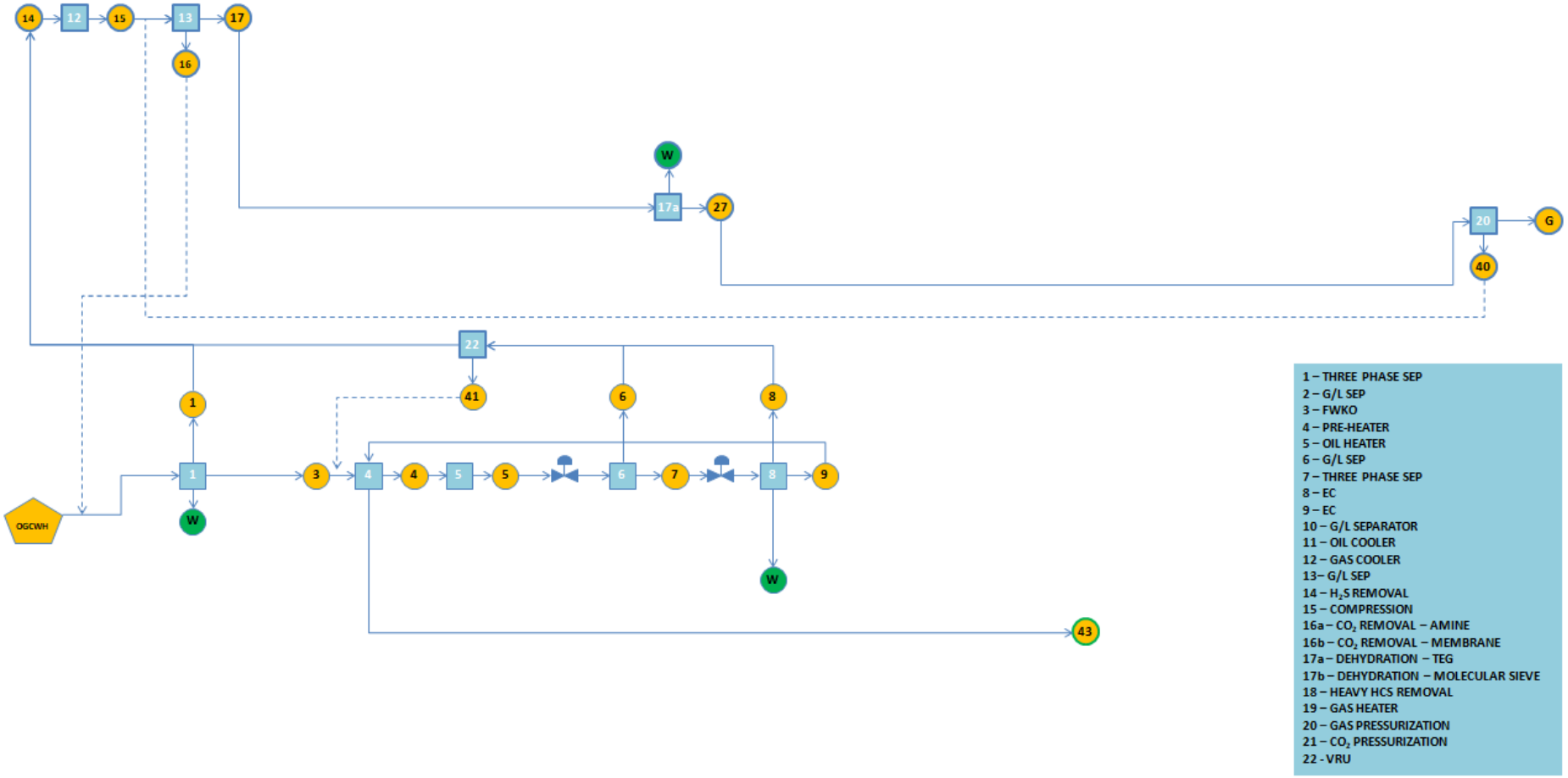

Source: author

Figure 7-4: Fluid 1 – Flowsheet 2 (F1F2)

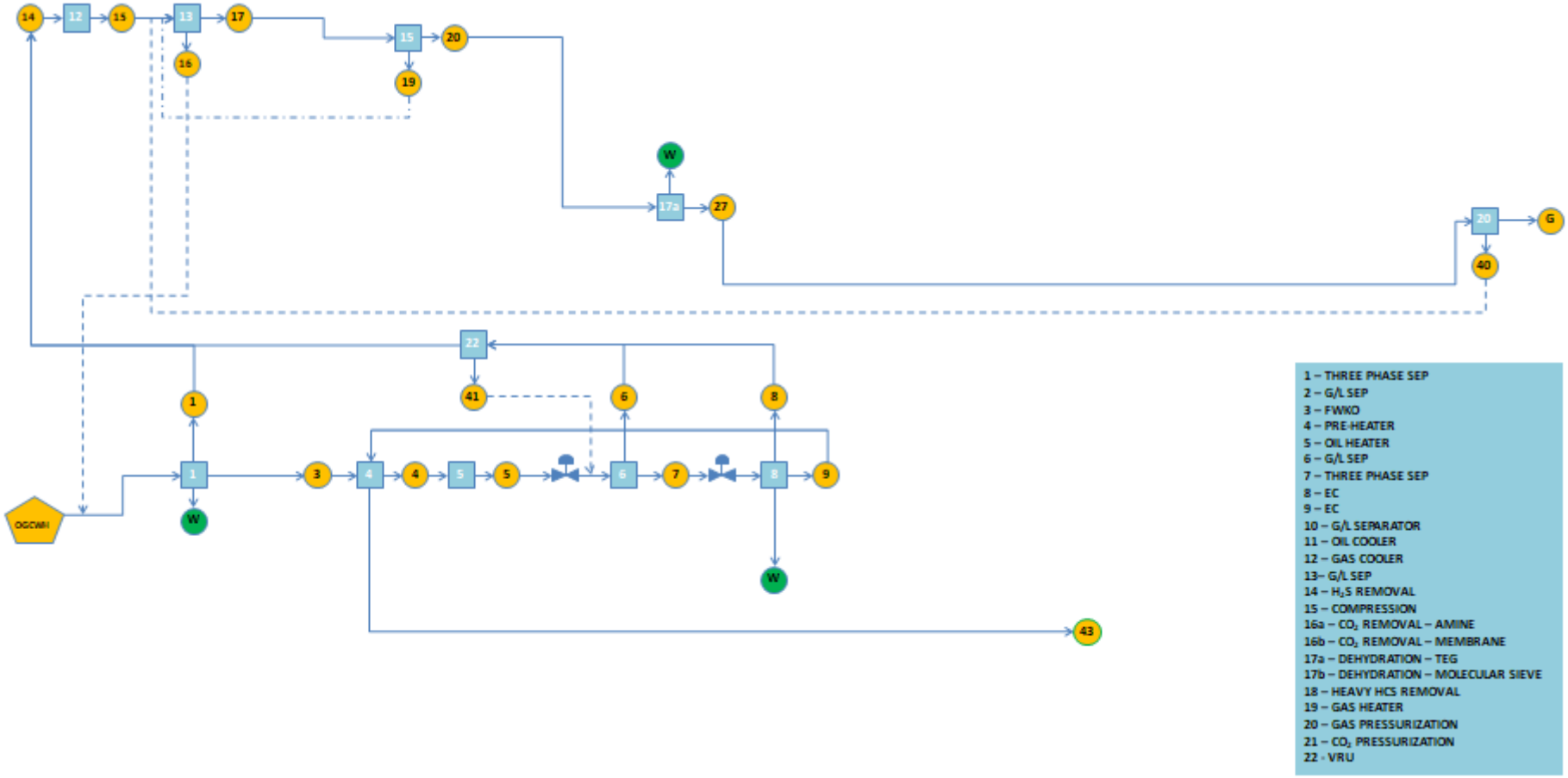

Source: author

Figure 7-5: Fluid 1 – Flowsheet 3 (F1F3)

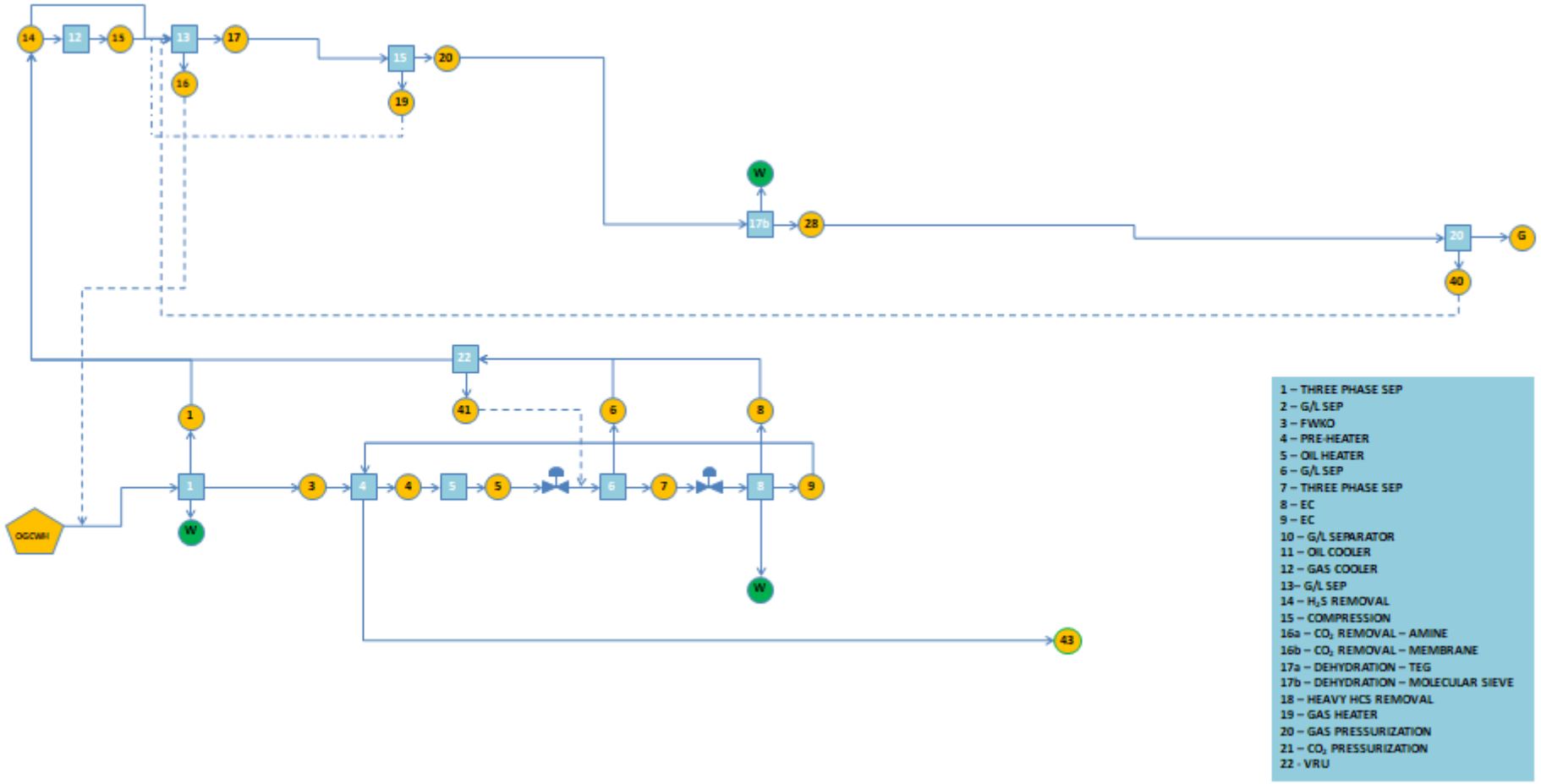

Source: author

Figure 7-6: Fluid 2 – Flowsheet 1 (F2F1)

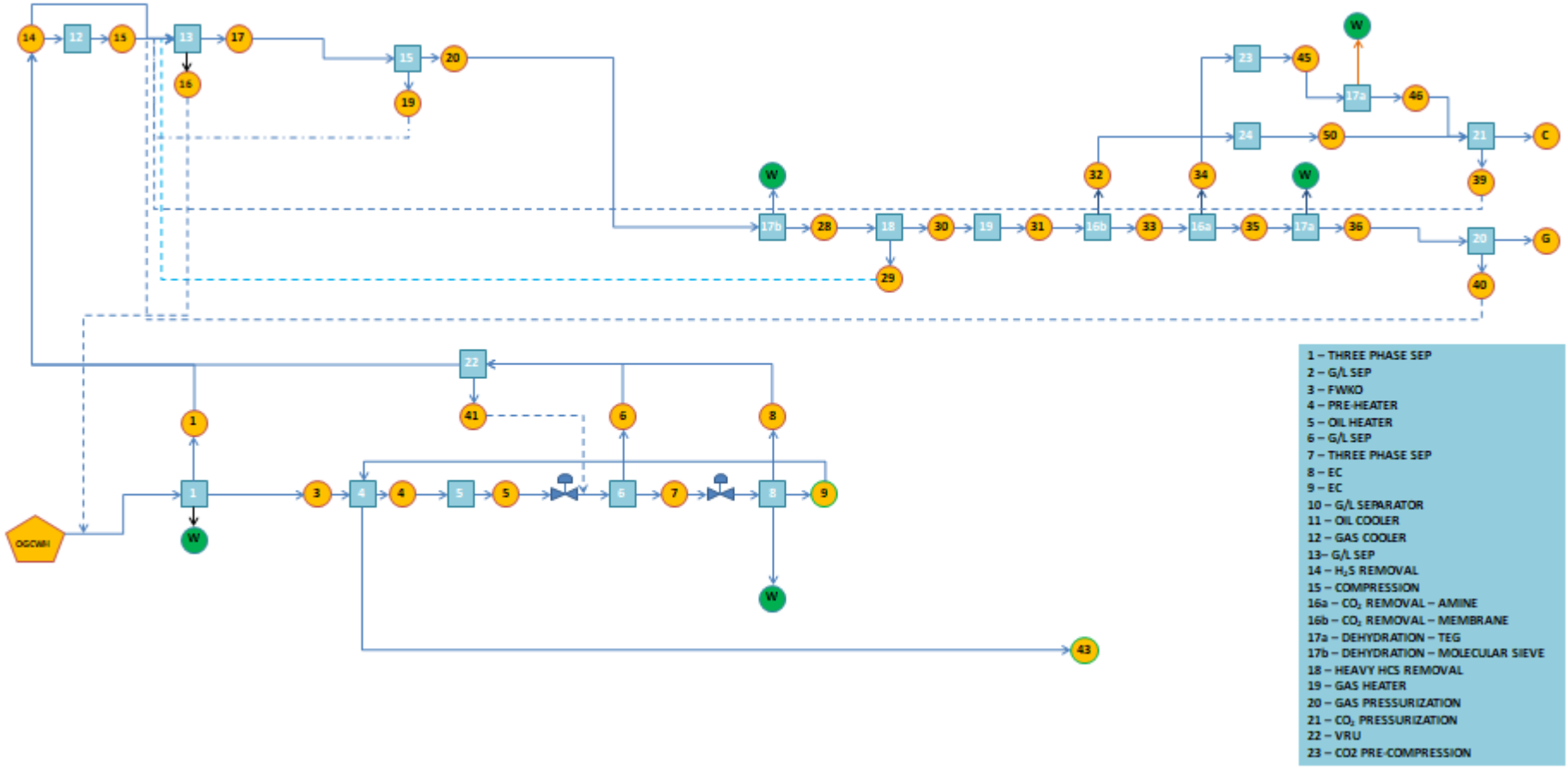

Source: auhor

Figure 7-7: Fluid 2 – Flowsheet 2 (F2F2)

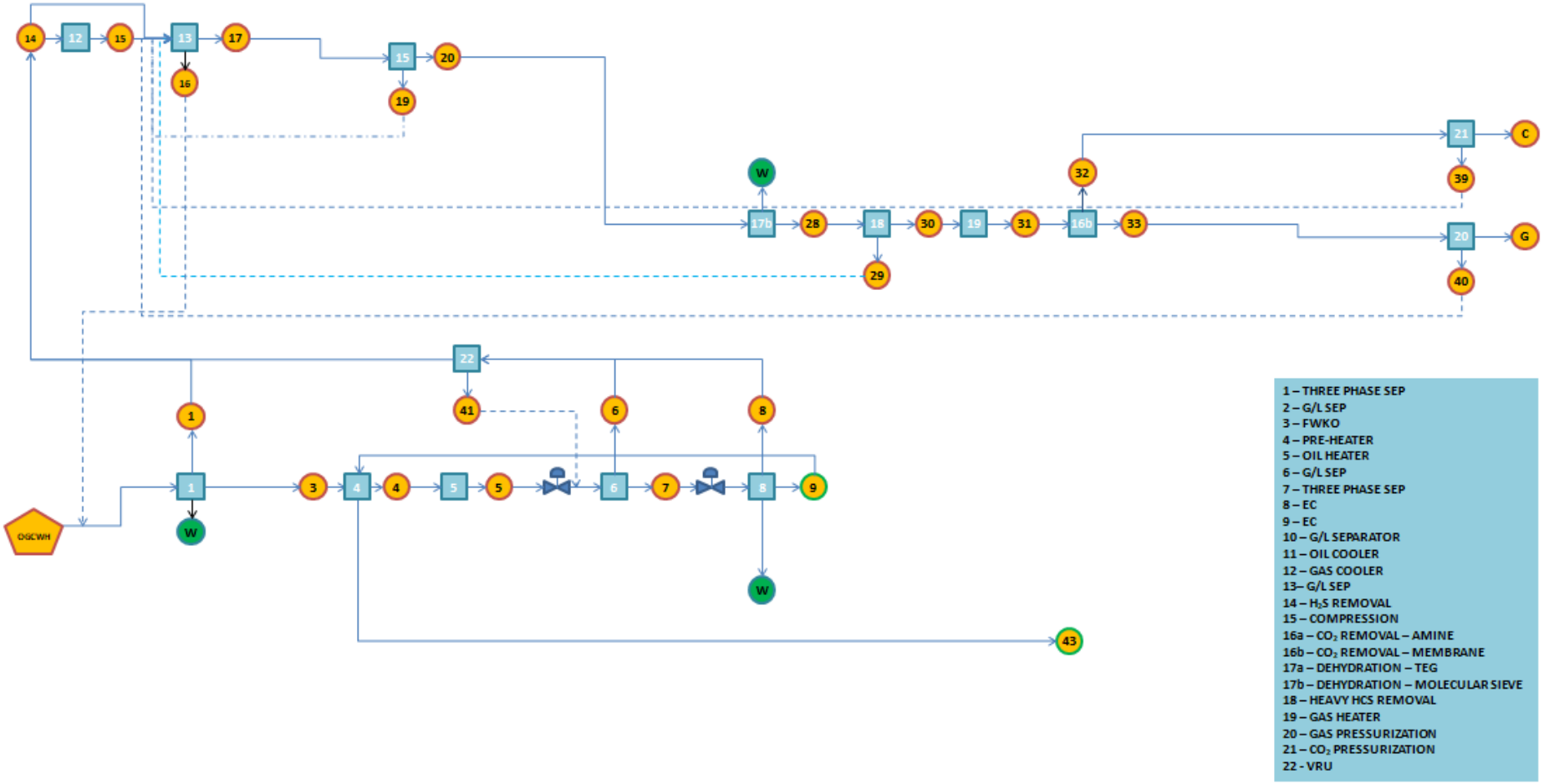

Source: author

Figure 7-8: Fluid 2 – Flowsheet 3 (F2F3)

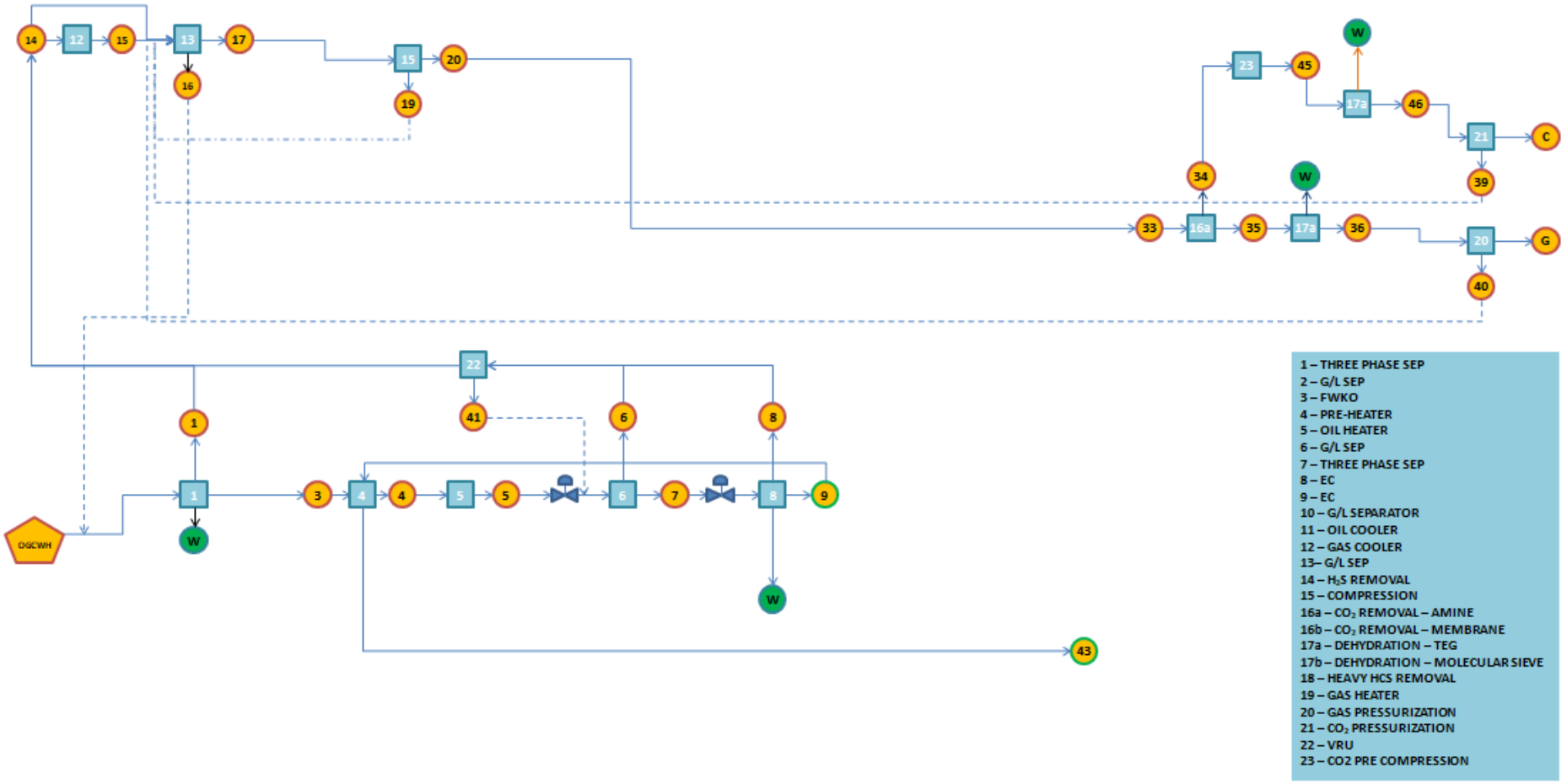

Source: author

7.5. **Generation of DOE dataset for fluid 1**

A dataset based on the SOBOL sequence has been created for flowsheet F1F2. A scatter plot of the dataset suggests good distribution of the points as there are no relevant empty spaces.

Figure 7-9: Plot of dataset generated by SOBOL sequence – F1

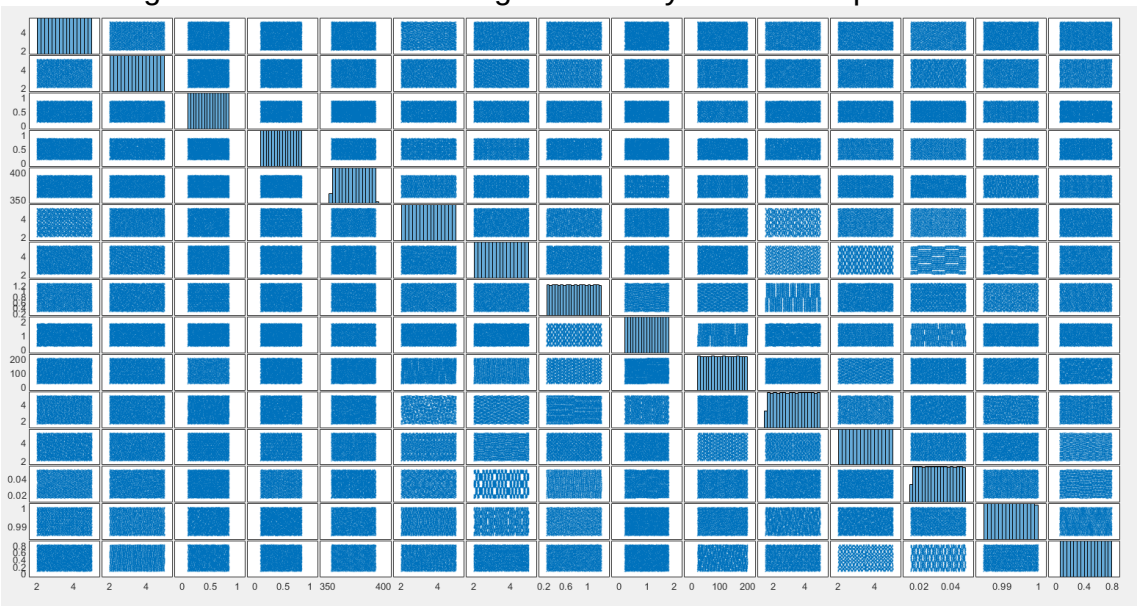

7.6. **Sensitivity analysis and determination of initial population on system level for fluid 1**

The initial population was determined by running the objective function several times, varying the input values, until a large set of feasible points is obtained. From this large set, an initial population is randomly chosen in order to initialize the optimization. The size of the initial population depends on the number of inputs.

The sensitivity analysis based on SS-ANOVA, considering two-way interaction between the independent variables, led to the following results:

Figure 7-10: SS-ANOVA – Fluid 1 - Oil Production

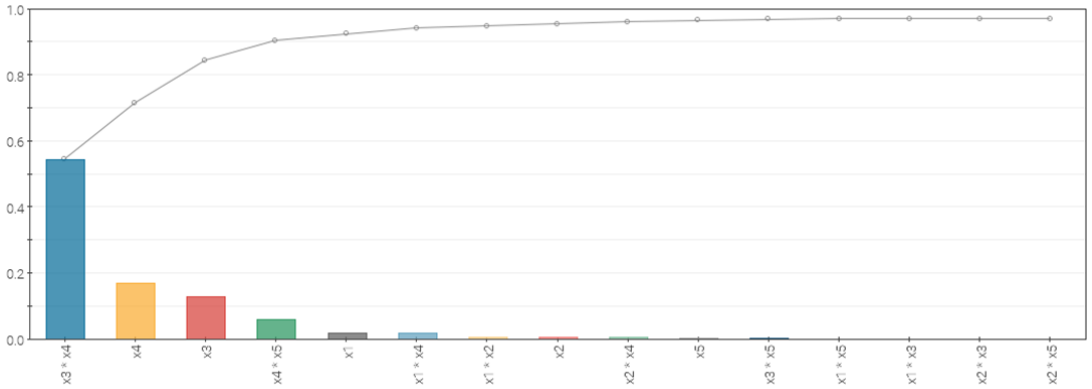

Figure 7-11: SS-ANOVA – Fluid 1 – Dry Weight

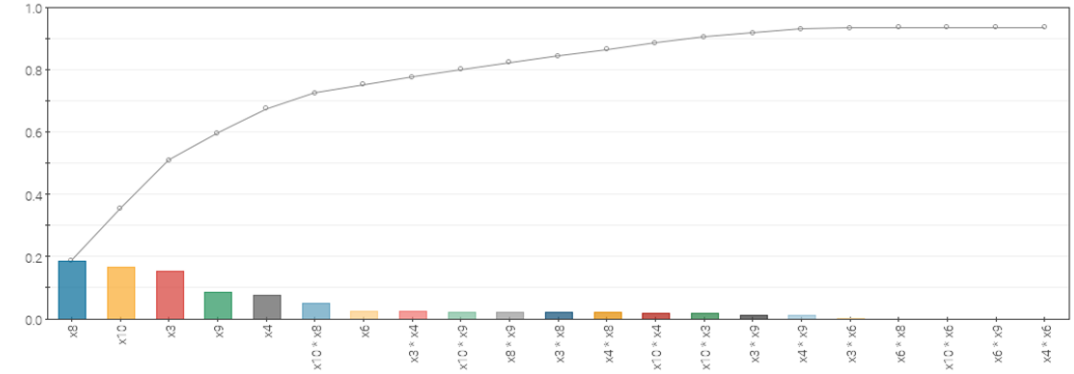

Figure 7-12: SS-ANOVA – Fluid 1 – Area

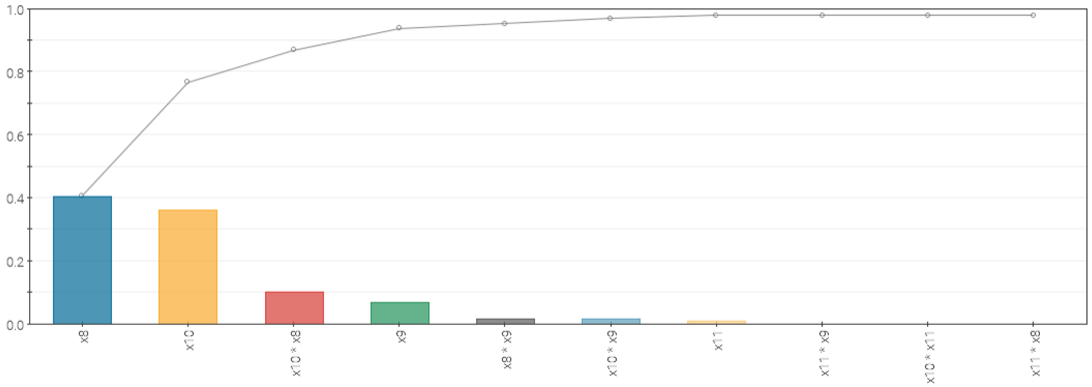

The sensitivity analysis based on regression trees, considering two leaves per node, led to the following results:

Figure 7-13: Predictor Importance based on Regression Tree – Fluid 1 – Oil Production

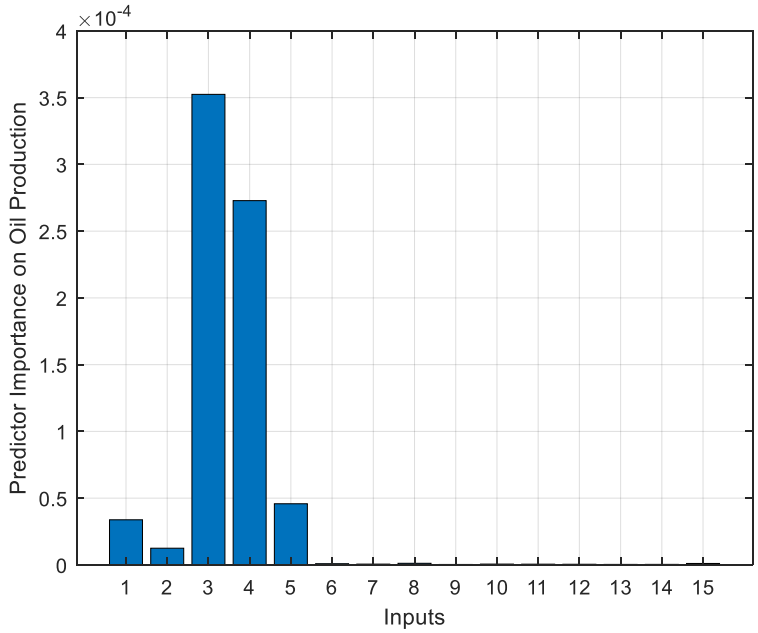

Figure 7-14: Predictor Importance based on Regression Tree – Fluid 1 – Equipment Dry Weight

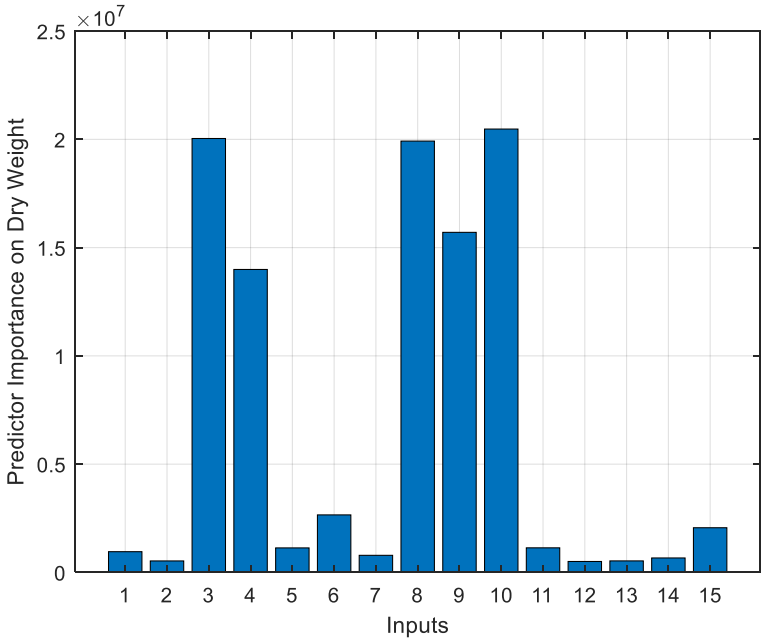

Figure 7-15: Predictor Importance based on Regression Tree – Fluid 1 – Equipment Footprint

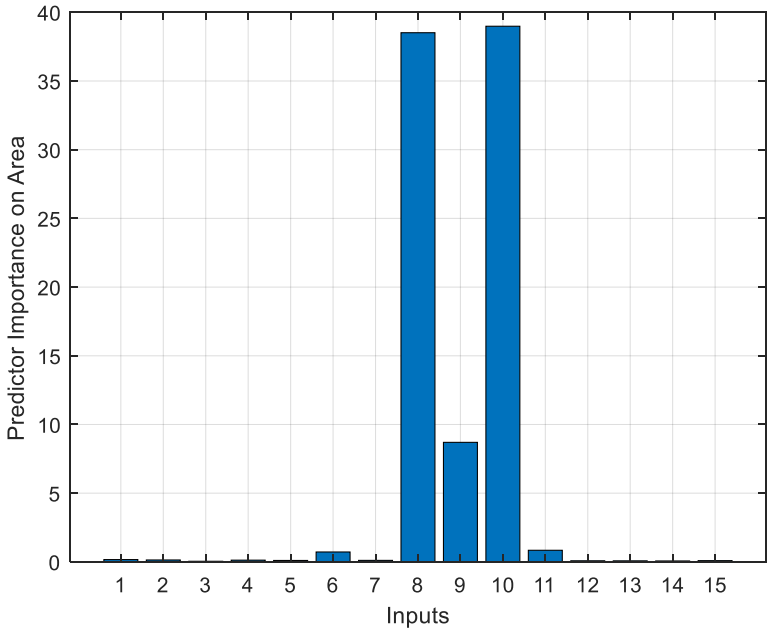

Table 7-3 shows the comparison of SS-ANOVA and regression tree analyses. The inputs marked with Y are the ones that showed relevant significance. There was a very good agreement between the SS-ANOVA and the regression tree, except for input 15, which was deemed relevant by the regression tree in the estimation of dry weight, and input 6, which was deemed relevant by the regression tree in the estimation of area.

Input 6 was already considered relevant by both methods in the estimation of area, therefore it is maintained. Input 15 is the pressure increase provided by the compression system upstream the dehydration unit. Such compression system, in addition to provide part of the required pressure for the gas to be treated and exported, also separates part of the water saturated in the gas, alleviating the dehydration unit. The higher the pressure increase the higher the amount of water separated by the compression system, but the higher pressure will increase design pressure of the vessels installed downstream, increasing the dry weight, therefore it is recommended to maintain I15 as a parameter to be optimized.

Table 7-3: Comparison of SS-ANOVA and Regression Tree results for F1

Input	Oil		Dry Weight		Footprint	
	SS-ANOVA	RTREE	SS-ANOVA	RTREE	SS-ANOVA	RTREE
I1	Y	Y	N	N	N	N
I2	Y	Y	N	N	N	N
I3	Y	Y	Y	Y	N	N
I4	Y	Y	Y	Y	N	N
I5	Y	Y	N	N	N	N
I6	N	N	Y	Y	N	Y
I7	N	N	N	N	N	N
I8	N	N	Y	Y	Y	Y
I9	N	N	Y	Y	Y	Y
I10	N	N	Y	Y	Y	Y
I11	N	N	N	N	Y	Y
I12	N	N	N	N	N	N
I13	N	N	N	N	N	N
I14	N	N	N	N	N	N
I15	N	N	N	Y	N	N

From this screening analysis the following inputs have not shown significance in the estimation of any of the objectives, and therefore can be discarded from the optimization process, adopting fixed values: I7 (E6 L/D ratio), I12 (V-E8 L/D ratio), I13 (TEG specific rate), and I14 (TEG concentration).

Parameters I3 and I4 influence the RVP oil specification, parameters I8, I9 and I10 the BS&W oil specification, and I13 and I14 the export gas water concentration specification. In case the screening analysis comprising the optimization objectives indicated that any of such parameters should be removed from the optimization process, two possibilities would arise: 1) adopting a fixed value that would most likely guarantee that the associated constraint would be met for most of the objective function runs along the optimization process or 2) in case the first option is not possible, run a new screening analysis for the constraints and maintain the parameters that influence such constraints.

In the case of fluid 1, parameters I3, I4, I8, I9 and I10 remained after the screening analysis involving the optimization objectives, so achieving the BS&W

and RVP oil specifications along the optimization process is not a concern. Regarding the export gas water concentration specification, the first option explained in the previous paragraph applies, as the behavior of the TEG process model enables setting I13 and I14 with the most conservative values and ensures that the associated specification is met along the optimization process.

The final inputs for each of the flowsheets of fluid 1 are shown in Table 7-4:

Table 7-4: Final inputs for each of fluid 1 flowsheets

Input	Description	LB	UB	F1F1	F1F2	F1F3
I1	E1 internal diameter (m)	2	5	Y	Y	Y
I2	E1 L/D ratio	2	5	Y	Y	Y
I3	Pressure drop E5 to E6 (%)	10	85	Y	Y	Y
I4	Pressure drop E6 to V-E8 (%)	10	85	Y	Y	Y
I5	E8 temperature (K)	353.15	393.15	Y	Y	Y
I6	E6 internal diameter (m)	2	5	Y	Y	Y
I8	Space between electrodes E8 (m)	0.25	1.25	Y	Y	Y
I9	Length of electrodes in E8 (m)	0.2	1.8	Y	Y	Y
I10	Number of electrodes in E8	20	200	Y	Y	Y
I11	V-E8 internal diameter (m)	1.5	5	Y	Y	Y
I15	Level of pressurization in E-15	0.05	0.80	N	Y	Y

7.7. **Genetic algorithm-based optimization for fluid 1**

The results from fluid 1 flowsheets optimization are shown below. The Pareto fronts and 2D charts are seen from Figure 7-16 to Figure 7-24. It is observed an asymptotic behavior between oil production and dry weight, and between oil production and footprint. The variation of oil production is very low, roughly 1%, but the variation of both dry weight and footprint is quite significant, especially in flowsheets 2 and 3.

In Figure 7-22 it is observed the possibility to produce 223 kg/s and impose 1000 ton to the platform, or produce 222.5 kg/s and impose less than 500 ton

(flowsheet 2). In terms of footprint, still for flowsheet 2, it is possible to produce 223 kg/s and impose around 570 m^2 to the platform, or produce 222.5 kg/s and impose 350 m^2. Flowsheet 3 has significant more equipment dry weight than flowsheets 1 and 2 due to the use of molecular sieves instead of TEG. The relationship between equipment dry weight and footprint, as seen in Figure 7-24 tends to show an asymptotic behavior in flowsheet 1, but no recognized pattern for flowsheets 2 and 3.

Flowsheet 1 equipment dry weight variation is governed by equipment E1 and E4, as seen in Figure 7-25. The variations of inputs I1 and I2 were high, so E1 design varied from high diameter and short length to low diameter and long length. Heat exchanger E4 dry weight is governed by variation of the temperature in the electrostatic coalescer (I5). The higher I5 the higher the heat exchange in E4, increasing both dry weight and footprint.

Flowsheet 2 equipment dry weight variation is governed by equipment E1, E6, E15 and E20 as seen in Figure 7-26. Regarding E1 dry weight variation, the explanation is the same of flowsheet 1. Regarding E6 dry weight variation, it is mainly governed by variation of its internal diameter (I6) and to a lesser extent the pressure drop between E5 and E6 (I3). The higher the pressure drop the lower the pressure in E6, which will decrease the wall thickness for a given internal diameter.

Flowsheet 3 equipment dry weight variation is governed by equipment E1, V-E8, E-15, E17B and E-20 as seen in Figure 7-27. Regarding E1 dry weight variation, the explanation is the same of flowsheet 1. The V-E8 dry weight variation is governed by the pressure drop between E6 and V-E8 and V-E8 internal diameter. The higher the pressure drop the lower the pressure in V-E8, which will decrease the wall thickness for a given internal diameter. The higher the internal diameter, the higher the wall thickness, increasing the dry weight. The dry weight variations of E15, E17B and E20 have to be analyzed together. The higher the level of pressurization in E15 (I15), the lower the amount of water to be separated in the dehydration unit and the lower the required pressurization in E20, since pressure drop in the dehydration unit is negligible.

As a consequence, the higher the dry weight of E15 the lower the dry weight of E20, as both work together providing the required export pressure.

Flowsheet 1 equipment footprint variation is governed by equipment E6 and V-E8, as seen in Figure 7-28. Equipment E6 footprint variation is governed by E6 internal diameter (I6), as the length of the separator is given by the multiplication of the slenderness ratio by the internal diameter. The V-E8 footprint variation is governed by its internal diameter (I11), which is multiplied by the slenderness ratio to give the separator length.

Flowsheet 2 equipment footprint variation is governed by equipment E1, E6, E15 and E20 as seen in Figure 7-29. For separators E1 and E6, their footprint variations are explained by the variations of the internal diameters (I1 and I6), which multiply the respective slenderness rations to give the separator lengths. The level of pressurization in E15 (I15) directly influences E15 and E20 sizes, as power demand significantly influences the size. The higher the power demand in E15, the lower in E20.

Flowsheet 3 equipment footprint variation is governed by equipment V-E8, E17B and E-20, as seen in Figure 7-30. The V-E8 footprint variation is governed by variation of its internal diameter (I11), which multiplies the slenderness ration in order to give the separator length. The footprint variation of E17B is governed by the level of pressurization in E15 (I15), as the higher the pressure in the molecular sieve the lower the amount of water to be separated and the amount of adsorbent, reducing the overall dehydration unit size. The footprint variation in E20 is governed by the level of pressurization in E15 (I15), as the higher the pressurization in E15 the lower in E20, reducing its size.

Figure 7-31 and Figure 7-32 show that oil specifications have been met, in many cases over specification occurred.

Heating demand varies in all flowsheets, as seen in Figure 7-33 to Figure 7-35, due to variation of temperature in the electrostatic coalescer (I5). Power demand slightly varies due to variation in gas production, which is driven by the pressure drop in the valves (I3 and I4). Cooling demand is driven by the compression systems E15 and E20.

Figure 7-16: Pareto Front for F1F1

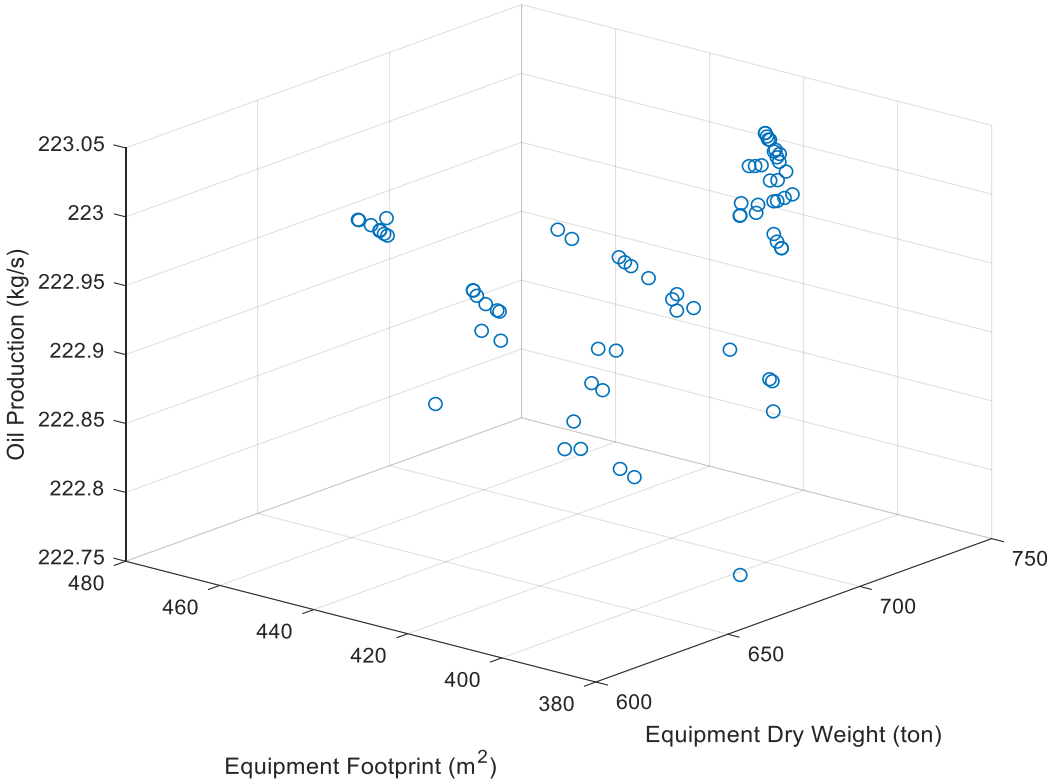

Figure 7-17: Pareto Front for F1F2

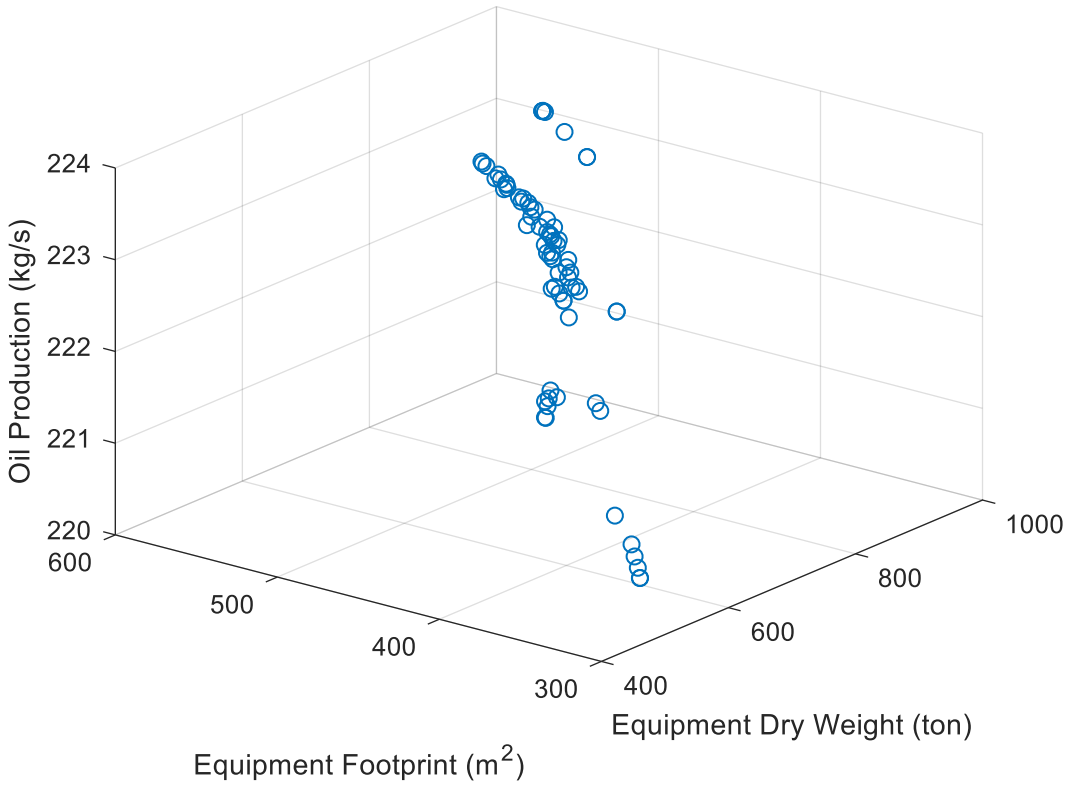

Figure 7-18: Pareto Front for F1F3

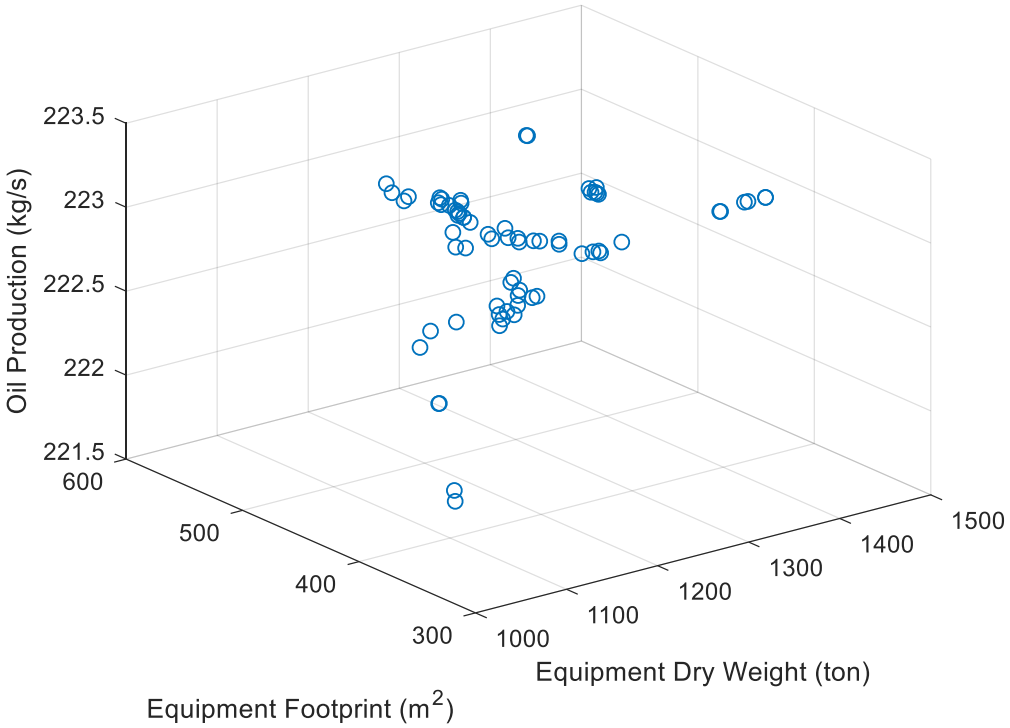

Figure 7-19: Boxplot of optimized inputs for F1F1

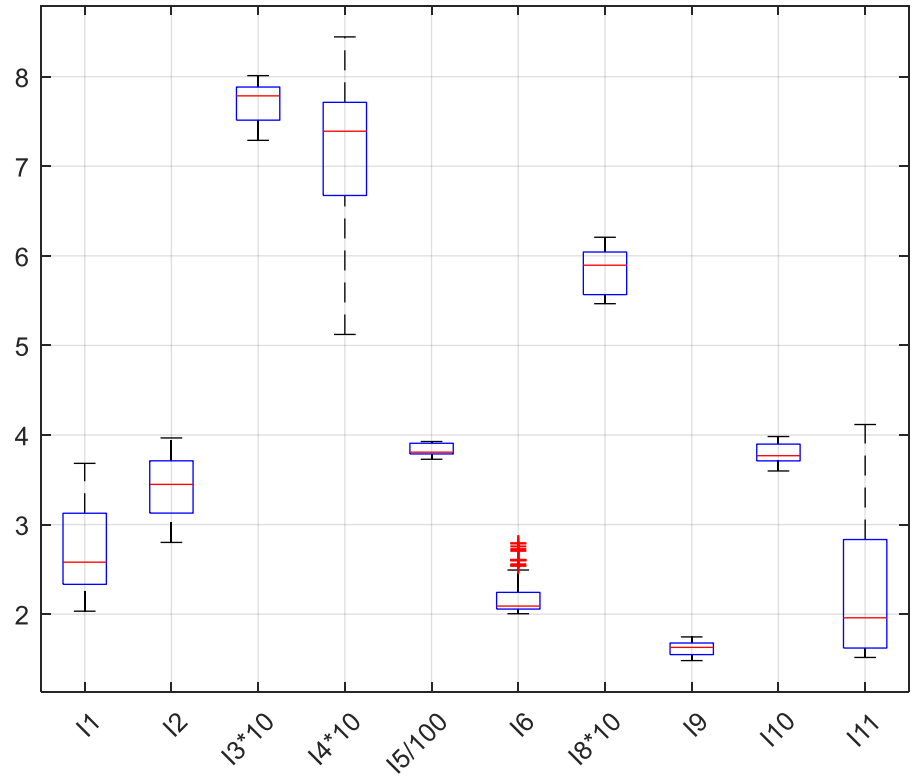

Figure 7-20: Boxplot of optimized inputs for F1F2

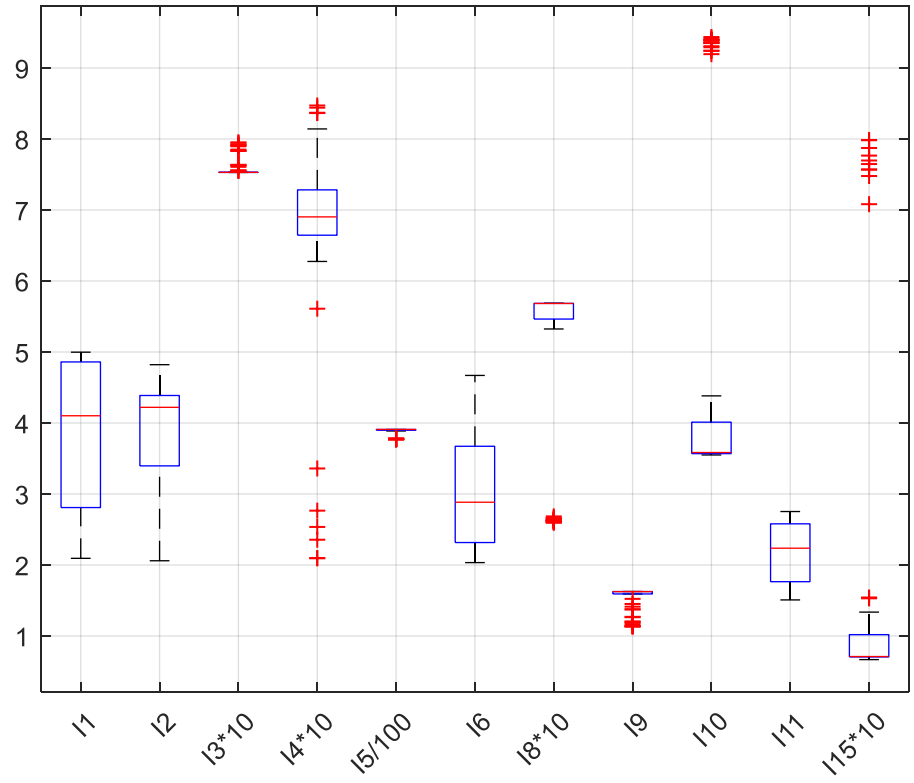

Figure 7-21: Boxplot of optimized inputs for F1F3

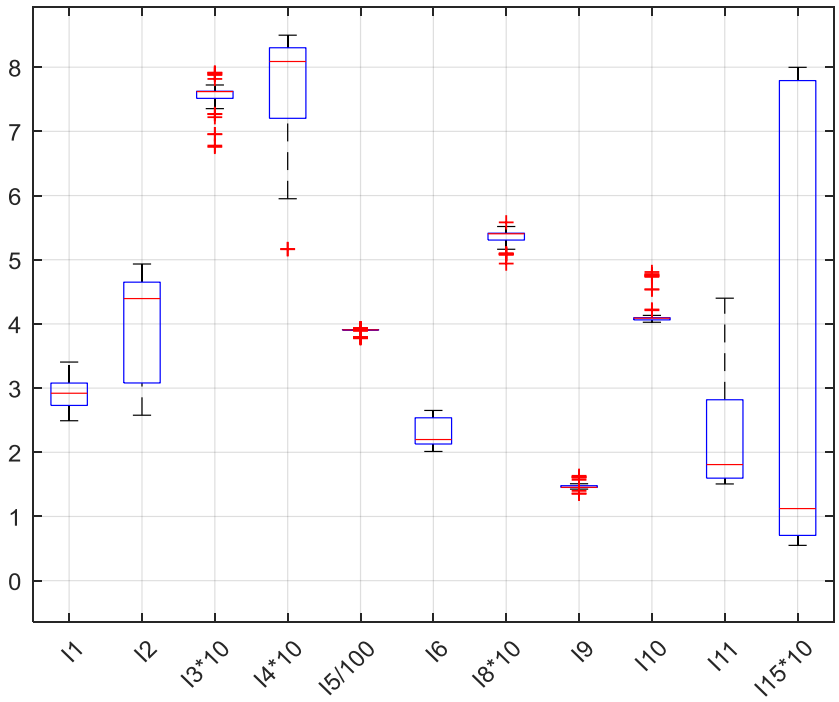

Figure 7-22: Relationship between Oil Production and Dry Weight (Fluid 1)

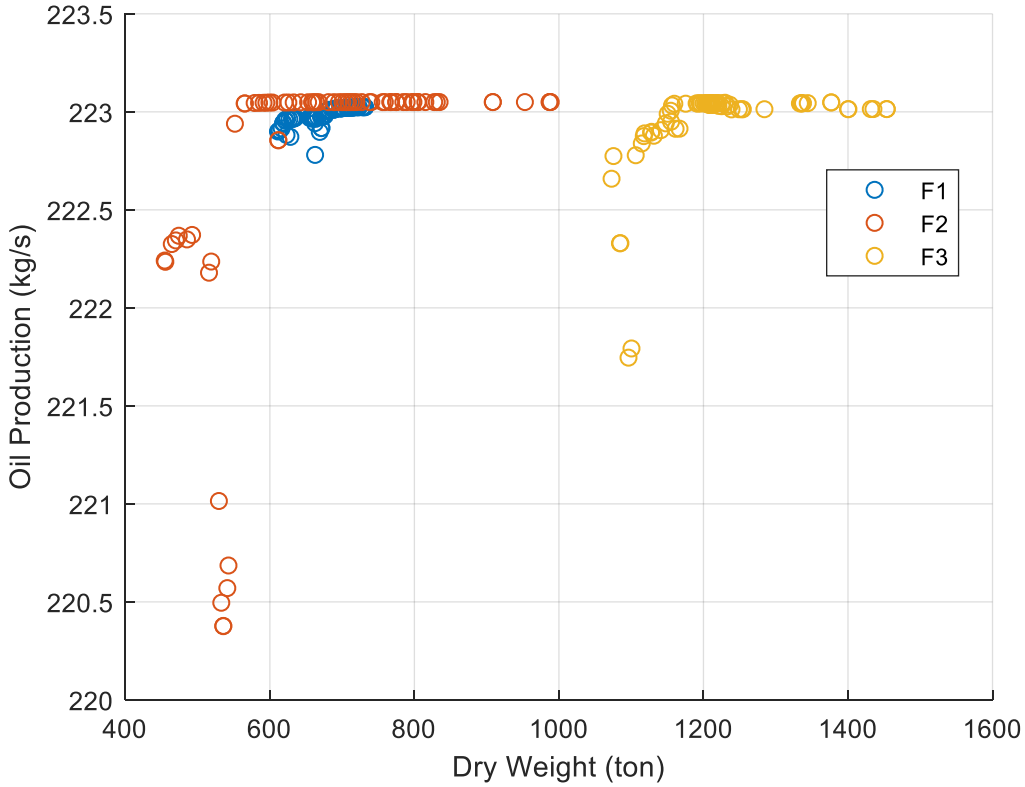

Figure 7-23: Relationship between Oil Production and Footprint (Fluid 1)

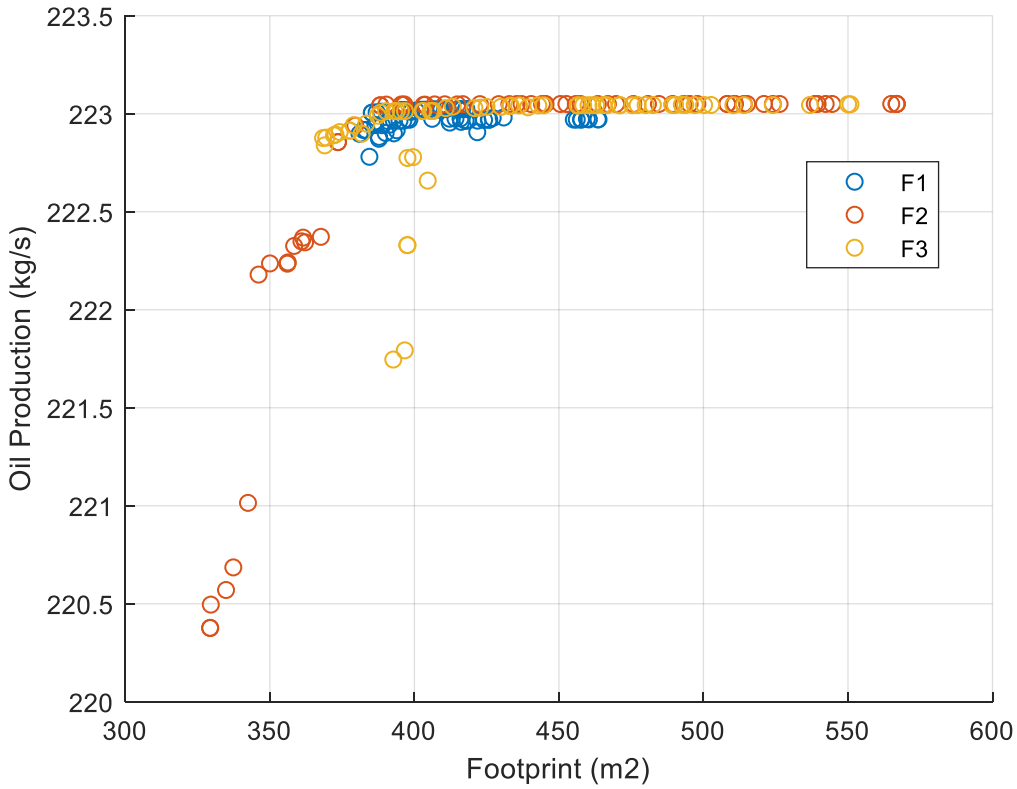

Figure 7-24: Relationship between Dry Weight and Footprint (Fluid 1)

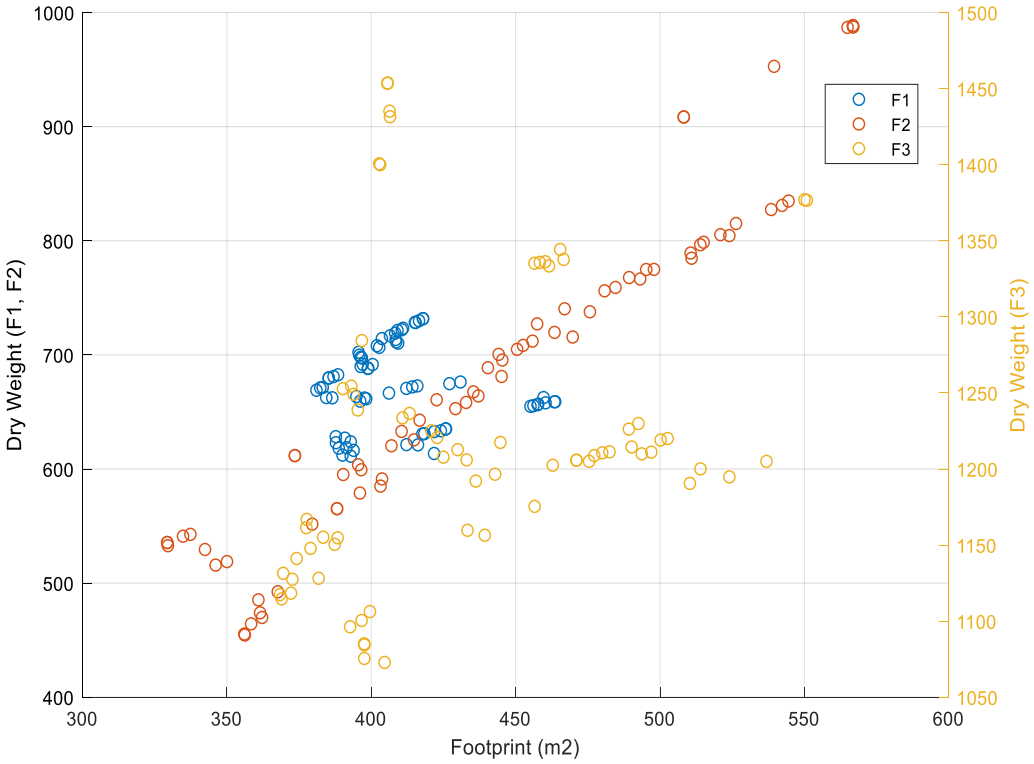

Figure 7-25: Equipment dry weight variation in F1F1

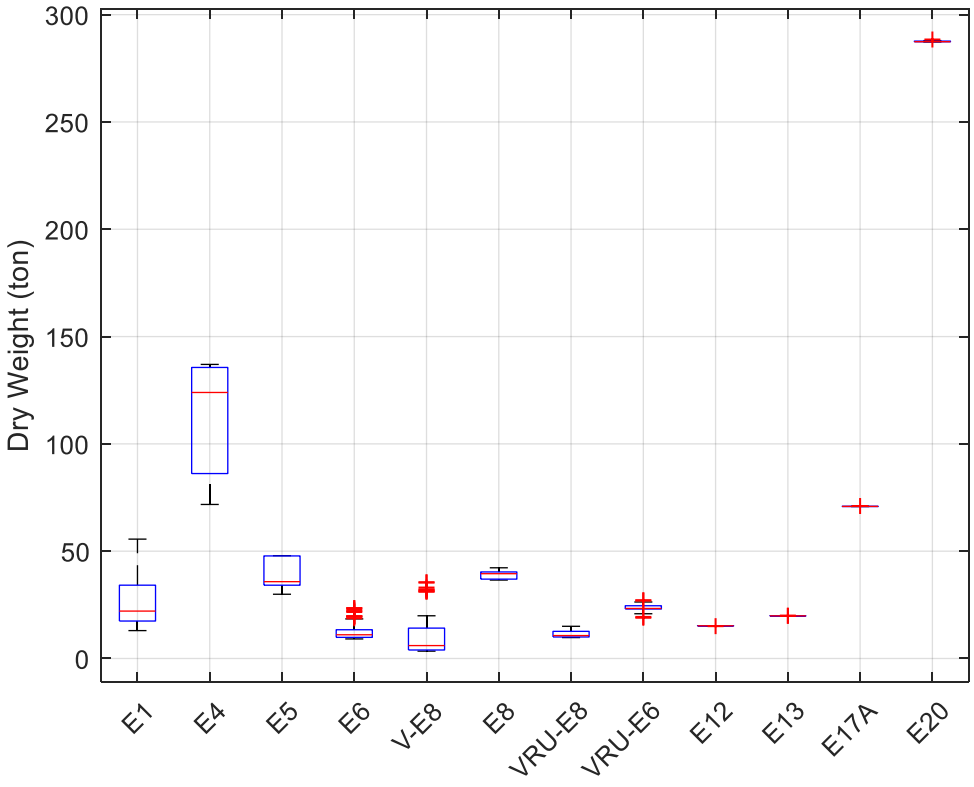

Figure 7-26: Equipment dry weight variation in F1F2

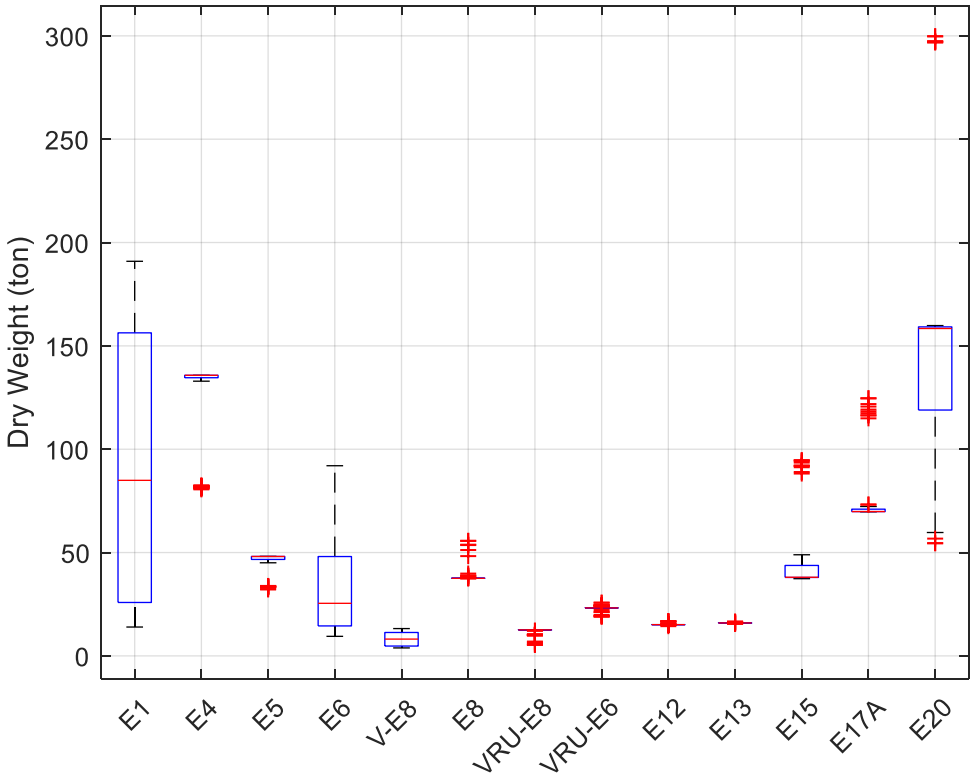

Figure 7-27: Equipment dry weight variation in F1F3

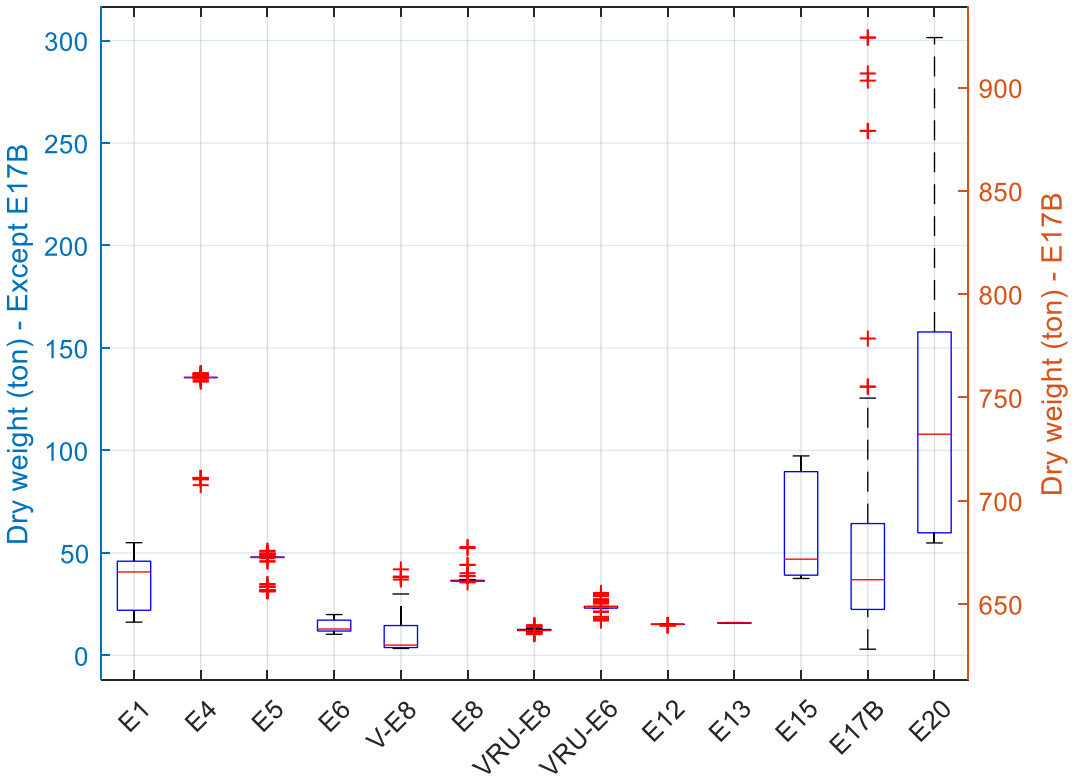

Figure 7-28: Equipment footprint variation in F1F1

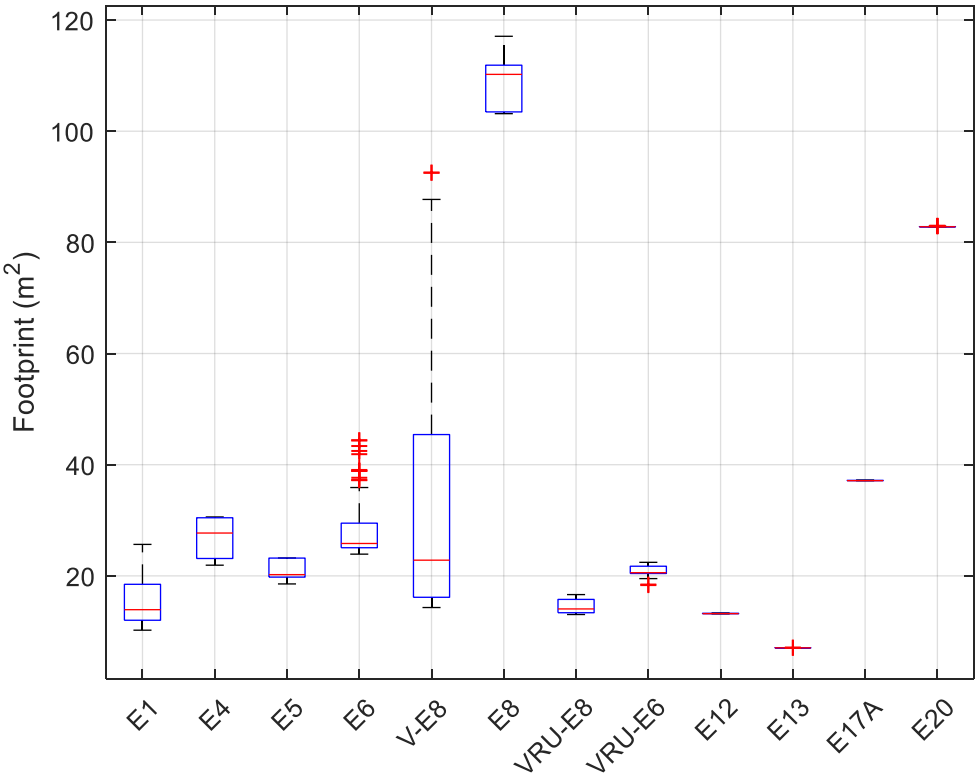

Figure 7-29: Equipment footprint variation in F1F2

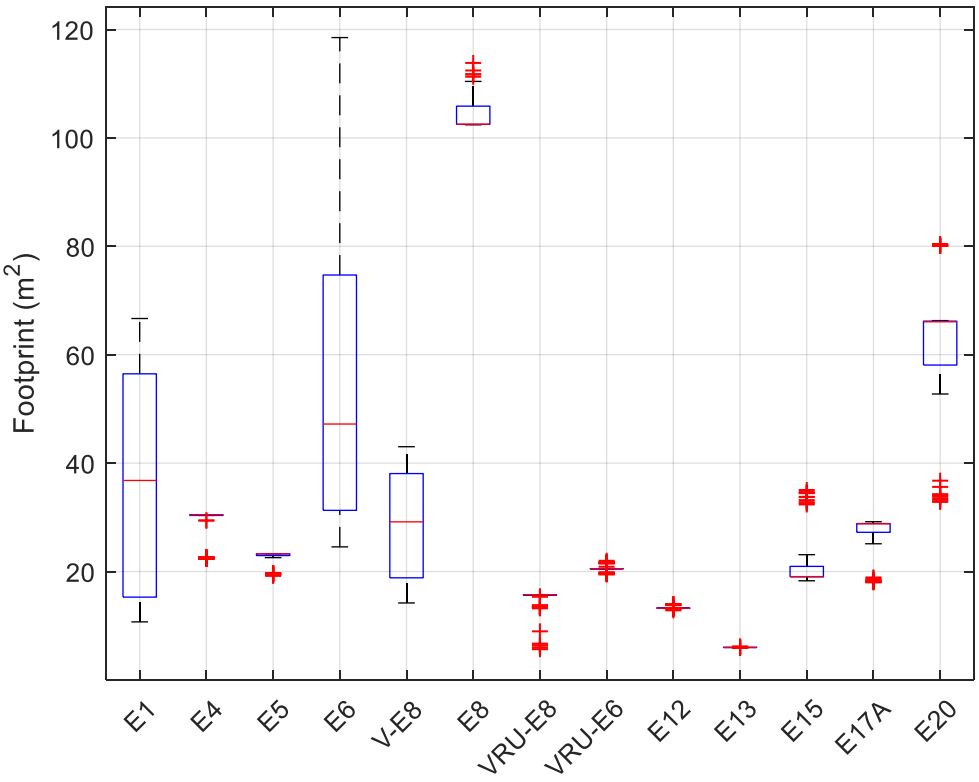

Figure 7-30: Equipment footprint variation in F1F3

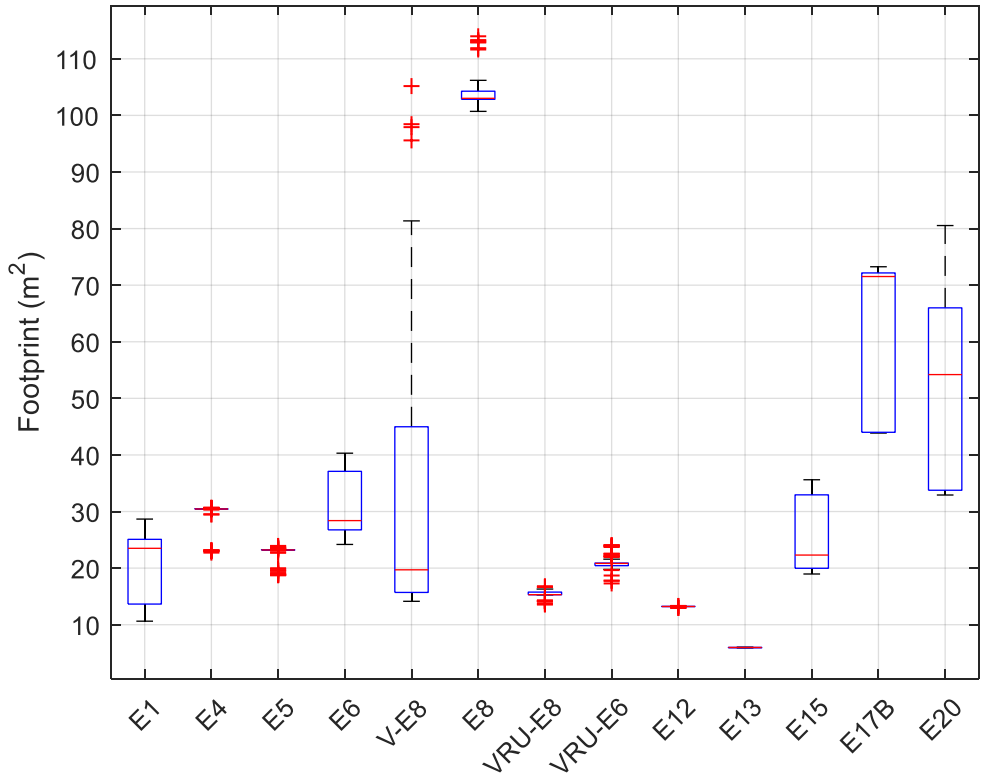

Figure 7-31: Deviation in BS&W specification for fluid 1 flowsheets

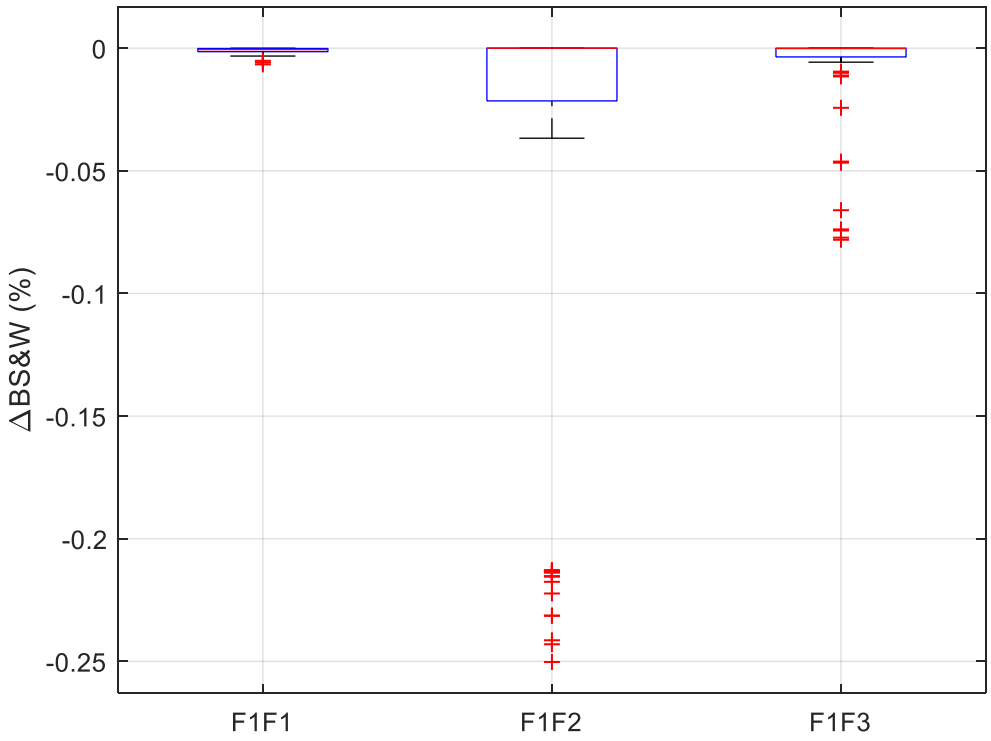

Figure 7-32: Deviation in RVP specification for fluid 1 flowsheets

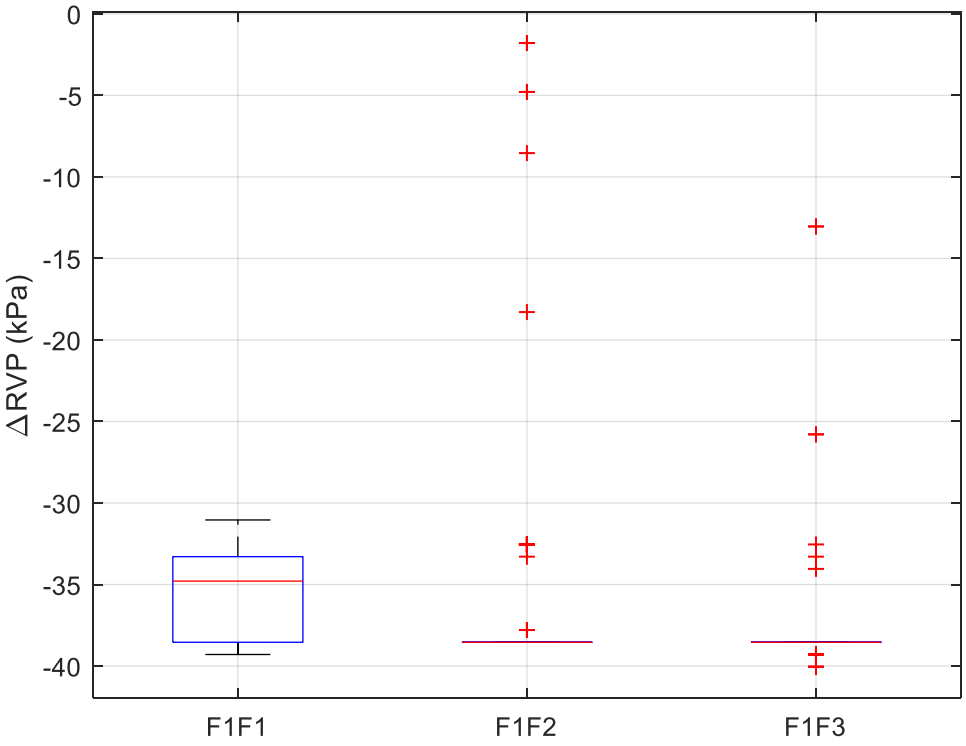

Figure 7-33: Energy demands for F1F1

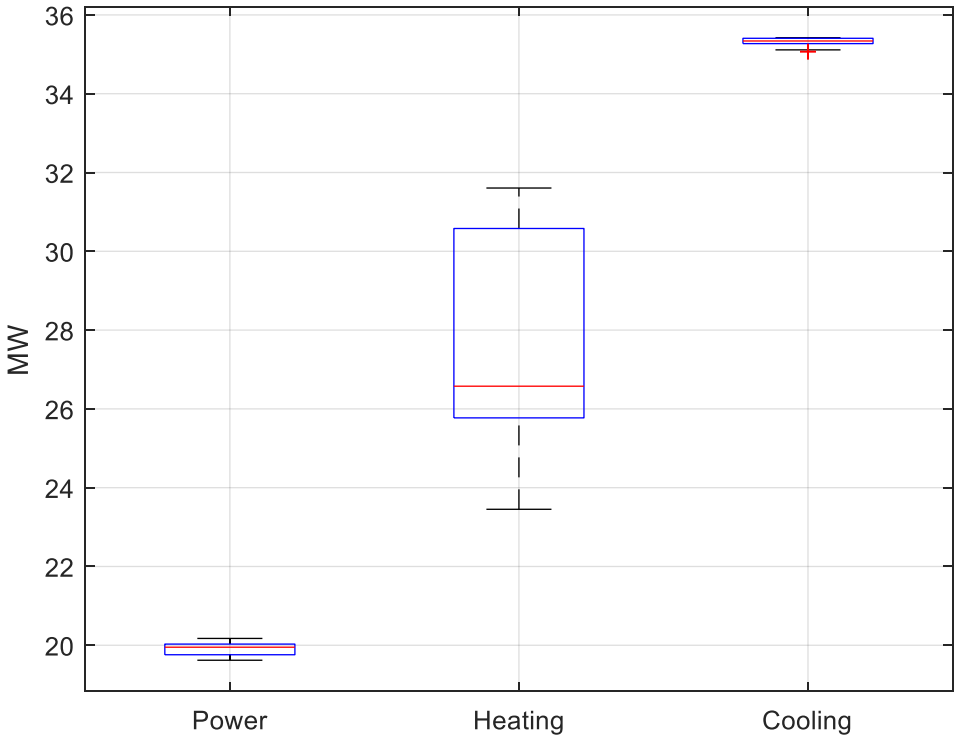

Figure 7-34: Energy demands for F1F2

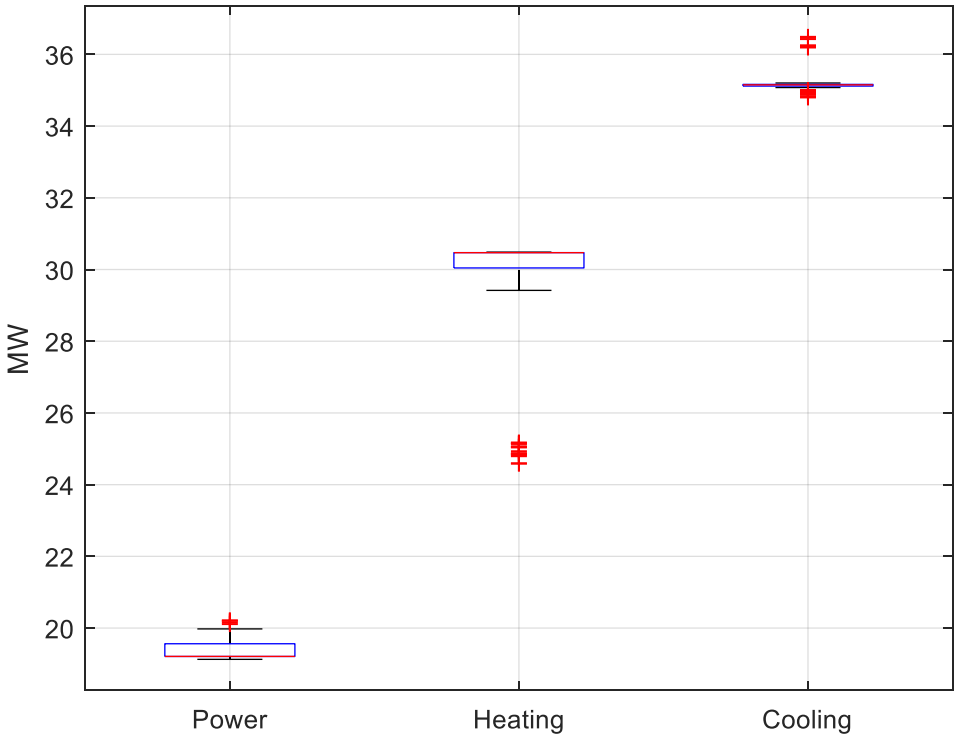

Figure 7-35: Energy demands for F1F3

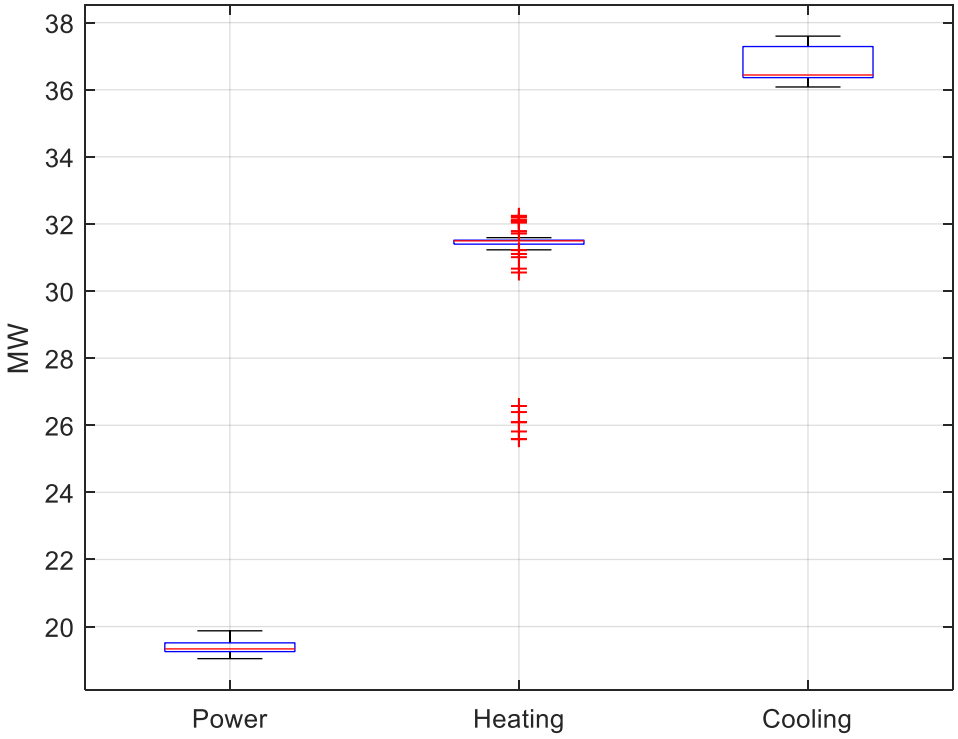

7.8. **Comparison of optimized flowsheets for fluid 1**

Fluid 1 flowsheet results are consolidated in Table 7-5.The percentages below each best attribute represent how better the attribute is with respect to the other flowsheets

F1F2 presents the lowest dry weight among the three flowsheets, at 454 ton, which is 25.6% lower than the lowest dry weight of F1F1 and 57.7% lower than the lowest dry weight of F1F3. F1F2 takes advantage of the combination of pre-compression (E15) and the TEG dehydration unit. A compression system upstream the dehydration unit reduces the amount of water to be separated in the dehydration unit as some water is separated in the knock-out drums part of the compression system. The TEG dehydration system is lighter than molecular sieves, which are based on 2 x 100% vessels and a heavy adsorbent, while the TEG system is based in 1 x 100% absorber and structural packing that is lighter than the adsorbent. The stripper columns in the TEG system have low diameter and height, not significantly influencing the TEG system dry weight.

The lowest footprint of F1F2 is also the lowest among the three flowsheets, at 329 m^2, which is 13.6% lower than the lowest footprint of F1F1 and 10.6% lower than the lowest footprint of F1F3. The combination of pre-compression (E15) and TEG dehydration system leads to a more compact system. There is a clear reduction of TEG unit footprint in F1F2 compared to F1F1, as the minimum footprint in F1F2 is 18 m^2 and in F1F1 37 m^2.The median of the molecular sieve footprint in F1F3 is approximately 70 m^2, while the median of the TEG footprint in F1F2 is 30 m^2 and 38 m^2 in F1F1. The pre-compression system in F1F2 reduced the TEG system size by 8 m^2 on average compared to F1F1.

Maximum oil production is almost identical among the three flowsheets, which is expected as the oil section is identical regardless of the flowsheet, and the condensation in the gas section is negligible.

Minimum heating demand is higher in F1F3, as molecular sieve demands more heating than TEG. Minimum cooling demand is higher in F1F3, driven by the need to cool regeneration gas from the molecular sieve process. Both

dehydration technologies were able to meet the 10 ppmv specification. The TEG system is lighter, smaller, and less energy intensive than molecular sieve.

It is worth to emphasize that the best values tend to not occur simultaneously, as each point in the Pareto Front will have its respective attributes. In addition, there is a clear trade-off between oil production and dry weight or footprint, as oil production can be slightly increased if E1, E6 and V-E8 can separate more dispersed oil from the non-oil continuous phases. The separators can achieve higher efficiency if their dimensions are increased.

Table 7-5: Performance of fluid 1 flowsheets

Attribute	**F1F1**		**F1F2**		**F1F3**	
	Best	Worst	Best	Worst	Best	Worst
Oil production (kg/s)	223.02 (+0.1%)	222.78	223.05 (+1.2%)	220.37	223.05 (+0.6%)	221.74
Equipment Dry Weight (ton)	611 (-16.4%)	731	454 (-54.1%)	989	1,073 (-26.1%)	1,453
Equipment Footprint (m^2)	381 (-17.7%)	463	329 (-42%)	567	368 (-33.2%)	551
Power demand (MW)	19.6 (-3%)	20.2	19.1 (-5.4%)	20.2	19.0 (-4%)	19.8
Heating demand (MW)	23.4 (-25.9%)	31.6	24.6 (-19.1%)	30.4	25.6 (-20.5%)	32.2
Cooling demand (MW)	35.1 (-0.8%)	35.4	34.8 (-4.6%)	36.5	36.1 (-4%)	37.6

Considering the best attributes of each flowsheet in a spider chart leads to Figure 7-36, indicating that F1F2 is the best flowsheet if equal weight is given to each attribute.

Figure 7-36: Fluid 1 flowsheets best attributes

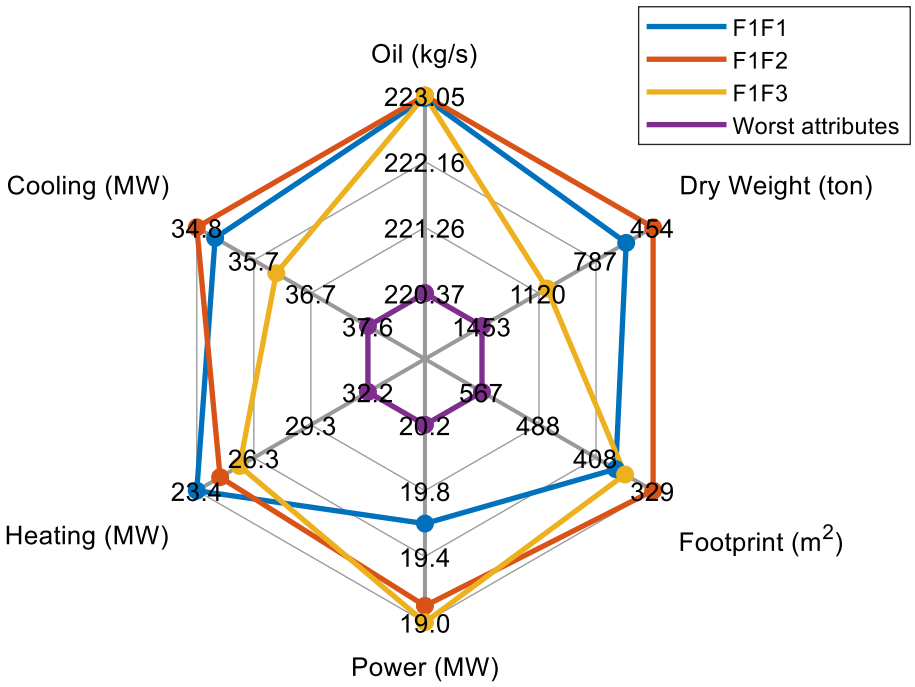

7.9. **Identification of most complex flowsheet for fluid 2**

As seen in Table 7-6, fluid 2 flowsheets have more initial inputs than fluid 1 flowsheets due to more complex gas treatment.

Inputs I1 to I13 are included in fluid 1 initial optimization input. In section 7.4 it was explained their importance in the optimization process.

In a membrane system, each stage has at least two inputs that can be optimized: membrane area (I16 and I17) and pressure drop (I18 and I19). The first membrane stage also includes the inlet temperature (I15) and pressure (dictated by I13). Such parameters directly influence the efficiencies of CH_4 and CO_2 recoveries in the permeate stream, as seen in equations 6.15-1 and 6.15-2, therefore they have to be initially included in the optimization. The higher the membrane area the higher the skid footprint, as per equation 6.15-3. The higher the membrane area the higher the number of membrane elements, increasing the dry weight. Separating CO_2 at higher pressures will contribute to reduce total required pressurization in the system, reducing power demand., .

The level of depressurization in E18 (I14) combined with the level of pressurization in E15 (I13) and the membrane inlet temperature (I15) are the key parameters influencing condensation inside the membrane system, which is not allowed as the membrane structure can be compromised. Therefore I14 is included as initial optimization parameter.

In the MEA system of F2F3, inlet temperature and pressure can be varied due to the existence of the pre-compression system (E15). The regression tree based MEA system model accepts inlet temperature from 273.15 to 333.15 K. The minimum process fluid temperature the cooling medium allows is 313.15 K, as seawater inlet at 25°C and adopted approach of 15°C in the intercoolers leads to 40°C (313.15K) minimum discharge temperature in the compression system. Therefore, inlet MEA temperature will only vary from 313.15 to 333.15 K. In F2F1, the MEA inlet pressure and temperature are dictated by the characteristics of the permeate stream, so they are no longer inputs. In F2F2 there is no MEA system.

As seen in Table 7-6, there are 23 inputs for F2F1, 19 inputs for F2F2, and 18 inputs for F2F3. The screening analysis is then based on F2F1.

7.10. **Generation of DOE dataset for fluid 2**

The required time to converge a complex mass and energy balance involving several equipment in oil and gas processing, like F2F1, may not lead to reasonable optimization duration. The way F2F1 is modeled in this work is still not leading to fast convergence. Understanding S14, based on the oil processing optimization, may enable splitting optimization in two smaller problems: the oil processing section optimization and the gas processing section optimization. Such split will reduce optimization time significantly. Such hypothesis will be analyzed when the oil section is optimized and data from S14 is obtained.

Table 7-6: Inputs of Fluid 2 flowsheets

Input	Description	LB	UB	F2F1	F2F2	F2F3
I1	E1 internal diameter (m)	2	5	Y	Y	Y
I2	E1 L/D ratio	2	5	Y	Y	Y
I3	Pressure drop E5 to E6 (%)	10	85	Y	Y	Y
I4	Pressure drop E6 to V-E8 (%)	10	85	Y	Y	Y
I5	E8 temperature (K)	353.15	393.15	Y	Y	Y
I6	E6 diameter (m)	2	5	Y	Y	Y
I7	E6 L/D ratio	2	5	Y	Y	Y
I8	Space between electrodes in E8 (m)	0.25	1.25	Y	Y	Y
I9	Length of electrodes in E8 (m)	0.2	1.8	Y	Y	Y
I10	Number of electrodes in E8	20	200	Y	Y	Y
I11	V-E8 diameter (m)	1.5	5	Y	Y	Y
I12	V-E8 L/D ratio	2	5	Y	Y	Y
I13	Level of pressurization in E-15	5%	50%	Y	Y	Y
I14	Level of depressurization in E-18	10%	95%	Y	Y	N
I15	Inlet temperature membrane 1st stage (K)	303.15	353.15	Y	Y	N
I16	Membrane specific area 1st stage ($m^2/(Sm^3/h)$	0.4	2.1	Y	Y	N
I17	Membrane specific area 2nd stage ($m^2/(Sm^3/h)$	0.4	2.1	Y	Y	N
I18	Pressure drop permeate side 1st stage (%)	40	90	Y	Y	N
I19	Pressure drop permeate side 2nd stage (%)	40	90	Y	Y	N
I20	TEG specific rate (m^3 TEG/kg H_2O) – export	0.015	0.05	Y	N	Y
I21	TEG mass fraction (%) - export	98.5	99.995	Y	N	Y
I22	TEG specific rate (m^3 TEG/kg H_2O) – CO_2 inj	0.015	0.05	Y	N	Y
I23	TEG mass fraction (%) – CO_2 inj	98.5	99.995	Y	N	Y
I24	MEA inlet temperature (K)	313.15	333.15	N	N	Y

Generation of DOE Dataset and Determination of Initial Population for Fluid 2A DOE dataset has been created using inputs 1 to 12 from Table 7-2, and a regression tree analysis was conducted to verify the importance of each of the **oil processing section** parameters. Figure 7-37 suggests that the DOE dataset covers the spectrum of all the inputs:

Figure 7-37: Plot of dataset generated by SOBOL sequence – F2 – Oil Processing Section

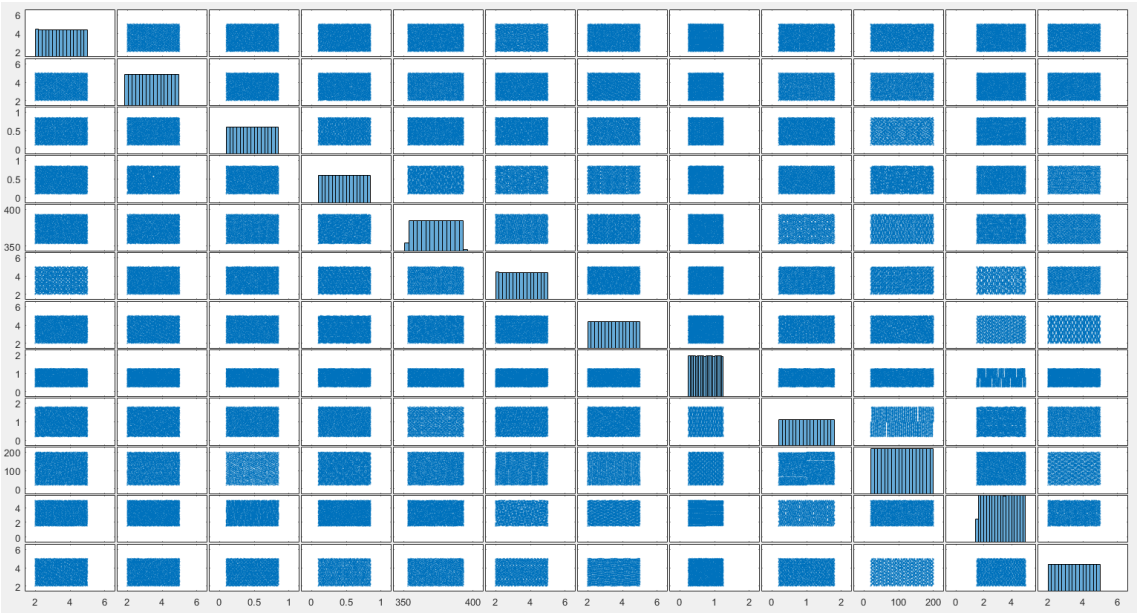

The gas plant optimization is based on heating demand, instead of hydrocarbon condensate, as third objective because it is a strong indicator of fuel gas demand and also because hydrocarbon condensate flowrate should not significantly affect oil production. The MEA technology strongly influences heating demand, so not considering in the optimization any parameter that influence fuel gas demand could potentially favor maximization of inlet CO_2 concentration in the MEA plant as its equipment footprint and dry weight may be lower than CO_2 removal membranes.

Another DOE dataset has been created for the gas processing section of F2F1, using inputs I13 to I23 of F2F1. Analyzes based on regression trees and SS-ANOVA have been conducted to verify the importance of each parameter on the gas plant equipment dry weight and footprint, and heating demand.

Figure 7-38 suggests that the gas plant DOE dataset covers the spectrum of all inputs.

Figure 7-38: Plot of dataset generated by SOBOL sequence – F2F1 – Gas Plant

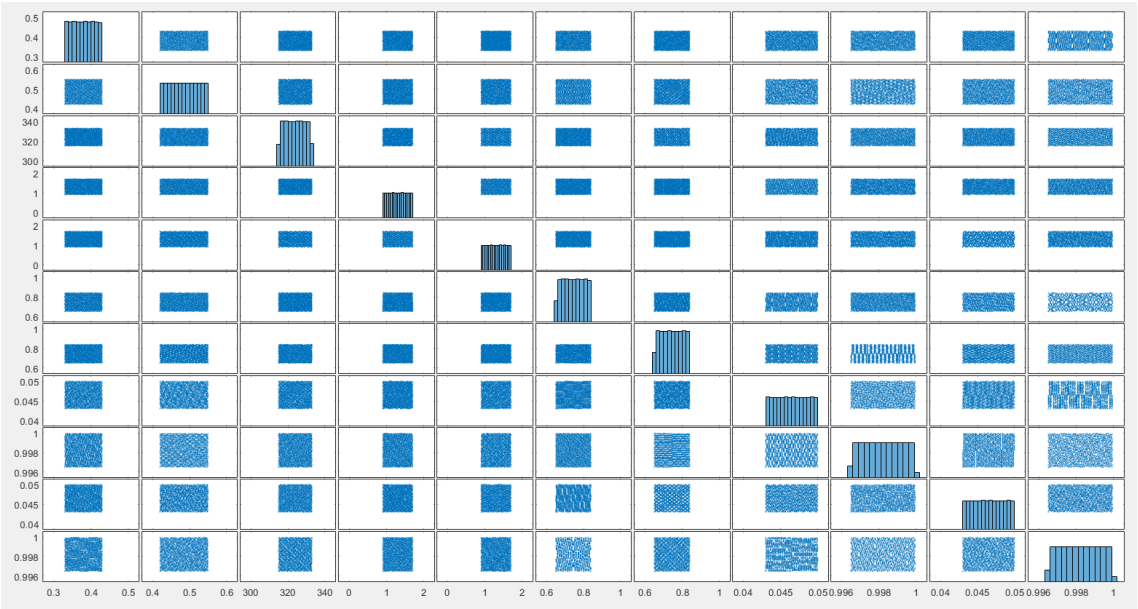

The initial population has been determined by running the objective function several times, varying the input values, until a large set of feasible points is obtained. From this large set, an initial population is randomly chosen in order to initialize the optimization. The size of the initial population depends on the number of inputs.

7.11. **Sensitivity analysis on system level and determination of initial population for fluid 2**

The initial population was determined by running the objective function several times, varying the input values, until a large set of feasible points is obtained. From this large set, an initial population is randomly chosen in order to initialize the optimization. The size of the initial population depends on the number of inputs.

Starting with the gas processing section, the SS-ANOVA results are shown in the following charts, where I1 to I11 are respectively I13 to I23:

Figure 7-39: SS-ANOVA – F2F1 Gas Processing Section – Equipment Dry Weight

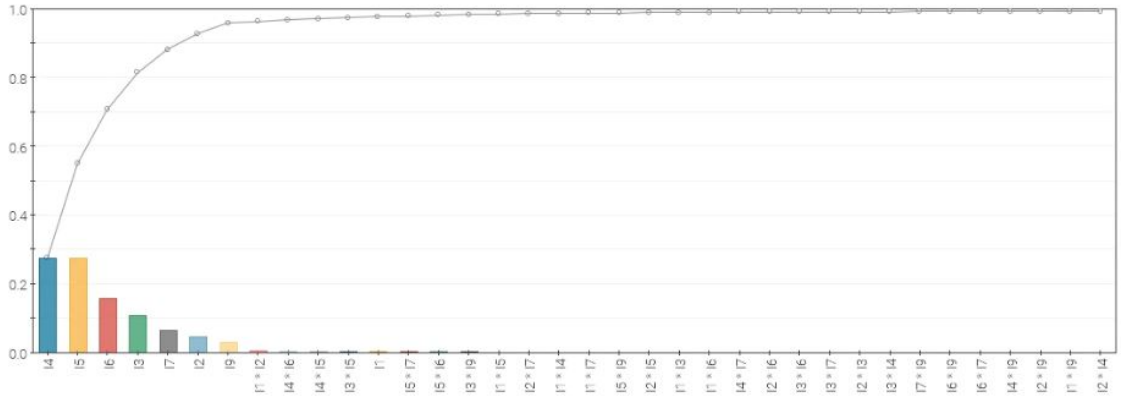

Figure 7-40: SS-ANOVA – F2F1 Gas Processing Section – Equipment Footprint

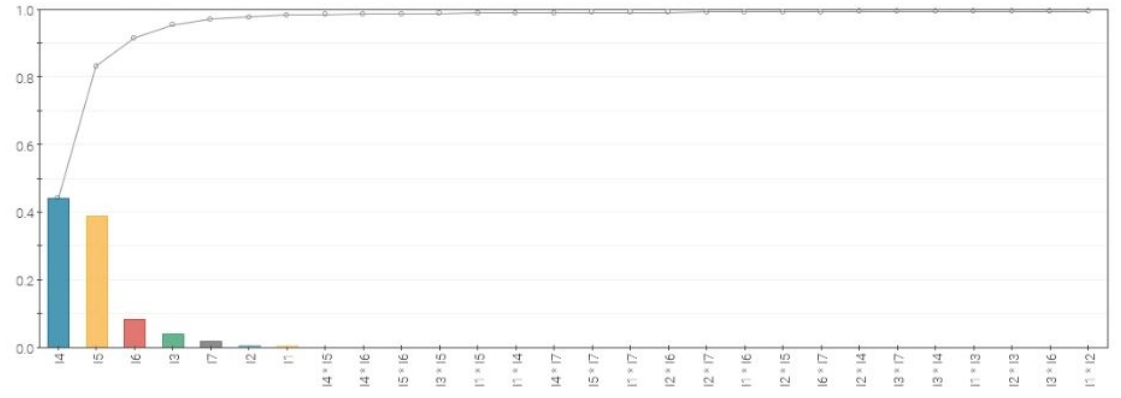

Figure 7-41: SS-ANOVA – F2F1 Gas Processing Section – Heating Demand

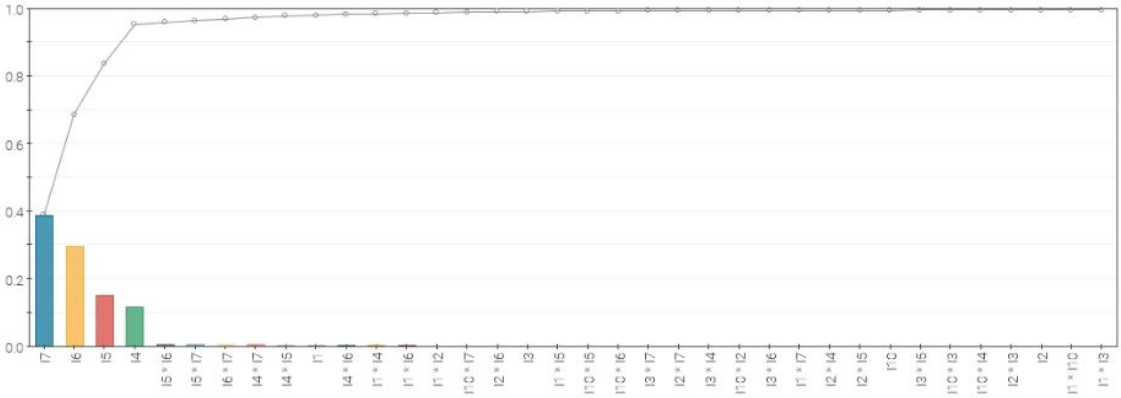

The regression tree results are shown in the following charts, where I1 to I11 are respectively I13 to I23:

Figure 7-42: Predictor Importance based on Regression Tree – F2F1 Gas Processing Section – Equipment Dry Weight

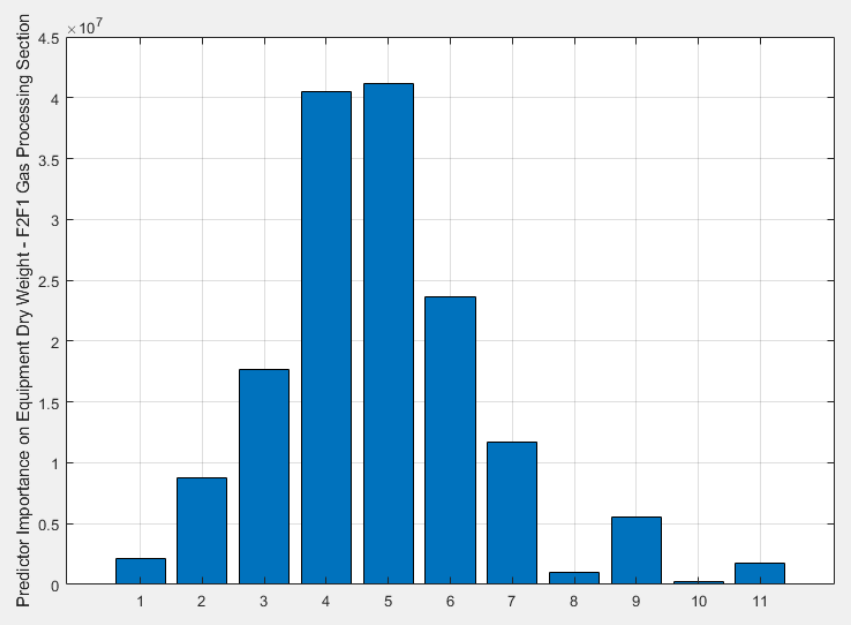

Figure 7-43: Predictor Importance based on Regression Tree – F2F1 Gas Processing Section – Equipment Footprint

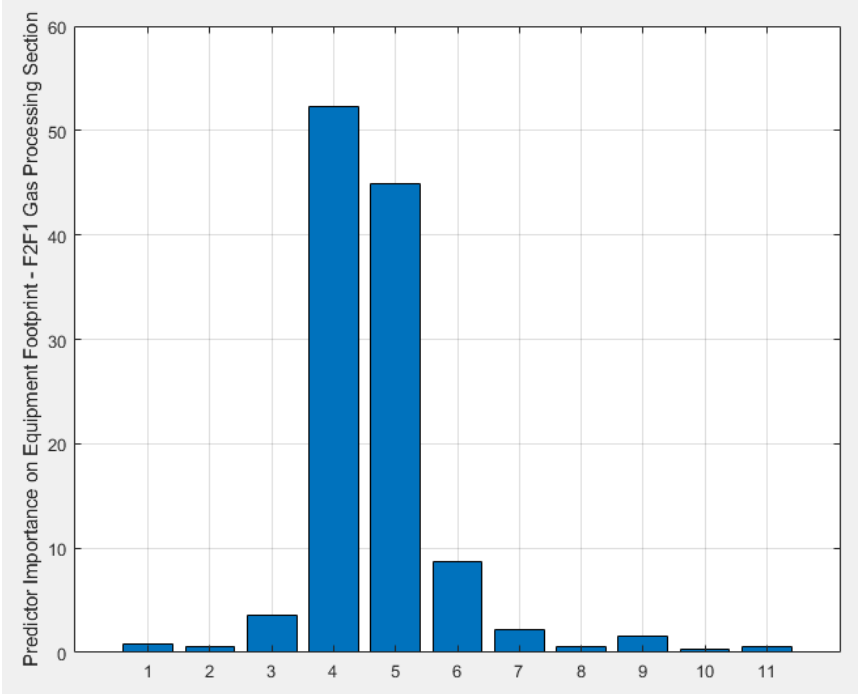

Figure 7-44: Predictor Importance based on Regression Tree – F2F1 Gas Processing Section – Heating demand

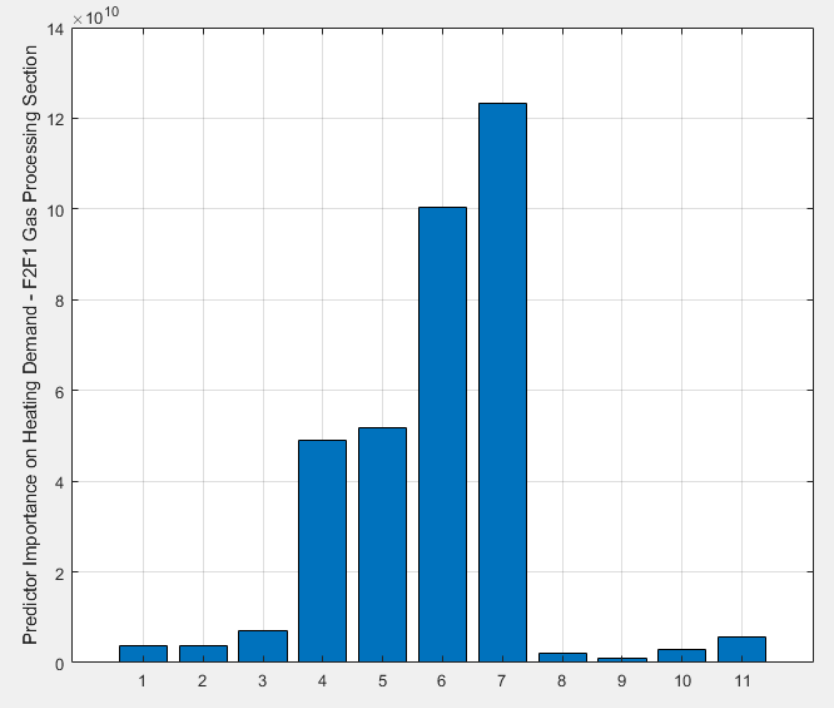

Table 7-7 shows the comparison between the SS-ANOVA and Regression Tree results, showing an excellent agreement:

Table 7-7: Comparison of SS-ANOVA and Regression Tree results for F2F1 Gas Plant

INPUT	Dry Weight		Footprint		Heating	
	SS-ANOVA	RTREE	SS-ANOVA	RTREE	SS-ANOVA	RTREE
I13	N	N	N	N	N	N
I14	Y	Y	N	N	N	N
I15	Y	Y	Y	Y	N	N
I16	Y	Y	Y	Y	Y	Y
I17	Y	Y	Y	Y	Y	Y
I18	Y	Y	Y	Y	Y	Y
I19	Y	Y	Y	Y	Y	Y
I20	N	N	N	N	N	N
I21	Y	Y	N	N	N	N
I22	N	N	N	N	N	N
I23	N	N	N	N	N	N

The sensitivity analysis carried out for the gas processing section of F2F1 depended on narrow ranges (narrower than the minimum and maximum bounds set in the optimization process) for certain variables, in order to lead to feasible gas plants in all the DOE dataset, ensuring quality of the screening analysis. Parameter I13 (pressurization in E-15) together with parameter I14 (pressure

drop in E18) are very important to ensure feasibility of the CO_2 removal by the membrane process, so discarding any of such parameters will decrease the ability of the optimization process to find feasible solutions. Therefore, even though the screening analysis shows that parameter I13 does not significantly affect any objectives, it will be maintained in the optimization process. The other parameters that showed little influence on the objectives, I20, I22 and I23, will not be considered in the optimization process, adopting fixed conservative values that will not affect feasibility of the gas plant.

For the oil section, the sensitivity analysis was purely based on regression trees given the good agreement with SS-ANOVA in previous analyses and also due to the fact that a comparison between SS-ANOVA and regression tree was already done for fluid 1.

The importance of each input on each of the objectives (oil production, equipment dry weight and equipment footprint) is shown in the following figures:

Figure 7-45: Predictor Importance based on Regression Tree – Fluid 2 Oil Section – Objective: Oil Production

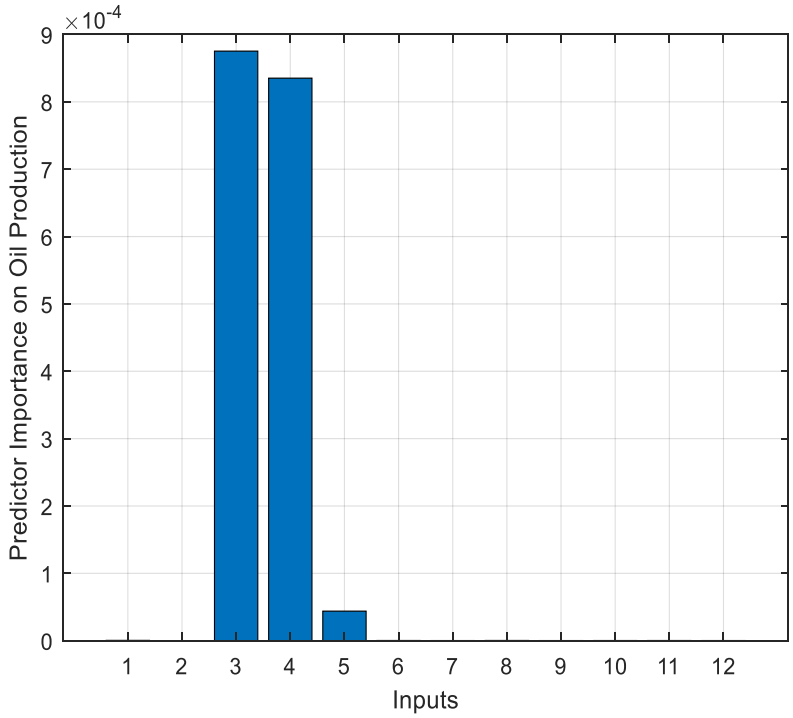

Figure 7-46: Predictor Importance based on Regression Tree – Fluid 2 Oil Section – Objective: Equipment Dry Weight

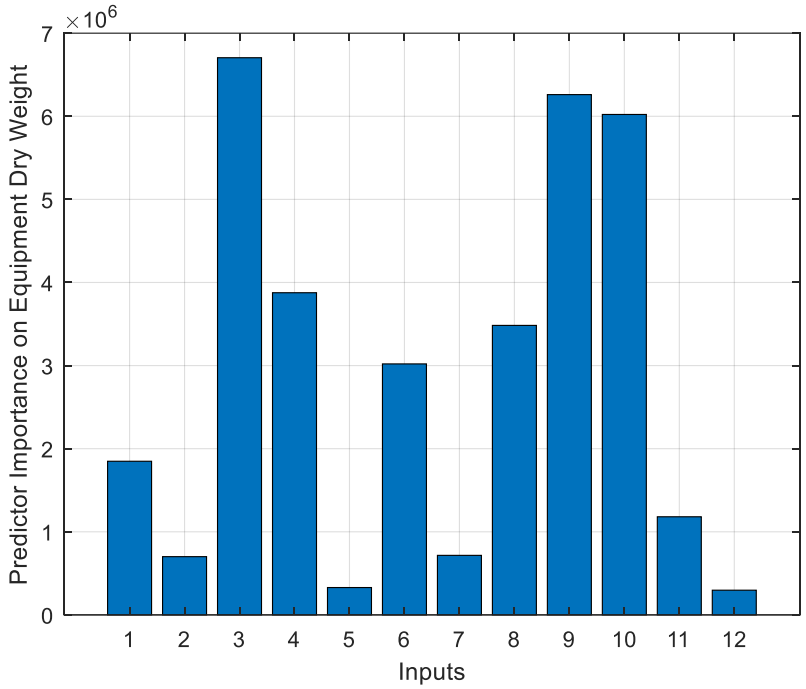

Figure 7-47: Predictor Importance based on Regression Tree – Fluid 2 Oil Section – Objective: Equipment Footprint

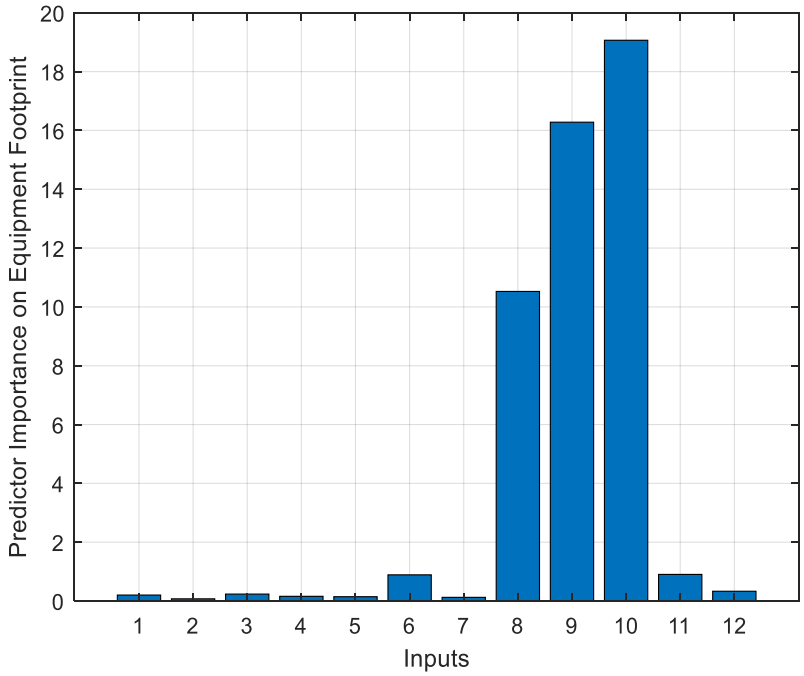

Table 7-8 shows that only I12 does not significantly influence any the objectives, so it can be removed from the optimization process. Fluid 2 has more light components than F1, so it was expected that design parameters

involved in gas separation (like I7, which was removed from F1 optimization) would present more influence at least in dry weight and footprint.

Table 7-8: Regression Tree results for Fluid 2 Oil Section

INPUT	OIL	DRY WEIGHT	FOOTPRINT
I1	N	Y	N
I2	N	Y	N
I3	Y	Y	N
I4	Y	Y	N
I5	Y	N	N
I6	N	Y	Y
I7	N	Y	N
I8	N	Y	Y
I9	N	Y	Y
I10	N	Y	Y
I11	N	Y	Y
I12	N	N	N

7.12. **Genetic algorithm-based optimization for fluid 2**

Starting from the oil section, which is common for all flowsheets, the results are shown in the following charts.

As seen in fluid 1, the relationship between fluid 2 oil production, equipment dry weight and equipment footprint is the same: an asymptotic pattern that leads to relevant change in equipment dry weight or footprint while oil production variation is negligible. The RVP specification leads to low variation of oil production, which is ultimately governed by variation of separation efficiency of oil droplets from gas and water continuous phases, as in certain designs it may be higher than the threshold of 99%, and by variation of BS&W (as seen in Figure 7-55 content in the export oil, which is lower than the specification in certain designs, reducing oil production (the oil export BS&W is computed as oil production).

The first stage separator (E1) governs the variation of dry weight and footprint, as seen in Figure 7-53 and Figure 7-54, given the high variation of I1 and I2 as seen in Figure 7-49. Other equipment that relevantly influenced dry weight are E4 and E6. As I5 (temperature in electrostatic coalescer) varied from 360 to 395K, as shown in Figure 7-49, the heat exchange also varied in E4, leading to

variation in both dry weight and footprint. Another parameter that can affect E4 dry weight is the pressure in the electrostatic coalescer, governed by I4. Even though the pressure in the electrostatic coalescer is low, as the oil is already stabilized in such step, variation in such pressure will change the design pressure in E4 shell, changing the dry weight. The dry weight variation of E6 is explained by the variation of I3 (pressure drop from E5 to E6), which changes the amount of gas and the residence time for the gas continuous phase in E6, and parameters I6 and I7, which are respectively the internal diameter and slenderness ratio of the vessel.

Other pieces of equipment that relevantly influenced footprint were E6, V-E8, E8 and VRU-E8. The variation of E6 footprint is governed by variation of its dimensions (I6 and I7). V-E8 footprint variation is explained by I11 variation (internal diameter), as it is multiplied by the slenderness ratio to give the separator length. Parameters I8 (space between electrodes) and I10 (number of electrodes) presented high variation, explaining the variation of E8 footprint. The variation of VRU-E8 footprint is governed by E8 pressure (which is influenced by I3 and I4), as the lower the pressure in the electrostatic coalescer the higher the power demand, which increases the size of the compressor.

Energy demands are shown in Figure 7-56. Heating varies mainly due to variation temperature in the electrostatic coalescer. Cooling and power are mainly related to the vapor recovery units, which work with different inlet conditions depending on inputs I3, I4 and I5.

Figure 7-48: Pareto Front for fluid 2 oil section

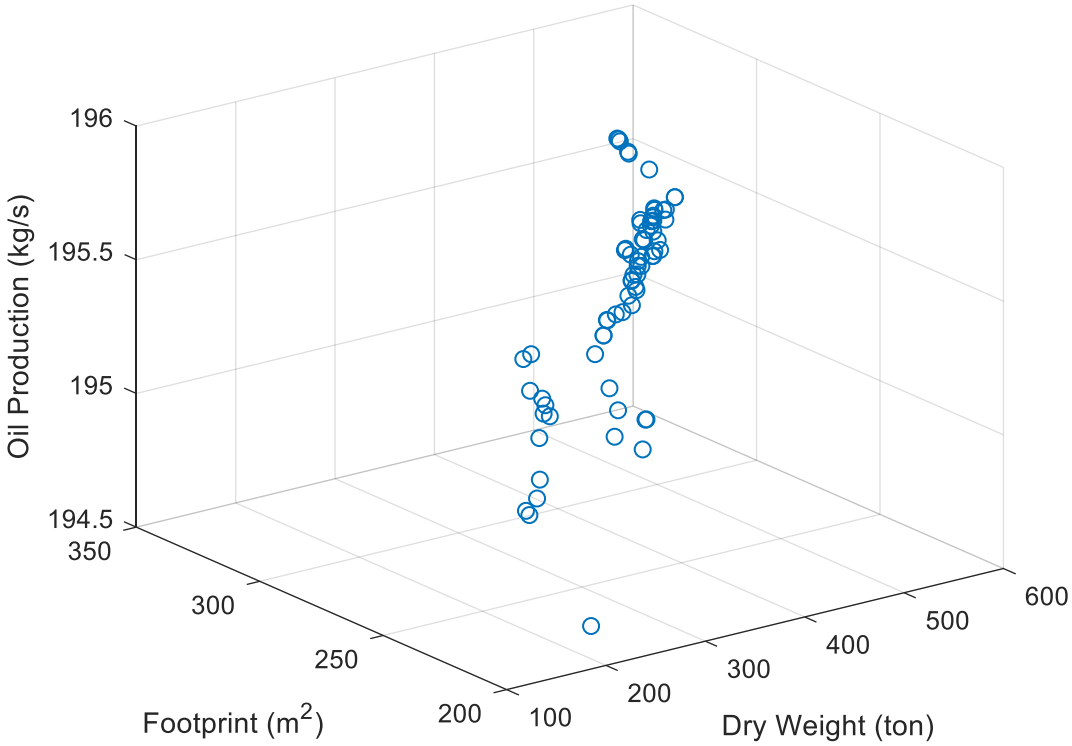

Figure 7-49: Boxplot of optimized inputs for fluid 2 oil section

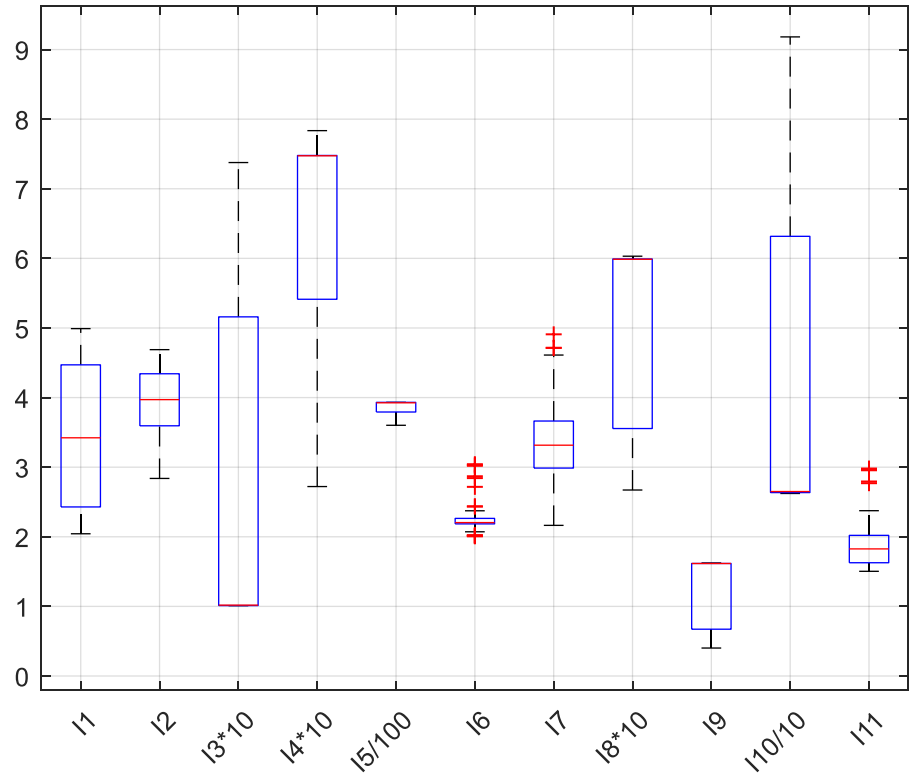

Figure 7-50: Relationship between oil production and equipment dry weight for fluid 2 oil section

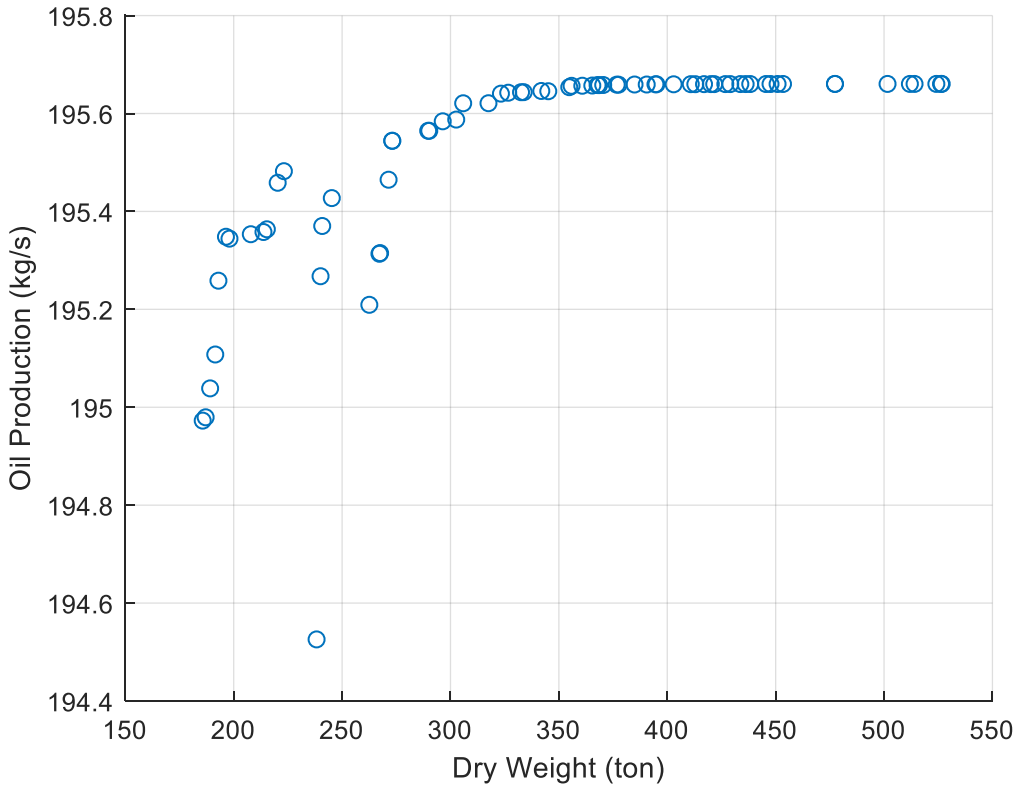

Figure 7-51: Relationship between oil production and equipment footprint for fluid 2 oil section

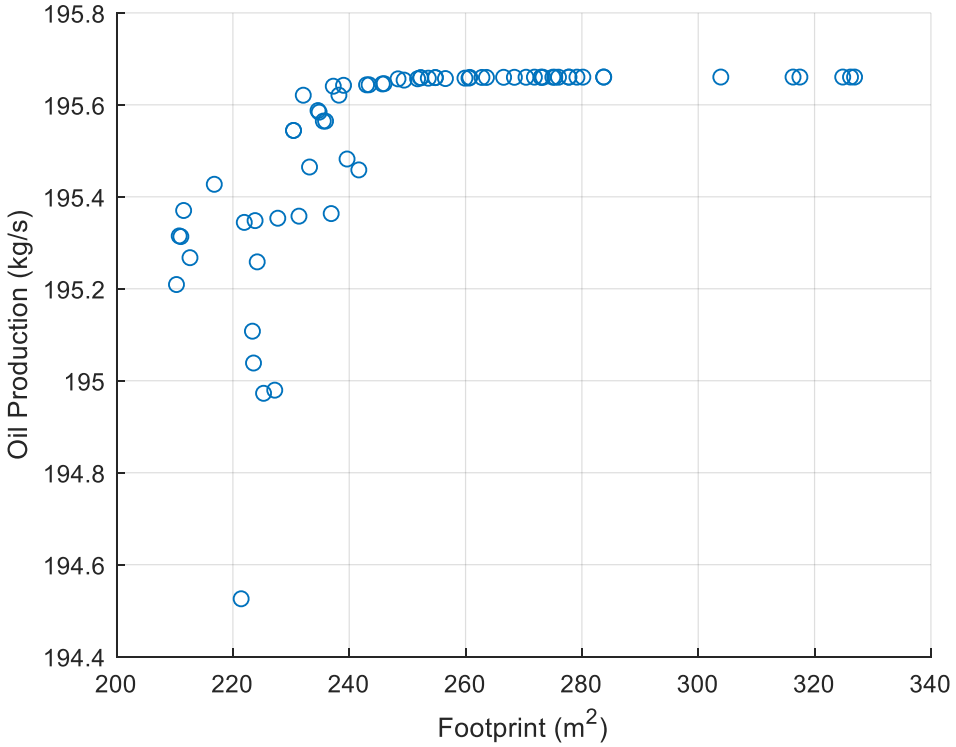

Figure 7-52: Relationship between equipment dry weight and footprint for fluid 2 oil section

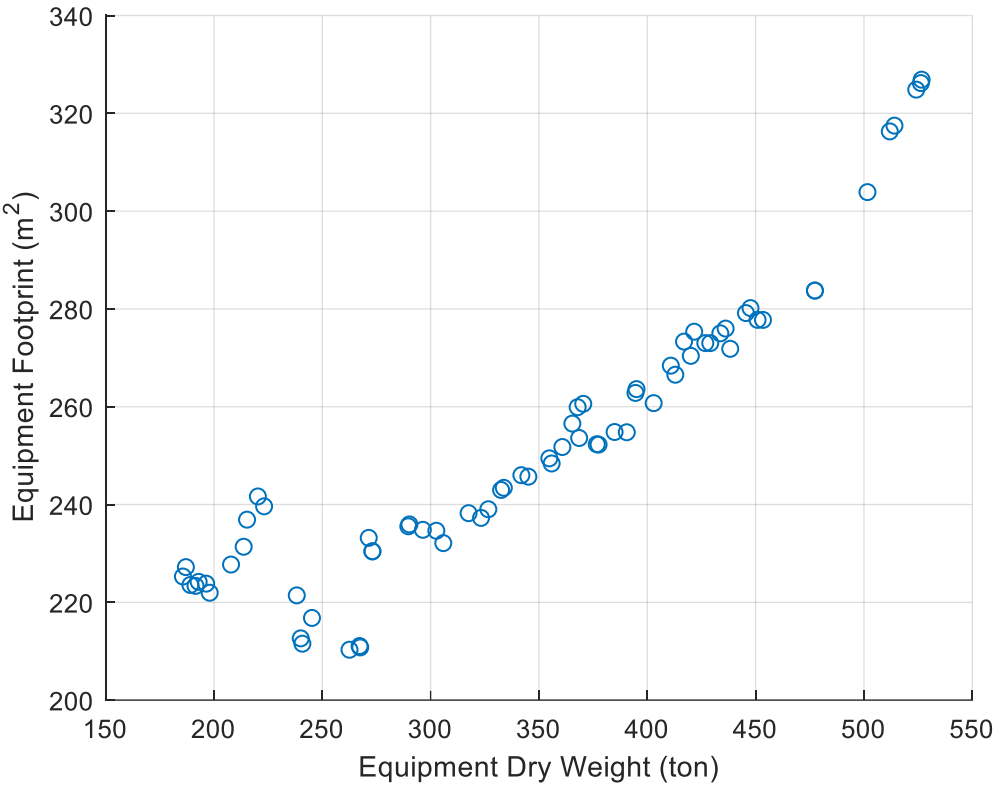

Figure 7-53: Equipment dry weight variation in fluid 2 oil section

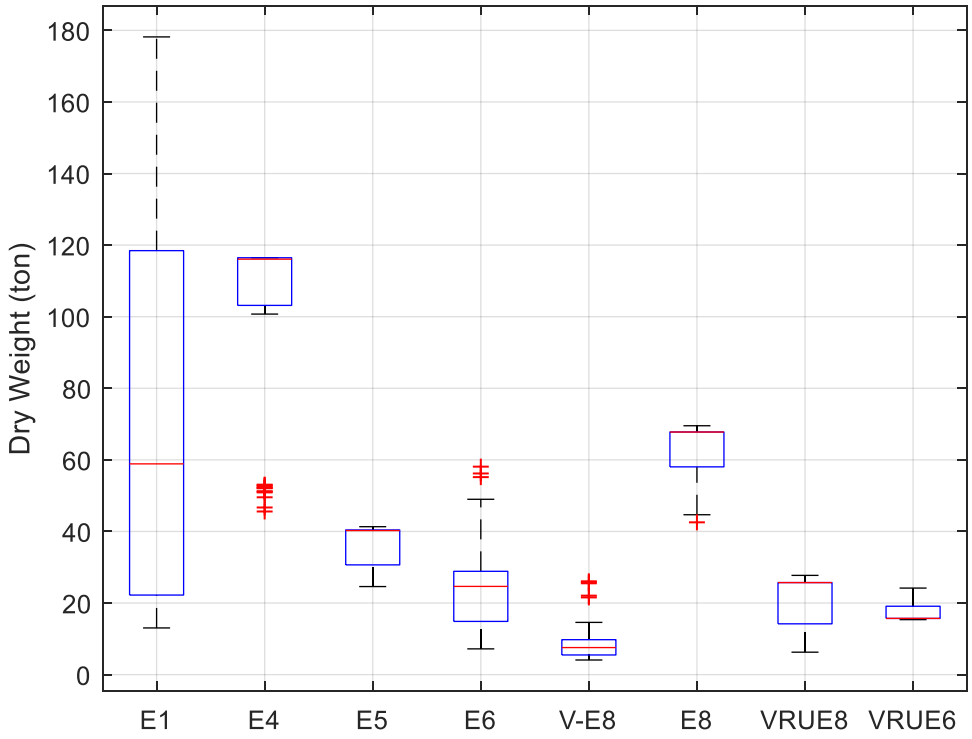

Figure 7-54: Equipment footprint variation in for fluid 2 oil section

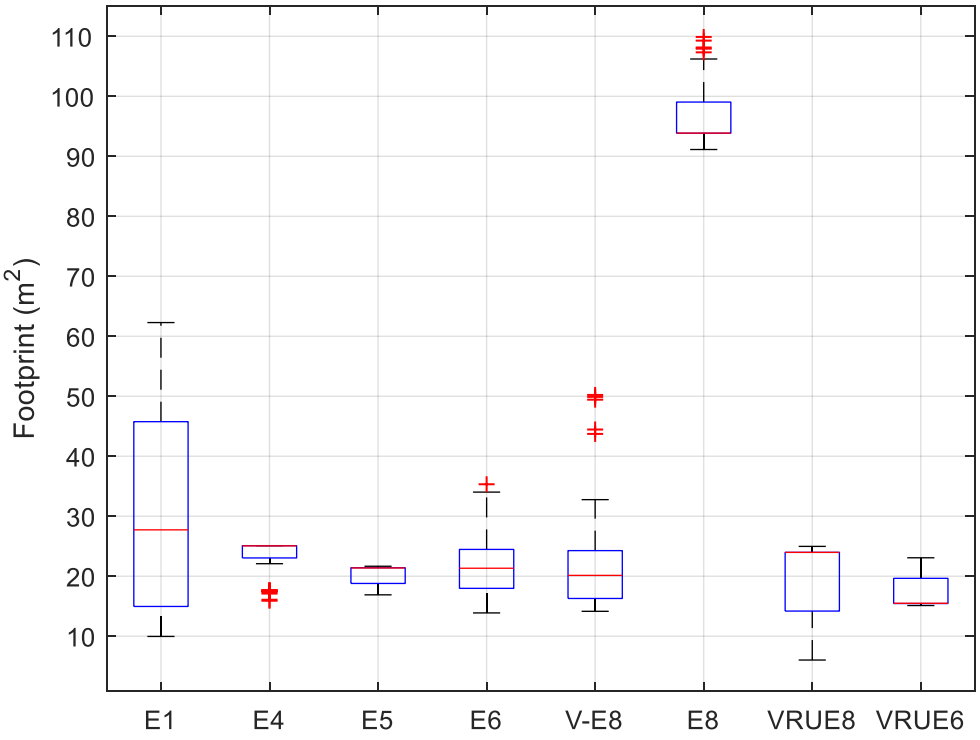

Figure 7-55: Deviation in RVP and BS&W specification for fluid 2 oil

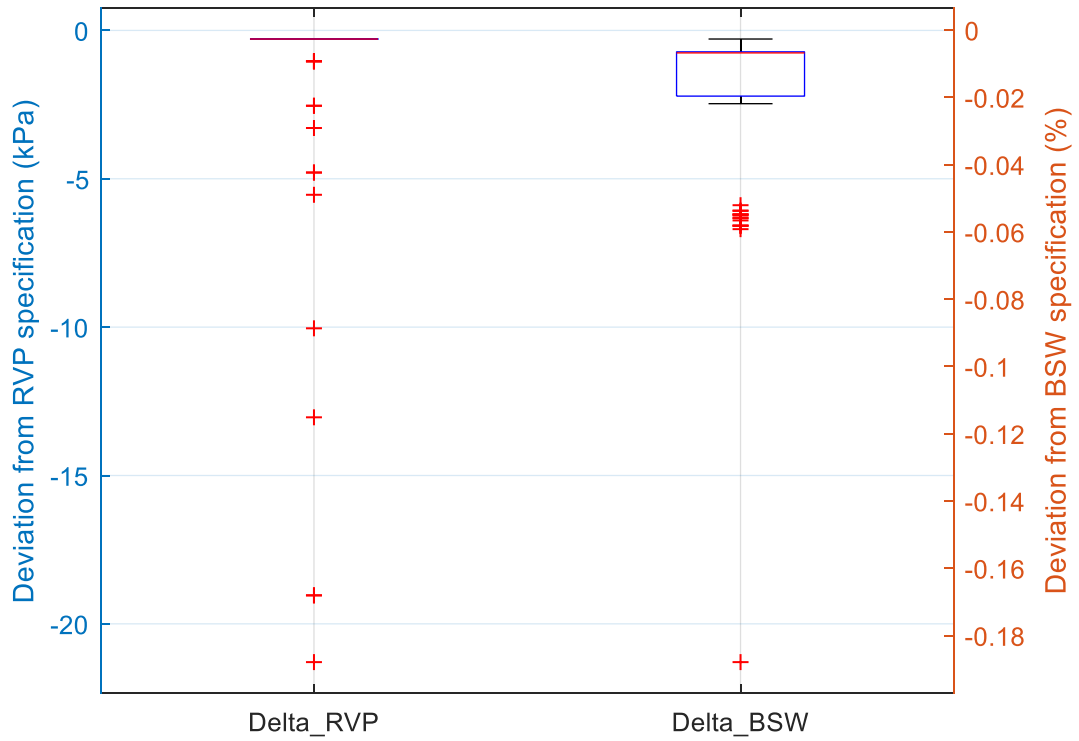

Figure 7-56: Energy demands for fluid 2 oil section

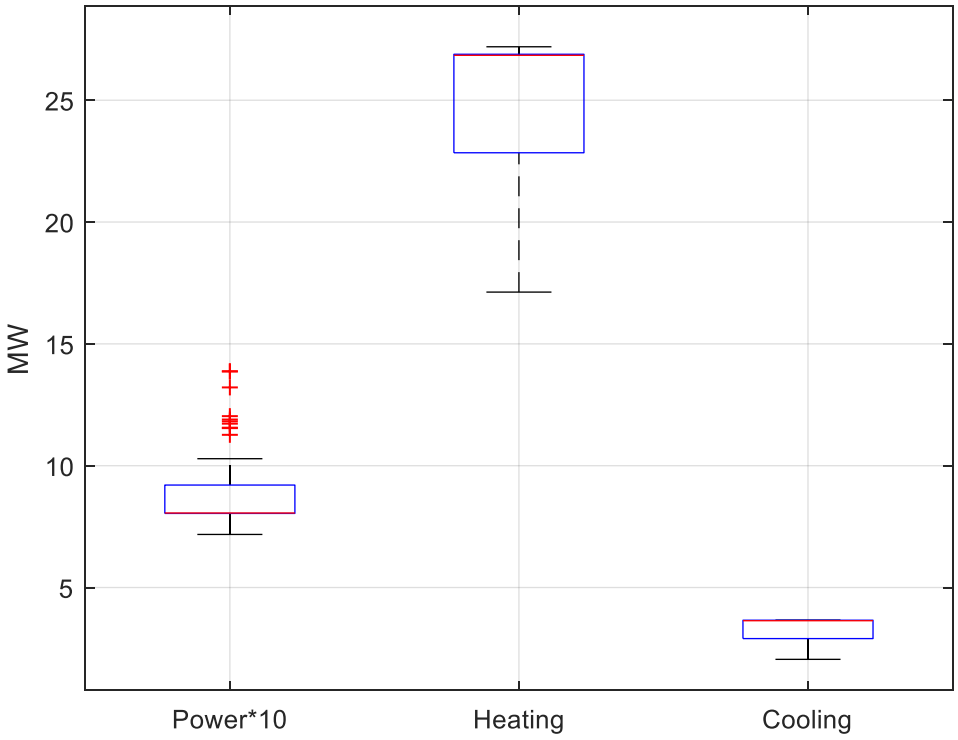

In order to assess the hypothesis of splitting the optimization between the oil and gas section, the characteristics of stream S14 have been extracted from the optimized oil section, as seen in the following figures.

Figure 7-57: Boxplot of S14 mass flowrate and temperature

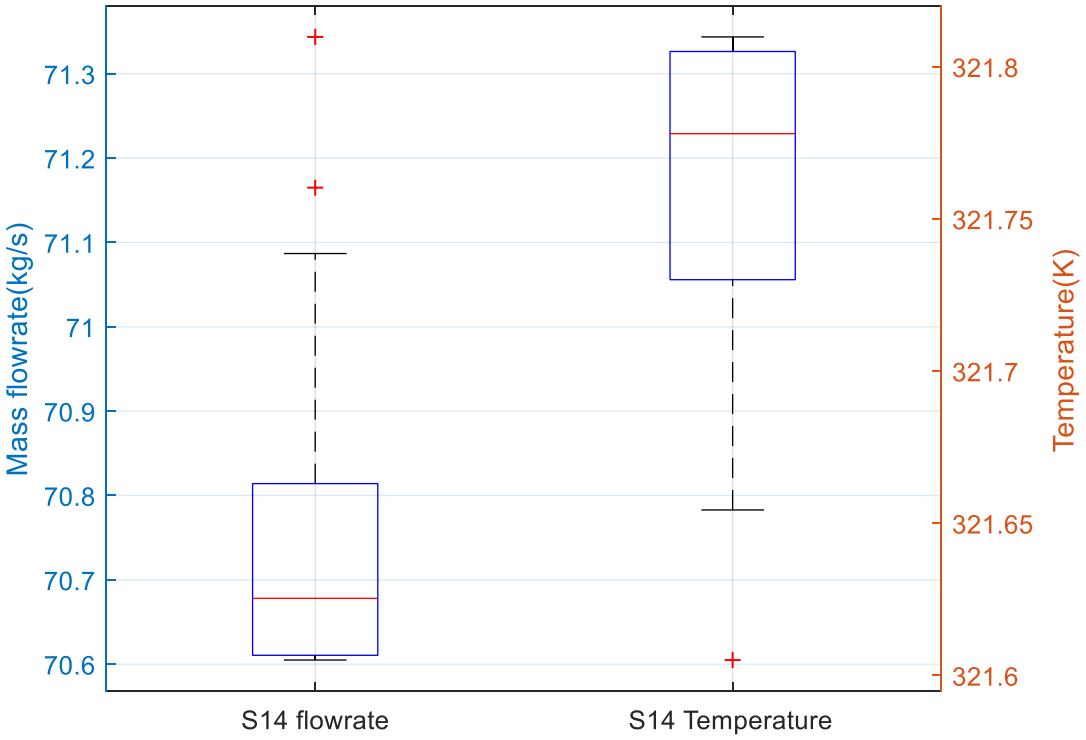

Figure 7-58: Boxplot of S14 methane and ethane molar fractions

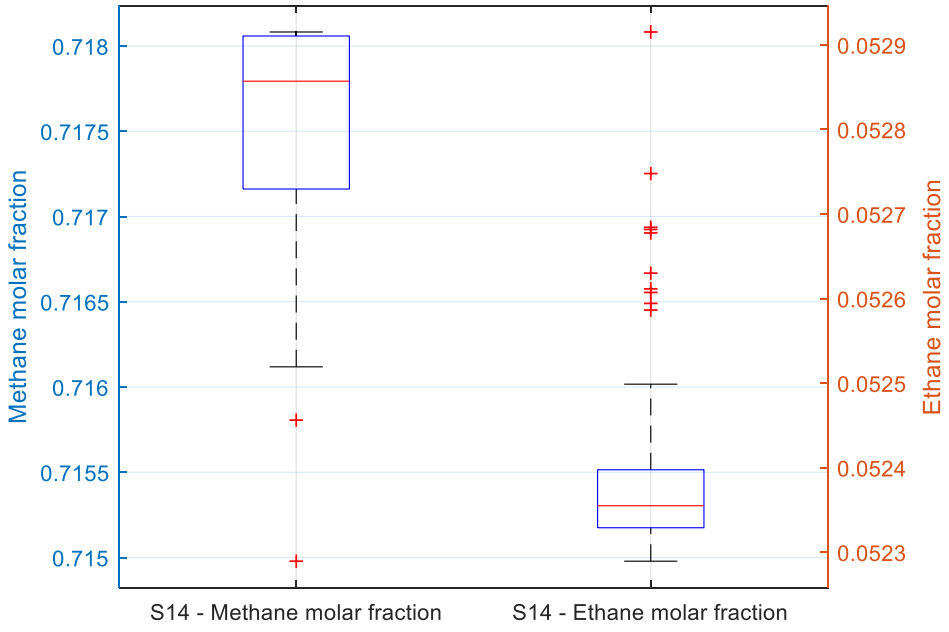

Figure 7-59: Boxplot of S14 propane, i-butane and n-butane molar fractions

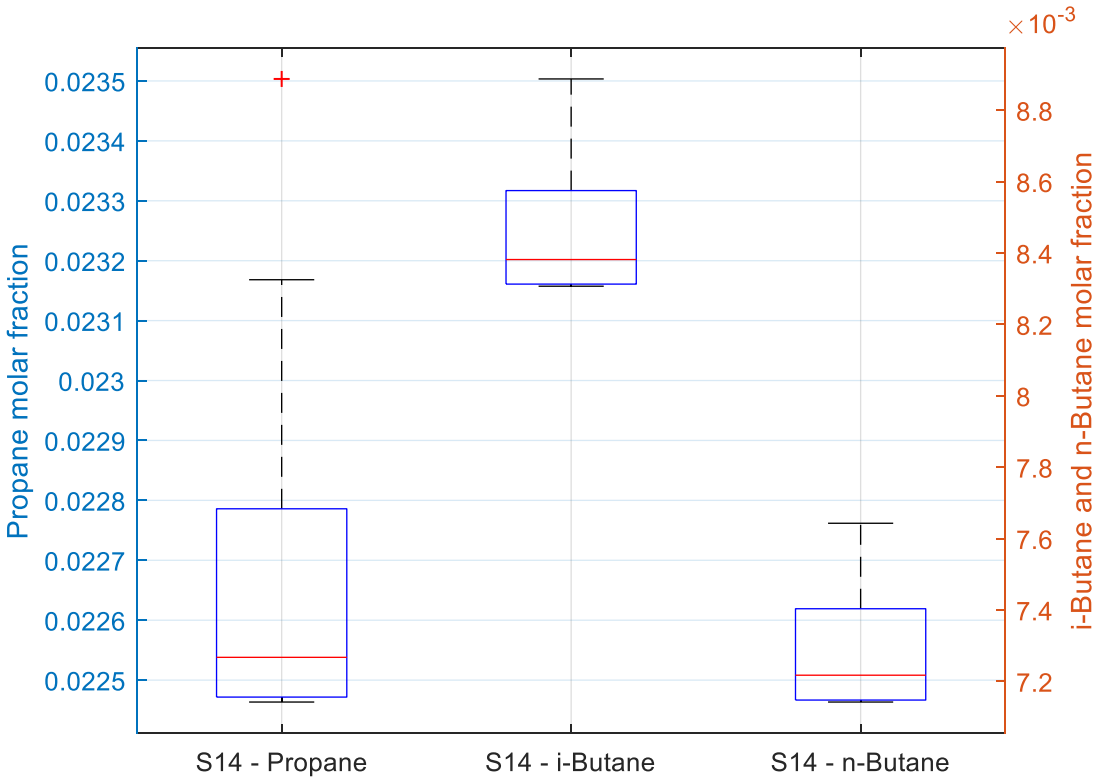

The pressure of S14 is constant and equal to E1 pressure, which is also constant. Figure 7-57 to Figure 7-59 show that variations of S14 mass flowrate, temperature, methane, ethane, propane, i-butane and n-butane compositions are very low. The molar fractions of other components also present very low variation. The relative standard deviation (ratio of standard deviation by the mean) shows the extent of variability in relation to the mean of the population, indicating if the variation of a certain parameter is significant. The relative standard deviation of each of the aforementioned S14 parameters is shown in Table 7-9.

All S14 parameters showed relative standard deviation lower than 1%, indicating that they are almost constant. Therefore, the optimization of F2 flowsheets can be performed in two steps: oil processing section optimization and gas processing section optimization.

Table 7-9: Relative standard deviation of certain S14 characteristics

Parameter	Relative standard deviation (%)
Mass flowrate	0.2400
Temperature	0.0149
Methane	0.0983
Ethane	0.0023
Propane	0.0102
i-Butane	0.0180
n-Butane	0.0194

The gas processing section optimization results are shown in the next charts for each of the processing schemes: F2F1, F2F2 and F2F3.

Starting with F2F1, the Pareto Front comprised of heating demand, equipment dry weight and footprint in shown in Figure 7-60 and. the two-dimensional relationships between such objectives are shown in Figure 7-61, Figure 7-62, and Figure 7-63.

Inputs have varied according to Figure 7-68:. Inputs I18 and I19 (pressure drop in the membrane stages) have not varied significantly, with majority of points between 0.89 and 0.90 for I18 and between 0.88 and 0.90 for I19. In addition, the TEG mass fraction (I21) in the export gas TEG system has not varied significantly. These three inputs will hardly explain any of the outputs variations. The membranes (E16B) performance variation is governed by the inlet pressure variation, which is a function of I13 and I14, the inlet temperature (I15) and the specific areas (I16 and I17).

The dry weight is driven by the molecular sieve (E17B), membrane system (E16B) and MEA (E16A), as seen in Figure 7-64, which also present the highest variations. The variation of the molecular sieve dry weight is driven by the variation of the level of pressurization in E-15 (I13), which governs the amount of water to be separated and the design pressure. In the pressure range resulted from variation of I13, increase of adsorption pressure increased the

molecular sieve system dry weight as additions in vessel dry weights (due to higher design pressure) were higher than savings due to lower amount of adsorbent (due to lower water load with pressure increase). The membrane system dry weight varies due to the variation of parameters I16 and I17 (membrane specific areas in first and second stages respectively), which govern the number of membrane elements. The MEA dry weight variation is governed by its inlet CO_2 concentration, which varied from approximately 0.035 to 0.060, as seen in Figure 7-65. As one of the optimization objectives is minimization of heating demand, when seeking for such objective the optimization algorithm will prioritize CO_2 separation in the membrane as the heating demand is much lower than the MEA system, leading to an increase of dry weight as the MEA system is lighter than the membrane system according to the equipment design methods adopted in this work. Other equipment presented high dry weight variations, but their dry weights are much lower than the molecular sieve, membrane system and MEA system. For instance, the dry weight of E19 varied from 0 ton (as in certain points of the Pareto Front no heating was necessary to prevent condensation within the membranes) to 12 ton. The E24 dry weight variation is governed by variation of inlet pressure and flowrate, which depends on the level of pressurization in E15 (I13) and the membrane specific areas (I16 and I17). The dry weight variation of E23 is governed by variations in membrane performance governed by inputs I15, I16 and I17, sending more or less CO_2 to be separated in the MEA system. The dry weight variation of E20 is driven by the level of pressurization in E15 (I13) and the level of depressurization in E18 (I14), which drives the inlet membrane pressure and the inlet pressure in E20. The E20 dry weight is also sensitive to the inlet flowrate, which is driven by the amount of reject generated by the membrane system that feeds the MEA system. The TEG dehydration units (export gas and CO_2 injection) dry weights mainly vary due to the variation of the inlet flowrates, which are dependent on the variation of the membranes performance.

The footprint is governed by the membrane system (E16B), which also presents high variation, as seen in Figure 7-66. Given the heating demand optimization objective, in order to minimize heating the optimization algorithm will prioritize

CO_2 separation in the membranes. On the other hand, to minimize footprint and dry weight, the optimization algorithm will favor CO_2 separation in the MEA system. These are the reasons explaining the variation of parameters I16 and I17, which governs the membrane skid footprint. The MEA system (E16A) footprint presented some variation as the parameters that influence footprint, according to Figure 6-35, also varied: inlet temperature from 296 K to 332 K, inlet CO_2 molar fraction from 0.035 to 0.06, and inlet mass flowrate from 42 kg/s to 51 kg/s. The footprint variations of compressors E20, E21, E24 and E23 are explained by the same reasons of dry weight. Although the dry weight variation of the molecular sieve is high, the footprint variation is low. The diameter of the adsorption vessel, the equipment with the highest footprint, is proportional to the cubic root of the adsorbent volume according to equation 6.11-2, so increasing the adsorbent volume will not lead to the same rate of increase of the diameter.

The total energy demands (power, heating, cooling) distributions are shown in Figure 7-72: and per equipment in Figure 7-73, Figure 7-74, and Figure 7-75.

Heating demand is driven by the MEA system, which also presents certain variation due to the variation of inlet CO_2 molar fraction and flowrate. Heating demand variation in the gas heater (E19) and molecular sieve (E17B) are also significant, respectively varying due to variation of I15 (inlet membrane temperature) and I13 (level of pressurization in E15, changing the water load to the dehydration unit). Heating demand in the CO_2 injection TEG system varies due to variation of CO_2 flowrate separated in the MEA system and heating demand in export hydrocarbon gas system varies due to variation of the hydrocarbon gas flowrate. Both flowrates depend on the level of CO_2 separation in the membrane system. Heating demand in the molecular sieve varies from 1.95 to 2.35 MW, driven by I13. Even though higher pressure decreases the water load and the amount of adsorbent, the adsorption vessel wall thickness increases, requiring more energy to heat the vessel, which ultimately increases the overall heating demand in the regeneration process when regeneration pressure (adopted as the same of adsorption pressure) increases.

Power demand is driven by compressors E15, E20 and E21, which cope with the highest flowrates and pressurizations. When CO_2 separation in the

membrane system is prioritized, power demand increases as pressure drop in the membrane system is much higher than the MEA system. Figure 7-67 shows such pattern, with power demand decreasing when heating demand increases. Power demands in compressors E23 (pre-compression for CO_2 rich stream from the MEA system) and E24 (pre-compression for CO_2 rich stream from the membrane system) are also significant, varying mainly due to variations of inlet flowrates, which vary due to the variation of membrane performance.

Cooling demand is driven by compressors E15, E20 and E21, as seen in Figure 7-75, as they present the highest power demands. Such demands vary due to the same reasons of power demand variations.

The hydrocarbon condensate flowrate generated by the hydrocarbon dew point control unit, shown in Figure 7-69, presented high variation, from 0.017 kg/s to 0.625 kg/s, explained by the high variations of inputs I13 (level of pressurization in E-15) and I14 (level of depressurization in the hydrocarbon dew point control unit). The higher the hydrocarbon condensate production the higher the power demand, so more liquid hydrocarbon can be produced at the expense of more energy. Anyway, part of the liquefied hydrocarbons may be vaporized when recycled to the oil section or stored at lower pressure. The amount of methane that has not permeated the membrane is known as methane recovery, as shown in Figure 7-70: , indicating that specified hydrocarbon gas production, as seen in Figure 7-71, significantly varies due to variation of the membranes performance.

Flowsheet F2F1 was also optimized using all the 14 initial inputs to verify benefits from the screening analysis. Such optimization took 87.2 hours whilst the optimization with the 11 screened inputs took 85.7 hours, only 1.8% time reduction. Best results were 1,123 m^2 equipment footprint, 2,793 ton equipment dry weight and 9.5 MW heating demand. In the optimization involving only the screened inputs, best results were 1,150 m^2 equipment footprint, 2,696 ton equipment dry weight and 8.6 MW heating demand. Results are similar, but it can be claimed that reducing the number of inputs led to both time reduction (could be higher if optimization tolerance was lower) and improvement of two objectives.

Figure 7-60: Pareto Front for F2F1 gas processing section

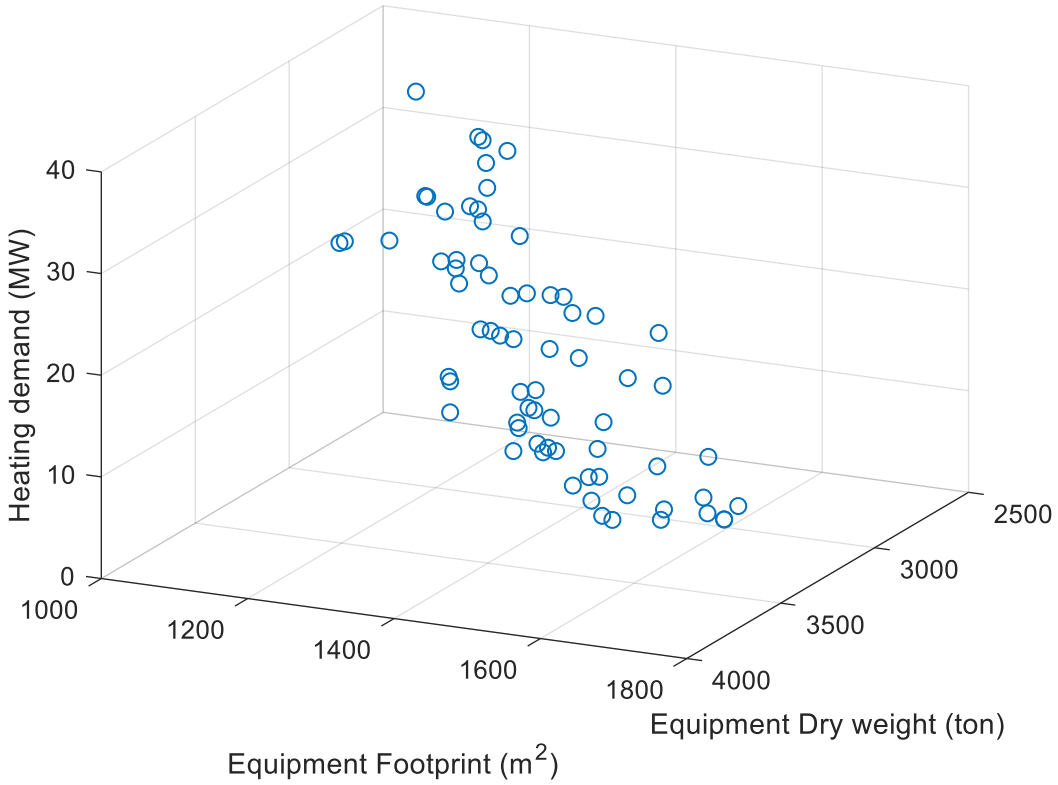

Figure 7-61: Equipment footprint x dry weight in F2F1 gas processing section

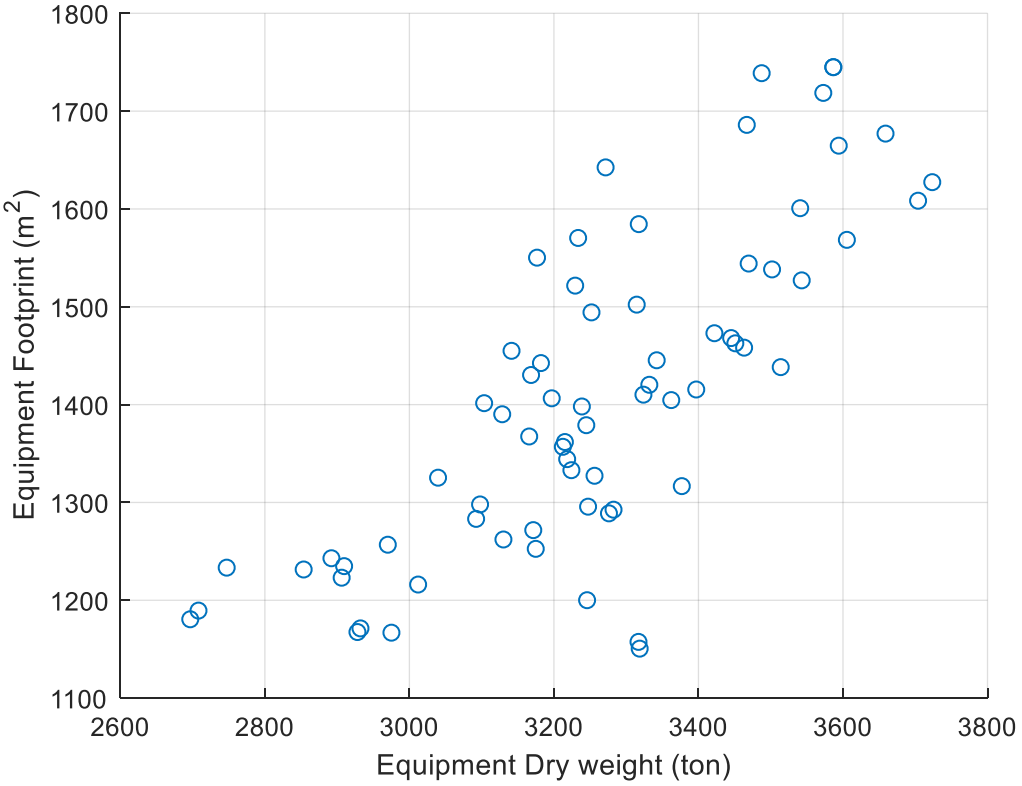

Figure 7-62: Equipment dry weight x heating demand in F2F1 gas processing section

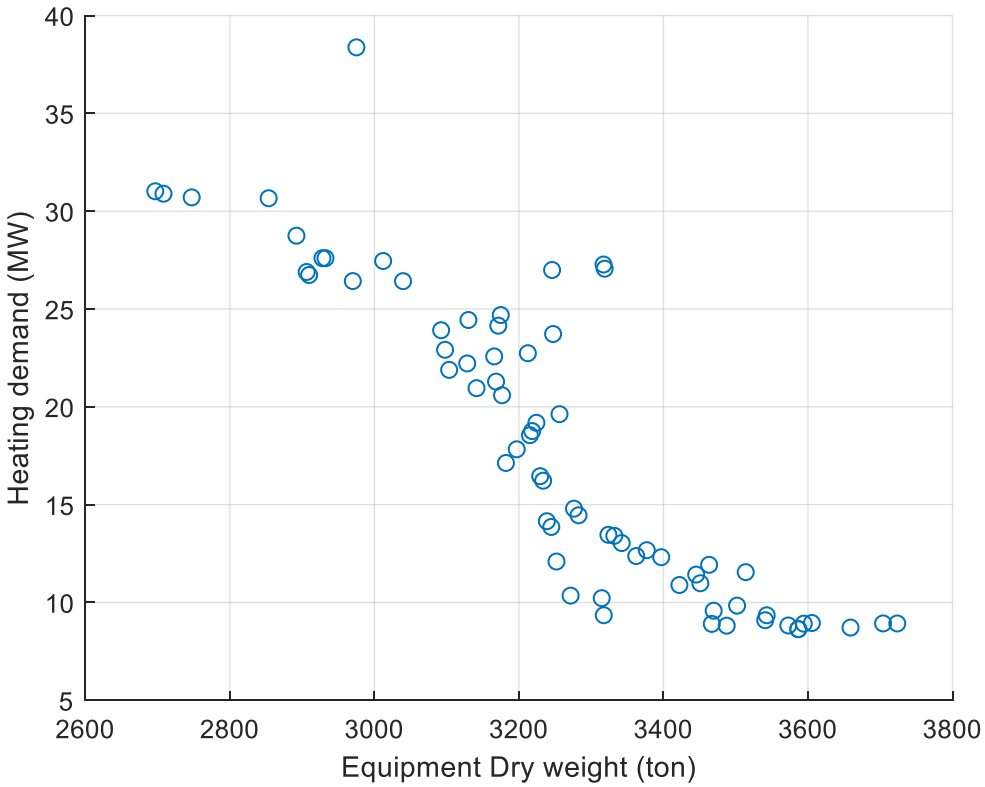

Figure 7-63: Equipment footprint x heating demand in F2F1 gas processing section

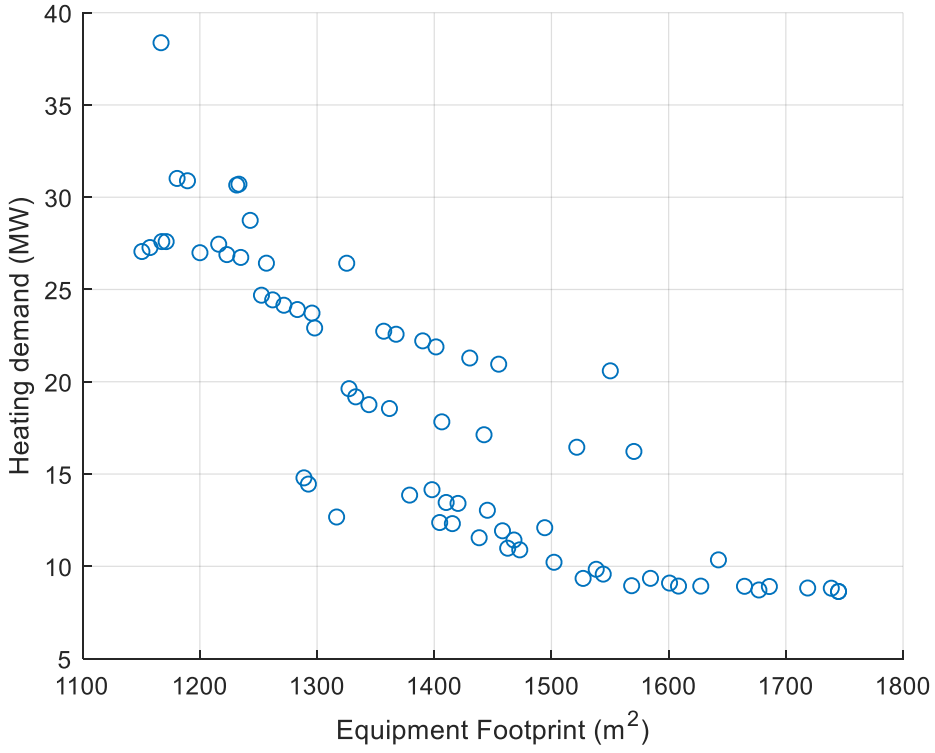

Figure 7-64: Equipment dry weight variation in F2F1 gas processing section

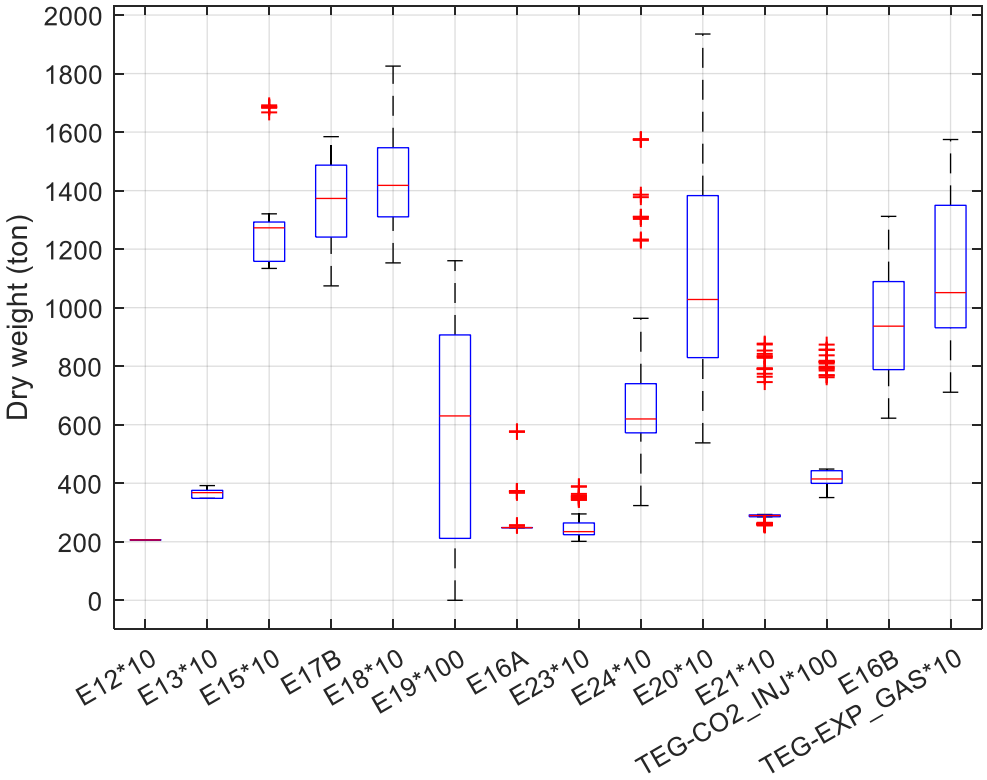

Figure 7-65: Influence of CO_2 molar fraction at MEA inlet in total equipment dry weight

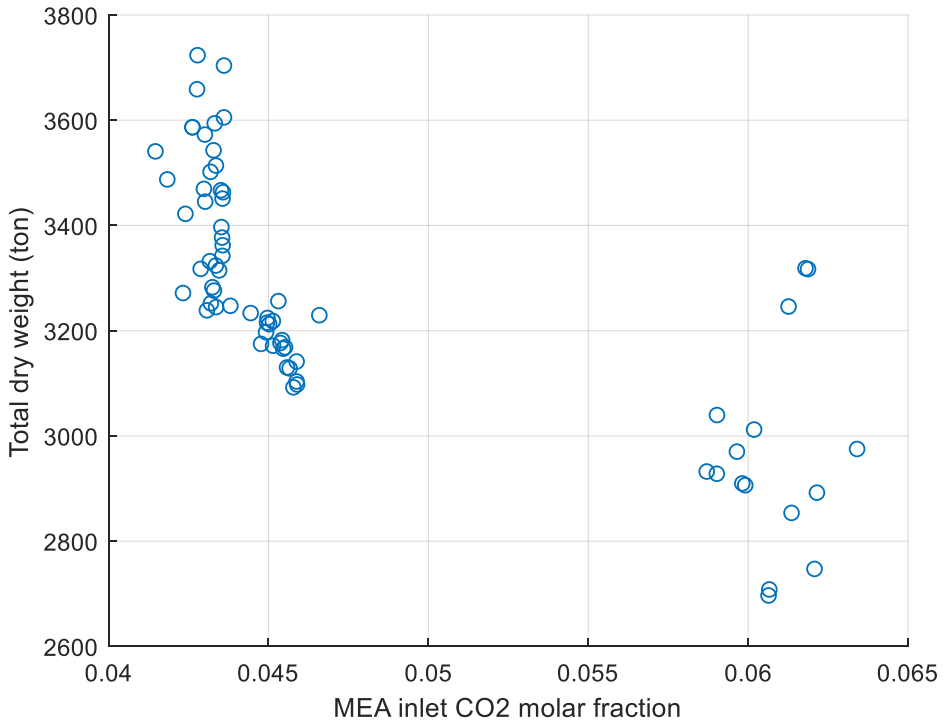

Figure 7-66: Equipment footprint variation in F2F1 gas processing section

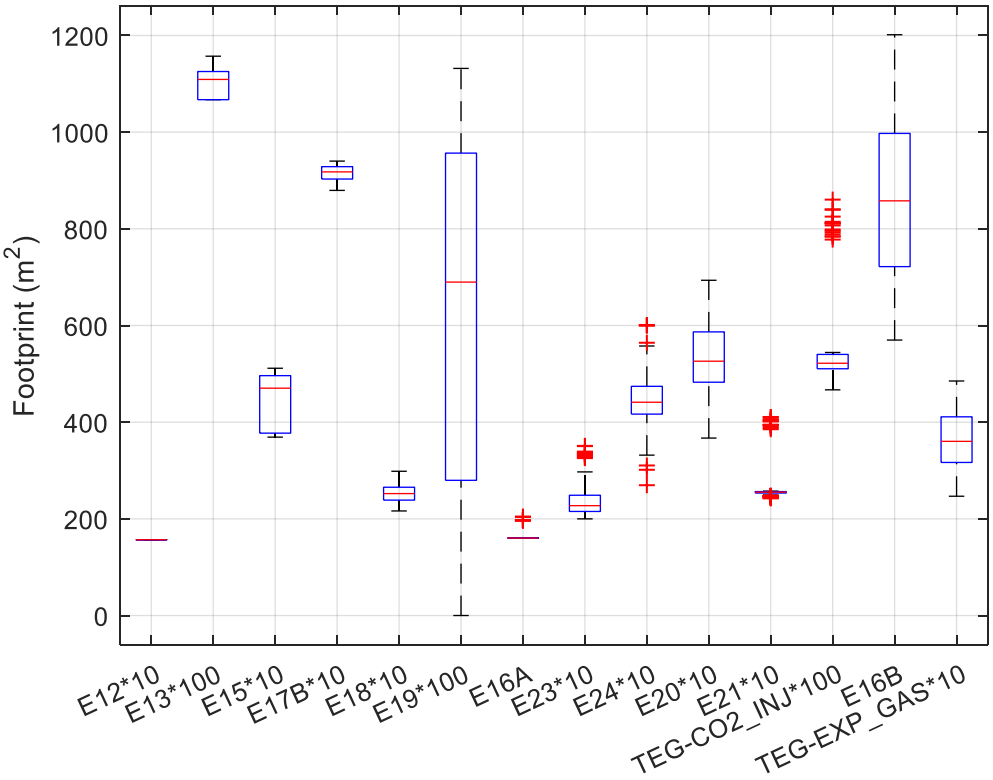

Figure 7-67: Heating demand x Power demand in F2F1 gas processing section

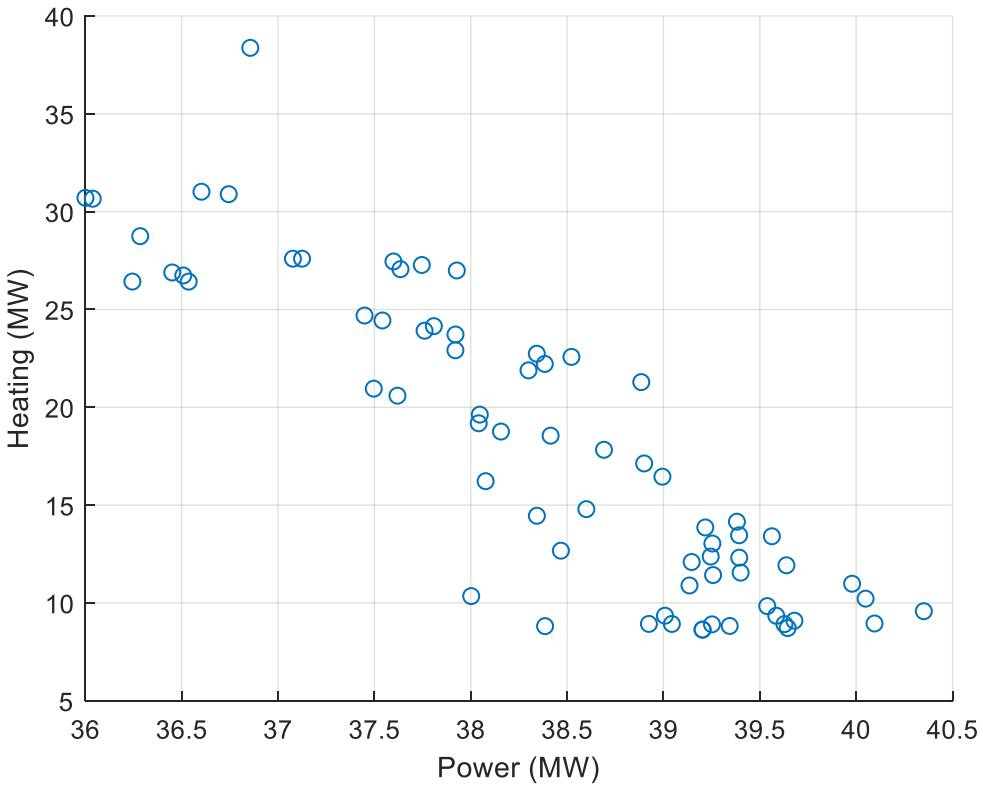

Figure 7-68: Variation of inputs in F2F1 gas processing section optimization

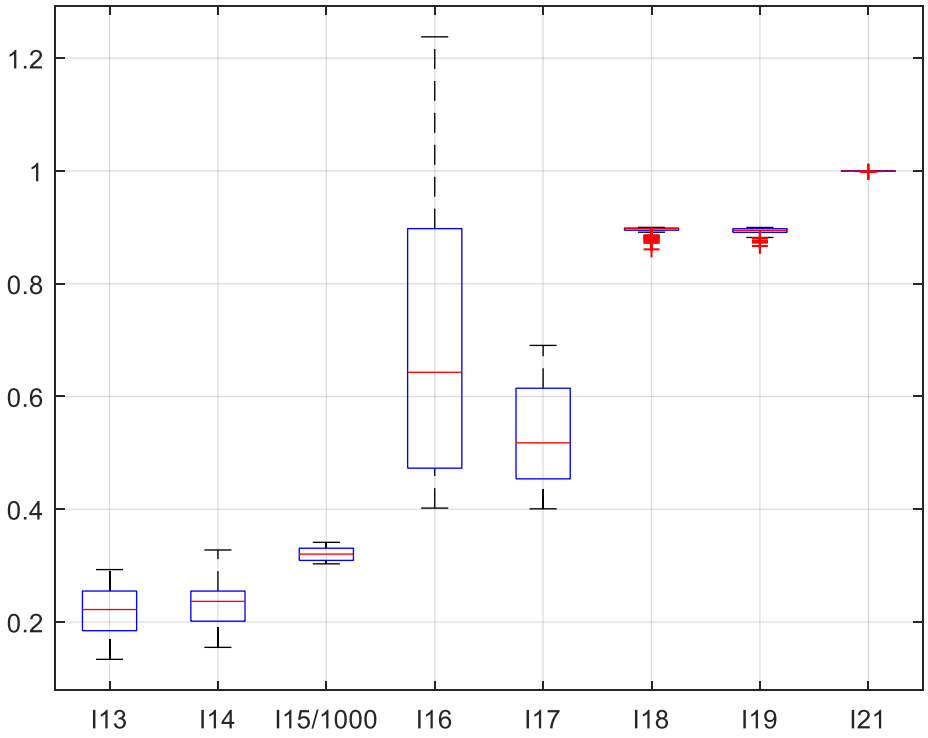

Figure 7-69: S16 mass flowrate distribution in F2F1 gas processing section optimization

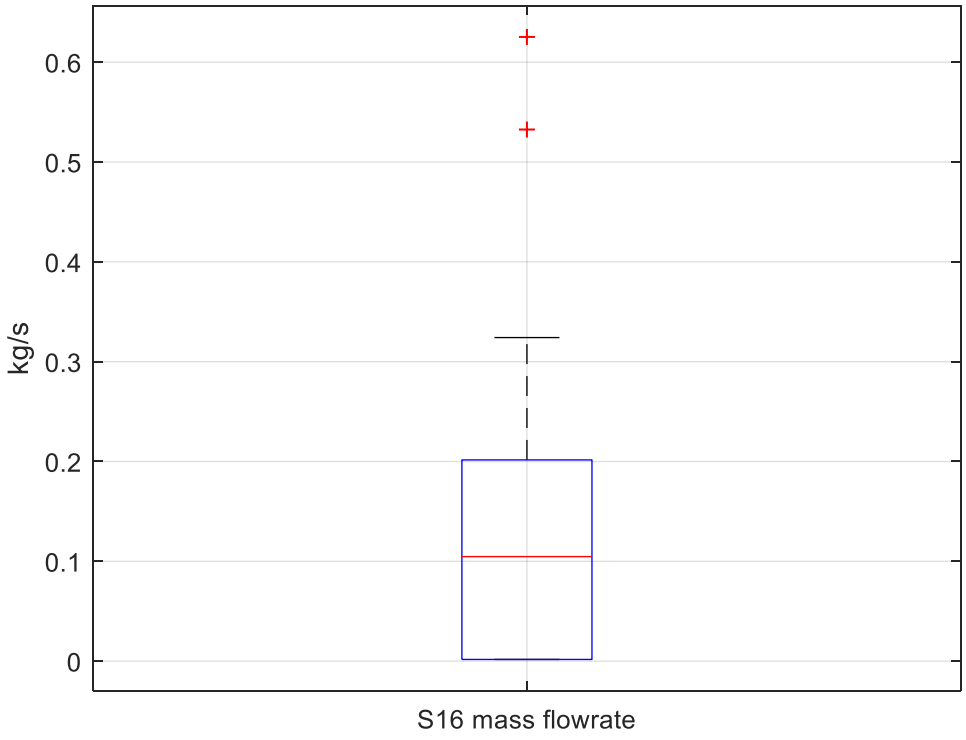

Figure 7-70: Methane recovery in reject stream (S33) of membrane system in F2F1 gas processing section optimization

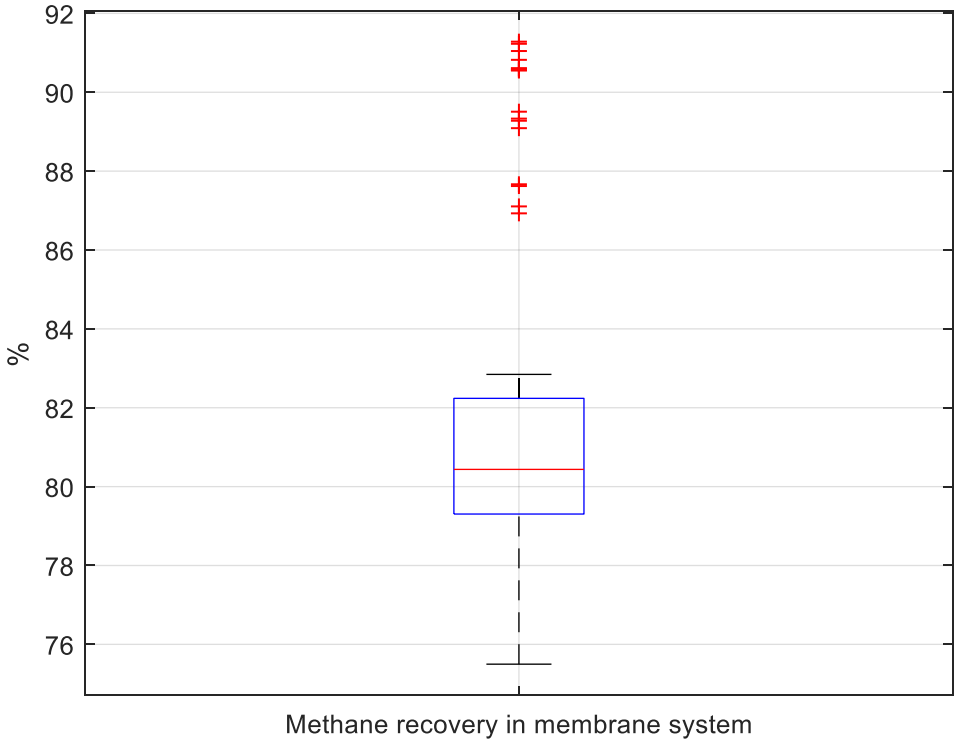

Figure 7-71: Specific gas mass flowrate distribution in F2F1 gas processing section

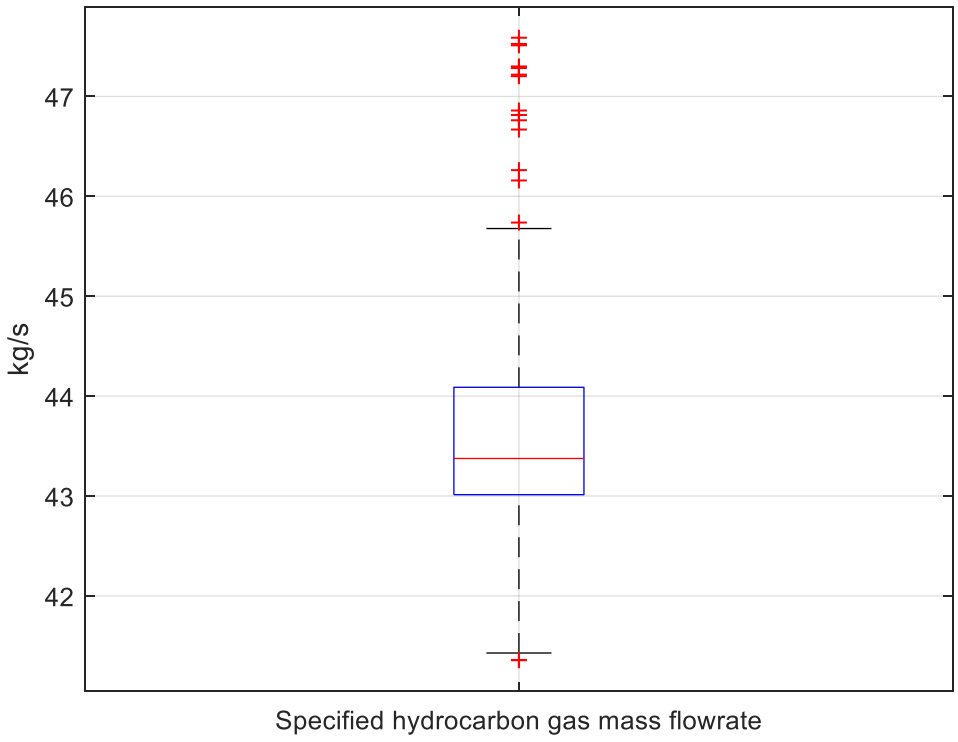

Figure 7-72: Energy demands in F2F1 gas processing section

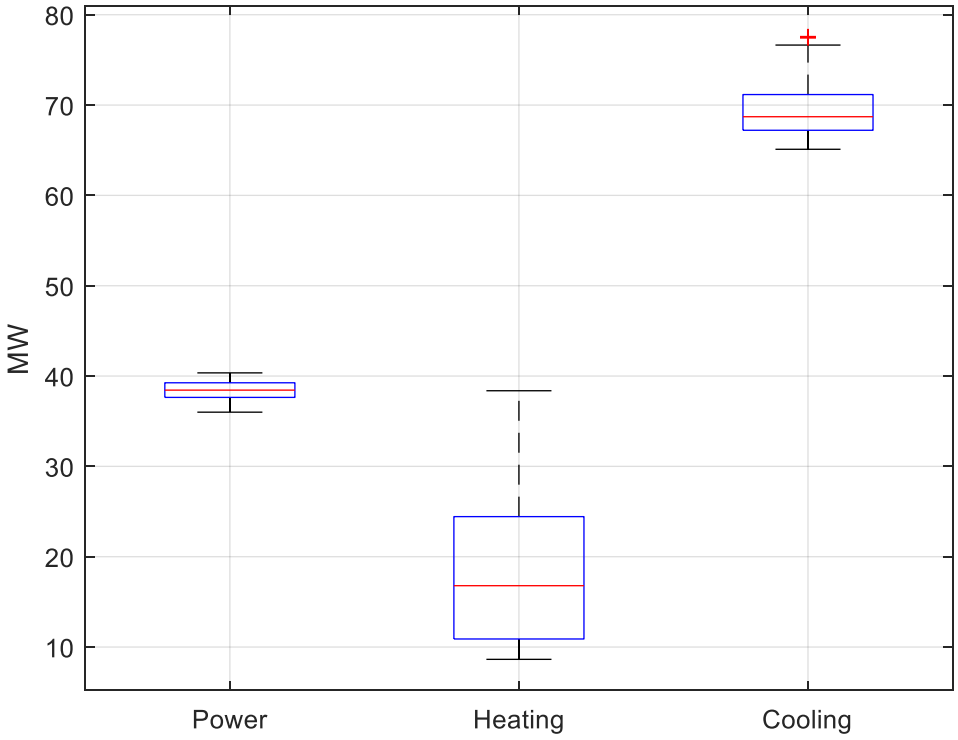

Figure 7-73: Heating demand variation in F2F1 gas processing section

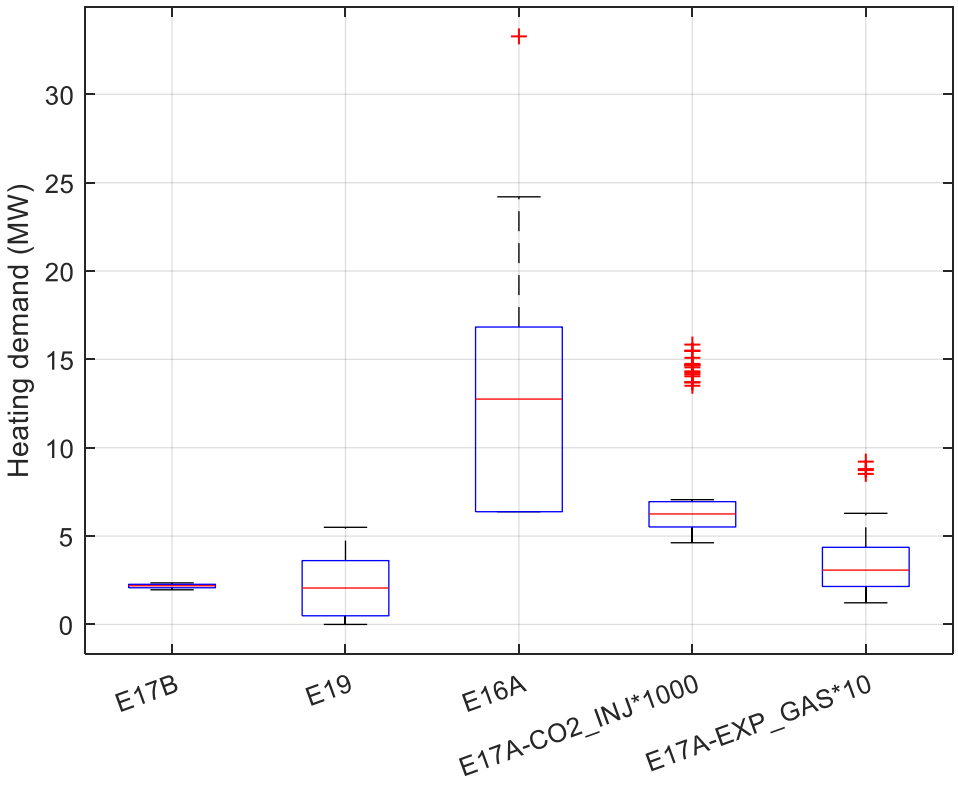

Figure 7-74: Power demand variation in F2F1 gas processing section

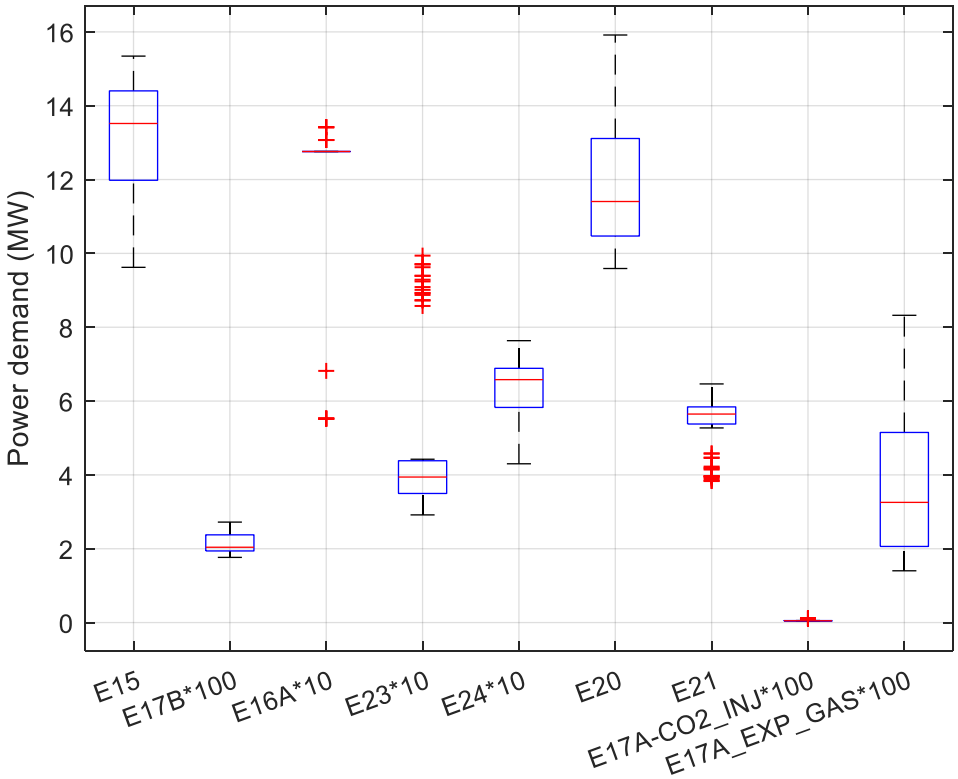

Figure 7-75: Cooling demand variation in F2F1 gas processing section

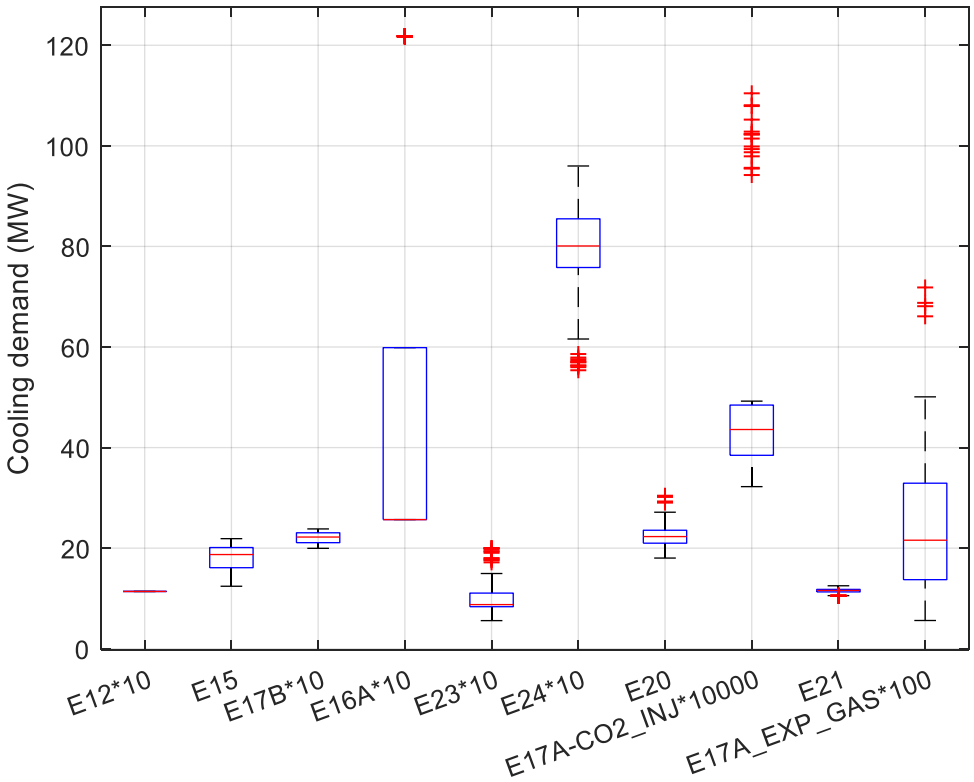

The Pareto Front comprised of heating demand, equipment dry weight and footprint in shown in Figure 7-76 for F2F2. The two-dimensional relationships between such objectives are shown in Figure 7-77, Figure 7-78, and Figure 7-79.

The equipment dry weight tends to grow with increase of equipment footprint, but in certain cases such pattern is not seen. Heating demand falls in an asymptotic pattern with increase of equipment dry weight or footprint.

Inputs varied according to Figure 7-80. Inputs I18 and I19 (pressure drop in the membrane stages) have not varied significantly, with majority of points between 0.893 and 0.90 for I18 and between 0.89 and 0.90 for I19. Therefore such inputs will hardly explain variation of any of the outputs.

The equipment dry weight is driven by the membrane system (E16A) and the molecular sieve (E17B), as seen in Figure 7-81. The membrane system dry weight is governed by variation of I15, I16 and I17, and molecular sieve dry weight variation is driven by I13, varying the water load to the unit and its design pressure. Within the pressure range resulting from I13 variation, the molecular sieve dry weight showed a maximum at 0.4 (which leads to a pressure of approximately 112 bar), and then decreases. Other equipment presented relevant variation, such as the compressors, dew point control unit and gas heater. The dew point control unit dry weight variation is driven by I15 variation, since higher inlet membrane temperature will require less cooling in the unit. The gas heater dry weight variation is driven by I15 variation, as higher inlet membrane temperature will require more heating in E19..

The equipment footprint is also driven by the membrane system (E16A), as seen in Figure 7-82. The total membrane area increases when inlet temperature (I15) decreases, as seen in Figure 7-83. As heating is one of the optimization objectives, the optimization algorithm will explore the region where heating is minimum, which requires increase of membrane area. The molecular sieve (E17B) footprint variation is not negligible, explained by variation of I13, which varies water load and design pressure. The footprint has a maximum of 99.6 m^2 at I13 equal to 0.35 (101 bar) and a minimum of 86.3 m^2 at I13 equal to 0.5 (134

bar), showing the opposite effects of reduced water load and increase design pressure when pressure increases.

The variation of heating demand is mainly explained by variation of membrane inlet temperature (I15), which varied from 307 K to 338 K. Even though the heat exchange in E19 significantly varies, its footprint and dry weight are not responsible for the main variation of total equipment footprint and dry weight, which is explained by the membrane system.

The relationship between heating and power demand is seen in Figure 7-84. There is a peak in power demand when heating demand is between 3 MW and 4 MW, where the level of depressurization in the hydrocarbon dew point control unit (I14) and the level of pressurization in E-15 (I13) peak, according to Figure 7-85, increasing power demand.

Hydrocarbon condensate flowrate in the hydrocarbon dew point control unit is shown in Figure 7-86, presenting high variation between minimum (0.1265 kg/s) and maximum (2.7956 kg/s), caused by the variations of inputs I13 and I14.

Methane recovery in the membrane system is shown in Figure 7-88, explaining the variation of specified hydrocarbon gas as seen in Figure 7-87.

Power demand is driven by compressors E15, E20 and E21, which also present the highest variations, according to Figure 7-91. The membrane performance influences power demand in E20 and E21 since methane recovery varies, changing the flowrates of reject and permeate streams. Variation of input I13 influences power demand in E15. The power demand variation directly influences compressors dry weight and footprint, as seen in Figure 7-81 and Figure 7-82.

Cooling demand is also governed by compressors E15, E20 and E21, as seen in Figure 7-92, and the reasons explaining the variations are the same as power demand.

Figure 7-76: Pareto Front for F2F2 gas processing section

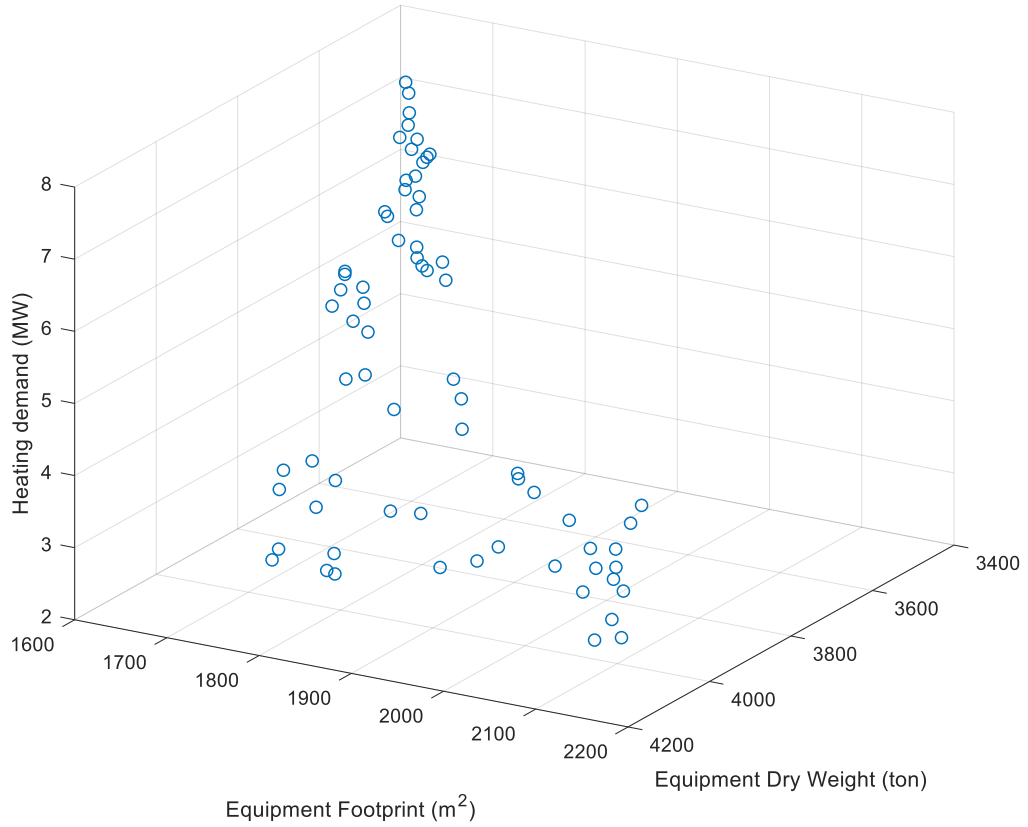

Figure 7-77: Equipment footprint x dry weight for F2F2 gas processing section

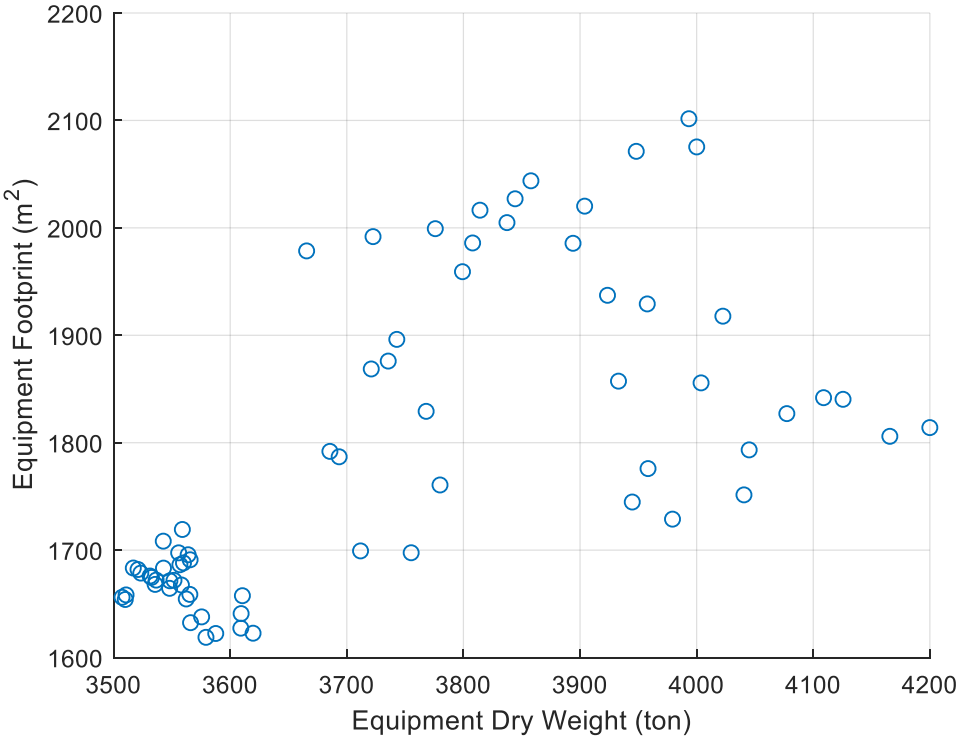

Figure 7-78: Equipment dry weight x heating demand for F2F2 gas processing section

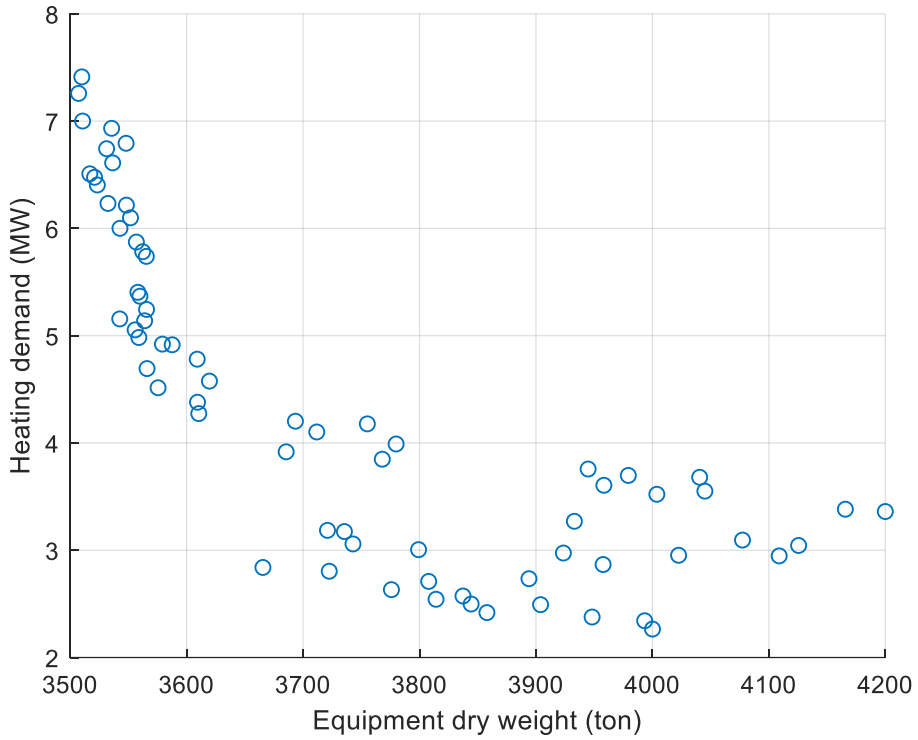

Figure 7-79: Equipment footprint x heating demand for F2F2 gas processing section

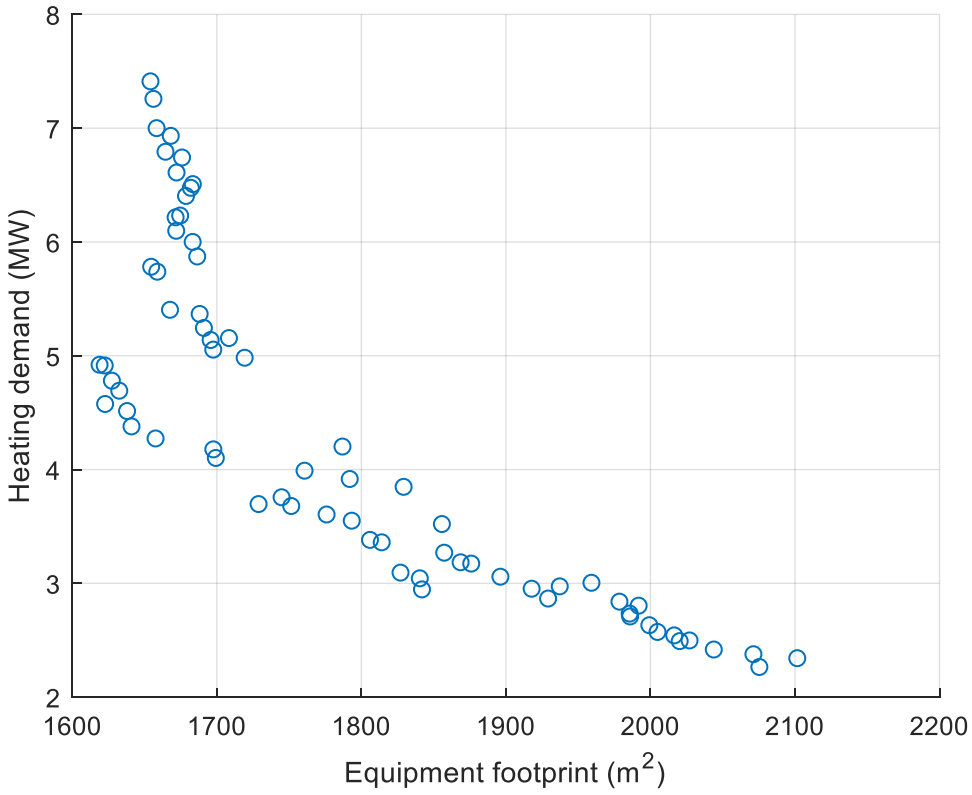

Figure 7-80: Inputs variation in F2F2 gas processing section

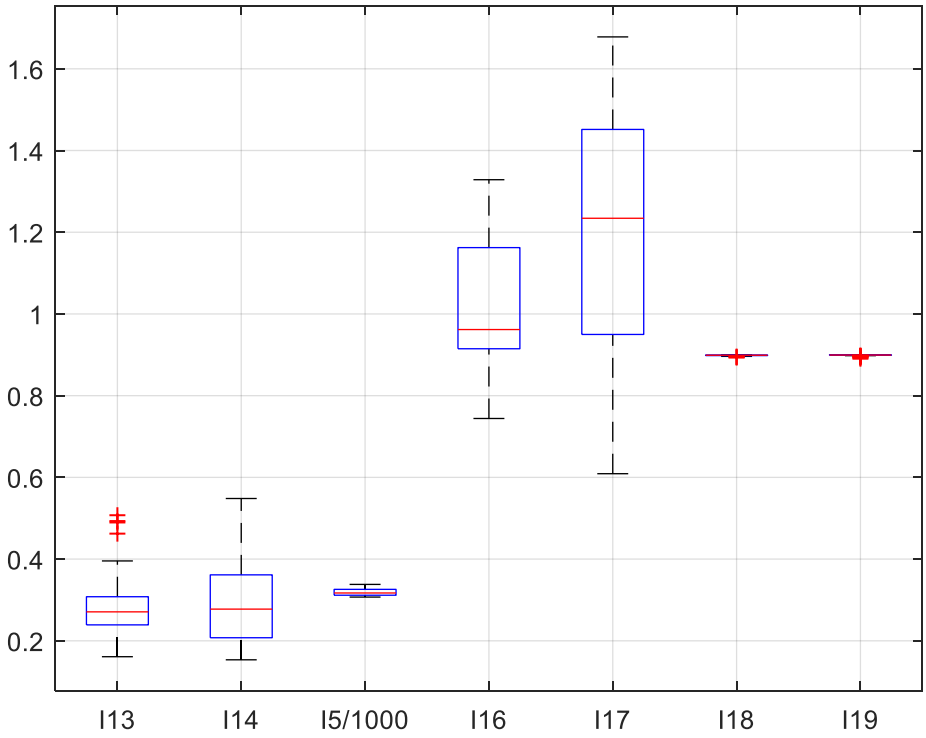

Figure 7-81: Equipment dry weight variation in F2F2 gas processing section

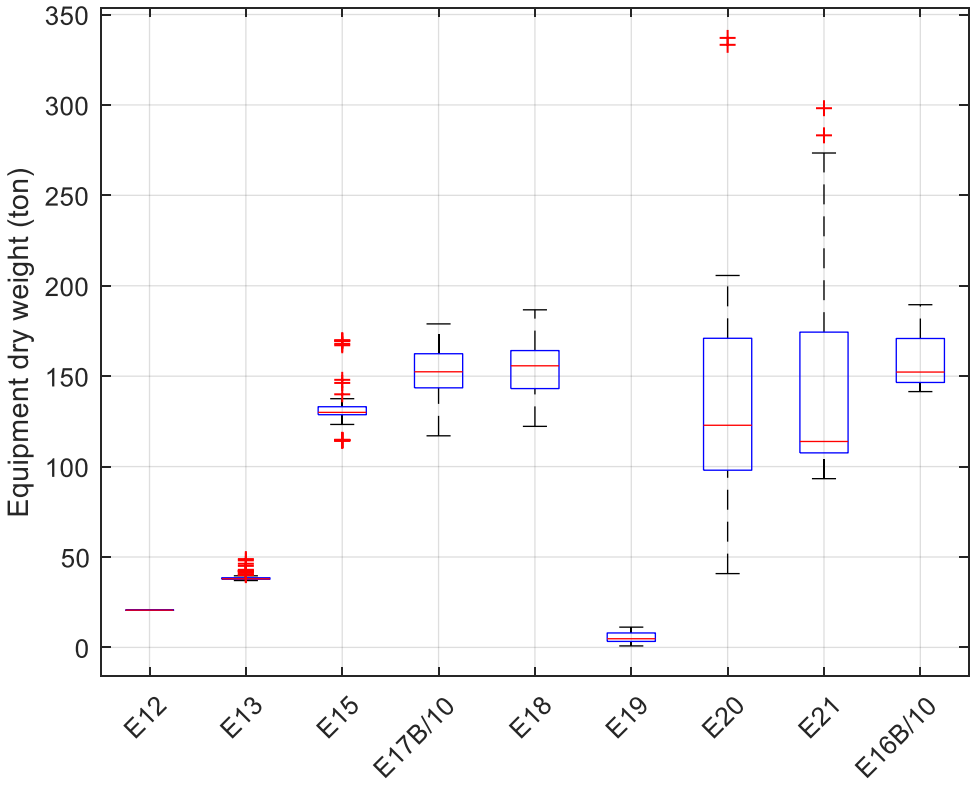

Figure 7-82: Equipment footprint variation in F2F2 gas processing section

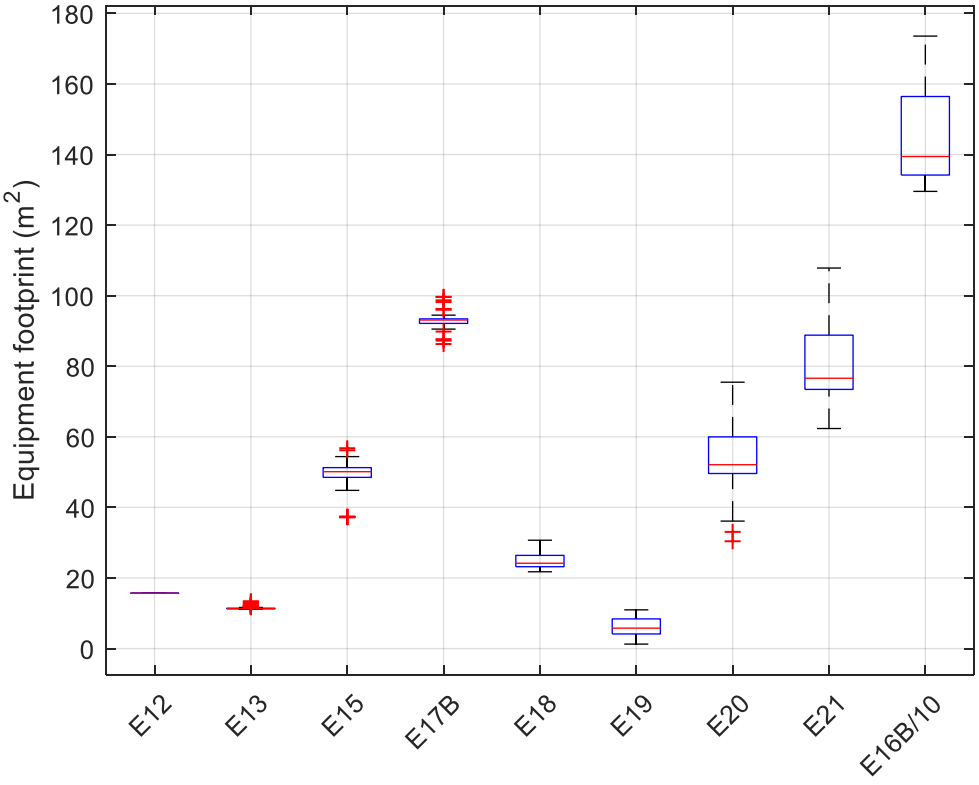

Figure 7-83: Membrane skid areas as function of membrane inlet temperature

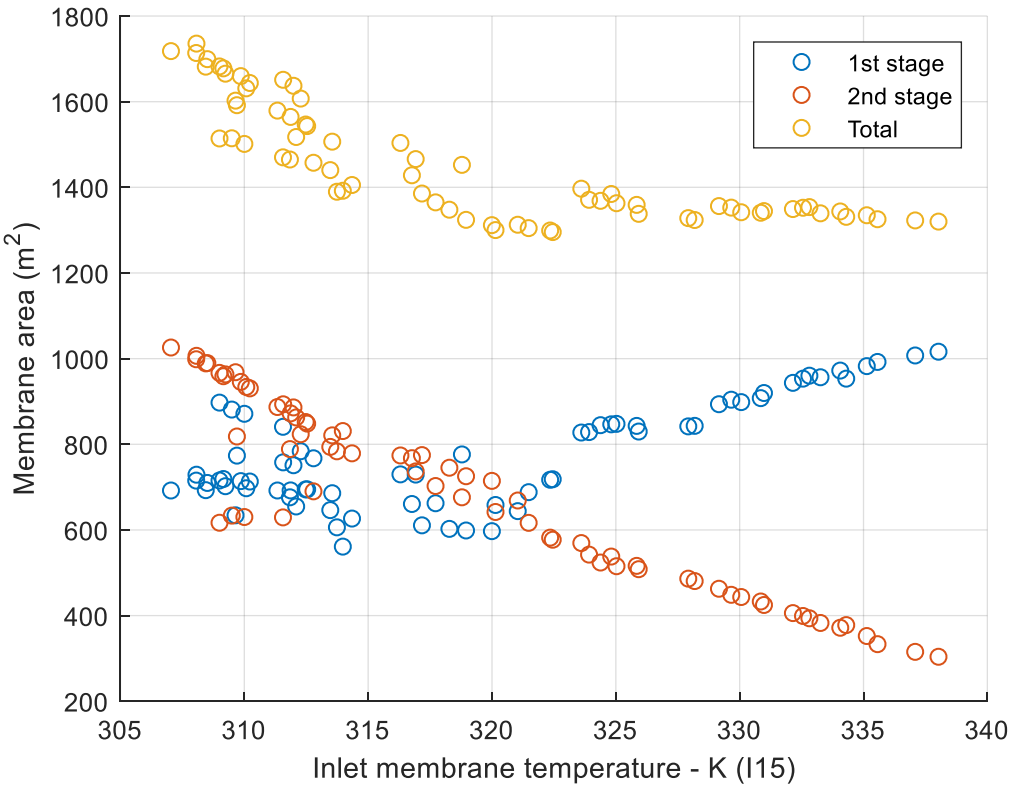

Figure 7-84: Heating demand x Power demand for F2F2 gas processing section

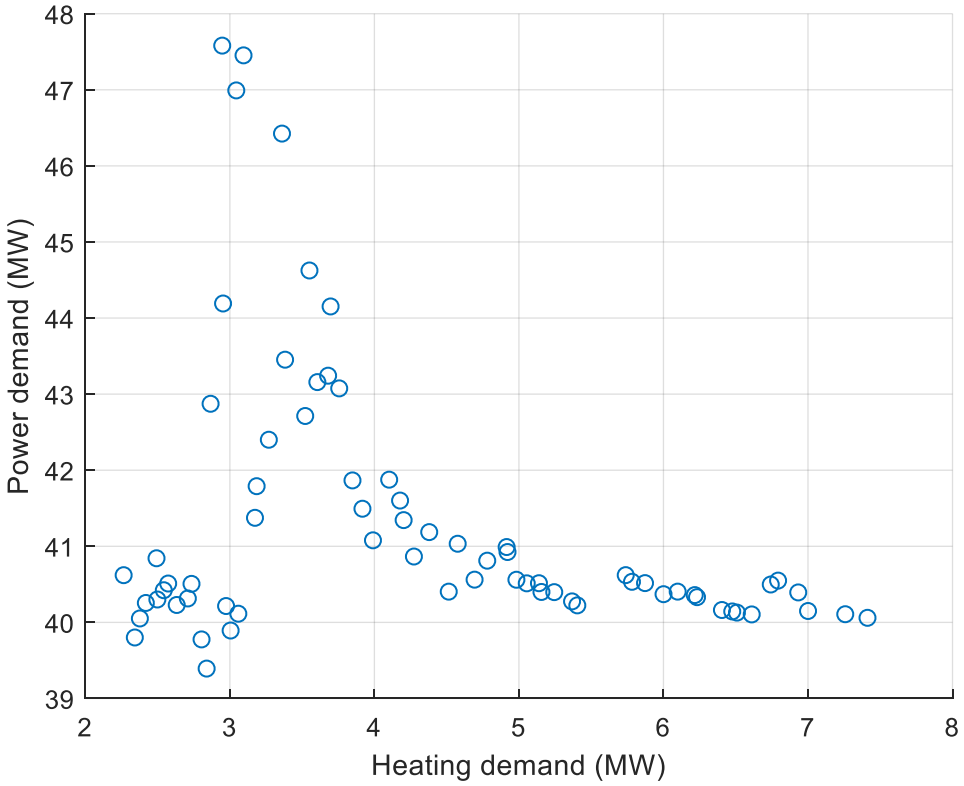

Figure 7-85: Heating variation due to I13 and I14

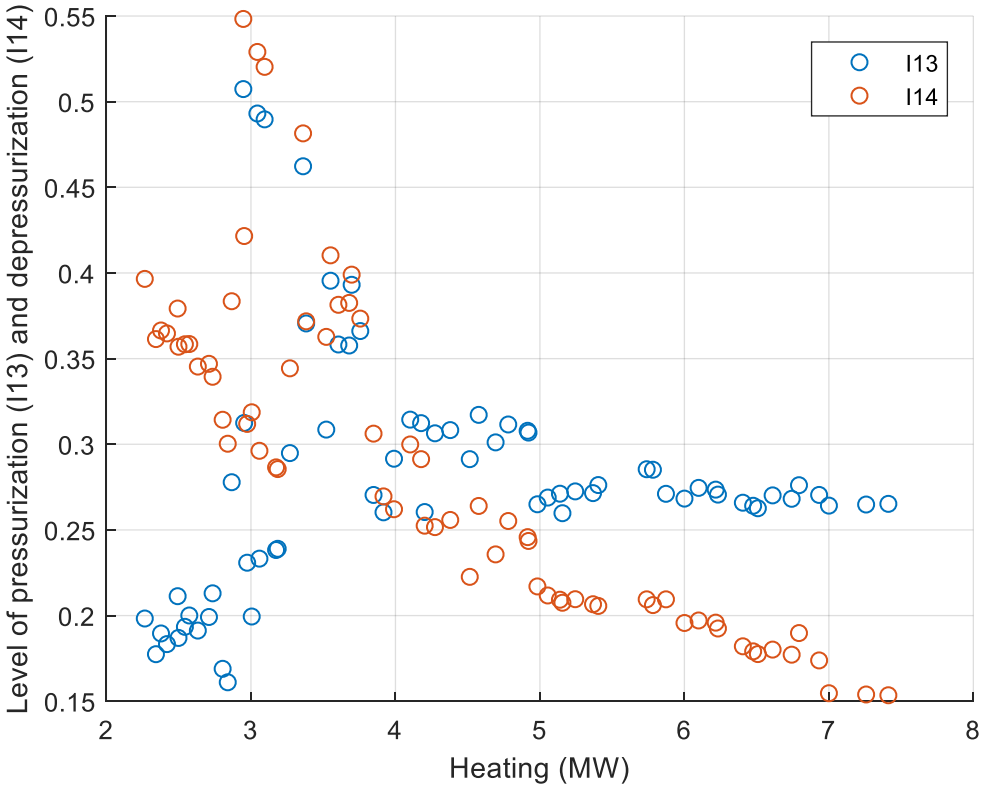

Figure 7-86: S16 mass flowrate distribution in F2F2 gas processing section optimization

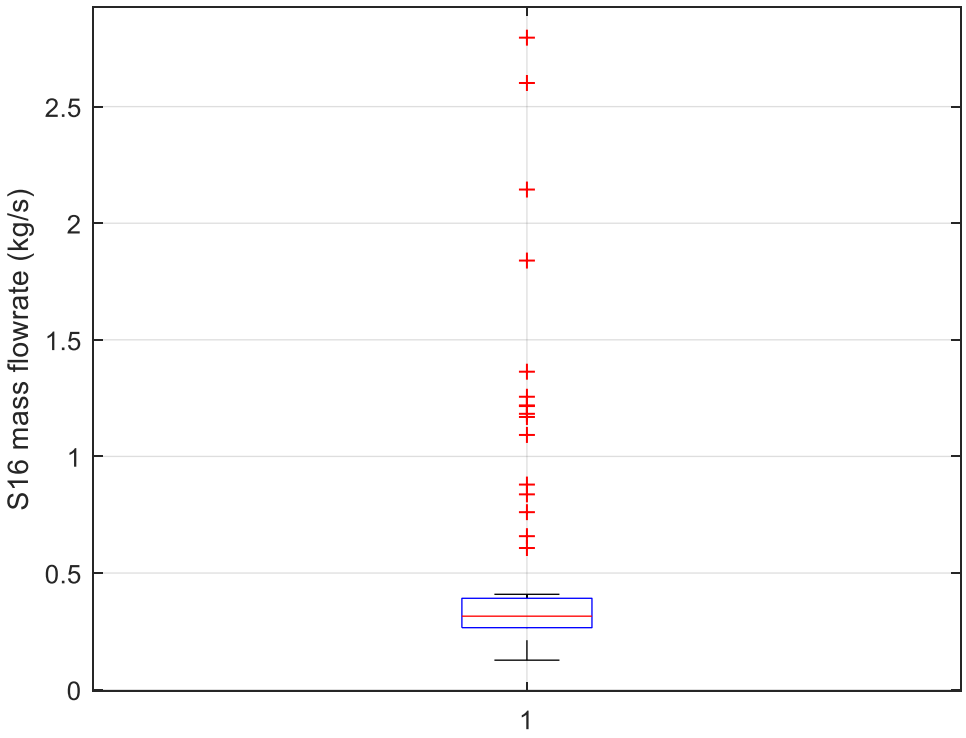

Figure 7-87: Methane recovery in reject stream (S33) of membrane system for F2F2 gas processing section optimization

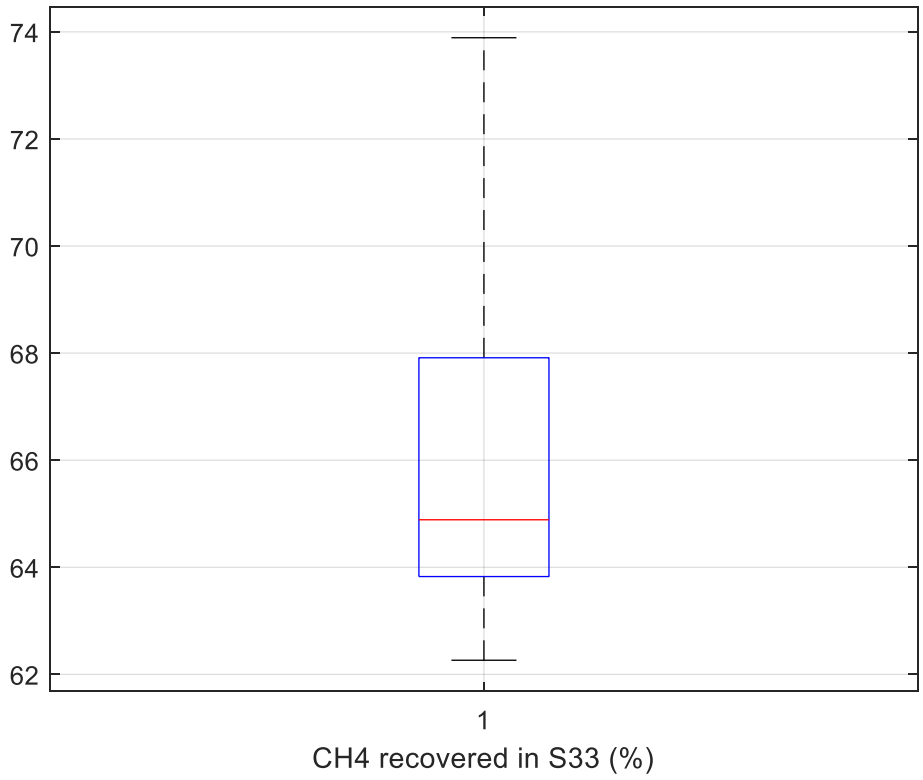

Figure 7-88: Specific gas mass flowrate distribution in F2F2 gas processing section

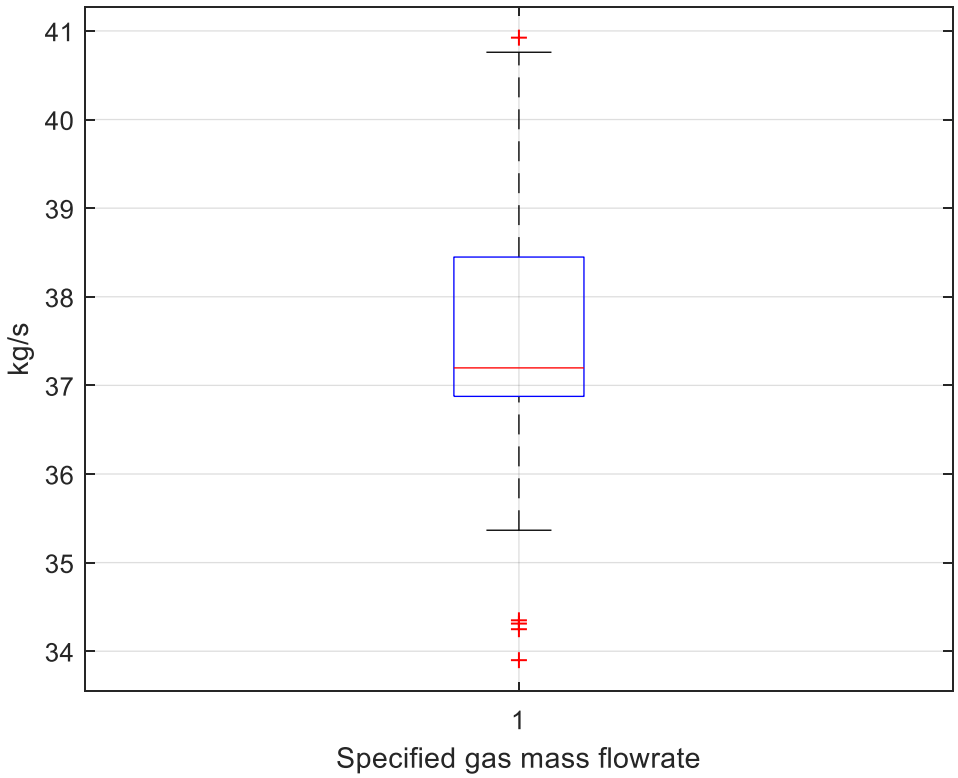

Figure 7-89: Energy demands for F2F2 gas processing section

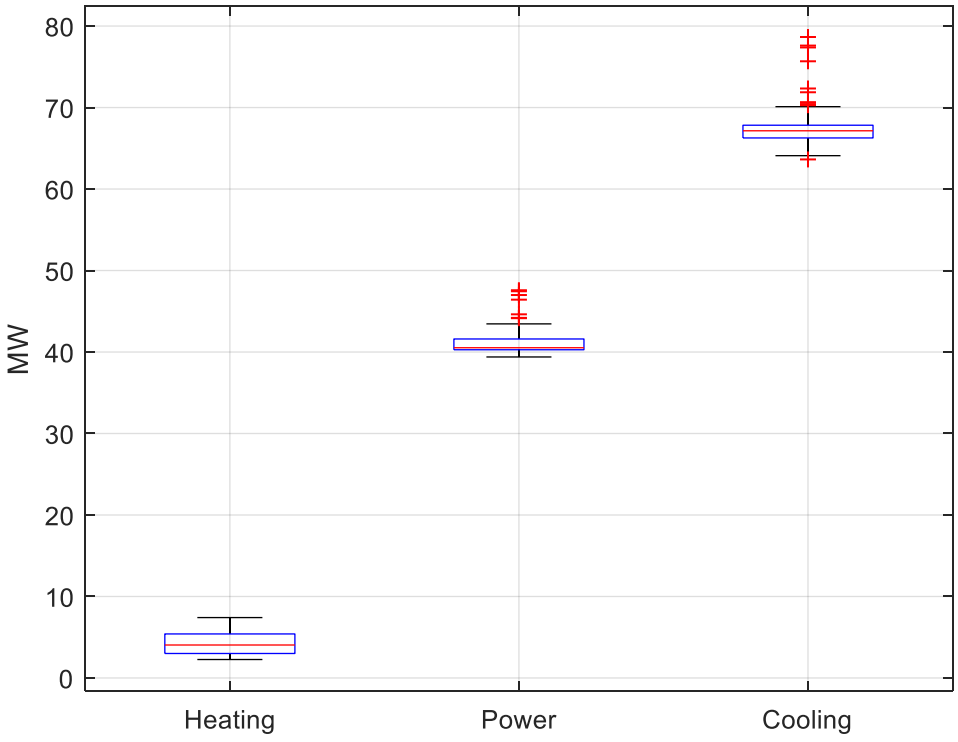

Figure 7-90: Heating demand variation in for F2F2 gas processing section

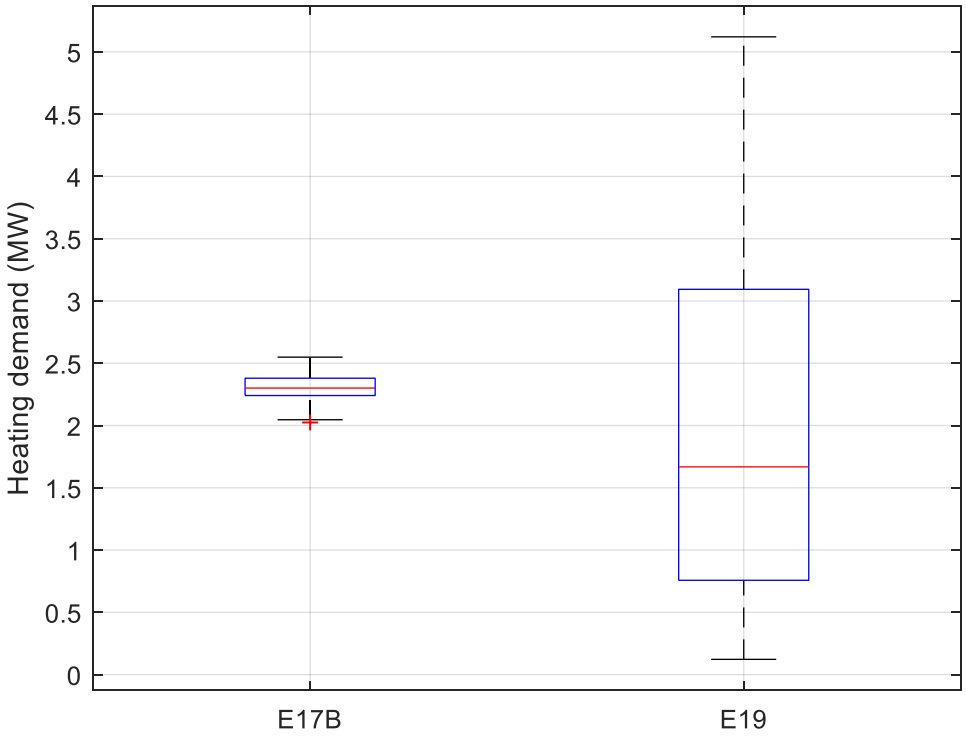

Figure 7-91: Power demand variation in for F2F2 gas processing section

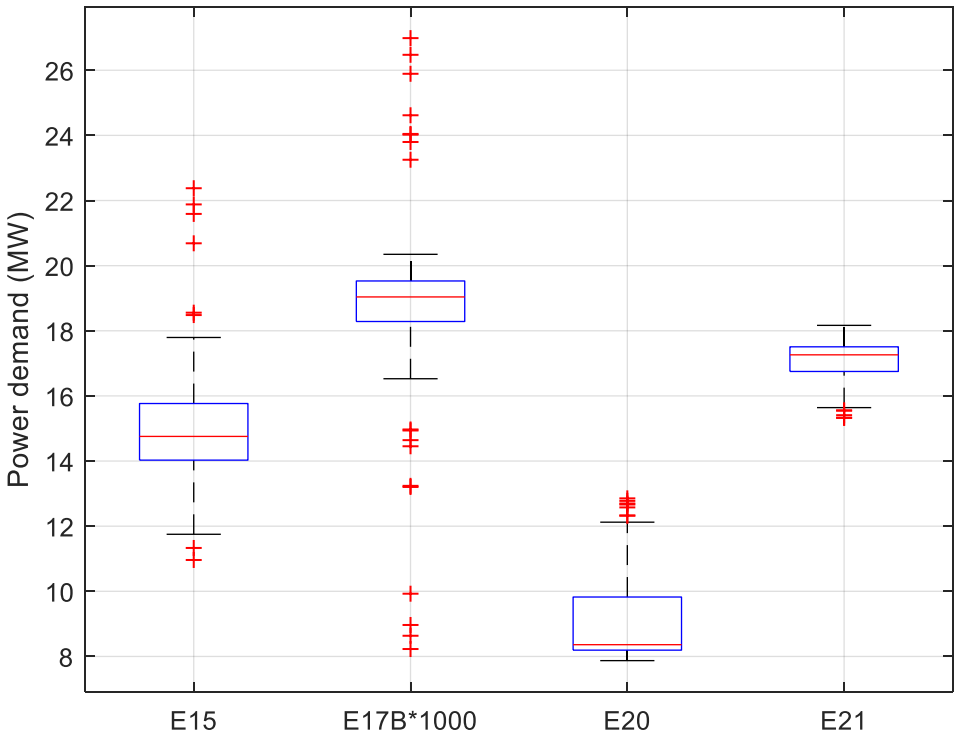

Figure 7-92: Cooling demand variation in F2F2 gas processing section

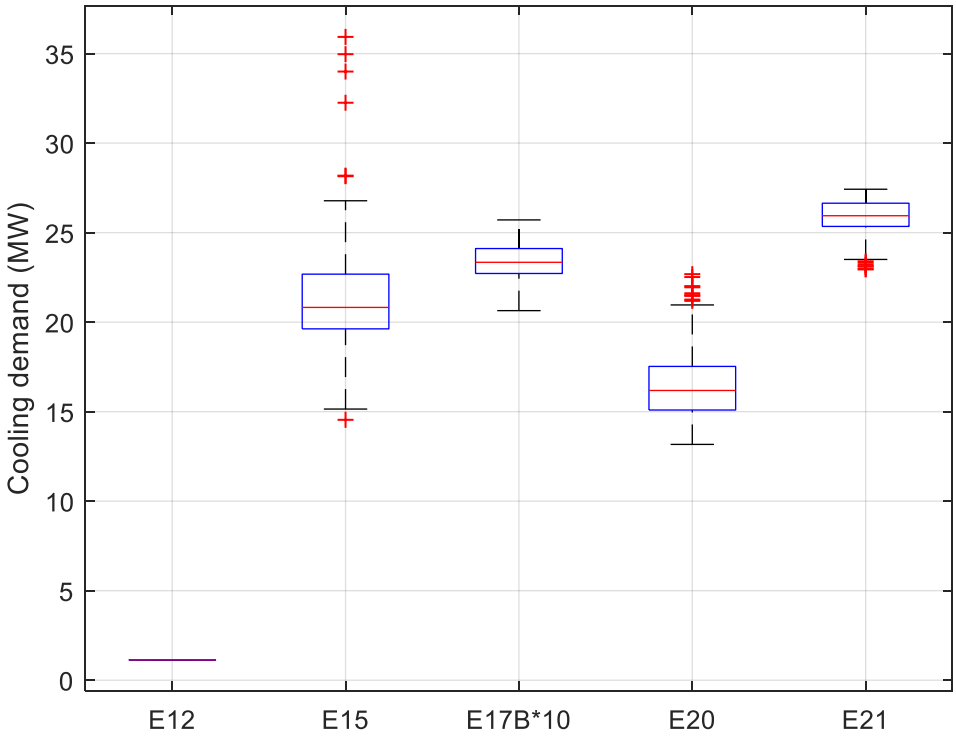

The Pareto Front comprised of heating demand, equipment dry weight and footprint in shown in Figure 7-93 for F2F3. The two-dimensional relationships between such objectives are shown in Figure 7-94, Figure 7-95 and Figure 7-96.

The inputs varied according to Figure 7-98. Inlet MEA temperature (I24) varied from 313.16 K to 327.15 K. Level of pressurization in E-15 (I13) varied from 0.16 to 0.5. TEG mass concentration in export gas dehydration varied from 0.9988 to 0.9998, which is a small variation and will hardly explain the variation of any of the outputs.

The heating demand is driven by the MEA system (E16A), as seen in Figure 7-103, presenting very low variation as the CO_2 molar fraction variation in the inlet stream, the only parameter that influences specific heating consumption in the MEA system, is negligible. There is some heating variation in the export gas TEG system, driven by the level of pressurization in E-15 and inlet temperature in the MEA system (I24), as higher absorption pressure and lower absorption temperature will lead to a dryer export gas feeding the dehydration unit. The

MEA system generates a CO_2 rich stream (composition comprises CO_2 and H_2O) in the stripper section (constant pressure) that is cooled to 40°C after leaving the system in order to reduce the amount of water to be separated in the TEG process. Therefore the CO_2 injection stream characteristics feeding compressor E23, TEG system and E21 are approximately constant, reason why such equipment present negligible variation of dry weight, footprint, power, heating and cooling.

The equipment dry weight is driven by the MEA system, followed by the export gas TEG unit and compressors E23, E20, E21 and E15, as seen in Figure 7-99. Only two different dry weights for the MEA system occurred: 959 ton or 735 ton. The highest MEA system dry weight is associated with lower temperature (I24), confirming the dependence with temperature, as seen in Figure 6-34. It has not been verified influence of pressure, also expected as per Figure 6-34. The two other variables that influence the MEA system dry weight, CO_2 molar fraction and mass flowrate, do not vary, therefore only one parameter (temperature) responded for the variation, limiting the ability of the regression tree to provide better predictions. The export gas TEG unit dry weight variation is explained by the same reasons of the heating demand variation. The variation of the E15 and E20 dry weight is governed by I13 variation, as more pressurization in E15 leads to less pressurization in E20.

The equipment footprint is driven by the MEA system, and the variation is governed by the MEA system, followed by compressors E20 and E15, and the TEG unit, as seen in Figure 7-100. The variation is explained by the same reasons of dry weight. In the case of the MEA system, higher temperatures led to lower footprint.

Power demand is driven by compressors E15, E23, E21 and E20, with variation governed by E15 and E20 due to the variation of the level of pressurization in E15 (I13). Cooling demand also varies due to such reason. Power demand varies in the export gas TEG process due to variable inlet water concentration driven by variation of I13 and I24, changing absorption conditions. Within the TEG system power is governed by the pump sending lean TEG from the reboiler to the absorption column, so with variable water content to be

separated, the lean TEG flowrate varies, leading to variation in the TEG solution flowrate and pump power demand.

As seen in Figure 7-101, the specified hydrocarbon gas flowrate is nearly constant (in few cases there is small condensation in the compression system E-15). There are no methane losses.

Figure 7-93: Pareto Front for F2F3 gas processing section

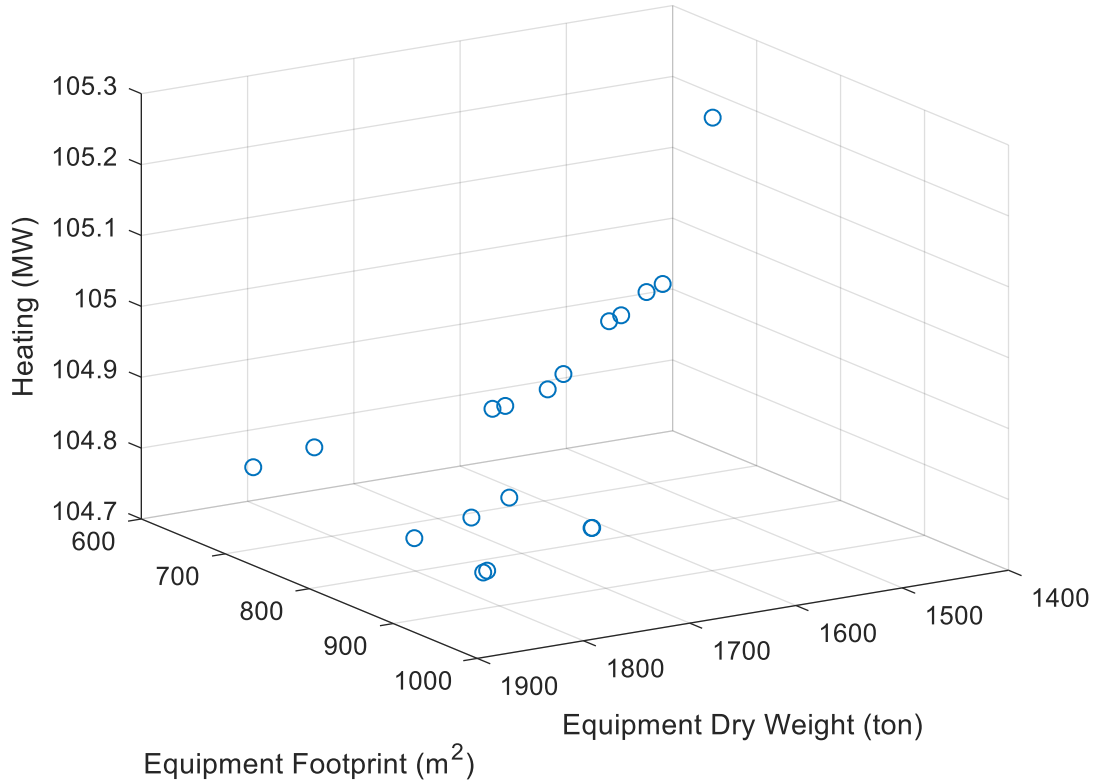

Figure 7-94: Equipment footprint x dry weight for F2F3 gas processing section

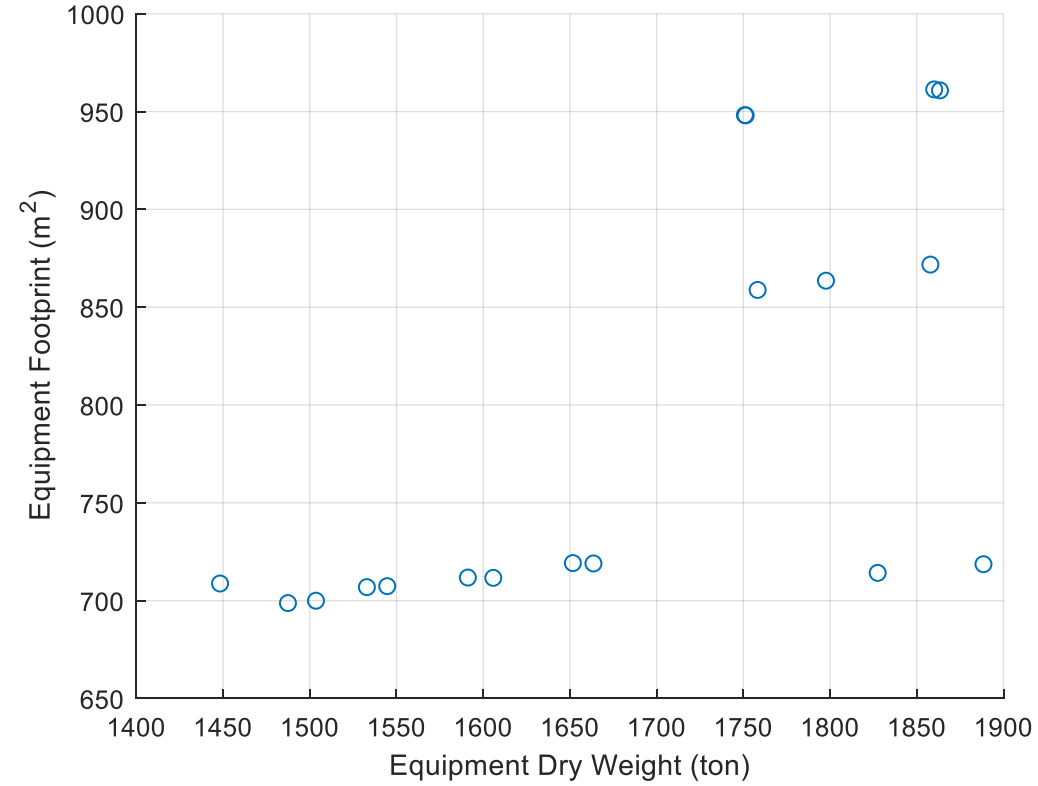

Figure 7-95: Equipment dry weight x heating demand for F2F3 gas processing section

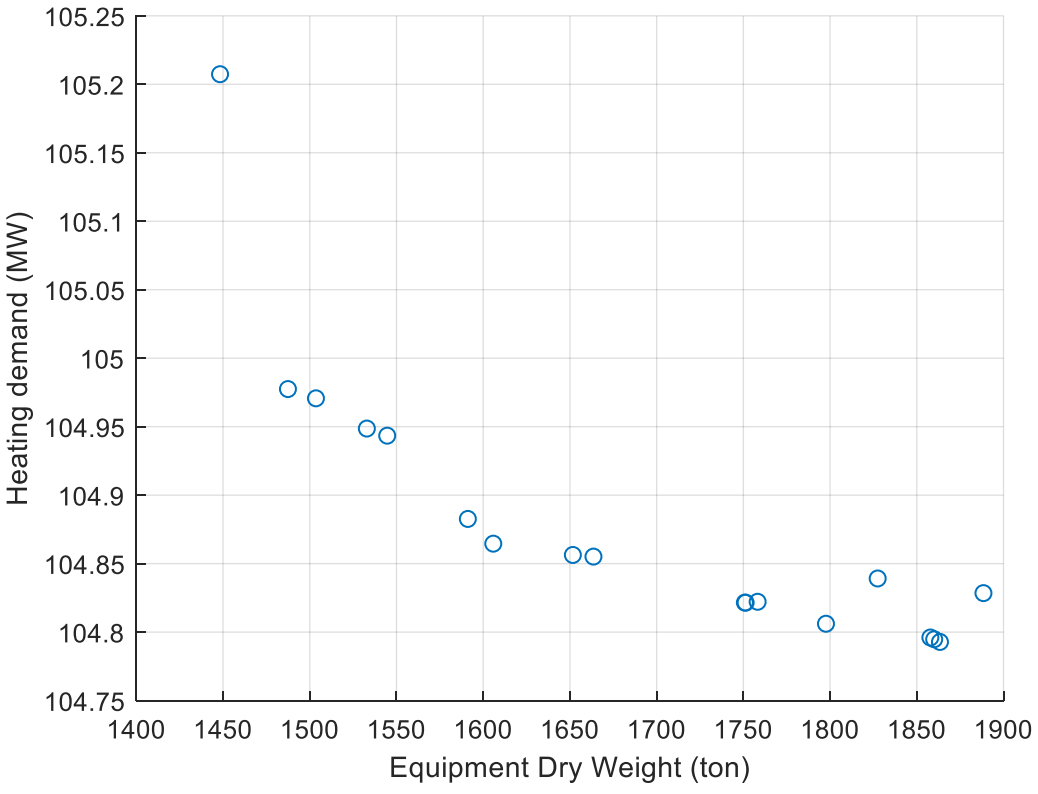

Figure 7-96: Equipment footprint x heating demand for F2F3 gas processing section

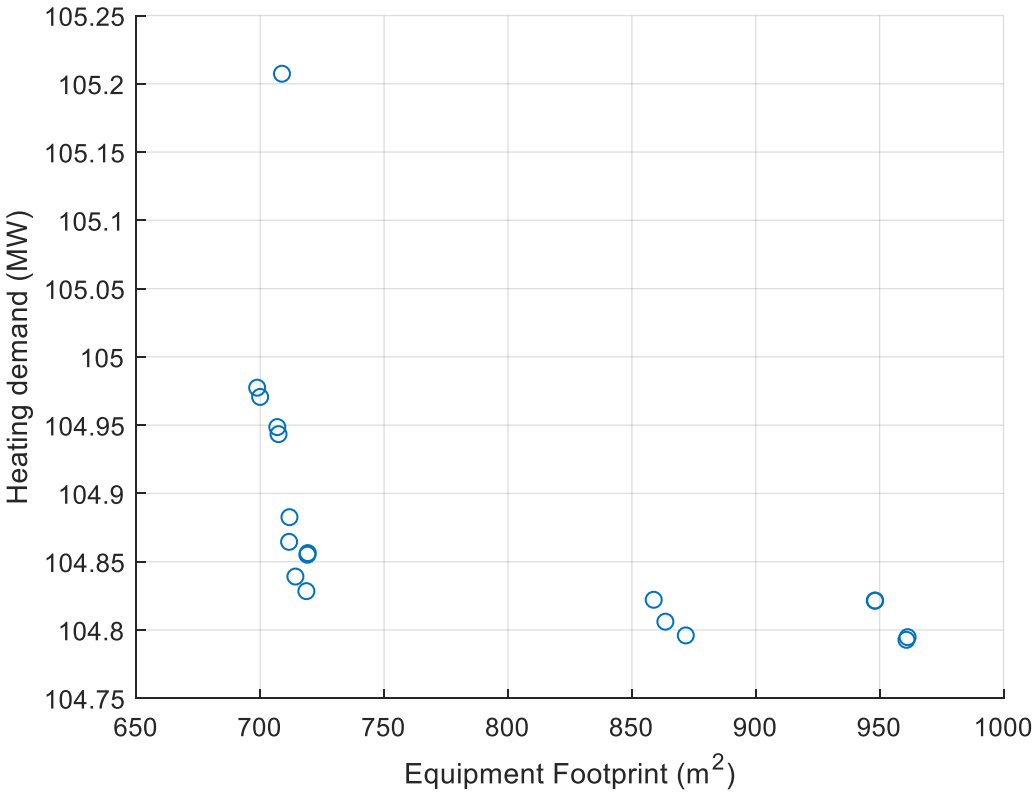

Figure 7-97: Heating demand x Power demand for F2F3 gas processing section

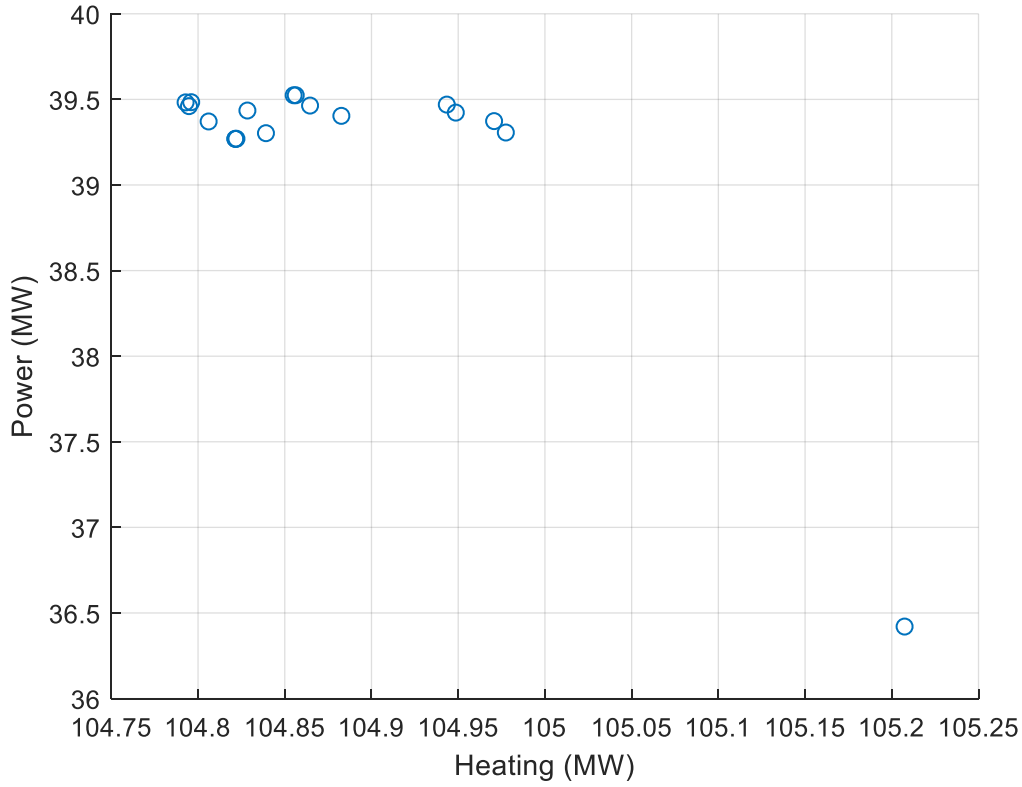

Figure 7-98: Variation of inputs of F2F3 gas processing section optimization

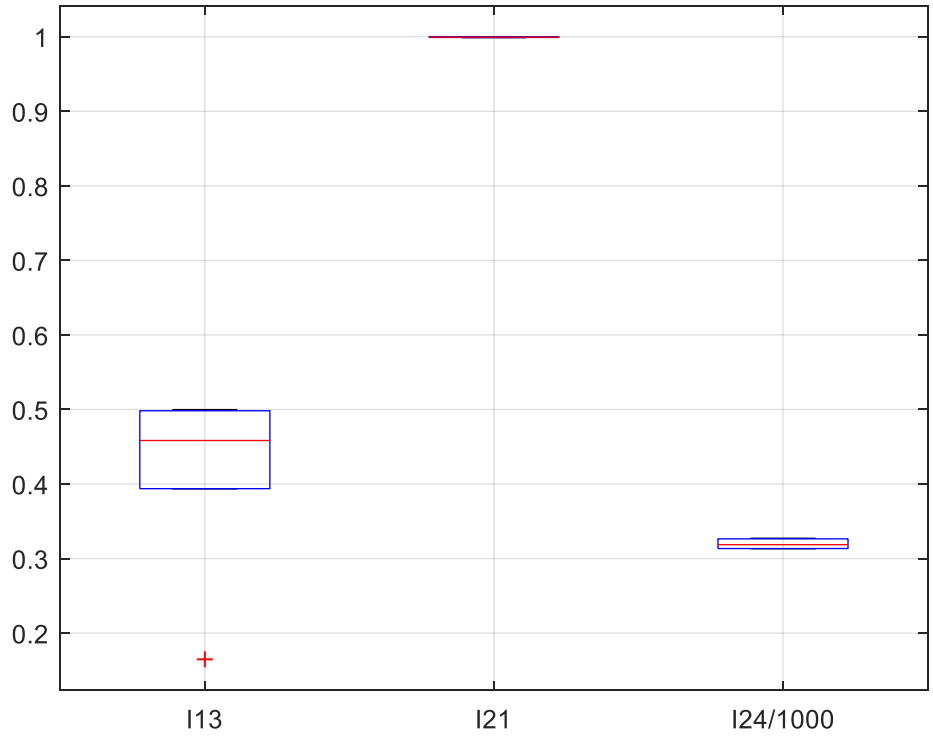

Figure 7-99: Equipment dry weight variation in F2F3 gas processing section

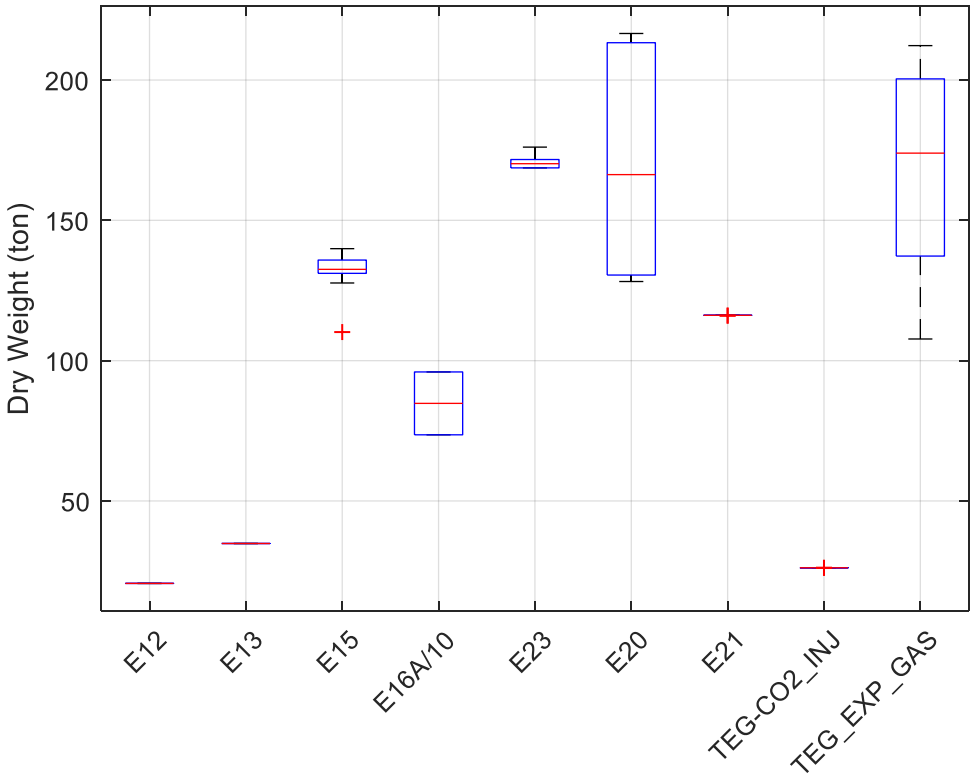

Figure 7-100: Equipment footprint variation in F2F3 gas processing section

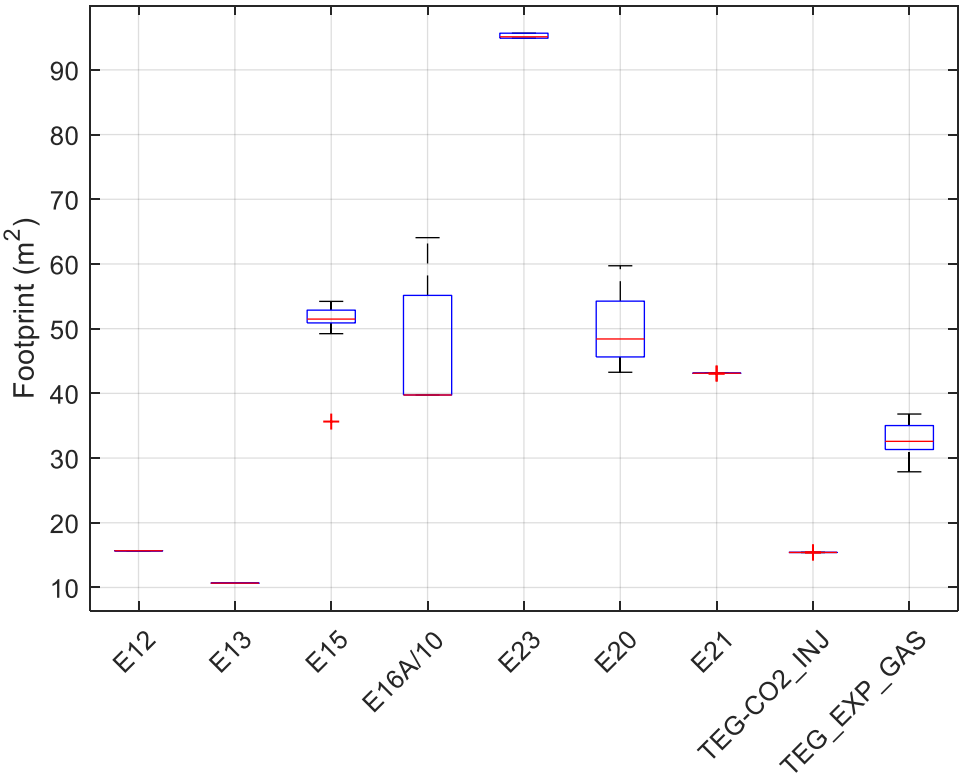

Figure 7-101: Specific gas mass flowrate distribution of F2F3 gas processing section

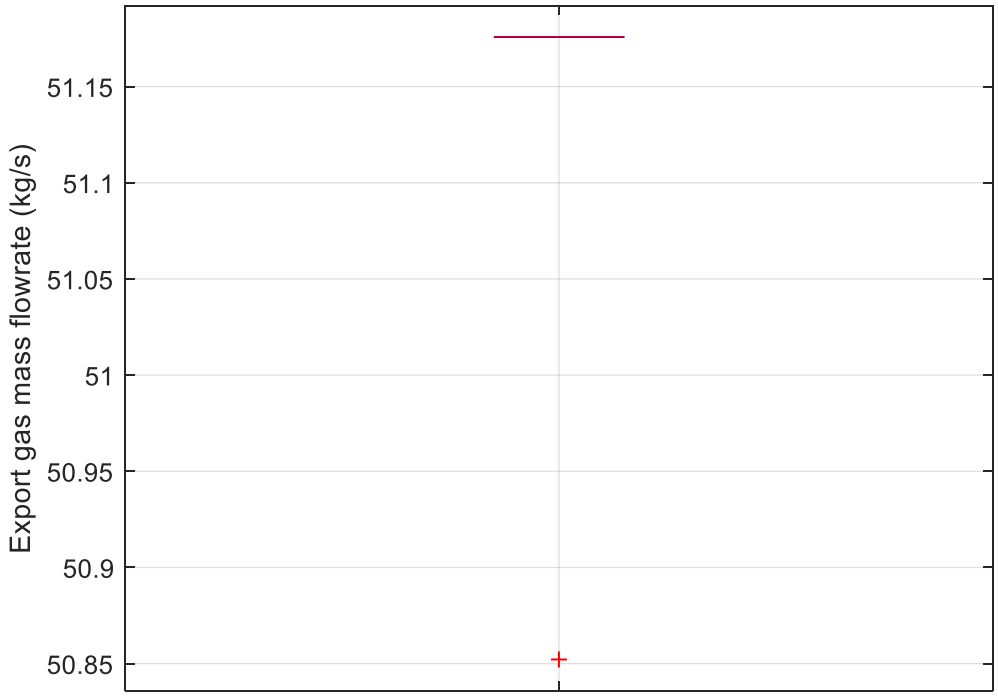

Figure 7-102: Energy demands in F2F3 gas processing section

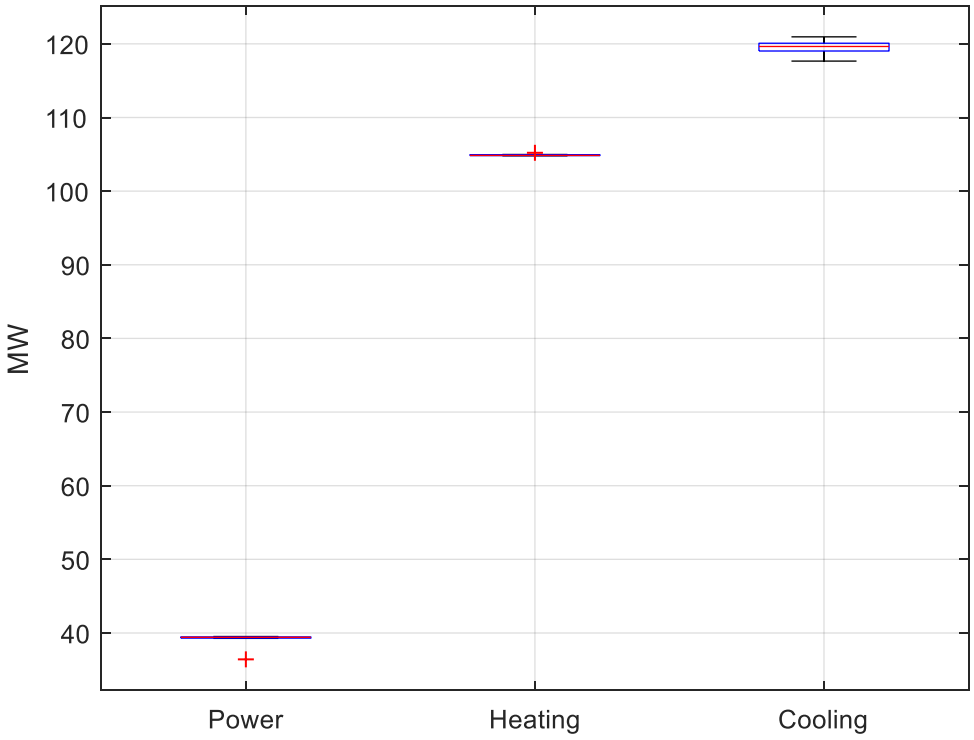

Figure 7-103: Heating demand variation in F2F3 gas processing section

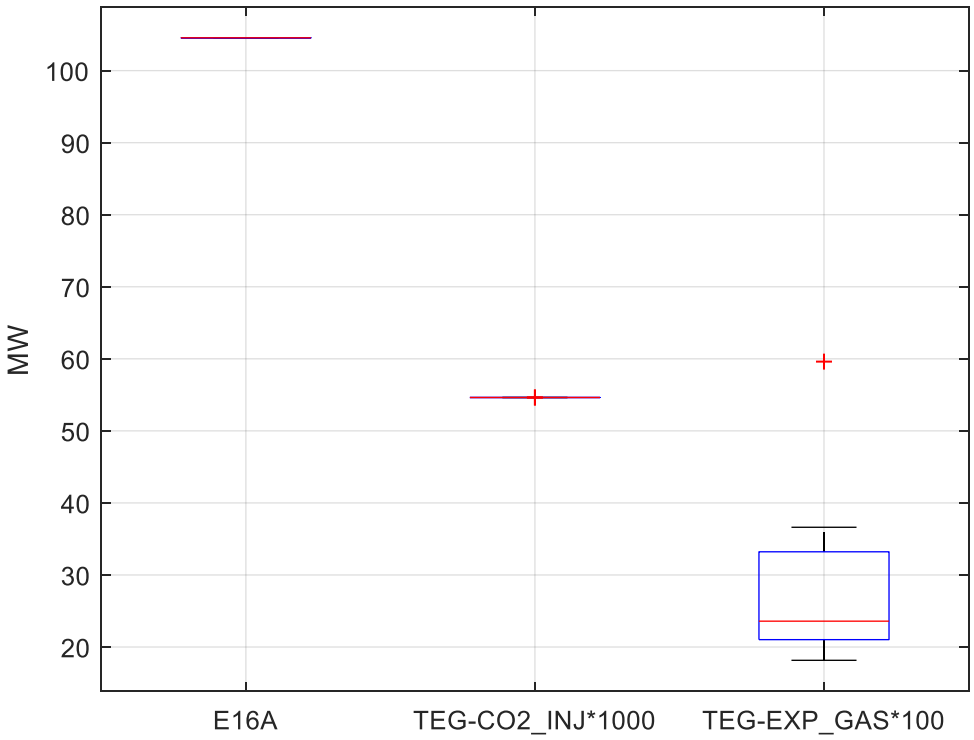

Figure 7-104: Power demand variation in F2F3 gas processing section

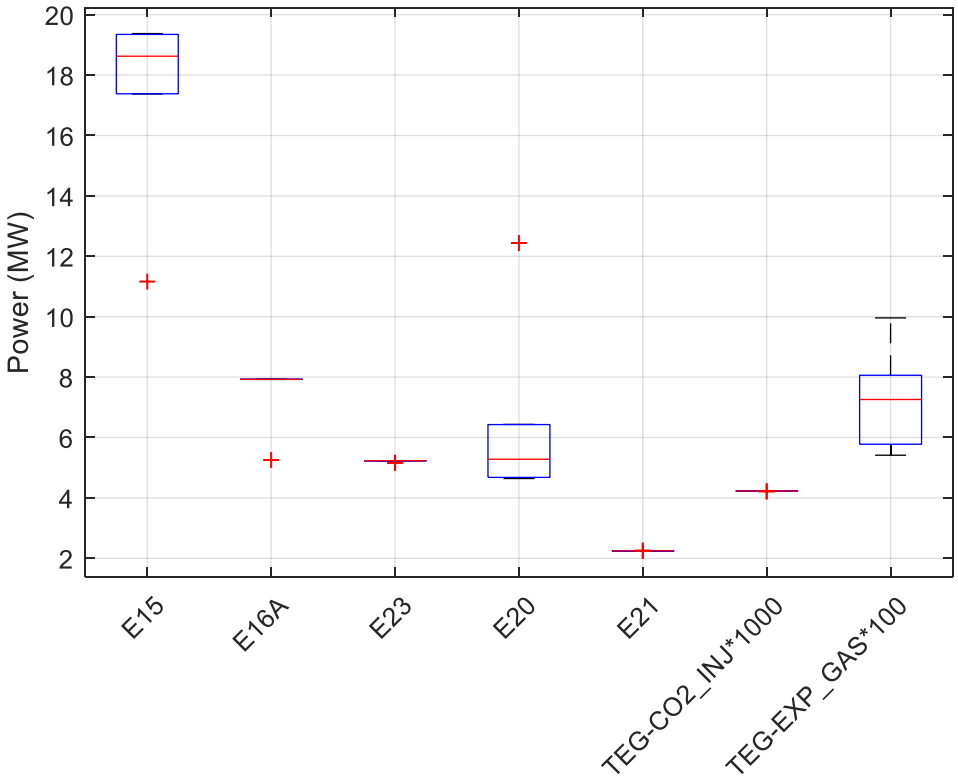

Figure 7-105: Cooling demand variation in F2F3 gas processing section

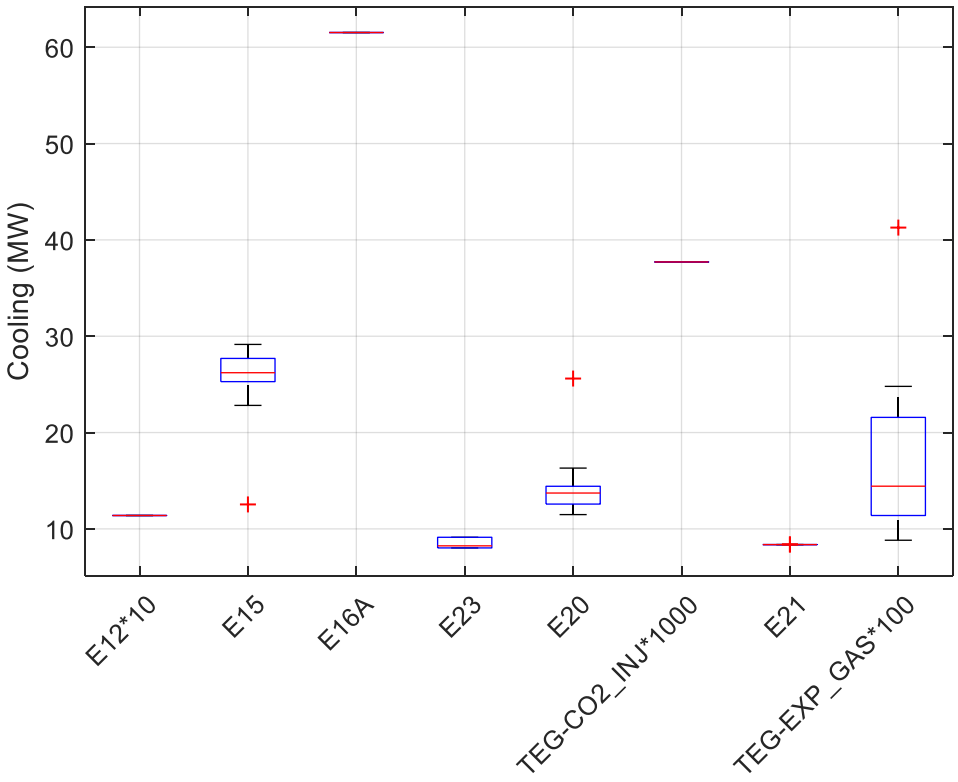

Comparison of the performance of the gas processing sections of the three flowsheets leads to Table 7-10. The percentages below each best attribute represent how better the attribute is with respect to the other flowsheets.

Flowsheet F2F3 presents the lowest equipment footprint, at 699 m^2, which is 39.2% lower than F2F1 lowest equipment footprint and 56.8% lower than F2F2 lowest equipment footprint. A CO_2 separation system purely based on the MEA system is less intensive in footprint than a system based on cellulose acetate membranes, which requires not only the membranes but a complex pre-treatment system to protect the membranes from condensation, comprised of molecular sieves for gas dehydration, a hydrocarbon dew point control unit and a gas heater. Although a system based on MEA will depend on TEG dehydration units for export gas and CO_2 injection, they do not impose that much footprint compared to the pre-treatment system. In F2F1 and F2F1, the membrane system respectively imposed medians of approximately 850 m^2 and 1400 m^2, while the MEA system in F2F1 and F2F3 respectively imposed medians of 180 m^2 and 400 m^2. Therefore the MEA system imposes less footprint than the membrane system.

Flowsheets F2F3 also presents the lowest dry weight, at 1449 ton, which is 46.2% lower than the lowest dry weight of F2F1 and 58.7% lower than the lowest dry weight of F2F2. The explanation is similar to the footprint: membranes and the complex pre-treatment system are more intensive in equipment dry weight than a system based on MEA. The median membrane dry weight is 950 ton in F2F1 and 1500 ton in F2F2, whilst the median MEA dry weight is 250 ton in F2F1 and 735 ton in F2F3.

Table 7-10: Comparison of best values for each of the attributes of the gas processing section of fluid 2 flowsheets

Attributes	**F2F1**		**F2F2**		**F2F3**	
	Best	Worst	Best	Worst	Best	Worst
Equipment Footprint (m^2)	1,150 (-34.1%)	1,745	1,619 (-22.9%)	2,101	699 (-27.2%)	961
Equipment Dry Weight (ton)	2,697 (-27.6%)	3,723	3,507 (-16.5%)	4,200	1,449 (-23.2%)	1,888
Power demand (MW)	36.0 (-10.7%)	40.3	39.4 (-17.2%)	47.6	36.4 (-7.8%)	39.5
Heating demand (MW)	8.6 (-77.5%)	38.3	2.2 (-70.3%)	7.4	104.8 (-0.38%)	105.2
Cooling demand (MW)	65.1 (-16%)	77.5	63.6 (-19.1%)	78.6	117.6 (-2.7%)	120.9
Specified hydrocarbon gas flowrate (kg/s)	47.6 (+15.2%)	41.3	40.9 (+20.6%)	33.9	51.2 (+0.6%)	50.9
Hydrocarbon condensate (kg/s)	0.63 (+37,058 %)	0.0017	2.79 (+2,146%)	0.13	0.0017 (0%)	0.0017

Regarding dry weight and footprint, F2F3 gas processing section presented the best results, explained by the use of the MEA system instead of membranes, which by the design implemented in this work impose more dry weight and footprint to the topsides. The second best performance is the gas processing section of F2F1, which combines the membrane system and MEA. A gas plant fully relying on membranes (F2F2) for gas treatment presents footprint and dry weight considerably higher than F2F1 (41% higher footprint, 30% higher dry weight) and F2F3 (132% higher footprint, 142% higher dry weight).

Heating demand is the main disadvantage of F2F3 gas processing section. The MEA system requires high heating consumption to regenerate the amine solution, reason why researchers are looking for solutions that are easier to regenerate. The heating consumption of F2F3 is 1,118% higher than F2F1 and 4,663% higher than F2F2. The heating demand of F2F1 is 290% higher than F2F2 as part of the CO_2 separation is performed by the MEA system.

Power demand in F2F2 is the highest (9.4% higher than F2F1 and 8.2% higher than F2F3) as only membranes are used to separate CO_2. The power demand of F2F3 is the lowest as pressure drop is negligible in the MEA absorber while the pressure drop in the reject side of the membranes is not irrelevant (assumed 2 bar in each stage). In addition, F2F1 and F2F2 require heavy hydrocarbon removal by Joule-Thomson effect, which decreases pressure. Comparing the reduction of CO_2 pressure in the MEA process (as the rich amine is depressurized from the absorber pressure to the stripper pressure) to the membrane process indicates that the MEA process leads to lower pressure drop.

Cooling demand is higher in F2F3 (81% higher than F2F1 and 85% than F2F2) due to the need to cool the CO_2 stream separated in the MEA process in order to reduce the water to be separated in the TEG process and to feed the reinjection compressor with as low as possible temperature to maximize compression ratio. The best cooling demand in F2F2 is approximately equal to F2F1 as the optimization process of F2F1, in certain points of the Pareto Front, reduced the CO_2 concentration at the inlet of the MEA process in order to minimize heating demand (one of the optimization objectives), reducing the cooling demand as the MEA process operated with very low inlet CO_2 concentration. In such case, the penalty is higher equipment footprint and dry weight as the CO_2 separation is more dependent on the membranes.

The specified hydrocarbon gas flowrate is the highest in F2F3 (7.5% higher than F2F1 and 25.2% higher than F2F2) as no methane is lost to the CO_2 injection stream, which occurs in F2F1 and F2F2 as part of the methane permeates the membranes. Due to the use of the MEA system in part of the CO_2 separation in F2F1, more (16.3% higher) specified gas is produced than F2F2.

Hydrocarbon condensate production is the highest in F2F2 as required pre-treatment upstream membranes is more intense than F2F1 as only membranes are used in the CO_2 separation process. The hydrocarbon dew point control unit leads to high pressure drop and resulting Joule-Thomson cooling. There is little

hydrocarbon condensate in F2F3 as it is only possible within the compression system E-15.

Given the high discrepancy regarding heating demand, it is possible to state that F2F3 is not a good process for the considered associated gas stream as it would lead to very high consumption of fuel gas, significantly increasing the carbon footprint of the process. In situations where footprint and/or weight are severe constraints in the platform, it makes sense to consider process F2F1 instead of F2F2, even though fuel gas consumption and system complexity are higher. In the future it is planned to incorporate a power generation model to estimate fuel gas consumption, enabling estimation of the carbon footprint, which would be one of the ultimate attributes to compare flowsheets.

The presence of relevant amount of CO_2 leads to a drastic increase of the equipment footprint and dry weight, in addition to increased energy demands. These are the main reasons why the oil industry is looking for smarter ways to separate CO_2, such as subsea separation.

The ultimate fluid 2 best attributes, considering the oil and gas processing sections, are shown in Table 7-11. The percentages below each best attribute represent how better the attribute is with respect to the other flowsheets.

Considering the variable best attributes of each flowsheet in a spider chart leads to Figure 7-106, indicating that F2F1 is the best flowsheet if equal weight is given to each attribute, although its system complexity is higher than the other flowsheets. Such fact is in line with the processing scheme proposed by Reis et al. (2018), who claims that combining membranes with chemical absorption leads to higher flexibility at the specific context of processing variable raw gas flowrate and CO_2 molar fraction.

Table 7-11: Ultimate Fluid 2 best attributes

Attribute	F2 oil section	F2F1	F2F2	F2F3
Oil Production (kg/s)	195.6 (common to all flowsheets)			
Equipment Footprint (m^2)	210.3	1,360.9	1,829.1	909.2 (-33%/-50%)
Equipment Dry Weight (ton)	185.7	2,882.5	3,693.0	1,634.4 (-43%/-56%)
Power demand (MW)	0.71	36.7 (-8%/-1%)	40.1	37.1
Heating demand (MW)	17.1	25.7	19.3 (-25%/-79%)	121.9
Cooling demand (MW)	2.05	67.1	65.6 (-2.2%/-45.1%)	119.6
Specified hydrocarbon gas flowrate (kg/s)	NA	47.6	40.9	51.2 (+8%/+25%)
Hydrocarbon condensate (kg/s)	NA	0.63	2.79 (+342%/ +164,000%)	0.0017

Figure 7-106: Fluid 2 flowsheets best attributes

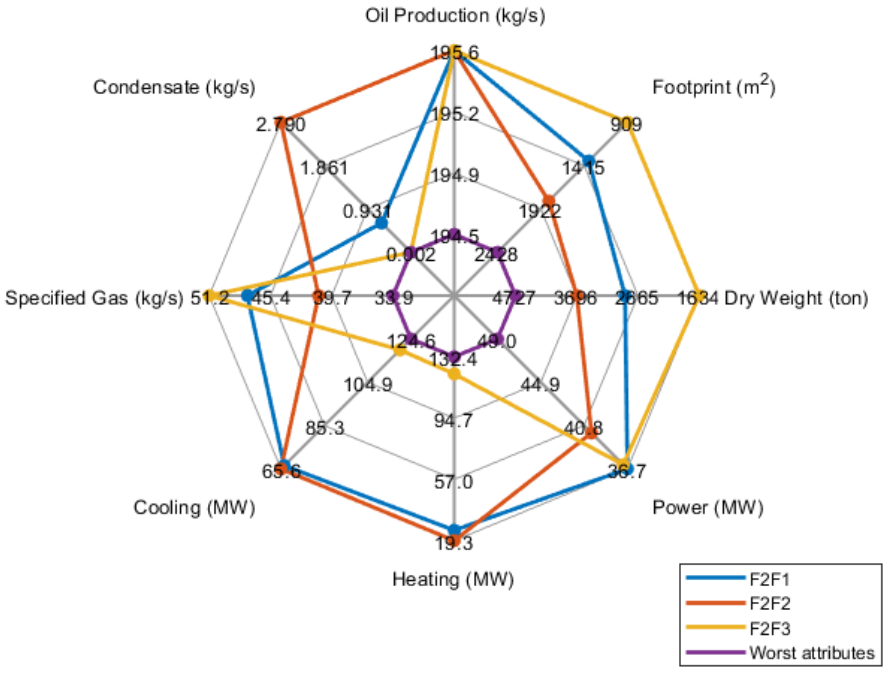

Chapter 8

8. Conclusions and suggested future works

In all considered fluids and respective flowsheets, optimization results showed the possibility of producing oil at a flowrate very close to the maximum identified in the Pareto front, while equipment footprint and weight can be significantly reduced. Considering the best attributes of fluid 1 flowsheets, adopting flowsheet F1F2 will lead to an equipment dry weight reduction of 25.6% compared to F1F1 and 57.7% compared to F1F3, while equipment footprint is 13.6% lower than F1F1 and 10.6% lower than F1F3. Considering the best attributes of fluid 2 flowsheets, F2F3 presents the lowest equipment dry weight and footprint, but at the expense of much higher heating demand, which is 374% higher than F2F1 and 531% higher than F2F2, likely not feasible due to cost and carbon footprint constraints.

When wellstream CO_2 content is significant (in the case of fluid 2), the gas processing section imposes significant equipment footprint and dry weight due to the increased complexity of gas treatment. The gas processing section in F2F1 responds for 85% of the equipment footprint and 94% of the equipment dry weight, in F2F2 89% of the equipment footprint and 95% of equipment dry weight, and in F2F3 % 77% of the equipment footprint and 89% of equipment dry weight. In addition, energy demands increase when compared to a fluid with low CO_2 content (in the case of fluid 1), due to energy intensive processes (membrane separation, molecular sieve, hydrocarbon dew point control unit, MEA system). Such findings are in line to the current target of separating CO_2 in a smarter way, such as subsea separation. The MEA process ended up imposing less dry weight and footprint to the platform, which is not in line to the typical understanding that membrane separation is lighter and more compact. The gas processing section of F2F2, which only uses membranes for CO_2 separation, imposed 1,619 m^2 and 3,507 ton, while F2F1, which combines membranes (bulk CO_2 separation) and MEA (CO_2 polishing), imposed 1,150 m^2 (-29%) and 2,697 ton (-23%). Such conclusion may change if the models of such technologies are enhanced and modularization is considered.

The use of two parametric analysis methods (regression tree and SS-ANOVA) combined with SOBOL experimental design showed similar results in all analyses, contributing to the quality of the optimization process, identifying the inputs that should be discarded from the optimization. In fluid 1 optimization, 4 of 15 inputs (26%) were discarded considering the inputs of the most complex flowsheet (F1F2), while in fluid 2 optimization 3 of 11 inputs (27%) were discarded considering the gas processing section of the most complex flowsheet (F2F1) and 1 of 11 inputs (8%) of the oil processing section of the most complex flowsheet. Optimization of the gas processing section of F2F1 led to 85.7 hours using the 11 screened inputs and 87.2 hours using the 14 initial inputs, showing that the parametric analysis slightly increased efficiency of the optimization process for the given optimization tolerance.

The use of the regression tree technique to provide fast estimation for the MEA process attributes enabled the genetic-algorithm based optimization for flowsheets dependent on MEA for part of the topsides processing system. When fast estimations of MEA attributes (e.g. footprint, dry weight, heating) are not possible, global optimizations based on the genetic algorithm would lead to prohibitive convergence time for processing systems depending on MEA. Whilst a simulation of a MEA system case based on the phenomenological model may take several minutes, the simulation by the regression tree takes in the order of milliseconds.

The general-purpose mathematical programming process synthesis and optimization tool, with an immediate application in topsides oil & gas processing systems synthesis and optimization, fully implemented in Matlab and independent of commercial process simulators and optimizers, is a powerful tool to synthesize and optimize topsides oil & gas processing systems, contributing to objectives such as footprint reduction, dry weight reduction, decarbonization, and cost reduction. It can also be used as a digital twin by coupling online data with the simulator, enabling optimization of the processing plant parameters along the field life. It is the first time (as no other example has been found according to the literature review) such a tool is developed, contributing to close the gap identified by Chen & Grossmann (2017).

The quality of the results is limited by the quality of the equipment models. Some of them have not been validated against operational data or specialized software. Nevertheless, it is believed the main conclusions will not significantly change if the equipment models are updated in the future as such models have been implemented based on recognized publications and expert knowledge. On the other hand, layout and modularization may change conclusions as, for example, membrane systems may be installed favoring vertical configuration, reducing the skid footprint.

It is possible to conclude that two innovations have arisen from this work:

- a system level optimization of topsides oil & gas processing plants, aiming minimization of footprint and dry weight and maximization of oil production;
- use of two techniques for sensitivity analysis, regression tree and SS-ANOVA, increasing confidence in the results.

In order to enhance the quality of the synthesis and optimization framework, the following is suggested:

- Automate the creation of the superstructure by developing an algorithm that is capable of connecting equipment between each other based on imposed constraints and characteristics of the streams generated by each equipment;
- Automate the extraction of flowsheets from the superstructure by developing an algorithm that accounts for the connections between the equipment;
- Consider variation of inlet conditions along the field life, obtaining the best flowsheet for each set of inlet conditions and compare them (in case a single flowsheet is not the best for all sets of inlet conditions), identifying the best one and how it can be adapted to cope with all sets of inlet conditions.

In order to enhance the quality of the developed topsides process simulator and optimizer, the following is suggested:

- Validate the design of the following equipment: horizontal 3-phase and gas-liquid separators based on Stokes law, shell & tube heat exchanger, electrostatic coalescer, and MEA absorption;

- Enhance estimation of wellstream inlet conditions at the platform, modeling effects such as shearing rate influence on amount of emulsioned water,
- Enhance modeling of 3-phase and gas-liquid separators, considering aspects such as influence of temperature on amount of emulsified water, coalescence and breakage of droplets, surge volume, mass diffusion between phases, sand removal, foaming and chemicals dosing (e.g. demulsifier, anti-foaming);
- Enhance modeling of cellulose acetate membrane separation, improving temperature profile estimation and considering potential H_2S separation;
- Enhance modeling of amine-based systems for CO_2 separation, including methods to quickly estimate steady-state equilibrium of non-linear systems of reactions (instead of only considering the main reaction) and more options of amine solutions (e.g. MDEA, MDEA + Piperazine);
- Include more equipment, such as other types of CO_2 separation membranes (e.g. hollow fiber), heat exchangers (e.g. plate, printed circuit), heavy hydrocarbons removal from associated gas (e.g. propane refrigeration);
- Include modularization and other relevant topsides processes and structures that add weight and footprint, such as produced water treatment, seawater treatment, power generation, pipe racks, accommodations, enabling more accurate estimation of total dry weight and footprint;
- Estimate if performance of any equipment is significantly reduced due to motions of the platform, information that can later be used to impose more constraints to equipment design;
- Model and incorporate emergent technologies to related to associated gas and CO_2, verifying economic impact and influence on dry weight, footprint and carbon footprint;
- Incorporate a cost model, including several hull types, to estimate operational and capital expenditure, in order to better compare the flowsheets.

9. Bibliography

AACE International. Cost Estimate Classification System - As Applied in Engineering, Procurement, and Construction for the Process Industries. 2011.

Albahri, T.A., Khor, C.S., Elsholkami, M., & Elkamel, A.. Optimal Design of Petroleum Refinery Configuration Using a Model-Based Mixed-Integer Programming Approach with Practical Approximation. Industrial & Engineering Chemistry Research. 2018, 57(22), 7555-7565. https://doi.org/10.1021/acs.iecr.7b04507.

Allahyarzadeh-Bigdoli, A., Salviano, L.O., Dezan, D.J., de Oliveira Junior, S., Yanagihara, J.I. Energy optimization of an FPSO operating in the Brazilian Pre-salt. Energy. 2018, 164, 390-399. https://doi.org/10.1016/j.energy.2018.08.203.

Allahyarzadeh-Bigdoli, A., Dezan, D.J., Salviano, L.O., de Oliveira Junior, S., Yanagihara, J.I. FPSO fuel consumption and hydrocarbon liquids recovery optimization over the lifetime of a deep-water oil field. Energy 2019, 181, 927-942. https://doi.org/10.1016/j.energy.2019.05.146.

AMI Applied Membranes INC. AMI 2.5" DIA. END PORT FRP MEMBRANE HOUSING PRESSURE VESSELS. 2021. Available at <https://www.appliedmembranes.com/media/wysiwyg/pdf/vessels/codeline_80h100_membrane_housing_drawing.pdf>. Accessed 08-08-2020.

Armstrong J., Sams G.W. Oil Dehydration Improved by Dual Frequency Electrostatic Process. International Petroleum Technology Conference. 2007, IPTC 11285. https://doi.org/10.2523/IPTC-11285-MS.

Arnold, K. & Stewart, M. Surface Production Operations. Volume 1. 2008.

Arora J.S., Elwakeil, O.A., Chahande, A.I., Hsieh, C.C. Global optimization methods for engineering applications: a review. Structural Optimization. 1995, 9, 137-159. https://doi.org/10.1007/BF01743964.

Babi, D.K., Lutze, P., Woodley, J.M., Gani, R. A process synthesis-intensification framework for the development of sustainable membrane-based operations. Chemical Engineering and Processing: Process Intensification. 2014, 86, 173-195. https://doi.org/10.1016/j.cep.2014.07.001.

Backi, C.J., Grimes, B.A., Skogestad, S. A Control- and Estimation-Oriented Gravity Separator Model for Oil and Gas Applications Based upon First-Principles. Industrial & Engineering Chemistry Research. 2018, 57, 7201-7217. https://doi.org/10.1021/acs.iecr.7b04297.

Bahadori, A., Vuthaluru, H.B. Simple methodology for sizing of absorbers for TEG (triethylene glycol) gas dehydration systems. Energy. 2009, 34, 1910-1916. https://doi.org/10.1016/j.energy.2009.07.047.

Bahadori, A., Vuthaluru, H.B., Mokhatab, S. Method Accurately Predicts Water Content of Natural Gases. Energy Sources. 2009, 31, 754-760. https://doi.org/10.1080/15567030801901562.

Baidoo, M.F., Snarvold, K.S., Hodneland, S., Brodtkorb, T.W. Process design and economical investigation of natural gas dehydration plants. Norwegian University of Science and Technology. 2011. Available at <https://folk.ntnu.no/skoge/diplom/prosjekt11/Natural-gas-dehydration-design-project/project-baidoo-snarvold-hodneland-brodtkorb.pdf/>. Accessed 10-18-2019.

Baldea, M. From process integration to process intensification. Computers and Chemical Engineering. 2015, 81, 104-114. https://doi.org/10.1016/j.compchemeng.2015.03.011.

Bertran, M.O., Frauzem, R., Arcilla, A.S., Zhang, L., Woodley, J.M., Gani, R. A generic methodology for processing route synthesis and design based on superstructure optimization. Computers and Chemical Engineering. 2017, 106, 892-910. https://doi.org/10.1016/j.compchemeng.2017.01.030.

Bothamley, M. Quantifying Oil/Water Separation Performance in Three-Phase Separators—Part 1. Oil Gas Facilities. 2017, https://jpt.spe.org/quantifying-oilwater-separation-performance-three-phase-separatorspart-1/ (accessed 20.09.2019).

Boyd, N. G. Topsides Weight Reduction Design Techniques for Offshore Platforms. Offshore Technology Conference. 1986, OTC 5257.

Chen, Q., Grossmann, I.E. Recent Developments and Challenges in Optimization_Based Process Synthesis. The Annual Review of Chemical and Biomolecular Engineering. 2017, 8, 249-283. https://doi.org/10.1146/annurev-chembioeng-080615-033546.

Cremaschi, S. A perspective on process synthesis: Challenges and prospects. Computers and Chemical Engineering. 2015, 34, 35-44. https://doi.org/10.1016/B978-0-444-63433-7.50005-5.

Daichendt, M. M., Grossmann, I. E. Integration of hierarchical decomposition and mathematical programming for the synthesis of process flowsheets. Computers and Chemical Engineering. 1998, 22 (1-2), 147-175. https://doi.org/10.1016/S0098-1354(97)88451-7.

de Andrade, A. M. T., Vaz, C.E.M., Ribeiro, J., Lopreato, L.G.R., Nascimento, R.F.S. Offshore Production Units for Pre-Salt Projects. Offshore Technology Conference. 2015, OTC 25961.

Deb, K. Multi-Objective Optimization using Evolutionary Algorithms. Wiley. 2001.

Deb, K., Pratap, A., Agarwal, S., Meyarivan, T. A Fast and Elitist Multiobjective Genetic Algorithm: NSGA-II. IEEE Transactions on Evolutionary Computation. 2002, 2, 182-197. https://doi.org/10.1109/4235.996017.

Demirel, S.E., Li, J., Hasan, M.M. Systematic process intensification using building blocks. Computers & Chemical Engineering. 2017, 105, 2-38. https://doi.org/10.1016/j.compchemeng.2017.01.044.

DiGullio, R., McGregor, W., Teja, A. Thermal Conductivities of Ethanolamines. Journal of Chemical Engineering & Data. 1992, 37, 242-245. https://doi.org/10.1021/je00006a029.

Douglas, J. M. A Hierarchical Decision Procedure for Process Synthesis. AIChE Journal. 1985, 31(3), 353-362. https://doi.org/10.1002/aic.690310302

DOW. Triethylene Glycol - Product Information. 2007.

Dresser-Rand. DATUM Centrifugal Compressors. Available at <https://hickman-shearer.co.uk/wp-content/uploads/2020/06/vdocuments.mx_dresser-rand-datum-compressors.pdf>. Accessed 03-20-2019.

D'Souza, R., Basu, S. Importance of Topsides in Design and Selection of Deepwater Floating Platforms. Offshore Technology Conference. 2011, OTC 22403. https://doi.org/10.4043/22403-MS.

Dunn, R. F., El-Halwagi, M. M. Process integration technology review: background and applications in the chemical process industry. Journal of Chemical Technology and Biotechnology. 2003, 78, 1011-1021.

Echeverry, J.S., Acherman, S.R., Lopez, E.A. Peng-Robinson equation of state: 40 years through cubics. Fluid Phase Equilibria. 2017, 447, 39-71. https://doi.org/10.1016/j.fluid.2017.05.007.

Esparragoza, J.J., Silva, G.A., Hlavinka, M.W., Bullin, J.A. How to Estimate Reid Vapor Pressure (RVP) of Blends. Encyclopedia of Chemical Processing and Design. 1994, 47, 415-424. https://www.bre.com/PDF/How-to-Estimate-Reid-Vapor-Pressure-(RVP)-of-Blends.pdf/ (accessed 10.02.2019).

Farkas, T., Rev, E., Lelkes, Z. Process flowsheet superstructures: Structural multiplicty and redundancy Part I: Basic GDP and MINLP representations. Computers and Chemical Engineering. 2005, 29(10), 2180-2197. https://doi.org/10.1016/j.compchemeng.2005.07.007.

Fettaka, S., Thibaut, J., Gupta, Y. Design of shell-and-tube heat exchangers using multiobjective optimization. International Journal of Heat and Mass Transfer. 2013, 60, 343-354.

Flores, H. A. R. Estudo do Processo de Absorção e Dessorção na Solução Aquosa de Metildietanolamina e Piperazina. PhD Thesis. Universidade de São Paulo. 2015.

Ghaedi, M., Ebrahimi, A.N., Pishvaie, M.R. Application of genetic algorithm for optimization of separator pressures in multistage production units. Chemical Engineering Communications 2014, 201(7), 926-938. https://doi.org/10.1080/00986445.2013.793676.

González-Delgado, Á.-D., Kafarov, V., El-Halwagi, M. Development of a topology of microalgae-based biorefinery: process synthesis and optimization using a combined forward-backward screening and superstructure approach. Clean Techn Environ Policy. 2015, 17, 2213-2228. https://doi.org/10.1007/s10098-015-0946-5.

Gooty, R. T., Agrawal, R., Tawarmalani, M. An MINLP formulation for the optimization of multicomponent distillation configurations. Computers and Chemical Engineering. 2019, 125, 13-30. https://doi.org/10.1016/j.compchemeng.2019.02.013.

GPSA - Gas Processors Suppliers Association. Engineering Data Book. 2004,12 ed.

Greer, T. Modeling and Simulation of Post Combustion CO2 Capturing. Master Thesis - Telemark University College. 2008.

Grossmann, I. E., Harjunkoski, I. Process systems Engineering: Academic and industrial perspectives. Computers and Chemical Engineering. 2019, 126, 474-484. https://doi.org/10.1016/j.compchemeng.2019.04.028.

Gu, C. Smoothing Spline ANOVA Models. 2 ed. Springer. 2013.

Hardle, W. K., Simar, L. Applied Multivariate Statistical Analysis. 4 ed. Springer. 2014.

Hoff, K. A. Modeling and Experimental Study of Carbon Dioxide Absorption in a Membrane Contactor. PhD Thesis. Norwegian University of Science and Technology. 2013.

Hwang, J., Lee, K.Y. Optimal liquefaction process cycle considering simplicity and efficiency for LNG FPSO at FEED stage. Computers and Chemical Engineering. 2014, 63, 1-33. https://doi.org/10.1016/j.compchemeng.2013.12.007.

Hwang, J.H., Roh, M.I., Lee, K.Y. Determination of the optimal operating conditions of the dual mixed refrigerant cycle for the LNG FPSO topside liquefaction process. Computers and Chemical Engineering. 2013, 49, 25-36. https://doi.org/10.1016/j.compchemeng.2012.09.008.

IEA, International Energy Agency. Total Primary Energy Demand (TPED), World in the New Policies Scenario. 2018A.

IEA, International Energy Agency. Offshore Energy Outlook. 2018B.

Independent Project Analysis. Megaprojects - Concepts, Strategies, and Practices for Success - Module 9 - Translating Ideas and Data to Scope (FEL 2). 2013.

Jayarathna, S.A., Weerasooriyat, A., Dayarathna, S., Eimer, D.A., Melaaen, M.C. Densities and Surface Tensions of CO2 Loaded Aqueous Monoethanolamine Solutions with r = (0.2 to 0.7) and T = (303.15 to 333.15) K. Journal of Chemical & Engineering Data. 2013, 58(4), 986-992. https://doi.org/10.1021/je301279x.

Jia, F., Lichti, D. A Comparison of Simulated Annealing, Genetic Algorithm and Particle Swarm Optimization in Optimal First-Order Design of Indoor TLS Networks. ISPRS Annals of the Photogrammetry, Remote Sensing and Spatial Information Sciences, IV-2. 2017. https://doi.org/10.5194/isprs-annals-IV-2-W4-75-2017.

Keil, F. J. Process intensification. Reviews in Chemical Engineering. 2018, 34, 135-200. https://doi.org/10.1515/revce-2017-0085.

Khajehesamedini, A., Anzai, T.K., Castor Jr, C.A., Nele, M., Pinto, J.C. Hybrid Modeling of the Electrocoalescence Process in Water-in-Oil Emulsions. Energy & Fuels. 2018, 32, 5596-5610. https://doi.org/10.1021/acs.energyfuels.7b03602.

Kim, W. S., Yamg, D. R., Moon, D. J., Ahn, B. S. The process design and simulation for the methanol production on the FPSO (floating, production, storage and off-loading) system. Chemical Engineering Research and Design. 2014, 92(5), 931-940. https://doi.org/10.1016/j.cherd.2013.08.009

Kister, H.Z., Scherffius, J., Afshar, K., Abkar, E. Realistically Predict Capacity and Pressure Drop for Packed Columns. AiChE CEP. 2007, 28-38.

KLM Technology Group. Gas Sweetening Systems (Engineering Design Guideline). 2012.

KLM Technology Group. Gas Dehydration System Sizing, Selection, and Troubleshooting. 2015a.

KLM Technology Group. Mole Sieve Dehydration Design and Troubleshooting. 2015b.

Kong, Q., Shah, N. Development of an Optimization-Based Framework for Simultaneous Process Synthesis and Heat Integration. Industrial & Engineering Chemistry Research. 2017, 56, 5000-5013. https://doi.org/10.1021/acs.iecr.7b00549.

Koronaki, I.P., Prentza, L., Papaefthimiou, V.D. Parametric analysis using AMP and MEA as aqueous solvents for CO2 absorption. Applied Thermal Engineering. 2017, 110, 126-135. https://doi.org/10.1016/j.applthermaleng.2016.07.140.

Krishnamachari, R. S., Papalambros, P. Y. Hierarchical Decomposition Synthesis in Optimal Systems Design. Journal of Mechanical Design. 1997, 119(4), 448-457. https://doi.org/10.1115/1.2826389.

Li, J., Demirel, S.E., Hasan, M.M. Process Integration Using Block Superstructure. Industrial & Engineering Chemistry Research. 2018, 57, 4377-4398. https://doi.org/10.1021/acs.iecr.7b05180.

Li, L. Classification and Regression with Decision Trees. 2019. https://towardsdatascience.com/https-medium-com-lorrli-classification-and-regression-analysis-with-decision-trees-c43cdbc58054 (accessed 10.01.2021).

Li, X., Cui, C., Li, H., Gao, X. Process synthesis and simulation-based optimization of ethylbenzene/styrene separation using double-effect heat integration and self-heat recuperation technology: A techno-economic analysis. Separation and Purification Technology. 2019, 228, 1-10. https://doi.org/10.1016/j.seppur.2019.115760.

Liu, T., Gao, X., Wang, L. Multi-objective optimization method using an improved NGSA-II algorithm for oil-gas production process. Journal of the

Taiwan Institute of Chemical Engineers. 2015, 57, 42-53. https://doi.org/10.1016/j.jtice.2015.05.026.

Lohrenz, J., Bray, B.G., Clark, C.R. Calculating Viscosities of Reservoir Fluids from Their Compositions. Journal of Petroleum Technology. 1964, 16(10), 1171-1176. https://doi.org/10.2118/915-PA.

Lutze, P., Gani, R. & Woodley, J. M. Process intensification: A perspective on process synthesis. Chemical Engineering and Processing: Processing Intensification. 2010, 49(6), 547-558. https://doi.org/10.1016/j.cep.2010.05.002.

Ma, X. Using Classification and Regression Trees. Charlotte, NC: Information Age Publishing. 2018.

Mackowiak, J. Pressure Drop in Irrigated Packed Columns. Chem. Eng. Process. 1991, 29, 93-105. https://doi.org/10.1016/0255-2701(91)87018-X.

Mao, S., & Duan, Z. The Viscosity of Aqueous Alkali-Chloride Solutions up to 623 K, 1,000 bar, and High Ionic Strength. International Journal of Thermophysics. 2009, 30, 1510-1523. https://doi.org/10.1007/s10765-009-0646-7.

Manning, F.S., Thompson, R.E. Oilfield Processing Volume Two: Crude Oil. PennWell Books, Tulsa. 1995.

Marine Link. FPSO: Guide to Life Extension. 2015. Available at <https://www.marinelink.com/news/extension-guide-life398174>. Accessed in 10.10.2018.

Martín, M., Adams II, T.A. Challenges and future directions for process and product synthesis and design. Computers and Chemical Engineering. 2019, 128, 421-436. https://doi.org/10.1016/j.compchemeng.2019.06.022.

MathWorks, 2020. N-Way ANOVA. Available at: <https://www.mathworks.com/help/stats/n-way-anova.html#bqttd3j-3>. Accessed in 2020-09-25.

MathWorks, 2021. predictorImportance. Available at <https://www.mathworks.com/help/stats/compactclassificationtree.predictorimportance.html>. Accessed 2021-04-07.

Mikkelsen, R., Melo, D. Development of a Compact Topside Processing Facility. Offshore Technology Conference. OTC 24429. 2013. https://doi.org/10.4043/24429-MS.

Mokhatab, S., Poe, W.A., Speight, J. G. Handbook of Natural Gas Transmission and Processing. GPP, Burlington. 2006.

Moss, D., & Basic, M. Pressure Vessel Design Manual, fourth ed. Elsevier, Oxford. 2013.

Navid, A., Khalilarya, S., Abbasi, M. Diesel engine optimization with multi-objective performance characteristics by non-evolutionary Nelder-Mead algorithm: Sobol sequence and Latin hypercube sampling methods comparison

in DoE process. Fuel. 2018, 228, 349-367. https://doi.org/10.1016/j.fuel.2018.04.142.

Nayar, K.G., Sharqawy, M.H., Banchik, L.D., Lienhard, J.H. Thermophysical properties of seawater: A review and new correlations that include pressure dependence. Desalination. 2016, 390, 1-24. https://doi.org/10.1016/j.desal.2016.02.024.

Nichita, D.V., Leibovici, C.F. A rapid and robust method for solving the Rachford–Rice equation using convex transformations. Fluid Phase Equilibria. 2013, 353, 38-49. https://doi.org/10.1016/j.fluid.2013.05.030.

Nordin, A. Challenges in the industrial implementation of generative design systems: An exploratory study. Artificial Intelligence for Engineering Design, Analysis and Manufacturing. 2018, 32(1), 16-31. https://doi:10.1017/S0890060416000536

Øi, L., Fazlagic, M. Glycol Dehydration of Captured Carbon Dioxide Using Aspen HySys Simulation. Proceedings from the 55th Conference on Simulation and Modelling (SIMS 55). Linköping Electronic Conference Proceedings. 2014, 108:15, 167-174

Onda, K., Takeuchi, H., & Okumoto, Y. Mass Transfer Coefficients Between Gas and Liquid Phases in Packed Columns. Journal of Chemical Engineering of Japan. 1968, 1, 56-62. https://doi.org/10.1252/jcej.1.56.

Onel, O., Niziolek, A.M., Butcher, h., Wilhite, B.A., & Floudas, C.A. Multi-scale approaches for gas-to-liquids process intensification: CFD modeling, process synthesis, and global optimization. Computers & Chemical Engineering. 2017, 105, 276-296. https://doi.org/10.1016/j.compchemeng.2017.01.016

Ozbek H., Phillips S.L. Thermal Conductivity of Aqueous NaCl Solutions from 20C to 330C. Journal of Chemical Engineering & Data. 1980, 25(3), 263-267. https://doi.org/10.1021/je60086a001.

P.I.T. Pipe, 2021. ANSI Pipe Schedule Chart. Available at <https://www.pitpipe.com/pipe-schedule-chart.html>. Accessed 03-10-2020.

Peng, D.Y., Robinson, D. B. A New Two-Constant Equation of State. Industrial & Engineering Chemical Chemistry Fundamentals. 1976, 15(1), 59-64. https://doi.org/10.1021/i160057a011.

PetroSkills. TEG Dehydration: Stripping Gas Correlations for Lean TEG Regeneration. 2013. Available at < http://www.jmcampbell.com/tip-of-the-month/2013/07/teg-dehydration-stripping-gas-correlations-for-lean-teg-regeneration/> . Accessed 05-05-2019.

Petroskills. TEG Dehydration: Stripping Gas Charts for Lean TEG Regeneration. 2019. http://www.jmcampbell.com/tip-of-the-month/2013/07/teg-dehydration-stripping-gas-correlations-for-lean-teg-regeneration/ (accessed 10.04.2019).

Plaza, J.M., Wagener, D.V., Rochelle, G.T. Modeling CO2 Capture with aqueous monoethanolamine. International Journal of Greenhouse Gas Control. 2010, 4(2), 161-166. https://doi.org/10.1016/j.ijggc.2009.09.017

Portha, J.F., Falk, L., Commenge, J.M. Local and global process intensification. Chemical Engineering and Processing: Process Intensification. 2014, 84, 1-13. https://doi.org/10.1016/j.cep.2014.05.002.

PubChem, 2021. Cellulose Acetate. Available at: <https://pubchem.ncbi.nlm.nih.gov/compound/Cellulose-acetate>. Accessed 11-10-2020.

Quaglia, A., Sarup, B., Sin, G., Gani, R. A systematic framework for enterprise-wide optimization: Synthesis and design of processing networks under uncertainty. Computers & Chemical Engineering. 2013, 59, 47-62. https://doi.org/10.1016/j.compchemeng.2013.03.018.

Reis, A.C., de Medeiros, J.L., Nunes, G.C., Araújo, O.Q. Upgrading of natural gas ultra-rich in carbon dioxide: Optimal arrangement of membrane skids and polishing with chemical absorption. Journal of Cleaner Production. 2017, 165, 1013-1024. https://doi.org/10.1016/j.jclepro.2017.07.198.

Reis, A., de Medeiros, J., Nunes, G., Araújo, O. Lifetime oriented design of natural gas offshore processing for cleaner production and sustainability: High carbon dioxide content. Journal of Cleaner Production. 2018, 200, 269-281.

Ricco, L., Rigoni, E., Turco, A. Smoothing Spline ANOVA for Variable Screening. Dolomites Research Notes on Approximation. 2013, 6, 130-139. 10.14658/pupj-drna-2013-Special_Issue-13.

Rigoni, E., Ricco, L. Esteco Technical Report 2011-007: Smoothing Spline ANOVA for Variable Screening. 2011.

Rossi, F., Colombo, S., Pierucci, S., Ranzi, E., Manenti, F. Upstream Operation in the Oil Industry: Rigorous Modeling of an Electrostatic Coalescer. Engineering. 2017, 3(2), 220-231. https://doi.org/10.1016/J.ENG.2017.02.013.

Santos, M.G., Correia, L.M., de Medeiros, J.L., Araújo, O.Q. Natural gas dehydration by molecular sieve in offshore plants: Impact of increasing carbon dioxide content. Energy Conversion and Management. 2017, 149, 760-773. https://doi.org/10.1016/j.enconman.2017.03.005.

Sawamura, S., Egoshi, N., Setoguchi, Y., Matsuo, H. Solubility of sodium chloride in water under high pressure. Fluid Phase Equilibria. 2007, 254, 158-162. https://doi.org/10.1016/j.fluid.2007.03.003.

Sams, G, Sellman, E.L., Mandewalkar, P.K. Compact Electrostatic Treaters for Floating Offshore Production Facilities. Offshore Technology Conference. 2013. OTC 24303. https://doi.org/10.4043/24303-MS.

Serth, R. W. Process Heat Transfer Principles and Applications. Elsevier, Kingsville. 2007.

Shah, R. K., Sekulic, D. P. Fundamentals of Heat Exchanger Design. John Wiley & Sons Inc., New Jersey. 2003.

Shah, V.H., Agrawal, R. A Matrix Method for Multicomponent Distillation Sequences. AIChE Journal. 2010, 56(7), 1759-1775. https://doi.org/10.1002/aic.12118.

Sharqawy, M.H., Lienhard, J.H., Zubair, S.M. Thermophysical properties of seawater: a review of existing correlations and data. Desalination and Water Treatment. 2010, 16, 354-380. https://doi.org /10.5004/dwt.2010.1079

Shoaib, A. M., Bhran, A.A., Awad, M.E.. El-Sayed, N.A., Fathy, T. Optimum operating conditions for improving natural gas dew point and condensate throughput. Journal of Natural Gas Science and Engineering. 2018, 49, 324-330. https://doi.org/10.1016/j.jngse.2017.11.008.

Singh, V., Gu, N. Towards an integrated generative design framework. Design Studies. 2012, 33(2), 185-207. https://doi.org/10.1016/j.destud.2011.06.001.

Skiborowski, M. Process synthesis and design methods for process intensification. Current Opinion in Chemical Engineering. 2018, 22, 216-225. https://doi.org/10.1016/j.coche.2018.11.004.

Sobrino, M., Concepción, E.I., Hernández, Á.G., Martín, M.C., Segovia, J.J. Viscosity and density measurements of aqueous amines at high pressures: MDEA-water and MEA-water mixtures for CO2 capture. Journal of Chemical Thermodynamics. 2016, 98, pp. 231-241. https://doi.org/10.1016/j.jct.2016.03.021.

Souza, M. L. Process Plant Layout Optimization of an FPSO. IEEE Latin America Transactions 2019, 17(10), 1724-1732. https://doi.org/10.1109/TLA.2019.8986451.

Spivey, J.P., McCain, W.D., North, R. Estimating Density, Formation Volume Factor, Compressibility, Methane Solubility, and Viscosity for Oilfield Brines at Temperatures From 0 to 275° C, Pressures to 200 MPa, and Salinities to 5.7 mole/kg. Journal of Canadian Petroleum Technology. 2004, 43, 52-61. https://doi.org/10.2118/04-07-05.

Stewart, M. I. Surface Production Operations - Design of Gas-Handling Systems and Facilities. 3 ed. GPP. 2014.

Suemar, P., Fonseca, E.F., Coutinho, R.C., Machado, F., Fontes, R., Ferreira, L.C., Nele, M. Quantitative Evaluation of the Efficiency of Water-in-Crude-Oil Emulsion Dehydration by Electrocoalescence in Pilot-Plant and Full-Scale Units. Industrial & Engineering Chemistry Research. 2012, 51, 13423-13437. https://doi.org/10.1021/ie202489g.

Sung-Kyoom, K., Myung-Il, R., Ki-Su, K. Arrangement Method of Offshore Topside Based on an Expert System and Optimization Technique. Journal of Offshore Mechanics and Arctic Engineering 2017, 139(2), 1-19. https://doi.org/10.1115/1.4035141.

Tanker Shipping & Trade. 2013. Available at <https://ww2.eagle.org/content/dam/eagle/articles/TankerShippingandTrade_August%202013_Class%20is%20Concentrating%20on%20Extending%20FPSO%20Service%20Length_Gareth%20Burton.pdf>. Accessed 10-09-2018.

Tenne, Y. A Simulated Annealing Based Optimization Algorithm. Computational Optimization in Engineering - Paradigms and Applications. 2017. https://doi.org/10.5772/66455

Tonkovich, A. L., Jarosch, K., Arora, R., Silva, L., Perry, S., McDaniel, J., Daly, F., Litt, B. Methanol production FPSO plant concept using multiple microchannel unit operations. Chemical Engineering Journal. 2008, 135, 2-8. https://doi.org/10.1016/j.cej.2007.07.014.

Toolbox, T. E. Engineering Toolbox. 2020. Available at <https://www.engineeringtoolbox.com/pumps-temperature-increase-d_313.html>. Accessed 04-15-2020.

Tso, W.W., Niziolek, A.M., Onel, O., Demirhan, C.D., Floudas, C.A., Pistikopoulos, E. N. Enhancing natural gas-to-liquids (GTL) processes through chemical looping for syngas production: Process synthesis and global optimization. Computers and Chemical Engineering. 2018, 113, 222-239. https://doi.org/10.1016/j.compchemeng.2018.03.003.

Tula, A.K., Eden, M.R., Gani, R. Process synthesis, design and analysis using a process-group contribution method. Computers and Chemical Engineering. 2015, 81, 245-259. https://doi.org/10.1016/j.compchemeng.2015.04.019.

Twu, C.H. An Internally Consistent Correlation for Predicting the Critical Properties and Molecular Weights of Petroleum and Coal-Tar Liquids. Fluid Phase Equilibria. 1984, 16(2), 137-150. https://doi.org/10.1016/0378-3812(84)85027-X.

Twu, C.H. Internally Consistent Correlation for Predicting Liquid Viscosities of Petroleum Fractions. Ind. Eng. Chem. Process Des. Dev. 1985, 24, 1287-1293. https://doi.org/10.1021/i200031a064.

Veloso, T.G.C., Sotomonte, C.A.R., Coronado, C.J.R., Nascimento, M.A.R. Multi-objective optimization and exergetic analysis of a low-grade waste heat recovery ORC application on a Brazilian FPSO. Energy Conversion and Management 2018, 174, 537-551. https://doi.org/10.1016/j.enconman.2018.08.042.

Venkatarathnam, G., Oellrich, L.R. Identification of the phase of a fluid using partial derivatives of pressure, volume, and temperature without reference to saturation properties: Applications in phase equilibria calculations. Fluid Phase Equilibria. 2011, 301, 225-233. https://doi.org/10.1016/j.fluid.2010.12.001.

Venkatasubramanian, V. The Promise of Artificial Intelligence in Chemical Engineering: Is It Here, Finally?. American Institute of Chemical Engineers Journal. 2019, 65(2), 466-478. https://doi.org/10.1002/aic.16489.

Wahab, M.N., Meziani, S.N., Atyabi, A. A Comprehensive Review of Swarm Optimization Algorithms. PLoS ONE. 2015, 10(5): e0122827 https://doi.org/10.1371/journal.pone.0122827

Whitley, D. A genetic algorithm tutorial. Statistics and Computing. 1994, 4, 65-85. https://doi.org/10.1007/BF00175354.

Wu, J., Qian, X., Wang, M. Y. Advances in generative design. Computer-Aided Design. 2019, 116.

Wu, W., Henao, C.A., Maravelias, C.T. A superstructure representation, generation, and modeling framework for chemical process synthesis. AIChE Journal. 2016, 62(9). https://doi.org/10.1002/aic.15300.

Yeomans, H., Grossmann, I. E. A systematic modeling framework of superstructure optimization in process synthesis. Computers and Chemical Engineering. 1999, 23(6), 709-731. https://doi.org/10.1016/S0098-1354(99)00003-4.

Yuan, Z., Chen, B. Process Synthesis for Addressing the Sustainable Energy Systems and Environmental Issues. Process Systems Engineering. 2012, 58(11), 3370-3389. https://doi.org/10.1002/aic.13914.

Yuan, Z., Chen, B., Gani, R. Applications of process synthesis: Moving from conventional chemical processes towards biorefinery processes. Computers and Chemical Engineering. 2013, 49(11), 217-229. https://doi.org/10.1016/j.compchemeng.2012.09.020.

Zhang, Y., Sunarso, J., Liu, S., Wang, R. Current status and development of membranes for CO2/CH4 separation: A review. International Journal of Greenhouse Gas Control. 2013, 12, 84-107. https://doi.org/10.1016/j.ijggc.2012.10.009.

Zilinskas, A., Zhigljavsky, A. Stochastic Global Optimization: A Review on the Occasion of 25 Years of Informatica. Informatica. 2016, 27(2), 229-256. https://doi.org/10.15388/Informatica.2016.83.